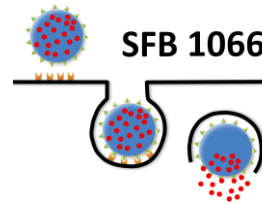




UNIVERSITÄTS**medizin.**
MAINZ

JOHANNES GUTENBERG
UNIVERSITÄT MAINZ



**Suitability of different multi-functionalized nanocarriers
aimed to address antigen presenting cells for
vaccination purposes, and parameters that regulate
unwanted accumulation of nanocarriers in the liver**

Dissertation

Zur Erlangung des Grades

„Doktor der Naturwissenschaften“

an der Johannes-Gutenberg-Universität Mainz

(Fachbereich Biologie)

vorgelegt von

Cinja Aline Kappel

geboren am 25. Juni 1988 in Karlsruhe

Mainz, Oktober 2019

D77 (Dissertation Johannes Gutenberg University Mainz)

Dekan: Prof. Dr. Walter Stöcker

Erstprüfer: 

Zweitprüfer: 

Tag der mündlichen Prüfung: 03.12.2019

„Was wir wissen, ist ein Tropfen; was wir nicht wissen, ein Ozean.“

Isaac Newton

DANKSAGUNG

[REDACTED]

[REDACTED]

[REDACTED]

[REDACTED]

[REDACTED]

[REDACTED]

DECLARATION OF AUTHORSHIP

I hereby confirm that I have authored this PhD thesis independently and without use of other than the indicated resources.

Mainz, October 7th 2019

Cinja Kappel

[REDACTED]

[REDACTED]

[REDACTED]

[REDACTED]

[REDACTED]

[REDACTED]

[REDACTED]

[REDACTED]

[REDACTED]

[REDACTED]

[REDACTED]

[REDACTED]

[REDACTED]

[REDACTED]

[REDACTED]

[REDACTED]

[REDACTED]

[REDACTED]

[REDACTED]

[REDACTED]

TABLE OF CONTENT

TABLE OF CONTENT.....	I
LIST OF FIGURES.....	II
LIST OF TABLES.....	III
ABBREVIATIONS	IV
1. ABSTRACT.....	II
2. SUMMARY	2
2.1 Key players and important organs of the immune system.....	2
2.2 Cancer immunotherapy	9
2.3 Nanomedicine	10
2.4 Use of nanoparticles for tumor therapy	12
2.4.1 Tumor-targeting nanoparticles	12
2.4.2 Nanoparticle-based tumor immunotherapy	13
2.5 Dendritic cells as target for nanoparticle-based vaccine	14
2.5.1 Intracellular Toll-like receptors as suitable PRRs for DC activation	20
2.5.2 C-type lectin receptors as targeting structures	24
2.5.2.1 DEC205 receptor	26
2.5.2.2 CD206 receptor.....	29
2.6 Influence of the liver on the biodistribution of nanoparticles	31
3. OUTLOOK.....	35
4. REFERENCES	38
5. APPENDIX	58
5.1 Publication 1	58
5.2 Publication 2.....	65
5.3 Publication 3.....	85
5.4 Publication 4.....	99
5.5 Publication 5.....	106
5.6 Publication 6.....	120
5.7 Publication 7.....	163

LIST OF FIGURES

Figure 1: Compartmentation of the spleen. Different zones also differ in their immune cell composition.....	4
Figure 2: Structure of the spleen and its blood vessels. Sections of the white pulp show the different zones.....	4
Figure 3: Section of the lymph node showing different compartments and vessels.....	5
Figure 4: Cellular composition of the liver (average frequencies of the various cell types are indicated, modified from Manna & Abdel-Wahhab 2016).....	7
Figure 5: Space of Disse and its associated cells	8
Figure 6: Different nanoparticle systems used in the field of nanomedicine	11
Figure 7: <i>In situ</i> vaccination of dendritic cells.....	16
Figure 8: TLR9 signalling after CpG ODN binding	22
Figure 9: Schematic construction of different C-type lectin receptors.....	25

LIST OF TABLES

Table 1: Percentage of the main immune cell populations in the secondary lymphoid organs.....	3
Table 2: Overview of the different nanoparticle formats biologically evaluated in this work	18

ABBREVIATIONS

APC	antigen presenting cell
BCR	B cell receptor
BMDC	bone marrow derived cell
CAR	chimeric antigen receptor
CD	cluster of differentiation
Clec9a	C-Type lectin domain containing 9A
CLR	C-type-lectin receptor
CpG	Cytosine-phosphate-Guanine
CRD	carbohydrate recognition domain
CTL	cytotoxic T cells
CTLA-4	cytotoxic T lymphocyte associated protein 4
DAMPs	damage-associated molecular patterns
DC	dendritic cell
DC-SIGN	dendritic cell-specific ICAM-grabbing non-integrin
DHPMA	2,3-dihydroxypropyl methacrylate
DNA	deoxyribonucleic acid
ECM	extracellular matrices

EPR	enhanced permeability and retention
Fab	fragment antigen binding
Fc	fragment crystallizable
FDA	food and drug administration
HPMA	hydroxypropylmethacrylamide
ICAM	intercellular adhesion molecule
IgG	immunoglobulin G
IL	interleukin
INF	interferon
IRAK-4	IL-1 receptor-associated kinase-4
IRF	interferon regulation factors
L18-MDP	L18-muramyl dipeptide
LMA	lauryl methacrylate
LPS	lipopolysaccharide
LSEC	liver sinusoidal endothelial cell
L-SIGN	liver/lymph node-specific intercellular adhesion molecule-3-grabbing integrin
LY75	lymphocyte Antigen 75
MAPK	mitogen-activated protein kinase
MART 1	melanoma antigen recognized by T cells 1

MBL	mannose-binding lectin
Mincle	macrophage-inducible C type lectin
mDC	myeloid dendritic cell
MHCI/II	major histocompatibility complex I/II
MyD88	myeloid differentiation primary response protein 88
NLR	<i>NOD-like</i> receptors
NOD	nucleotide-binding and oligomerization domain
NPC	non-parenchymal cells
ODNs	oligodinucleotides
OVA	ovalbumin
PAMPs	pathogen-associated molecular patterns
PD-1	programmed cell death protein 1
PDL-1	programmed cell death 1 ligand 1
pDC	plasmacytoid dendritic cell
PEG	polyethylene glycol
PRR	pattern recognition receptor
RES	reticuloendothelial system
RNA	ribonucleic acid
scFv	single chain variable fragments

SIINFEKL	one-letter code for a peptide sequence
SR	scavenger receptor
TAA	tumor-associated antigen
TCR	T cell receptor
T _h	T helper cell
TIR	Toll/IL-1-receptor
TLR	toll-like receptor
TME	tumor microenvironment
TMM	tumor micromilieu
TRAF3	TNF receptor-associated factor 3
TRIF	TIR-domain-containing adapter-inducing interferon- β
TRP-2	Tyrosinase-related Protein 2
TSA	tumor-specific antigen
T-VEC	Talimogen laherparepvec
WHO	world health organization
XCR1	X-C motif chemokine receptor 1

PREFACE

The present work summarizes and discusses the main results of the attached publications or manuscripts in preparation/submitted manuscripts prepared in cooperation with the Department of Organic Chemistry, the Department of Physical Chemistry (Johannes Gutenberg University, Mainz), Biopharmaceutical New Technologies (BioNTech, Mainz) Corporation and TRON–Translational Oncology (University Medical Center of the Johannes Gutenberg, Mainz). In the following passage the author contribution and a short summary for each published or unpublished work is listed.

Publication 1:

Selective Uptake of Cylindrical Poly(2-Oxazoline) Brush-AntiDEC205 Antibody-OVA Antigen Conjugates into DEC-Positive Dendritic Cells and Subsequent T-Cell Activation (Chemistry - A European Journal, Communication, 2014)

*Jasmin Bühler,[a, b] Sabine Gietzen,[a] Anika Reuter,[a, c] **Cinja Kappel,[e]** Karl Fischer,[a] Sandra Decker,[a] David Schäffel,[d] Kaloian Koynov,[d] Matthias Bros,*[e] Ingrid Tubbe,[e] Stephan Grabbe,*[c, e] and Manfred Schmidt*[a, b, c]*

[a] Institute for Physical Chemistry, University of Mainz, Jakob-Welder Weg 11, 55099 Mainz (Germany)

[b] Graduate School Materials Science, Staudinger Weg 9, 55128 Mainz (Germany)

[c] Max Planck Graduate Center, Staudinger Weg 9, 55128 Mainz (Germany)

[d] Max Planck Institute for Polymer Research, Ackermannweg 10, 55128 Mainz (Germany)

[e] Department of Dermatology, University Medical Center of the Johannes Gutenberg University Mainz, Langenbeckstrasse 1, 55131 Mainz (Germany)

[*] These authors contributed equally to this work.

The modification of nanocarriers with targeting antibodies allows a delivery of biological components to specific cell populations. In immunotherapy, DEC205 receptor positive dendritic cells (DCs) are a popular target since these cells can induce potent T cell immune responses. This publication presents a cylindrical brush polymer with poly-2-oxazoline side chains each one carrying an azide endgroup. Click conjugation of anti-

DEC205 antibody onto the polymer brush yielded a specific uptake into DEC205⁺ mouse bone marrow-derived dendritic cells (BMDCs), but not in DEC205⁻ BMDCs or non-DCs. BMDCs pre-treated with antibody and antigen conjugated multifunctional polymer brush resulted in a much stronger T-cell stimulatory capacity than pre-treatment with polymer-antigen conjugate or soluble antigen.

Author contribution:

- performance and evaluation of *in vitro* proliferation assays

Publication 2:

Targeting cells of the immune system: mannosylated HPMA-LMA block-copolymer micelles for targeting of dendritic cells (Nanomedicine, Research Article, 2016)

Nicole Mohr^{‡, 1}, Cinja Kappel^{‡, 2}, Stefan Kramer¹, Matthias Bros^{, 2}, Stephan Grabbe^{** , 2} & Rudolf Zentel^{***, 1}*

¹ Institute of Organic Chemistry, Johannes Gutenberg-University Mainz, Duesbergweg 10-14, 55099 Mainz, Germany

² Department of Dermatology, University Medical Center, Johannes Gutenberg-University Mainz, Obere Zahlbacher Straße 63, 55131 Mainz, Germany

‡ Authors contributed equally

The targeted delivery of antigen and stimulating adjuvant to antigen presenting cells (APCs) like dendritic cells (DCs) is a promising approach for tumor immunotherapy. We describe the suitability of mannosylated HPMA-LMA block copolymer micelles as DC targeted nanocarrier. Mannose conjugated HPMA-LMA block copolymer micelles showed a specific binding to mannose receptor (MR) expressing bone marrow derived dendritic cells (BMDCs) and splenic DCs. Confocal images and blocking assays with mannan revealed an uptake into BMDCs in a MR-dependent manner. In addition, HPMA-LMA block copolymer micelles loaded with L18-MDP induced DC activation.

Author contribution:

- performance and evaluation of all biological experiments
- preparation of the manuscript together with [REDACTED]

Publication 3:

Functionalization of Active Ester-Based Polymersomes for Enhanced Cell Uptake and Stimuli-Responsive Cargo Release (Biomacromolecules, Article, 2016)

Martin Scherer,[†] Cinja Kappel,[‡] Nicole Mohr,[†] Karl Fischer,[§] Philipp Heller,[†] Romina Forst,[†] Frank Depoix,^{||} Matthias Bros,[‡] and Rudolf Zentel[†]

[†] Institute of Organic Chemistry, Johannes Gutenberg-University Mainz, Duesbergweg 10-14, 55128 Mainz, Germany

[‡] Department of Dermatology, University Medical Center, Johannes Gutenberg-University Mainz, Obere Zahlbacher Straße 63, 55131 Mainz, Germany

[§] Institute of Physical Chemistry, Johannes Gutenberg University Mainz, Jakob-Welder-Weg 11, 55099 Mainz, Germany

^{||} Institute of Zoology, Johannes Gutenberg University Mainz, J.-J.-Becher-Weg 7, 55128 Mainz, Germany

This work describes the use of poly(2,3-dihydroxypropyl methacrylamide) (P(DHPMA))-based amphiphilic block copolymer vesicles (polymersomes) as potential nanovaccine targeting dendritic cells. To allow a pH-responsive disintegration for cargo release 2-(2,2-dimethyl-1,3-dioxolane-4-yl)ethyl methacrylate was incorporated into the hydrophobic block (lauryl methacrylate). The polymersomes showed only minor cytotoxicity and mannose as targeting structure provided selective targeting of bone marrow derived dendritic cells, which express the mannose receptor CD206.

Author contribution:

- **performance and evaluation of all biological experiments**

Publication 4:

PeptoSomes for Vaccination: Combining Antigen and Adjuvant in Polypept(o)ide-Based Polymersomes. (Macromolecular Bioscience, Communication, 2017)

*Benjamin Weber, **Cinja Kappel**, Martin Scherer, Mark Helm, Matthias Bros, Stephan Grabbe, and Matthias Barz**

B. Weber, Dr. M. Scherer, Dr. M. Barz: Institute of Organic Chemistry Johannes Gutenberg-University Mainz, Duesbergweg 10-14, 55128 Mainz, Germany, E-mail: barz@uni-mainz.de

C. Kappel, Dr. M. Bros, Prof. S. Grabbe: Department of Dermatology, University Medical Center, Johannes Gutenberg-University Mainz, Obere Zahlbacher Straße 63, 55131 Mainz, Germany

Prof. M. Helm: Department of Pharmacy and Biochemistry, Johannes Gutenberg-Universität Mainz, Staudinger Weg 5, 55128 Mainz, Germany

In this work, the first vaccine based on a PeptoSome containing a model antigen (SIINFEKL) and an adjuvant (CpG) is introduced. PeptoSomes are polypept(o)ide-based polymersomes built of a block copolymer with polysarcosine (PSar) as the hydrophilic block and poly(benzyl-glutamic acid) (PGlu(OBn)) as the hydrophobic one. Loaded with SIINFEKL and CpG bone marrow derived dendritic cells (BMDCs) engulfed the PeptoSomes in *in vitro* culture and led to their activation. Furthermore, DC-mediated antigen-specific T-cell proliferation was achieved which demonstrates the potential of PeptoSomes as a versatile platform for vaccination.

Author contribution:

- **performance and evaluation of all biological experiments**

Publication 5:

Protein corona-mediated targeting of nanocarriers to B cells allows redirection of allergic immune responses. (Journal of Allergy and Clinical Immunology, Article, 2018)

*Limei Shen, PhD,^a Stefan Tenzer, PhD,^b Wiebke Storck, MSc,^b Dominika Hobernik, MSc,^a Verena Katherina Raker, PhD,^a Karl Fischer, PhD,^c Sandra Decker, PhD,^c Andrzej Dzionek,^d Susanne Krauthäuser, PhD,^d Mustafa Diken, PhD,^e Alexej Nikolaev,^f Joachim Maxeiner, MSc,^g Petra Schuster,^g **Cinja Kappel, MSc,^a** Admar Verschoor, PhD,^h Hansjörg Schild, PhD,^{b*} Stephan Grabbe, MD,^{a*} and Matthias Bros, PhD^{a*}*

a: the Department of Dermatology, b: the Institute for Immunology, f: the Institute for

Molecular Medicine, and g: the Asthma Core Facility, Research Center for Immunotherapy,

University of Mainz Medical Center; c: the Department of Physical Chemistry,

University of Mainz; d: Miltenyi Biotec GmbH, Bergisch Gladbach; e: TRON-Translational

Oncology at the University Medical Center of the Johannes Gutenberg University

gGmbH, Mainz; and h: the Institute for Systemic Inflammation Research,

Universität zu Lübeck.

*These authors contributed equally to this work.

Here, we analysed the relevance of the protein corona on cell type-selective uptake of dextran-coated nanoparticles (DEX-NPs) and determined the outcome of vaccination with NPs that codeliver antigen and adjuvant in disease models of allergy. DEX-NPs triggered lectin-induced complement activation, yielding deposition of activated complement factor 3 on the DEX-NP surface. In the spleen, DEX-NPs targeted predominantly B cells through complement receptors 1 and 2. The DEX-NP vaccine provoked much stronger OVA-specific IgG_{2a} production than coadministered soluble OVA plus CpG oligodeoxynucleotides whereas the B-cell binding of the DEX-NP vaccine was critical for this antibody production. In a therapeutic setting, treatment of OVA-sensitized mice with the DEX-NP vaccine prevented induction of anaphylactic shock and allergic asthma accompanied by IgE inhibition. This intrinsic B-cell targeting property of lectin-coated NPs can be exploited for treatment of allergic immune responses.

Author contribution:

- assistance for *in vivo* experiments

Publication 6:

Sometimes less is more: Antibody surface density determines the biodistribution of peptobrush nanoparticles (submitted for ACS Nano)

Cinja Kappel, †

† Department of Dermatology, University Medical Center of the Johannes Gutenberg, University Mainz, Langenbeckstrasse 1, D-55131 Mainz, Germany

* Institute for Organic Chemistry, Johannes Gutenberg University, Duesbergweg 10-14, D-55099 Mainz, Germany

‡ Institute for Physical Chemistry, Johannes Gutenberg University, Welder Weg 11, D-55099 Mainz, Germany

TRON–Translational Oncology at the University Medical Center of the Johannes Gutenberg University GmbH, Freiligrathstr. 12, Mainz 55131, Germany

§ Max Planck Institute for Polymer Research, Ackermannweg 10, 55128 Mainz, Germany

§ Biontech AG, An der Goldgrube 12, 55131, Mainz

This work further elucidates the mechanisms of unwanted liver accumulation of nanocarriers decorated with targeting antibodies. We employed sarcosine-based peptobrushes as nanocarriers which are characterized by a long circulation time, and low organ accumulation as well as little unspecific cell binding. This peptobrush was conjugated with defined average numbers (2, 6 and 12) of an antibody specific for the surface receptor DEC205 that is expressed by conventional dendritic cells type 1 (cDC1). Our data point to a direct correlation between the number of antibodies per peptobrush and the extent of peptobrush accumulation in the liver. Intermediate and high antibody density are efficiently engaged and internalized by liver sinusoidal endothelial cells (LSEC), whereas Kupffer cells play a minor role. Subsequently, peptobrushes with intermediate/high antibody density reached cDC1 only at low extent, whereas conjugation of peptobrushes with 2 antibodies resulted in pronounced binding to target cells in

the spleen and only low liver accumulation. Additionally, blocking experiments revealed that liver sinusoidal endothelial cells (LSECs) bind antibody-conjugated peptobrushes via their Fc receptors, since these recognize the Fc part of the targeting antibody. These results suggest an advantage of lower antibody amounts in the design of targeted nanocarriers to prevent extensive liver accumulation.

Author contribution:

- **design, conduction and performance of all *in vitro* and *in vivo* biological experiments (except imaging)**
- **preparation of the manuscript together with [REDACTED] and [REDACTED]**

Publication 7:

Molecular Vaccines based on Cylindrical Bottlebrush Polymers: Influence of Size, Shape and Surface Functionality on Antigen specific Immunity (in preparation for ACS Nano)

[REDACTED] ***Cinja Kappel,**** [REDACTED]

‡Institute for Organic Chemistry, Johannes Gutenberg University, Duesbergweg 10-14, D-55099 Mainz, Germany

†Institute for Physical Chemistry, Johannes Gutenberg University, Welder Weg 11, D-55099 Mainz, Germany

#Max Planck Institute for Polymer Research, Ackermannweg 10, D-55128 Mainz, Germany

*Department of Dermatology, University Medical Center of the Johannes Gutenberg, University Mainz, Langenbeckstrasse 1, D-55131 Mainz, Germany

§TRON–Translational Oncology at the University Medical Center of the Johannes Gutenberg University GmbH, Freiligrathstr. 12, Mainz 55131, Germany.

‡Biopharmaceutical New Technologies (BioNTech) Corporation, An der

Goldgrube 12, Mainz 55131, Germany.

This work reports on the synthesis of differentially sized and shaped cylindrical brush polymers as nanovaccines. The cylindrical brush polymers consist of a polylysine backbone and polysarcosine side chains (peptobrushes) and are thus completely based on endogenous amino acids. The size, shape and surface functionality can be completely controlled chemically. A detailed protocol for the step-wise conjugation of the peptobrushes with the model antigen ovalbumin (OVA), the immune activator (CpG) and the targeting antibody (aDEC205) is described, that allows the precise control of the average number of each of these components per peptobrush. Peptobrushes were very well tolerated by cells, showed no aggregation in concentrated blood serum and extended circulation in the blood stream of mice after intravenous injection independent on size and shape. Interestingly the vaccine with the rod-like shape led to the most potent T cell proliferation response *in vitro* (OTI model) and was able to provide a protection from tumor growth in mice after subcutaneous vaccination. These findings underline the meaning of nanoparticle architecture to maximize immunity.

Author contribution:

- **performance and evaluation of some *in vitro* biological experiments**

1. ABSTRACT

The treatment of severe immune diseases such as cancer, allergy or autoimmunity demands new strategies to overcome the development of resistances or relapses. The employment of nanoparticles as carriers for the delivery of biological components targeting specific tissues or cell types might help to meet these challenges. Especially their employment for the vaccination of antigen presenting cells (APCs), a pivotal group of immune cells, has turned out to be a promising immunotherapeutic approach. In this case, nanocarriers ensure the co-delivery of antigen and adjuvant, the two components required for a vaccination.

The aim of this thesis was to investigate the potential of different types of nanoparticles for an *in situ* vaccination of APCs to induce an effective immune response. Therefore, inorganic and organic, polymer-based non-toxic nanoparticles were synthesized, and modified with various biological components with the aim to target and activate APCs. These nanocarriers were investigated in cell cultures and mouse models regarding their biodistribution, APC targeting efficiency and their capacity to induce T cell immune responses.

To achieve an active targeting of APCs their expression of C-type lectins which constitute pathogen recognizing receptors, were exploited. Natural ligands for these receptors or corresponding antibodies were attached to the nanocarriers which led to a successful targeting of dendritic cells and B cells *in vitro* and *in vivo*, as confirmed by flow cytometry and confocal microscopy. Comprehensive biodistribution experiments of sarcosine-based polymer brushes on organ and cellular level provided more insights into mechanisms leading to liver trapping of nanoparticles, which is often observed after their systemic application. This study revealed that antibody-coated polymer-brushes are cleared by Fc (fragment crystallizable) receptors of liver sinusoidal endothelial cells and indicated that a lower antibody density on nanocarriers is preferable since this largely prevented their recognition by Fc receptors compared to high antibody amounts, and thereby facilitated the intended dendritic cell (DC)-specific targeting.

Functionalization of the nanocarriers with a toll-like receptor (TLR) ligand or nucleotide-binding oligomerization domain (NOD)-like receptor (NLR) ligand as an adjuvant and SI-INFEKL/Ovalbumin (OVA), a protein derived from the chicken egg as model antigen led to a maturation of targeted dendritic cells *in vitro* and induced a T cell response *in vitro* and *in vivo*. Finally, the efficiency of this approach was confirmed in tumor and allergy mouse models.

To conclude, the obtained results indicate a functional activity of different nanocarriers, give new insights into the requirements for a nanoparticle-based APC vaccination and show that these can be fulfilled by several types of nanoparticles.

2. SUMMARY

2.1 Key players and important organs of the immune system

Mammals possess several defence barriers to prevent the entry of foreign materials or pathogens. These barriers encompass: i) the skin/mucosal microbiota which prevents the accumulation of virulent pathogens, ii) the stratum corneum as a physical barrier, iii) the presence of RNases and other enzymes intended to degrade pathogens. Besides the just mentioned passive mechanisms, the organism fends pathogens which overcame these barriers with a highly regulated system of various interacting cells and humoral components collaborating with each other. This immune system can roughly be divided into an innate and an adaptive part with cellular and humoral components on each side. Both are specialized to recognize and neutralize potentially harmful substances ¹.

APCs are important immune cell populations which induce tolerance under steady state conditions sparing the body's own tissues and cells and adaptive immune responses in case of an inflammation. Classical APCs are B cells, macrophages and dendritic cells which can detect and capture antigens or pathogens due to several cell surface receptors like members of the pattern recognition receptor (PRR) family or B cell receptors (BCRs) ^{2,3}. Afterwards the antigen/pathogen is engulfed and processed prior to its presentation in a major histocompatibility complex I (MHC I) or MHC II context ¹. Different types of APCs are found throughout the body, in various organs and in the blood, but the highest amounts are apparent in the secondary lymphoid organs, predominantly in the spleen and the lymph nodes. After antigen contact in the periphery dendritic cells have the possibility to migrate to draining secondary lymphoid organs where they prime antigen-specific T lymphocytes ⁴.

B cells mediate the humoral immune response, based on antibody production by plasma B cells. Their BCR detects antigen, phagocytoses and degrades it followed by the presentation of derived antigens on the cell surface in context with MHC II. Antigen-specific T helper (T_h) cells can then bind this antigen-MHC II complex with their T cell receptors (TCR) and initiate the activation of the B cell followed by the transformation to its plasma cell state. The thereby produced antibodies mark the pathogen leading to its destruction. Nevertheless, B cells can also be activated T cell-independently which often results in a rapid production of antibodies with lower affinity ^{5,6}.

Macrophages are large phagocytes which also present engulfed antigen and can enhance the T cell response although they are not capable of activating naïve T cells ^{7,8}.

Whereas some immune cells are clearly associated with either the innate immune system like natural killer cells or mast cells or with the adaptive part like T cells or B cells, DCs represent a crucial link between the first innate defence barrier and the adaptive pathogen-specific immune response ⁹⁻¹¹. Due to their high specialization to capture and degrade antigen, to migrate to the secondary lymphoid organs and efficiently activate naïve T cells, they are considered as professional APCs ¹²⁻¹⁴. Their name-giving, numerous long dendritic cell protrusions extend their membrane surface and allow, in combination with a high expression of MHC molecules, the presentation of large amounts of antigen. This presentation in an MHCI and MHCII complex initiates the activation of naïve cytotoxic T cells, by a process named cross-presentation, or activation of naïve T_h cells, depending on the DCs' subtype ¹⁵.

B cells and T cells are the main cell populations in the secondary lymphoid organs whereas DCs and macrophages are much rarer (table 1). The spleen is organized in different areas. It can be divided into a white and a red pulp layer. The white pulp is reached first by in-coming blood from the arterioles and contains most of the immune cells like T cells, dendritic cells and macrophages. The red pulp, responsible for removal of old erythrocytes and recycling platelets, also contains subtypes of dendritic cells and macrophages (figure 1 & figure 2) ^{1,16}. The lymph nodes are compartmentalized by trabeculae. B cells and dendritic cells are found in the primary lymphoid follicle of each compartment whereas T cells are located more towards the center in the paracortical area. The medullary cords near the center and the entrance of blood vessels contain mainly macrophages (figure 3) ¹.

Table 1: Percentage of the main immune cell populations in the secondary lymphoid organs

	B cells	T cells	DCs	Mphs
spleen	~ 50 %	~ 30 %	~ 2 %	1-2 %
lymph nodes	~ 12 %	~ 70 %	~ 1 %	1-2 %

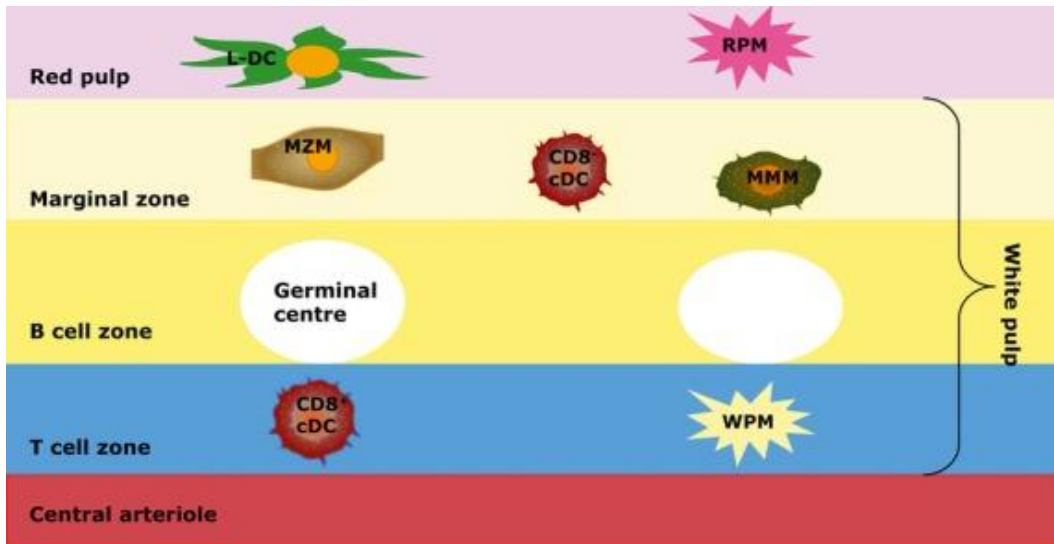


Figure 1: Compartmentation of the spleen. Different zones also differ in their immune cell composition.

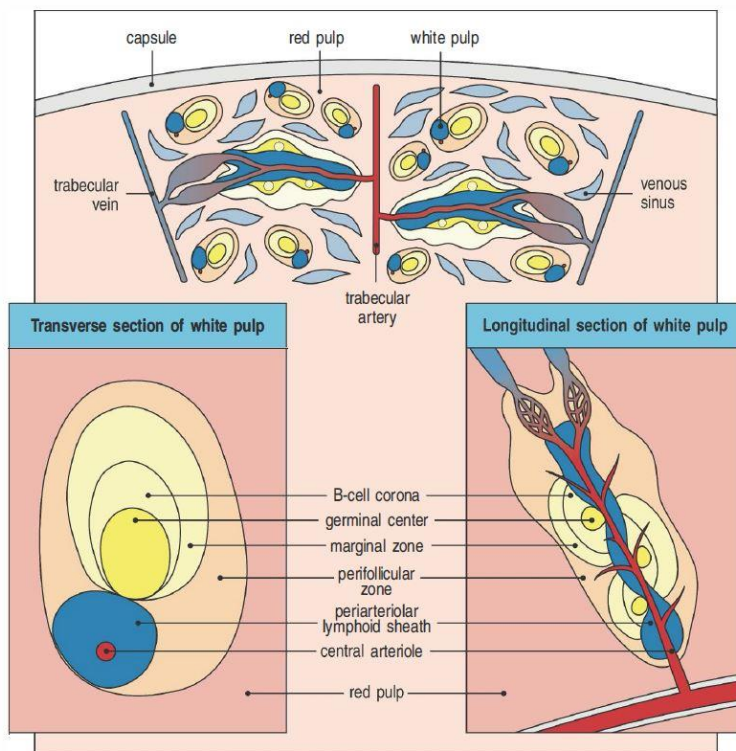


Figure 2: Structure of the spleen and its blood vessels. Sections of the white pulp show the different zones.

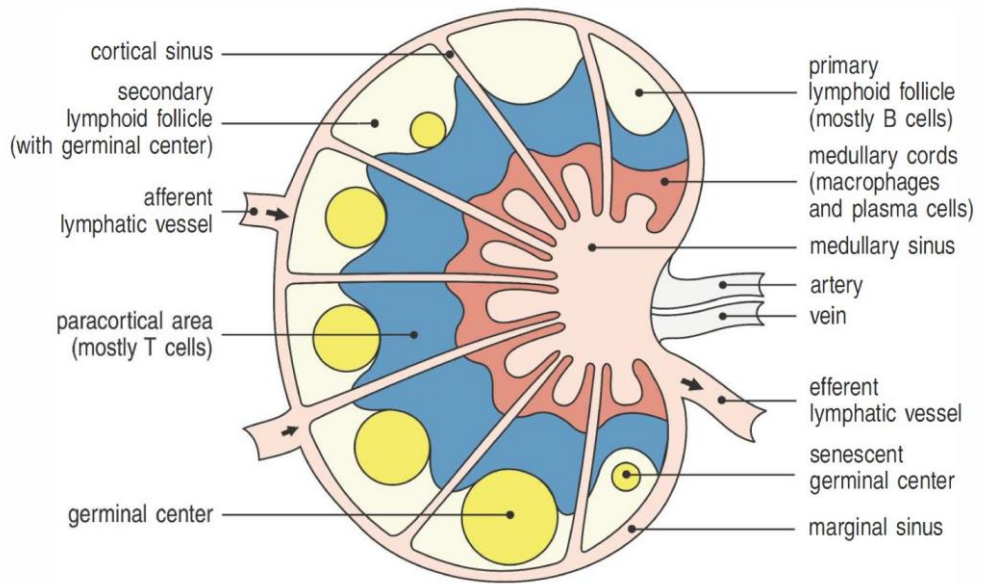


Figure 3: Section of the lymph node showing different compartments and vessels.

Although spleen and lymph nodes are considered as the key organs of action regarding T cell priming, the immunological functions of the liver get more and more attention. The liver is responsible for many different functions of the body. It acts primarily as a metabolizing organ. Besides filtration and inactivation of harmful substances, the liver additionally plays a role in the regulation of hormones, the glucose metabolism and in digestive processes ^{17,18}. But other than this it also displays some purposes in immune response regulation although it does not belong to the immunological organs per definition ^{19,20}.

There is a well-developed innate immune system within the liver which mainly shows high capacity to induce immune tolerance ²¹⁻²³ but there is also evidence for efficient innate immunity. Adaptive immunity, in contrast, is found only rarely in this organ ²⁴. As the liver is continuously exposed to foreign material like bacterial components coming from the digestive system, keeping up the tolerogenicity is very important. The liver cells can be classified in parenchymal cells and non-parenchymal cells (NPCs), including the immune cells. Within the NPCs around 25 % are lymphocytes, T cells, B cells and NK cells. About 20 % of the NPC population are Kupffer cells, the main group of liver macrophages, and only 1 % are resident dendritic cells. Besides the typical immune cells usually found in lymphoid organs, the liver NPCs are also composed of about 50 % liver sinusoidal endothelial cells (LSECs) (figure 4) ²⁵.

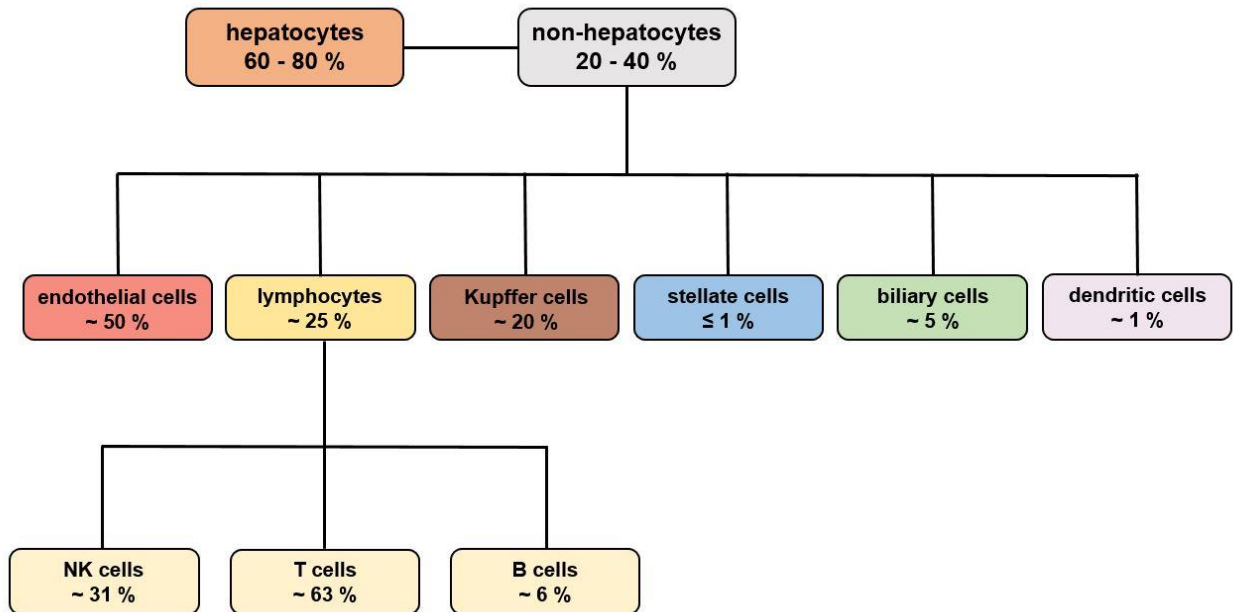


Figure 4: Cellular composition of the liver (average frequencies of the various cell types are indicated, modified from Manna & Abdel-Wahhab 2016).

These cells are specialized endothelial cells which line the liver sinusoid and form a border in the gap between blood cells and hepatocytes called space of Disse (figure 5) ²⁶. Morphologically, LSECs are highly fenestrated and deficient of a basement membrane making them highly permeable. Their fenestrae have a size of 50 to 150 nm in diameter dependent on their localization within the liver. Smaller ones can be found in the centrilobular region whereas larger ones are located in the periportal region ^{27,28}. Exposed to the venous portal blood coming from the digestive system LSECs clear the blood by guiding proteins, macromolecules or nano-sized materials like bacterial compounds through passing them onto hepatocytes and stellate cells (transcytosis) ²⁹. LSECs are also capable of endocytosis and possess the highest phagocytic capacity in the mammalian body. Additionally, they serve as a scaffolding several liver immune cell, like Kupffer cells, cling to and exert well-developed scavenger functions, since they express SR (scavenger receptor)-A (52), SR-B, and SR-H ³⁰. Further, LSECs express PRRs like CD206, L-SIGN (Liver/lymph node-specific intercellular adhesion molecule-3-grabbing integrin), the endocytic Fc gamma-receptor IIb2 and TLRs ³¹⁻³⁴ making them interesting regarding immune modulation. The tolerogenic environment within the liver is highly shaped by LSECs. Due to the continuous exposition to

lipopolysaccharides LPS derived from the gut, they are tolerant to consistent low concentrations and thereby contribute to maintenance of endotoxin tolerance within the liver. Only upon detection of a change in LPS concentration they release proinflammatory cytokines³⁵. They also act as sentinel cells modulating immune effector cells in the course of inflammation and play a role in hepatocyte infection^{36–38}. T cell activation can be reduced due to an interaction between the T cell associated CD44 and LSECtin³⁹ and LSECs are also reported to cross-present but rather induce antigen specific T cell tolerance⁴⁰. Notably, there is also evidence of cell killing by cytotoxic T cells after LSEC-mediated cross priming⁴¹. Even though, LSECs are not defined as APCs in a traditional way, they possess some of their features.

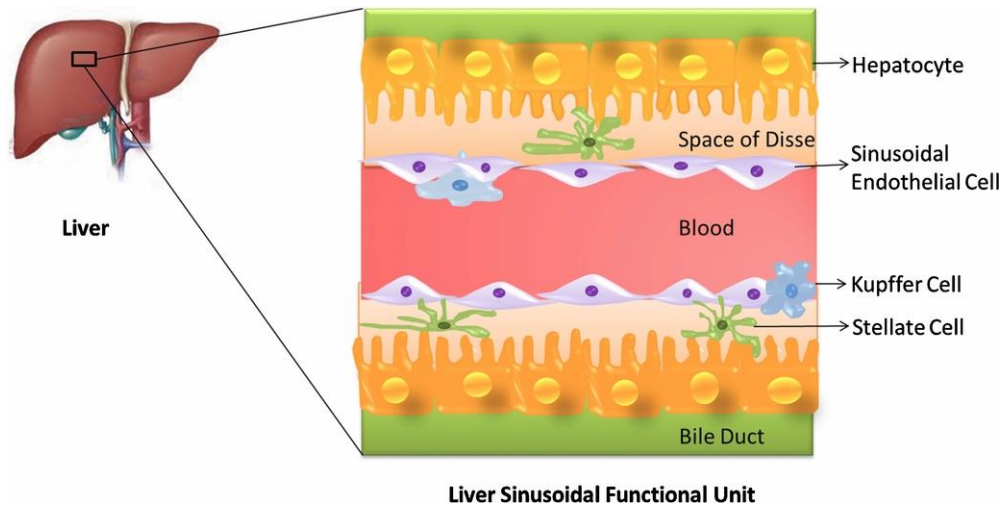


Figure 5: Space of Disse and its associated cells

2.2 Cancer immunotherapy

The term immunotherapy describes an intervention in the immune system at different checkpoints. In the field of tumor treatment this therapy is usually supposed to activate the body's own immune system and/or to abolish tolerance towards tumor cells. Non-specific immunotherapies using immunostimulatory agents like CpG ODNs (Cytosine-phosphate-Guanine oligonucleotides) ⁴² or cytokines like interleukins (IL) or interferons (INF), for example INF α in the treatment of melanoma ⁴³ lead to an improved action of immune cells like macrophages or natural killer cells which can destroy tumor cells, slow down tumor growth or prevent further metastasis ⁴⁴. So-called checkpoint inhibitors are another possibility, as these block essential protein interactions, leading to an amplified immune response. Antibodies against the cytotoxic T lymphocyte associated protein 4 (CTLA-4) (Ipilimumab, Tremelimumab) or anti-programmed cell death protein 1 (anti-PD-1)/ anti-programmed cell death 1 ligand 1 (anti-PDL-1) (Nivolumab, Atezolizumab), for example, are effective treatments for advanced melanoma and many other cancerous diseases ^{45,46}. As of late there is also the option of oncolytic virus therapy: In 2015, the food and drug administration (FDA) approved talimogene laherparepvec (Imlygic), or T-VEC a genetically modified herpes simplex virus ⁴⁷. For the treatment of malignancies of the hematopoietic system chimeric antigen receptor (CAR) T cell therapies have become successful. In this process, T cells are removed from the patient's blood and genetically modified in a way that the T cells *de novo* express an tumor antigen specific receptor and are able to destroy the dangerously altered cells after reinjection in the patient's body ⁴⁸.

Vaccines designed to prevent cancer are already in the clinical daily routine and protect from virus infections which are highly associated with carcinogenesis ⁴⁹. Unfortunately, only few cancer types fall into this category which is the reason why ongoing research also focusses on production of a direct vaccination against tumor antigens and thereby prevent tumor formation. And even therapeutic vaccinations like autologous- and allogenic cell-based vaccines can be an innovative treatment option for patients even in the case of already existing cancer diseases ⁵⁰⁻⁵². In the case of autologous cell vaccines dendritic cells are removed from the patient's blood and pulsed with lysates of the patient's tumor cells to provide tumor-associated antigens (TAAs) and exposed to an immune adjuvant to stimulate the cells. Afterwards, these activated dendritic cells, presenting tumor antigens, are reinjected into the patient to achieve an activation of cytotoxic T cells and/or T_h cells. Allogenic cell-based vaccines are using lysates of tumor cells not belonging to the patient but including TAAs or the dendritic cells are genetically modified in a way that they express and present the TAA.

Despite great progress in the field of cancer immunotherapy, there are still many challenges to overcome. Off target effects, insufficient immunogenicity or low bio stability are common problems. In several cases these difficulties can be solved with the help of diverse nanoparticles. Tumor necrosis factor α (TNF α) for example, a potent cytokine, has very severe toxic effects when applied systemically⁵³. Treatment is therefore limited to local administration with techniques like isolated limb perfusion⁵⁴. Instead TNF α embedded in a nanocarrier can be given intravenously as it is less toxic and accumulates preferably in tumor tissues due to the enhanced permeability and retention (EPR)-effect while sparing healthy cells⁵⁵. Nanoparticles can also modulate immune tolerance and inhibitory effects. It has been reported that T cells, often anergic in the TME, can be restored with their proliferative capacity by IL-2 functionalized nanocapsules⁵⁶. Tumor cells themselves can also be targeted and reformed from an immune suppressive to a vulnerable state with the help of inhibitors incorporated in nanoparticles for example⁵⁷. Regarding cancer vaccination, nanoparticles are designed to act as a platform delivering high amounts of tumor associated antigen and stimulating adjuvants to APCs followed by a T cell immune response against the tumor cells. The employment of nanoparticles for tumor therapy and for a (tumor-) immunotherapy are covered more in detail in the next sections.

2.3 Nanomedicine

Nanomedicine represents a branch of nanotechnology used and developed in the medical and pharmaceutical fields. Formulations used in the domain of nanomedicine are often called nanocarriers or nanoparticles and are widely defined as particles with a size range between 10-100 nm in one dimension (recommendation of the 2011 European Commission), although a general definition in terms of size is missing and there are plenty of nanoparticles with a size of several hundred nanometers. Exploiting the versatility of nanoparticles implies expectations for diagnostic and therapeutic purposes of several diseases. There are many different forms of nano-scaled particles and multiple ways to classify them. To broadly define them three groups can be differentiated: one dimensional, two dimensional and three dimensional nanoparticles⁵⁸. A more material-focused differentiation categorizes polymer-based nanoparticles, lipid-based nanoparticle, inorganic nanoparticles, viral nanoparticles and drug-conjugates (figure 6)

⁵⁹.

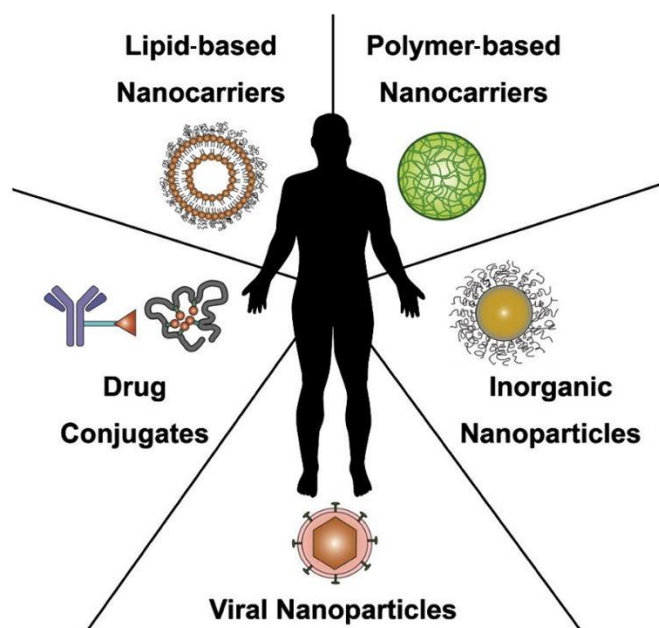


Figure 6: Different nanoparticle systems used in the field of nanomedicine

Their numerous differences regarding shape and material go with their specific advantages and consequently create a wide field of application possibilities in medicine. For example, silver particles in wound healing are potent at reducing infections because of an intrinsic antibiotic activity and can also improve skin graft adherence^{60,61}. Nanoparticles which address tumor cells in a passive way by exploiting the well-studied EPR effect or actively (targeted) equipped with ligands or receptor specific antibodies⁶² can be beneficial in many ways. From receiving more precise diagnosis in combination with medical imaging or by detection of cancer biomarkers⁶³ to a transport of chemotherapeutics to the tumor site in order to minimize toxic side effects⁶⁴. In the field of tissue engineering nanoparticles can build scaffolds for cells and in this manner serve to correct bone defects for example⁶⁵ by mimicking the fibers of the natural extracellular matrices (ECM). A more elaborately usage of nanocarriers is their employment as gene delivery systems. After overcoming challenges like efficient endolysosomal escape and proper release of deoxyribonucleic acid (DNA) into the nucleus these particles could even lead to a restored protein expression due to an insertion or replacement of a missing or defective gene⁶⁶. Another more advanced but still not well engineered application is the vaccination of immune cells in order to (re)program the immune system to fight cancer or infectious diseases⁶⁷⁻⁷⁰ or deficiencies in immune tolerance like in allergy or autoimmune diseases⁷¹⁻⁷³.

2.4 Use of nanoparticles for tumor therapy

Cancer is the second leading cause of death referring to the world health organization (WHO) and its treatment remains a challenge in many cases. Insufficient tumor toxicity and unacceptable side effects of chemotherapeutics or radiation therapy can be a problem. And even though there are more advanced therapeutic options available nowadays like inhibitors and small molecules, they can lead to a prolonged lifetime but do not implicate a cure for the patients because of upcoming tumor resistance against these agents.

2.4.1 Tumor-targeting nanoparticles

Nanoparticles might offer a solution for these kinds of problems as they are able to decrease drug resistance⁷⁴, to enhance solubility⁷⁵ by entrapping water insoluble agents into water soluble liposomes for example⁷⁶ which allows dose reduction also due to the potential to deliver drugs in a cell type-specific manner by targeting⁷⁷ resulting in a lower toxicity⁷⁸. Moreover, they can provide longer circulation in the body compared to application of free drug⁷⁹, and enhance therapy effectiveness for example in thermo-radiotherapy by increasing apoptosis of tumor cells due to cytotoxic effects of the nanoparticles^{80,81}. In the last few years scientific work concerning nanopharmaceuticals for diagnosis and treatment of cancer diseases has vastly increased as indicated by the rise in publications in this field. One focus of improving nanopharmaceuticals is to make chemotherapeutic therapy less toxic and simultaneously more effective. So far, chemotherapeutics have to be applied intravenously in most cases which means that the drug can distribute throughout the whole body. To reach metastasis this circumstance can be beneficial, but unfavorable for healthy cells which are damaged by treatment as well resulting in numerous severe side effects. Nanoparticulate formulations of the same drug can increase tumor accumulation, due to the EPR effect or active targeting of surface receptors highly expressed by tumor cells, and thereby reduce the dose which involves reduction of side effects and there is evidence that they enhance drug stability and bioavailability as well. There are basically two ways to obtain accumulation of drugs used for diagnosis but also for therapy within the tumor mass. Passive targeting is enabled by the EPR effect as already mentioned above. It is based on a higher vascularization and higher permeability of blood vessels within the tumor which leads to a higher retention of the nanoparticles^{62,82}. The other possibility is an active targeting using ligands specific for receptors overexpressed by tumor cells, like

folic acid or transferrin^{83,84}, but also antibodies⁸⁵ or carbohydrate moieties binding to lectin receptors can provide active targeting⁸⁶. These kinds of application aspects of nanoformulations are already evaluated in the clinic or in ongoing clinical studies and some nanocarrier-based drug delivery systems have been licensed for tumor therapy. Primarily, liposomes have been successfully translated into the clinic. Over twenty years ago Doxil® was approved as the first nano-drug, a liposomal nanoformulation of the chemotherapeutic doxorubicin used for the treatment of several types of cancer^{87,88}.

2.4.2 Nanoparticle-based tumor immunotherapy

A fast-developing approach is the immunotherapy of tumor diseases driven by nanoparticles. The basic principle is to exploit the patient's immune system to induce and shape anti-tumor immune responses. Immune cells can detect and fight potentially harmful pathogens like bacteria, parasites but also virus infected and malignant cells. The immune system destroys malignant cells daily. Nevertheless, in some cases the immune system fails in detecting or killing tumor cells for various reasons. Tumor-mediated immune deviation and tolerance induction, due to down-regulation of antigen-presenting surface receptors (MHC I) and subsequent impaired self-antigen presentation⁸⁹, which T cells need to recognize as a prerequisite for elimination of those cells, and expression of inhibitory receptors like PDL1⁹⁰, induction of regulatory cells and high levels of immunosuppressive mediators in the tumormicromillieu (TMM)^{91,92} are just some of the factors that contribute to tumor immune evasion. Nanotechnology could offer solutions to overcome these problems. As the size of nanoparticles is comparable to that of bacteria and viruses, they are prone to be taken up by immune cells like dendritic cells and macrophages. Reprogramming immune cells to ensure tolerance reduction and active immune response against tumor antigens can be an effective way to restore the body's own defense against altered cells. A popular concept to reach this is targeting APCs like macrophages or dendritic cells with nanocarriers. They can deliver tumor-associated/specific antigen and various immune-modulating agents into the cytoplasm or even into the cell nucleus of these cells and thereby induce either disruption of tolerance mechanism or directly promote an immune response against the tumor⁹³⁻⁹⁵. Applying antigen and an adjuvant detached includes the chance of a separated uptake by different APCs. An uptake of only one of these agents alone could provoke tolerance in the case of antigen and autoimmune reactions in the event of an exclusive uptake of adjuvant. In this case nanoparticle systems provide a platform to combine the two agents and thereby ensure co-administration to the up taking cells

and additionally protect the cargo ⁹⁶. Besides protein, nanoparticles can also vaccinate cells with a genetic cargo, coding for antigen and adjuvant for example, either ribonucleic acid (RNA)-or DNA-based ^{97,98}. The antigen incorporated in the particle or conjugated to the particle can be individualized for patient's tumor using either tumor-specific antigens (TSAs), exclusively expressed by tumor cells, or TAAs which are overexpressed in tumor cells. This kind of therapy opens up new possibilities not only for tumor patients but also for the treatment of allergies and auto-immune diseases.

2.5 Dendritic cells as target for nanoparticle-based vaccine

First identified by Ralph Steinman in 1973 dendritic cells as the main professional antigen presenting cells of the immune system constitute an important component of the immune system ⁹⁹. These cells possess some unique features like the capability to activate naïve T cells and to cross-present exogenous antigens via MHC I to CD8⁺ T cells but also induction of tolerance under homeostatic conditions. In the static state dendritic cells are termed "immature" and display high endocytic/phagocytic potential and lack the typical dendritically shaped appearance. Upon recognition of pathogen-associated molecular patterns (PAMPs) by PRRs like TLRs or C-type-lectin receptors (CLRs), as well as endogenous danger signals (DAMPs), maturation of the dendritic cell is initiated. Resulting cellular processes comprise the upregulation of costimulatory molecules including CD86, CD80 and CD40, the release of proinflammatory cytokines and cytoskeletal rearrangements associated with enhanced migratory behavior towards draining lymph nodes, and enhanced DC/T cell interaction ¹⁰⁰⁻¹⁰³. Meanwhile, pathogen-derived antigens are processed and presented in a MHC II and/or MHC I context which allows activation of antigen specific CD4⁺ and CD8⁺ T cells, respectively.

The essential role of DC in the induction and shaping of immune responses is utilized in vaccination-based therapies. The aim of a vaccination is the activation of dendritic cells followed by stimulation of effector immune cells, and ideally a long-lasting immunological memory. Despite vaccination options for other diseases like virus infection or allergy and autoimmune diseases the following sections will focus on vaccination as immunotherapy for cancer hereinafter. The FDA defines DC vaccines as "human cell, tissue, or cellular or tissue-based products". This classification includes whole cell vaccines like autologous or allogenic cancer vaccines with TAA-pulsed dendritic cells ¹⁰⁴⁻¹⁰⁶, as well as the possibility to vaccinate dendritic cells *in situ* with tumor-derived pro-

teins, peptides or genetic material coding for these. Nanoparticle systems are suitable vehicles to transport vaccination components like antigen and adjuvant, needed for proper activation, to dendritic cells. These carriers, in general, can protect the cargo from extracellular degradation¹⁰⁷ and facilitate, when equipped with targeting structures, predominant internalization by dendritic cells^{108,109}. Current research focusses on various types of nanocarriers for particle-based vaccinations although the translation into the clinic remains a challenge. In current preclinical studies, most of the nanoparticles designed for vaccination contain a (model) antigen like OVA or derived peptides to evoke T cell activation *in vitro* and *in vivo* and an adjuvant addressing TLRs or other intracellular PRRs for proper dendritic cell activation, and in some cases also a targeting structure^{110,111}. These multi-component particle systems are intended to lead to a dendritic cell mediated T effector cell immune response against tumor cells as illustrated in figure 7.

Concept of *in situ* dendritic cell vaccination via nanoparticle system

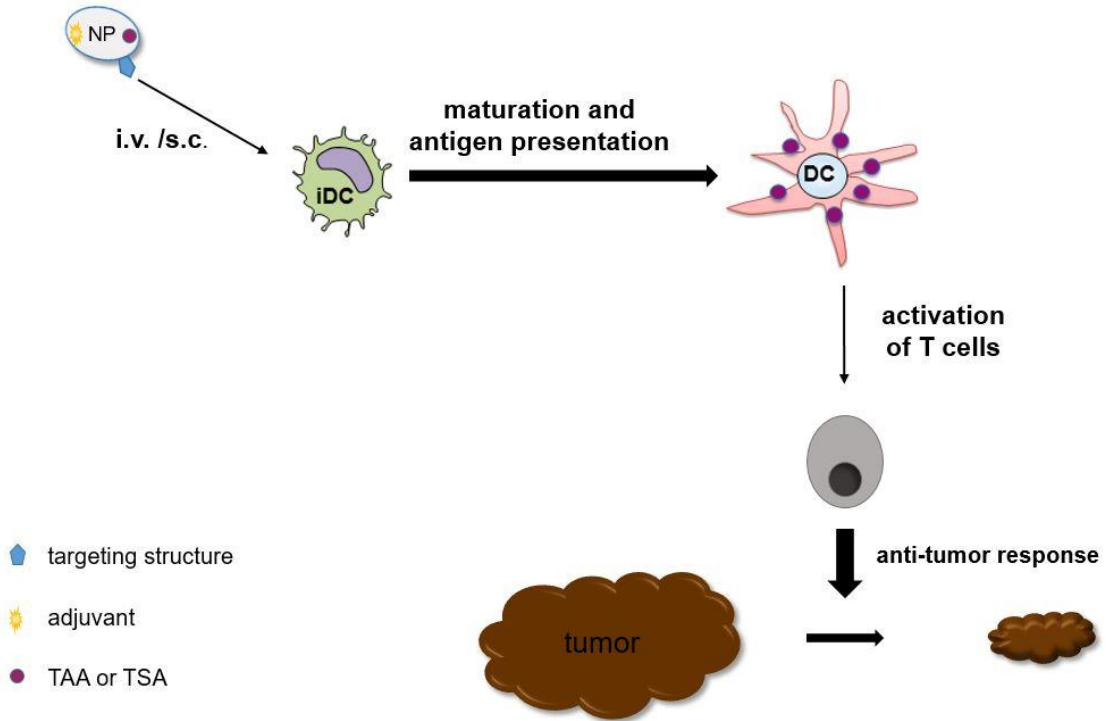


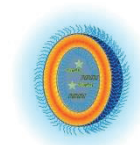
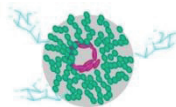
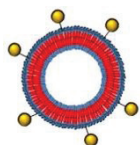
Figure 7: *In situ* vaccination of dendritic cells

As the aim of this work was to evaluate the suitability of different types of functionalized nano-carriers for vaccination with a focus on DCs. Several types of nanoparticles were provided by the cooperation partners listed down below. They differed in several aspects like material, shape, size, charge, surface properties and degradability. To address APCs we used mannose as a natural ligand for the mannose receptor CD206 expressed by DCs but also by macrophages¹¹²⁻¹¹⁵. For a DC targeted vaccination we used aDEC205, a monoclonal antibody against murine DEC205, a receptor almost exclusively expressed by DCs¹¹⁶. To activate APCs adjuvants were either conjugated to or incorporated into the nanocarrier depending on their structure. Therefore, we used the CpG ODNs as a TLR-ligand and L18-muramyldipeptide (L18-MPD) as NOD-ligand. To study the potential of APCs to process and present nanoparticle-delivered antigen, the OVA derived peptide sequence SIINFEKL or full OVA protein were used as model antigen. The tables below summarize the nanoparticle formats concerning their chemical properties and biologically active components (table 2).

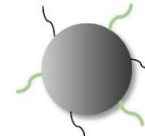
The nanoparticles used in this work were synthesized and characterized by the following research laboratories:

- group of PD Dr. Matthias Barz, Department for Organic Chemistry of the Johannes-Gutenberg-University Mainz
- group of Prof. Dr. Rudolf Zentel, Department for Organic Chemistry of the Johannes-Gutenberg-University Mainz
- group of Prof. Dr. Manfred Schmidt, Department for Physical Chemistry of the Johannes-Gutenberg-University Mainz
- Milteny biotec GmbH, Bergisch Gladbach

Table 2: Overview of the different nanoparticle formats biologically evaluated in this work



NP type	vesicle	micelle	vesicle
material	poly(2,3-dihydroxypropyl methacrylamide) (P(DHPMA))	(N-[2-hydroxypropyl]methacrylamide)-P(HPMA)-block-P(LMA)	poly-sarcosine (PSar) poly(benzyl-glutamic acid) (PGlu(OBn))
size (Rh)	101-137 nm	40-47 nm	39.2 nm
synthesis	RAFT-polymerization	RAFT-polymerization	ring-opening polymerization,
biological components	mannose ¹¹⁹	mannose, L18-MDP ¹²⁰	CpG ODN 1826, SIINFEKL ¹²¹



NP type	polymer-brush	polymer-brush	spherical inorganic NP
material	polylysine backbone and polysarcosine (PSar) side chains	N3-poly(2-ethyl-block-2-isopropyl-2-oxazoline)	dextran-coated iron oxide
size (Rh)	10-23 nm	26-42 nm	about 100 nm
synthesis	ring-opening polymerisation, "grafting from", technique	ring-opening polymerisation, "grafting through" technique	mixture of ferrous chloride and ferric chloride with dextran polymers
biological components	aDEC205, (OVA, CpG ODN 1826) in preparation	aDEC205, SIINFEKL, CpG ODN 1826 ¹¹⁷	OVA, CpG ODN 1826 ¹¹⁸

For the purpose to vaccinate specific cell types in general, several requirements need to be fulfilled by the nanocarrier itself. The optimal nanocarrier is supposed to be non-toxic, inert, bio-degradable, shows neither an aggregation in the blood nor an unspecific accumulation or uptake into non-target cells which provides long blood circulation half times. In the last twenty years, chemists have increasingly exploited various materials to meet these requirements. The materials used for the synthesis of the nanocarriers investigated in this work are designed to provide a so-called “stealth effect” which inhibits interaction with biological components that ensures a long circulation time and mainly consist of biodegradable, non-toxic materials. This stealth like effect is mainly provided by the application of polymers consisting of different organic molecules, namely HPMA, sarcosine and oxazoline^{122–125}. These molecules form a hydrophilic surface which is shown to have repelling effects towards proteins which also hinders the aggregation in blood serum¹²⁶. As a result, their employment in nanoparticle synthesis led to low unspecific binding to bone marrow derived dendritic cells (BMDCs) and primary splenic cell populations *in vitro*, but also to a blood circulation half time exceeding 24 h in mice (^{119,120,127}, ██████████ **Kappel et al. in preparation**¹). Although inorganic materials might be more stable, organic materials seem to be advantageous for targeted drug delivery because their size and surface can easily be modified. This flexibility in the design is important to adapt the nanoparticles characteristics towards an improved binding to the target cells. Besides the type of material, also the size and shape of nanocarriers can influence the efficiency of a cell vaccination. For this work either spherical or ellipsoidal or rod/worm-like shaped nanoparticles were used. We investigated the influence of differential sizes and shapes of sarcosine-based polymer brushes on biodistribution and vaccination efficiency. We observed no effect of the shape on the biodistribution, but an improved induction of an *in vitro* T cell proliferation response with the rod-like shaped peptobushes compared to the spherical peptobushes. (██████████ **Kappel et al. in preparation**). According to our findings, Niikura *et al.* have demonstrated that the uptake of nanorods and nanofibers is higher (amount of internalized nanoparticle per cell) compared to spherical shaped nanoparticles of the same size¹²⁸ which might have cause the observed difference in our studies. Nevertheless, this nanoparticle shape, as well as solid core spherical nanoparticles, often cannot provide sufficient cargo protection, as any kind of biological component is conjugated or adsorbed to the surface. In comparison, the structure of capsules such as vesicles or micelles allows incorporation of agents preventing them from degradation or unwanted interactions with biological components. HPMA/LMA-based micelles, used in

¹ in the following sections author or co-author contributions are written in bold

this work could only incorporate hydrophobic cargo because of their hydrophobic core¹²⁰. Compared to the vesicles, either HPMA- or sarcosine-based, which build a hydrophilic inner core and allowed to embed either hydrophilic or hydrophobic agents. Dendritic cells have been shown to take up nanoparticles in a size range from 2 nm up to 600 nm whereas some studies indicate that smaller nanoparticles are easier engulfed^{129–132}. The nanoparticles tested in this work were synthesized to display a hydrodynamic radius between 10 nm and 140 nm for an optimal uptake by DCs or other APCs (table 2). Furthermore, particles not larger than 25 nm allow a lymphatic transport to the lymph node which is advantageous with regard to a vaccination of immune cells, located there¹³³. Another influential factor on the uptake of nanoparticles by DCs represents their charge. Although positively charged nanoparticles are reported to show a higher uptake by dendritic cells, this might not be worthwhile in the case of a systemic application as cationic nanocarriers have been shown to predominantly accumulate in the lungs, whereas DCs are mainly found in the spleen and the lymph nodes¹³⁴. Taken together the described nanoparticles are ideal candidates for an APC focused vaccination, since they display no strong charge but long circulation times or at least low unspecific binding in *in vitro* cultures.

2.5.1 Intracellular Toll-like receptors as suitable PRRs for DC activation

TLRs belong to the group of PRRs. They are transmembrane proteins and can be located either in the cell membrane or intracellularly, for example in endosomes. There are twelve known TLRs in mice (TLR-1 to TLR-9, TLR 11 and TLR-13) and ten in human (TLR-1 to TLR-10). Regarding their structure, extracellularly and intracellularly located TLRs are very similar. The domain outside the cell or outside an endosome towards the cytosol, in case of intracellular TLRs, is rich in leucines and mediates the binding to the recognition sites. Each class of TLRs is specialized in the detection of certain PAMPs. TLR-4, as an example of an extracellular TLR-receptor, recognizes lipopolysaccharides found in the cell wall of gram-negative bacteria, whereas TLR-9, an intracellularly located receptor, recognizes unmethylated DNA^{135,136}. One can differentiate between a Myeloid differentiation primary response 88 (MyD88)-dependent TLR signaling pathway used by almost all TLRs and a Toll/IL-1-receptor (TIR)-domain-containing adapter-inducing interferon- β (TRIF)-dependent signaling pathway. The cytoplasmic domain is called Toll/IL-1-receptor (TIR)-domain and is associated with the protein MyD88. After binding of PAMPs to a TLR, the associated MyD88 recruits IL-1 receptor-associated kinase-4 (IRAK-4) and further enables activation of several other kinases leading to the activation of the transcription factor NF κ B, and thereby to the

expression of certain inflammatory cytokines¹³⁷. In the TRIF-dependent pathway, TRIF and TNF receptor-associated factor 3 (TRAF3) are involved in signal transduction leading to the expression of interferon- β due to interferon regulation factors (IRF) transcription factors¹³⁸. The possibility to modulate the immune system with TLR ligands seems obvious considering their task to trigger inflammation. In terms of dendritic cell vaccination many different TLR ligands can be used for stimulation of the cells in combination with an antigen. Very common ones are CpG-ODNs which are single strand DNA molecules containing repeating motifs of unmethylated cytosine and guanine. The backbone is at least partially phosphorothioated to prevent fast degradation by DNases. By binding TLR-9 of dendritic cells CpG-ODNs exert potent stimulation capacity by inducing NF κ B signaling as shown in figure 8¹³⁹. Proper dendritic cell stimulation is followed by pro-inflammatory cytokine release (IL-1 β , IL-6 and others) and upregulation of costimulatory molecules^{140,141}. In combination with presentation of antigen in an MHC I/MHC II context, the dendritic cell can then activate naïve T cells. NLRs are intracellular receptors playing, like TLRs, an important role in the pathogen recognition, predominantly microbial molecules, but are also able to detect tissue damage as a “danger signal”. In humans, there are 22 known NLRs, mainly expressed by various immune cells. The best studied, NOD1 and NOD2 receptor, also activate NF κ B and mitogen-activated protein kinase (MAPK) with the result of an increased expression of inflammation associated components like inflammation relevant cytokines or adhesive molecules to ensure proper migration of immune cells. Due to their high dendritic cell activation potency NOD-like receptors are increasingly employed for dendritic cell vaccination *via* nanoparticles. For this purpose various ligand types can be attached to or incorporated into the nanoparticles^{142,143}.

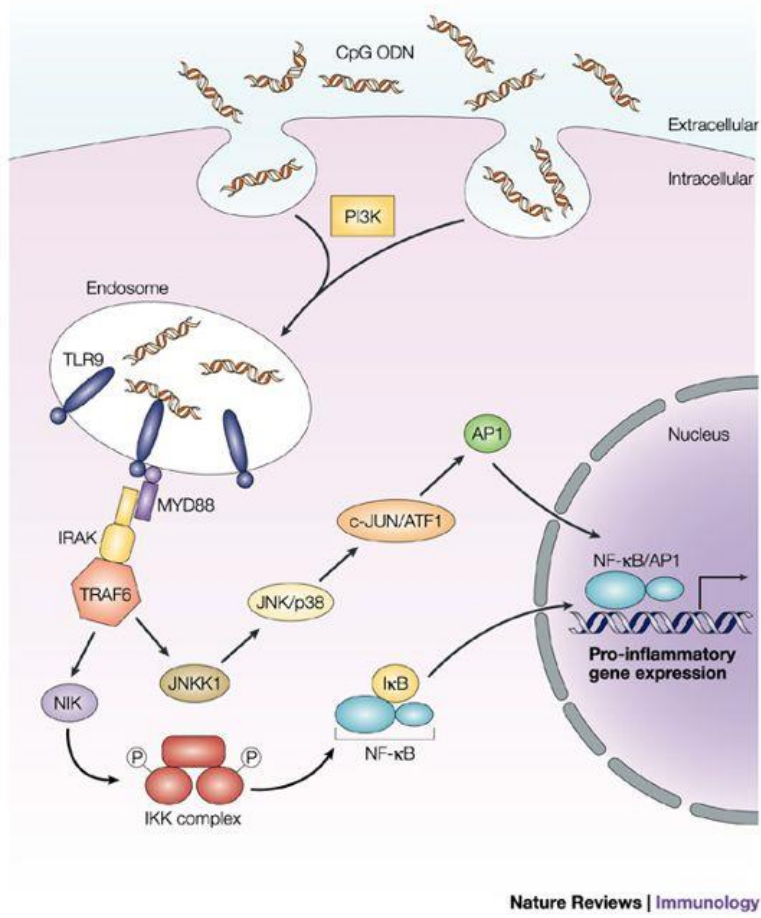


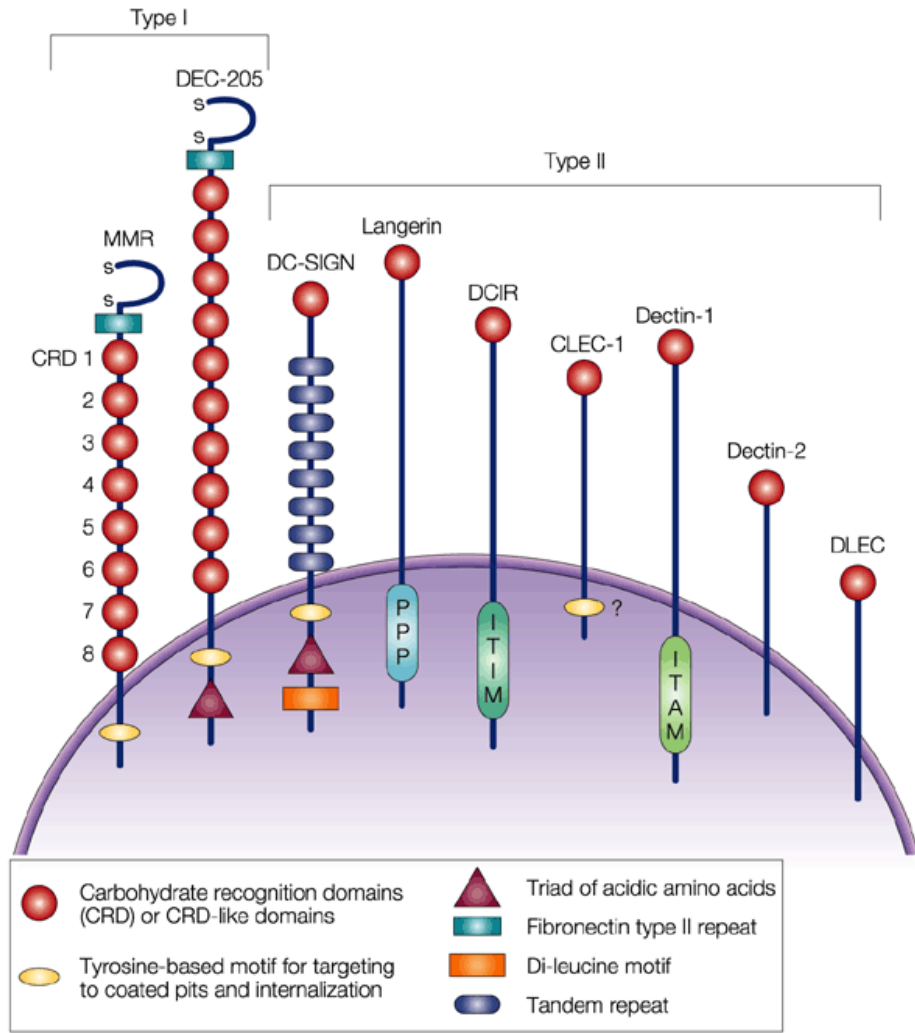
Figure 8: TLR9 signalling after CpG ODN binding

The described receptors can be addressed for an activation of dendritic cells, which is an important step regarding vaccination, as this allows proper T cell priming and activation if the application is combined with an antigen. For the studies discussed in this work, CpG ODNs (TLR9 ligand) or L18-MDP (bacterial peptidoglycan motif, NOD2 ligand) were either covalently conjugated to the nanoparticles (upper panel of table 2) or incorporated into micelles or vesicles (lower panel of table 2). As a model antigen either OVA protein from the chicken egg or the OVA peptide SIINFEKL was used (table 2). Afterwards, DC activation was assessed by detection of surfacemarker expression by flow cytometry and cytokine measurements. The incorporation of the two stimulating agents led to an activation of murine BMDCs as indicated by an upregulation of the activation-associated surface markers CD86, CD80 and MHCII ¹²⁰ and in the case of sarcosine-based vesicles also to an increased release of TNF α ¹³⁸. BMDCs *in vitro* pre-incubated with the peptide sequence SIINFEKL conjugated to oxazoline-based polymer brush were washed and cocultured with T cells. After stimulation with soluble lipopolysaccharides the dendritic cells induced a proliferation of cytotoxic T cell due to a successful uptake of the polymer brushes and presentation of SIINFEKL in an MHC context ¹¹⁹. T cell proliferation was also induced by BMDCs pretreated with sarcosine-based vesicles containing CpG ODNs and SIINFEKL and sarcosine-based polymer brushes conjugated with OVA and CpG ODNs (¹³⁸, [REDACTED] **Kappel *et al.* in preparation**). The latter could even prevent tumor growth in mice in a protective vaccination setting ([REDACTED] **Kappel *et al.* in preparation**). CpG ODNs are often used as an adjuvant for vaccination strategies against tumor and infectious diseases, as well as allergies ^{144–147}. By contrast, there are only few studies describing L18-MDP as an adjuvant for immunotherapeutic approaches. Nevertheless, we could observe that CpG ODNs conjugated to inert polymer brushes interfered with the targeting of lymphoid organs as they caused an accumulation in the liver (data not shown). This might be mediated by scavenger receptors as it is known that these bind negatively charged serum components and are expressed by a variety of liver cells ^{148–150}. This CpG oligo mediated liver accumulation might have been prevented by incorporation of the adjuvant into micelles or vesicular nanocarriers which release their cargo upon a stimuli inside the cell like we could show with DHPMA-based vesicles ¹¹⁹. Further, it remains to be investigated by comparative studies which TLR ligands or NOD ligands are best suited for the *in situ* activation of distinct APC populations and a specific nanoparticle type. Conjugation and embedding possibilities may vary within different nanoparticle types as well as the adjuvants' influence on their biodistribution or their activation efficiency. There is evidence that combinations of two or more TLR and NOD ligands addressing distinct receptors could confer a higher activation state of DC than when ap-

plied separately. It has also been reported that different types of adjuvants lead to differential T cell responses¹⁵¹. Solid ferrous nanoparticles conjugated with OVA antigen and CpG ODN 1826, published by **Shen, Kappel *et al.***, showed a B cell mediated T cell activation of a T_H1 type immune response, resulting in a production of OVA-specific IgG_{2a} antibodies instead of allergy associated IgE production and T_H2 type immune response. Further, this could prevent an anaphylactic shock and asthma in the setting of a therapeutic vaccination¹⁵². In summary, it depends on the type of nanoparticle and the desired T cell response which adjuvant yields the optimal activation of DCs or other APCs.

2.5.2 C-type lectin receptors as targeting structures

CLRs belong to the group of PRRs and constitute a large family of transmembrane proteins with the capability to bind various carbohydrate moieties in a calcium-dependent manner¹⁵³. CLRs are expressed by many cell types including several immune cells. One can distinguish between two groups, type I and type II CRLs. Receptors belonging to the type II cluster, like Dectin-1 or DC-SIGN (dendritic cell-specific ICAM-grabbing non-integrin) consist of a single carbohydrate recognition domain (CRD), while type I CLRs possess multiple CRDs (figure 9)¹⁵⁴. Because of their potential to recognize and bind carbohydrates on the surfaces of pathogens they constitute a crucial participant in the innate and adaptive immune system.



Nature Reviews | Immunology

Figure 9: Schematic construction of different C-type lectin receptors

In the mentioned concept of *in situ* DC vaccination the targeting structure can also be passed on, taking advantage of the high endocytic/phagocytic potential of dendritic cells. With regard to active targeting, most targeting units used are dendritic cell receptor ligands^{155,156} or antibody formats like monoclonal native antibodies^{157,158}, fragment antigen binding (Fab)-fragments¹⁵⁹ or single chain variable fragments (scFv)-antibodies¹⁶⁰ binding dendritic cell-specific or dendritic cell-associated receptors. A consideration for choosing an appropriate targeting option might be the proposed administration route. By subcutaneous or intradermal application, it is possible to reach migratory dermal dendritic cells, whereas an intravenous injection is supposed to result in a vaccination of dendritic cells primarily in the secondary lymphoid organs. Another important aspect is the fact that some dendritic cell populations are more qualified for a vaccination like CD8 α ⁺ dendritic cells in mice or their analogue in humans CD141⁺ dendritic cells. This subset, often termed as lymphoid dendritic cells, belongs to the group of cDC1 (conventional dendritic cells class I). Unlike CD8 α ⁻ dendritic cells, CD8 α ⁺ dendritic cells are capable of a process called “cross-presentation” which describes the ability to present exogenous antigens complexed with MHCI to cytotoxic CD8⁺ T cell and thereby activating these¹⁶¹. These so-called cytotoxic T lymphocytes (CTL) kill (virus-) infected cells or tumor cells. Many surface receptors are co-expressed with CD8 α like several members of the C-type lectin receptor family, explained in the next sections, which therefore constitute suitable targeting structures addressed by natural ligands like carbohydrate moieties or monoclonal antibodies. Additionally, many C-type lectin receptors are involved in antigen uptake what makes them even more suitable as vaccination candidates¹⁶². This fact and their unique property of cross-presentation make CD8 α ⁺ dendritic cells a popular target for nanoparticle-based vaccination.

2.5.2.1 DEC205 receptor

As CD8 α expression is associated with the potential of cross-presentation, the co-expressed receptor DEC205 often serves as target for dendritic cell specific antigen delivery^{144,163–165}. The multi-lectin receptor DEC205 (CD205), also known as LY75, belongs to the type 1 C-type lectin receptors and its name refers to the weight of 205 kDa. In humans, high expression of DEC205 can be found on monocytes and myeloid dendritic cells (mDCs). It is also expressed moderately on B cells and very low on plasmacytoid dendritic cell (pDCs), natural killer cells, T cells and macrophages¹⁶⁶. Murine DEC205 is primarily expressed by dendritic cells including CD8⁺ dendritic cells, dermal dendritic cells and Langerhans cells, but also on endothelial thymocytes^{112,167}.

Besides, an upregulation of DEC205 expression during DC maturation could be observed¹⁶⁸. The receptor consists of an extracellular part, an intracellular part and a transmembrane domain. The extracellular domain comprises of a cysteine-rich part (CR), a fibronectin type II domain and 10 carbohydrate recognition-like units and the cytoplasmic part of the receptor contains an acidic triad. The coding Ly75 gene is located on chromosome 2 in both human and mouse. Besides recognition of carbohydrate units, detection of necrotic or apoptotic cells has also been reported as a task of DEC205¹⁶⁹. The receptor also participates in antigen processing and is recyclable^{116,170}. Binding of external ligands leads to rapid internalization of receptor and ligand followed by degradation of the complexes in late endosomes¹⁷⁰. DEC205-mediated uptake of exogenous antigen allows presentation by MHC I (cross-presentation) and MHC II, and thereby enables CD4⁺ and CD8⁺ T cell activation. Another interesting aspect concerning vaccination is the co-expression of CD8 α with DEC205. Consequently antibody driven targeting of DEC205⁺ cells is popular for efficient cross-presentation of antigen^{164,171}.

To vaccinate specific APC populations active targeting with receptor ligands has become a promising tool. This work confirms the efficiency of DEC205 receptor focused dendritic cell targeting as *in vitro* experiments with BMDCs and primary mouse spleen cells revealed that oxazoline-based polymer brushes conjugated with a monoclonal antibody specific for this receptor specifically bind DEC205 positive DCs whilst binding to DEC205 negative DCs or non-DCs could not be observed¹²⁷. Furthermore, *ex vivo* analyses showed that aDEC205 antibody-conjugated sarcosine-based polymer brushes bind CD8 α ⁺ splenic DCs at significantly higher extent compared to their CD8 α ⁻ counterpart after intravenous application (**Kappel *et al.* in preparation**). Besides other concepts of targeting individual DC populations with nanoparticles, such as size conducted or natural ligands like carbohydrates^{172,173}, the concept of exploiting antibody formats for specific binding of distinct receptors expressed by the targeted DC subpopulation has been increasingly investigated in the last years^{174–176}. Compared to other targeting approaches this method is more specific and thereby minimizes a binding or uptake by other cells. Already in 2004, Steinman and coworkers reported a higher T cell immunity and even the induction of effector memory cells after application of aDEC205-OVA conjugates together with aCD40 as an adjuvant¹⁷⁷. In this study, antigen and adjuvant were applied separately which bears the risk to induce tolerance mechanisms or autoimmunity. Tolerance may be initiated by APCs which engulfed antigen alone and thereby miss an activating adjuvant, whereas autoimmunity may be caused by the stimulating effect of the adjuvants in the absence of exogenous antigen due to the

presentation of endogenous antigens in a stimulatory context. The nanocarriers described in the studies of this work, combine both components and ensure a specific immunity against the co-delivered antigen and in addition may increase binding to the target cell due to the presence of several targeting ligands leading to a higher binding avidity. The attachment of more than one of each biological active molecule to these nanocarriers ensured also a delivery of larger quantities compared to the application of a conjugate without nanoparticulate platform.

The capacity of DEC205⁺ DC to cross-present antigen to CTLs has proved to be advantageous for vaccination strategies since CTLs are able to efficiently destroy infected or cancerous cells^{175,178,179}. However, in human the expression of DEC205 is less restricted which might be a challenge for the translation to human therapeutic applications¹⁶⁶. Besides antibodies targeting the murine DEC205 receptor, there are many other receptors which are exploited for DC targeting. In a comparative study by Cruz *et al.* CD40-, DEC205- and CD11c addressing nanoparticles were tested with regard to their dendritic cell targeting efficiency, but also concerning their capacity to prime cytotoxic T cells¹⁵⁸. The nanoparticles conjugated with aCD40 as the targeting ligand showed a higher uptake capacity in DCs, but these were not superior concerning the priming of cytotoxic T cells. Alternative receptors highly coexpressed with CD8 α in human and murine DCs are Clec9a (C-Type lectin domain containing 9A) or XCR1 (X-C motif chemokine receptor 1)¹⁸⁰⁻¹⁸². Kronin *et al.* could prove the existence of a large CD8 α ^{low} DEC205^{high} DC population in murine lymph nodes¹⁸³. The expression of XCR1 might be more restricted to CD8 α , as XCR1 has been shown to be expressed by 70-90 % of CD8⁺ DCs¹⁸⁰. Yet, Kronin and coworkers also demonstrated that CD8 α ^{low} DEC205^{high} DCs are functionally equal to splenic CD8 α ^{high} DEC205^{high}¹⁸³. In addition XCR1 is conserved in human and mice which might facilitate the translation of research results and therapeutic approaches¹⁸⁵ and it has been recently shown that Clec9a and XCR1 are also involved in antigen uptake and presentation^{178,186}. With this knowledge Clec9a and XCR1 represent appropriate targeting alternatives to DEC205. Nevertheless, the functions of DEC205 in antigen uptake, processing and presentation have been studied in more detail and high-quality monoclonal antibodies are more affordable, which needs to be adapted for XCR1 and Clec9a. Taken together, prior to choosing a targeting ligand for vaccination of DCs, or APCs in general, it is crucial for the targeting efficiency to consider several aspects. First, the targeted receptor needs to be displayed by the target cell population, at sufficient extent for a nanocarrier to bind these. Simultaneously, this structure should not, or only slightly be expressed by other cells. Especially the expression of the targeted receptor by other cells within other or-

gans than the target organ can be challenging as these could trap particles at other sites as intended. As the aim in vaccination is mainly to achieve an uptake of antigen and adjuvant by APCs, the addressing receptor is preferably exclusively located in the secondary lymphoid organs. Further, the ligand should bind specifically to its supposed target and its density over the nanoparticles' surface must be high enough to ensure proper binding and uptake but low enough to prevent a total masking of the stealth property providing molecules and an over-crowding effect. Over-crowding can occur if a point of ligand (mostly antibodies) density is exceeded which can force the ligands to arrange in an advantageous way (Alkliany *et al.* in preparation). This might represent a challenge depending on the type of ligand or conjugation strategy.

2.5.2.2 CD206 receptor

The mannose receptor, also called CD206, represents another common target for vaccination^{187–189}. Like DEC205, this receptor also belongs to the group of type I C-type lectin receptors. There are similarities to DEC205 regarding the structure, but also the binding specificity and the recyclability. With 175 kDa CD206 is just slightly lighter than DEC205¹¹³. Mannose receptor C-Type 1 (MRC1) is the CD206-encoding gene and is conserved in mammals, but also fish or amphibia indicating its crucial tasks. This receptor can interact with glycoproteins and glycolipids found on microbes and viruses. Carbohydrate moieties like mannose, glucose and fucose lead to a binding by CD206. Mostly immune cells were shown to express this receptor, like macrophages in various tissues^{114,115,190} and immature dendritic cells^{191,192} but it is also found in the hepatic endothelium¹⁹³ and lymphatic endothelial cells¹⁹⁴. The CRDs allow detection of pathogens, leading to their engulfment and subsequent processing and presentation of derived antigens. Additionally, they play an important role in clearing the body from glycoproteins like hormones¹⁹⁵ or glycoproteins associated with inflammation like myeloperoxidase, which is necessary to prevent tissue damage¹⁹⁶. To exploit CD206 for dendritic cell targeting, several carbohydrates can be conjugated to nanocarriers, the most notably is mannose, which was also one method of this work.

HPMA-based micelles and DHPMA-based vesicles were conjugated with differential amounts of mannose and both yielded a targeting effect *in vitro* as demonstrated by an increased binding of mannosylated nanoparticles compared to their non-functionalized counterpart to BMDCs and a preferential uptake by CD206⁺ DCs^{119,120}. DHPMA vesicles with a mannosylation degree of 4.3 % showed a more effective binding to BMDCs than those with 2.2 % mannosylation degree which supports the idea of a higher binding avidity by augmenting the ligand density. Mannose is a very often used targeting

moiety for addressing APC. Predominantly, dendritic cells and macrophages are addressed by this approach, due to their expression of CD206. Within the C type lectin family several other receptors, beside CD206 recognize and bind mannose. Most of them are cell surface receptors, DC-SIGN expressed by dendritic cells or the macrophage-inducible C type lectin (Mincle), mainly expressed by macrophages^{197,198}. Yet, also a soluble receptor, the mannose-binding lectin (MBL) can detect mannose-containing structures. For the latter, we could also show an indirect involvement on the *in vivo* biodistribution of nanoparticles. Dextran-coated ferrous nanoparticles triggered the lectin-induced complement cascade upon recognition by MBL and thereby led to an integration of MBL-associated proteases in the corona coating the nanoparticles' surface¹¹⁸. As these enzyme activate C3 convertase, a component of the complement cascade, this factor adsorbed to the surface of the nanocarrier leading to an unintended B cell targeting in the spleen mediated by the complement receptors 1 and 2. Many nanoparticles form such a protein corona after contact with blood serum which is one reason for the differences between *in vitro* and *in vivo* behavior. The influence of the protein corona on different aspects gets increasingly important. Most of the work has investigated the challenges these alterations of the surface can cause, like altered biodistribution or cell uptake, as well as sterically hindrance or "masking" of targeting units^{199–203}. Our approach using the *in vivo* formed protein corona to target B cells constitutes an innovative way to exploit this often-unpreventable adsorption of serum proteins.

Compared to antibodies, mannose or other sugar moieties are a low-cost component. Further, these carbohydrates are easy to conjugate to nanoparticles in high amounts because of their small size. In addition, their structure is less prone to alterations induced by the conjugation to nanoparticles, whereas the more complex antibodies can lose their binding capacity during this process. The stability of mannose is also higher in comparison to antibodies which can be degraded by proteases. Nevertheless, the binding affinity of sugar moieties to C type lectin receptors is often lower compared to the binding of monoclonal antibodies²⁰⁴. Given that synthetic mannose structures, like tri-mannose have been designed, which combines three mannose units in one molecule²⁰⁵. These new structures but also increased amounts of mono-mannose lead to a higher binding avidity. As the monosaccharides are much smaller than antibodies the lower binding affinity might be easily compensable by increasing the ligand density per nanoparticle. The broader range of mannose binding receptors and their expression by several cell types can be challenging if exclusive targeting of one specific cell type is the primary aim. In this case, the characteristics of the nanoparticle itself can be chosen in a way that these are preferably engulfed by the targeted cell population. Howev-

er, the circumstance of reaching more than one cell type population also offers the chance to manipulate the immune response on various sites.

2.6 Influence of the liver on the biodistribution of nanoparticles

The use of nanoparticles for *in situ* dendritic cell vaccination still must overcome several challenges. Two main aspects need to be considered in the context of nanoparticle design. First, the carrier needs to be targeted towards the cells of interest. Afterwards, proper cell activation and antigen processing are necessary, followed by presentation to T cells. Especially if intravenous application is required or desired this factor can be critical because this implies the chance of accumulation in any organ throughout the body. The biodistribution of nanoparticles after intravenous administration depends on many factors. In general, particles often accumulate in blood-filtrating organs like kidney, spleen or liver which contain highly phagocytotic cells of the reticuloendothelial system (RES). The size and surface properties of nanocarriers influence the circulation time and the excretion pathway²⁰⁶. For particles smaller than 10 nm a renal excretion was reported²⁰⁷, whereas larger particles (≥ 100 nm) predominantly end up in the spleen or the liver²⁰⁸. Regarding uptake dependent on the size of the particles, there is a clear division of responsibility within the liver. Kupffer cells clear the blood from particles ≥ 200 nm, whereas LSECs phagocytose smaller particles²⁰⁹. The surface charge of nanoparticles has also an influence on biodistribution. Negatively charged or neutral particles show longer blood circulation, whereas positively charged nanoparticles tend to accumulate in the lungs, spleen and liver²¹⁰. Particularly the liver with its unique blood circulation and filtration properties can be difficult to evade. The temporary reduced speed of the blood flow in the sinusoids, its lobular composition and the presence of specialized phagocytotic cells like Kupffer cells and liver sinusoidal endothelial cells (LSECs) can contribute to trapping of nanomaterial leaving no chance for the target cells to take them up. Many studies about various nanoparticle systems have reported about liver accumulation^{211–214}. Diminishing this effect by choosing the proper size, charge and shape can contribute to reduce unspecific accumulation of nanoparticles. To reach their intended target cells, nanoparticles should provide a so-called stealth effect which means that interaction with biological compounds like serum components or cells is largely prevented. Molecules that provide this property are e.g. polyethylenglycol (PEG), poly(2-ethyl-2-oxazoline) or polysarcosine. But despite great efforts, many nanoparticle systems still accumulate in the liver, although their target cells are located in the spleen or lymph node. In many cases directing of carrier systems to

specific cells involves targeting units. Unfortunately, these targeting structures like carbohydrates or antibodies can alter the nanoparticle's surface leading to a decrease of the stealth effect due to a ligand overcrowding or by forming a protein corona for example²¹⁵. Besides that, popular targeting structures can lead to an active liver targeting as some receptors expressed by dendritic cells and macrophages are also expressed by liver immune cells^{31,216–218}.

As mentioned in the section above, it is a common problem that nanoparticles accumulate in the liver. In our experiments an inert sarcosine-based polymer brush was used as an optimal candidate for a comparative study about the correlation between the antibody density on nanoparticles and their biodistribution. This polymer brush showed a blood circulation half time over 24 h and was successfully conjugated with differential amounts of aDEC205 antibodies. The biodistribution after intravenous injection was investigated on organ level by *in vivo* and *ex vivo* imaging, as well as on cellular level for liver, spleen, and lymph nodes using flow cytometry. These experiments revealed a positive correlation between antibody amount per peptobrush and liver accumulation due to Fc receptor-mediated binding and uptake by liver endothelial cells (**Kappel *et al.* manuscript in preparation**). For the targeting of leucocytes in secondary lymphoid organs this insight indicates a superiority of lower antibody quantities on the nanocarrier. To our knowledge this study fills a gap of knowledge in the field of active targeting of nanoparticles. Certainly, these findings must not be true for any targeting approach but in the case of a non-site directed conjugation when the antibodies are attached to the nanocarrier at random sites this should be considered as the antibody's Fc portion might bind to Fc receptors, expressed by many cell types. Considering other methods of targeting like natural ligands, antibody formats like Fab fragments or scFv and a site directed attachment, more ligands per nanoparticle might provide better targeting effects as more ligands increase the avidity of the cell binding. Yet, in some circumstances increasing amounts of the targeting ligand can cause unpredictable alterations of the nanoparticles' biodistribution, cell uptake and toxicity^{219–221}. The so called "surface crowding effect" describes an unfavorable arrangement of antibodies on a surface due to the high packed density, which leads to steric hindrance limiting the accessibility of the Fab regions (██████ *et al.* in preparation). At the same time, a higher density of antibodies on a surface can force them to acquire a position that ensures easy availability of the Fab parts. The balancing act to find the best working ligand density on a targeted nanoparticle requires careful investigations which seem to have been neglected in the past. Aside from that, antibodies are expensive and a determination of the minimally needed antibody amount to reach a maximal targeting effect can contribute to a cost reduction of the nanoparticle synthesis. The literature confirms that in many

cases the correlation between the ligand density on the nanoparticles and their targeting or binding efficiency exhibits an “optimal ligand density with a plateau” (██████ *et al.* in preparation). This indicates that a saturation can exist and that there is no need to further increase the ligand amount beyond this point.

As previously described, in contrast to the secondary lymphoid organs, the liver predominantly mediates immune tolerance. Beside the livers' influence on the biodistribution as a sort of a trap for nanomaterial this also means that vaccination-induced adaptive immune responses might be weakened by unconventional APCs like LSECs or Kupffer cells, for example. *In vitro* binding studies of this work could also show a specific binding of polymer brush-antibody conjugates to liver DCs, indicating an expression of DEC205 by liver-resident DCs which is also supported by some publications^{222,223}. But even an nanoparticle uptake by liver DCs does not necessarily implicate the induction of an immune response, as liver DCs are mostly immature and secrete higher amounts of immune suppressive IL-10 but lower levels of IL-12 than DCs of the lymphoid organs²²⁴. The knowledge that the tolerance is not only restricted to the liver, but systemic^{225,226}, the unintended vaccination of certain liver immune cells could result in unwanted tolerance induction in the case of cancerous and infectious diseases. Considering that the frequency of DCs within the liver is lower than in the lymphoid organs, their uptake of nanoparticles may have minor effects. Especially with other highly phagocytotic cells as competitors like LSECs or Kupffer cells, which, in our work, were positive for nanoparticle to a much higher extent than liver DCs (**Kappel *et al.* in preparation**). Given that, the liver as a nanomaterial accumulating organ cannot be bypassed upon systemic application, it is also relevant that it might be possible to induce an immune response by targeting unconventional liver APCs. It is described that Kupffer cells and LSECs respond to the stimulation of various TLRs by secretion of cytokines associated with immune activation although their upregulation of co-stimulatory surface markers is often absent or only minor²²⁷. As these experiments were limited to *in vitro* studies, it further remains to confirm these results *in vivo*. One could assume that compared to conventional APCs higher amounts of stimulating adjuvants are required or/and simultaneous targeting of more than one cell population is necessary to induce an immune response in the tolerogenic liver environment.

To avoid the Fc receptor mediated uptake of antibody-conjugated nanocarriers, the use of Fab or scFv fragment might be an alternative and a step in the right direction. Site-directed attachment of full antibodies might work in theory^{228,229} but is not that simple to employ on a broad variety of nanoparticulate formats and especially hard to prove by chemical characterization. It remains to be investigated if mannose-conjugated nano-

particles could be superior in avoiding Fc receptor mediated uptake by LSECs. Since characterization studies of LSECs revealed the expression of mannose binding CD206 and L-SIGN²³⁰⁻²³², this approach could cause a liver accumulation as well. Biodistribution studies of the mannose conjugated nanoparticles presented in this work are missing and it needs to be investigated if the liver trapping does occur in this case too. The same applies to antibody fragments. Still, the influence of differential ligand amounts should be considered and tested additionally as this parameter might not only play a role in case of full antibody ligands.

3. OUTLOOK

The development of novel tumor therapies is urgently required as indicated by a rise of new cases and the development of resistances of tumors towards conventional therapies. The results described in this thesis highlight the possibilities of immunomodulating nanoparticles for the treatment of cancer and other immune diseases. This work demonstrated successful targeting of nano-vaccines to important immune cells (DCs and B cells) *in vitro* and *in vivo*. In addition, codelivery of antigen and adjuvant not only activated these cells, but also allowed the presentation of the antigen followed by the differentiation of effector T cells (^{119–121,127}, **Kappel et al. in preparation**, [REDACTED] **Kappel et al. in preparation**). Furthermore, *in vivo* experiments demonstrated the potential of these nano-vaccines for the treatment of tumor and allergy disease in a therapeutic setting ([REDACTED] **Kappel et al. in preparation**, ¹⁵²).

Still, some challenges remain, and further research needs to address these topics. Although aDEC205 antibody as a targeting ligand for cross-presenting DCs might be a promising tool for mouse, it cannot be translated directly to the human system since the expression of human DEC205 is less restricted to dendritic cells compared to its expression in the mouse. Recent detailed studies also revealed that the expression of DEC205 is not highly restricted to cross-presenting DCs. It remains to be evaluated by comparative experiments which receptor might represent a suitable alternative DEC205. In general, conjugation of an antibody to a nanoparticle in a site-directed manner may prevent liver accumulation due to binding of the Fc part of the antibody. Future studies are also necessary to improve the APC/DC activation efficiency of the nanocarriers. Unfortunately, in this work attempts to activate DCs *in vivo* with oxazoline-based polymer-brush conjugated CpG ODNs failed (data not shown). This might be caused by the adsorption of serum factors to the negatively charged CpG ODNs decreasing their stimulatory capacity or an increased liver accumulation due to Fc receptor mediated uptake into LSECs. Scavenger receptors found on LSECs could also bind CpG ODNs and initiate a premature engulfment which might hinder the accumulation of higher amounts in the secondary lymphoid organs. For types of nanoparticles not allowing incorporation of agents, alternatives need to be tested or CpG ODNs have to be disguised to prevent undesired binding. To increase the stimulatory capacity of nano-vaccines, several TLR- and NOD-ligands will also be co-delivered by one nanoparticle, which allows additive activation effects, already demonstrated by our group²³³. The use of specific tumor antigens, such as melanoma antigen recognized by T cells 1 (MART1)²³⁴ or Tyrosinase-related Protein 2 (TRP-2)²³⁵ is also planned.

Most importantly, the types of nanoparticles successfully tested in *in vitro* experiments should be used for *in vivo* testing, especially regarding therapeutic tumor mouse models to further investigate their potential to be applied in the clinic.

:

4. REFERENCES

1. Murphy, K. & Weaver, C. *Janeway. Janeway's Immunobiology* (2017). doi:10.1007/s13398-014-0173-7.2
2. Janeway, C. A. & Medzhitov, R. INNATE IMMUNE RECOGNITION. *Annu. Rev. Immunol.* **20**, 197–216 (2002).
3. Cambier, J. C., Pleiman, C. M. & Clark, M. R. Signal Transduction by the B Cell Antigen Receptor and its Coreceptors. *Annu. Rev. Immunol.* **12**, 457–486 (1994).
4. Kupiec-Weglinski, J. W., Austyn, J. M. & Morris, P. J. Migration patterns of dendritic cells in the mouse. Traffic from the blood, and T cell-dependent and -independent entry to lymphoid tissues. *J. Exp. Med.* **167**, 632–45 (1988).
5. Hoffman, W., Lakkis, F. G. & Chalasani, G. B Cells, Antibodies, and More. *Clin. J. Am. Soc. Nephrol.* **11**, 137–54 (2016).
6. Martin, F., Oliver, A. M. & Kearney, J. F. Marginal zone and B1 B cells unite in the early response against T-independent blood-borne particulate antigens. *Immunity* **14**, 617–29 (2001).
7. Malek, T. R. & Shevach, E. M. The Role of Macrophages in the Processing and Presentation of Protein Antigens to T Lymphocytes. in *Immunology* 141–155 (Springer US, 1984). doi:10.1007/978-1-4757-6784-1_9
8. Bar-Or, R. L. Feedback mechanisms between T helper cells and macrophages in the determination of the immune response. *Math. Biosci.* **163**, 35–58 (2000).
9. Lee, H. K. & Iwasaki, A. Innate control of adaptive immunity: Dendritic cells and beyond. *Semin. Immunol.* **19**, 48–55 (2007).
10. Zhang, Z. & Wang, F. S. Plasmacytoid dendritic cells act as the most competent cell type in linking antiviral innate and adaptive immune responses. *Cell. Mol. Immunol.* **2**, 411–7 (2005).
11. Reis e Sousa, C. Activation of dendritic cells: translating innate into adaptive immunity. *Curr. Opin. Immunol.* **16**, 21–5 (2004).
12. Hall, J. G. & Robertson, D. Phagocytosis, in vivo, of immune complexes by dendritic cells in the lymph of sheep. *Int. Arch. Allergy Appl. Immunol.* **73**, 155–61 (1984).

13. Sunshine, G. H. & Mitchell, T. J. Antigen presentation by spleen dendritic cells. *J. Invest. Dermatol.* **85**, 110s–114s (1985).
14. Steinman, R. M. Decisions About Dendritic Cells: Past, Present, and Future. *Annu. Rev. Immunol.* **30**, 1–22 (2012).
15. Ni, K. & O'Neill, H. The role of dendritic cells in T cell activation. *Immunol. Cell Biol.* **75**, 223–230 (1997).
16. Hey, Y. Y. & O'Neill, H. C. Murine spleen contains a diversity of myeloid and dendritic cells distinct in antigen presenting function. *J. Cell. Mol. Med.* **16**, 2611–9 (2012).
17. Genes, S. G. [Role of the liver in hormone metabolism and in the regulation of their content in the blood]. *Ark. Patol.* **39**, 74–80 (1977).
18. Adeva-Andany, M. M., Perez-Felpete, N., Fernandez-Fernandez, C., Donapetry-Garcia, C. & Pazos-Garcia, C. Liver glucose metabolism in humans. *Biosci. Rep.* **36**, e00416–e00416 (2016).
19. Böttcher, J. P. *et al.* Liver-primed memory T cells generated under noninflammatory conditions provide anti-infectious immunity. *Cell Rep.* **3**, 779–795 (2013).
20. Sander, L. E. *et al.* Hepatic acute-phase proteins control innate immune responses during infection by promoting myeloid-derived suppressor cell function. *J. Exp. Med.* **207**, 1453–1464 (2010).
21. Calne, R. Y. *et al.* Induction of immunological tolerance by porcine liver allografts. *Nature* **223**, 472–6 (1969).
22. Qiu, M., Chen, Y., Chen, L., Zeng, J. & Liu, J. Transforming growth factor β 1 and Fas ligand synergistically enhance immune tolerance in dendritic cells in liver transplantation. *J. Surg. Res.* **218**, 180–193 (2017).
23. Knolle, P. A. *et al.* Endotoxin down-regulates T cell activation by antigen-presenting liver sinusoidal endothelial cells. *J. Immunol.* **162**, 1401–7 (1999).
24. Gao, B., Jeong, W.-I. & Tian, Z. Liver: An organ with predominant innate immunity. *Hepatology* **47**, 729–736 (2007).
25. Mannaa, F. A. & Abdel-Wahhab, K. G. Physiological potential of cytokines and liver damages. *Hepatoma Res.* **2**, 131 (2016).
26. Kang, Y. B. (Abraham), Rawat, S., Cirillo, J., Bouchard, M. & Noh, H. (Moses). Layered long-term co-culture of hepatocytes and endothelial cells on a transwell

- membrane: toward engineering the liver sinusoid. *Biofabrication* **5**, 045008 (2013).
27. Wisse, E., De Zanger, R. B., Charels, K., Van Der Smissen, P. & McCuskey, R. S. The liver sieve: considerations concerning the structure and function of endothelial fenestrae, the sinusoidal wall and the space of Disse. *Hepatology* **5**, 683–92
 28. Xie, G., Wang, L., Wang, X., Wang, L. & DeLeve, L. D. Isolation of periportal, midlobular, and centrilobular rat liver sinusoidal endothelial cells enables study of zoned drug toxicity. *Am. J. Physiol. Liver Physiol.* **299**, G1204–G1210 (2010).
 29. Kempka, G. & Kolb-Bachofen, V. Binding, uptake, and transcytosis of ligands for mannose-specific receptors in rat liver: an electron microscopic study. *Exp. Cell Res.* **176**, 38–48 (1988).
 30. Smedsrød, B. Clearance function of scavenger endothelial cells. *Comp. Hepatol.* **3 Suppl 1**, S22 (2004).
 31. Malovic, I. *et al.* The mannose receptor on murine liver sinusoidal endothelial cells is the main denatured collagen clearance receptor. *Hepatology* **45**, 1454–1461 (2007).
 32. Gardner, J. P. *et al.* L-SIGN (CD 209L) is a liver-specific capture receptor for hepatitis C virus. *Proc. Natl. Acad. Sci. U. S. A.* **100**, 4498–503 (2003).
 33. Ganesan, L. P. *et al.* FcγRIIb on liver sinusoidal endothelium clears small immune complexes. *J. Immunol.* **189**, 4981–8 (2012).
 34. Martin-Armas, M. *et al.* Toll-like receptor 9 (TLR9) is present in murine liver sinusoidal endothelial cells (LSECs) and mediates the effect of CpG-oligonucleotides. *J. Hepatol.* **44**, 939–946 (2006).
 35. Uhrig, A. *et al.* Development and functional consequences of LPS tolerance in sinusoidal endothelial cells of the liver. *J. Leukoc. Biol.* **77**, 626–633 (2005).
 36. Kern, M. *et al.* Virally Infected Mouse Liver Endothelial Cells Trigger CD8+ T-Cell Immunity. *Gastroenterology* **138**, 336–346 (2010).
 37. Böttcher, J. P., Knolle, P. A. & Stabenow, D. Mechanisms balancing tolerance and immunity in the liver. *Dig. Dis.* **29**, 384–390 (2011).
 38. Knolle, P. A. & Wohlleber, D. Immunological functions of liver sinusoidal endothelial cells. *Cell. Mol. Immunol.* **13**, 347–353 (2016).

39. Tang, L. *et al.* Liver Sinusoidal Endothelial Cell Lectin, LSECTin, Negatively Regulates Hepatic T-Cell Immune Response. *Gastroenterology* **137**, 1498–1508.e5 (2009).
40. Limmer, A. *et al.* Efficient presentation of exogenous antigen by liver endothelial cells to CD8+ T cells results in antigen-specific T-cell tolerance. *Nat. Med.* **6**, 1348–1354 (2000).
41. Wohlleber, D. *et al.* TNF-induced target cell killing by CTL activated through cross-presentation. *Cell Rep.* **2**, 478–87 (2012).
42. Wysocka, M. *et al.* Enhancement of the host immune responses in cutaneous T-cell lymphoma by CpG oligodeoxynucleotides and IL-15. *Blood* **104**, 4142–4149 (2004).
43. MATTILA, K. *et al.* Long-term Survival of Stage IV Melanoma Patients Treated with BOLD Combination Chemotherapy and Intermediate-dose Subcutaneous Interferon-alpha. *Anticancer Res.* **38**, 6393–6397 (2018).
44. Wang, W. *et al.* Interleukin- 15 suppresses gastric cancer liver metastases by enhancing natural killer cell activity in a murine model. *Oncol. Lett.* **16**, 4839–4846 (2018).
45. Bajor, D. L. *et al.* Long-term outcomes of a phase I study of agonist CD40 antibody and CTLA-4 blockade in patients with metastatic melanoma. *Oncoimmunology* **7**, e1468956 (2018).
46. Zhao, L. *et al.* Rapid complete remission of metastatic melanoma after first-line treatment with nivolumab plus tumor-infiltrating lymphocytes. *Immunotherapy* **10**, 1133–1136 (2018).
47. Kaufman, H., Lilley, C., Ponce, R., Hughes, T. & Coffin, R. Critical analysis of an oncolytic herpesvirus encoding granulocyte-macrophage colony stimulating factor for the treatment of malignant melanoma. *Oncolytic Virotherapy* **3**, 11 (2014).
48. Ramos, C. A. & Dotti, G. Chimeric antigen receptor (CAR)-engineered lymphocytes for cancer therapy. *Expert Opin. Biol. Ther.* **11**, 855–873 (2011).
49. Zoler, M. L. Human papilloma virus linked to cervical (and other) cancers. *JAMA* **249**, 2997–9 (1983).
50. Palmer, D. H. *et al.* A phase II study of adoptive immunotherapy using dendritic cells pulsed with tumor lysate in patients with hepatocellular carcinoma.

- Hepatology* **49**, 124–132 (2009).
51. Li, C. *et al.* Allogenic dendritic cell and tumor cell fused vaccine for targeted imaging and enhanced immunotherapeutic efficacy of gastric cancer. *Biomaterials* **54**, 177–187 (2015).
 52. Nestle, F. O. *et al.* Vaccination of melanoma patients with peptide- or tumor lysate-pulsed dendritic cells. *Nat. Med.* **4**, 328–32 (1998).
 53. Rothstein, J. L. & Schreiber, H. Relationship of tumour necrosis factor and endotoxin to macrophage cytotoxicity, haemorrhagic necrosis and lethal shock. *Ciba Found. Symp.* **131**, 124–39 (1987).
 54. Vaglini, M. *et al.* Treatment of primary or relapsing limb cancer by isolation perfusion with high-dose alpha-tumor necrosis factor, gamma-interferon, and melphalan. *Cancer* **73**, 483–92 (1994).
 55. Li, Y. P. *et al.* Stealth polycyanoacrylate nanoparticles as tumor necrosis factor-alpha carriers: pharmacokinetics and anti-tumor effects. *Biol. Pharm. Bull.* **24**, 662–5 (2001).
 56. Frick, S. U. *et al.* Interleukin-2 Functionalized Nanocapsules for T Cell-Based Immunotherapy. *ACS Nano* **10**, 9216–9226 (2016).
 57. Kim, H. K. *et al.* BEZ235 (PIK3/mTOR inhibitor) Overcomes Pazopanib Resistance in Patient-Derived Refractory Soft Tissue Sarcoma Cells. *Transl. Oncol.* **9**, 197–202 (2016).
 58. Pokropivny, V. V. & Skorokhod, V. V. Classification of nanostructures by dimensionality and concept of surface forms engineering in nanomaterial science. *Mater. Sci. Eng. C* **27**, 990–993 (2007).
 59. Wicki, A., Witzigmann, D., Balasubramanian, V. & Huwyler, J. Nanomedicine in cancer therapy: Challenges, opportunities, and clinical applications. *J. Control. Release* **200**, 138–157 (2015).
 60. Gunasekaran, T., Nigusse, T. & Dhanaraju, M. D. Silver Nanoparticles as Real Topical Bullets for Wound Healing. *J. Am. Coll. Clin. Wound Spec.* **3**, 82–96 (2011).
 61. Bianco, C. *et al.* Silver percutaneous absorption after exposure to silver nanoparticles: A comparison study of three human skin graft samples used for clinical applications. *Burns* **40**, 1390–1396 (2014).
 62. Matsumura, Y. & Maeda, H. A new concept for macromolecular therapeutics in

- cancer chemotherapy: mechanism of tumoritropic accumulation of proteins and the antitumor agent smancs. *Cancer Res.* **46**, 6387–92 (1986).
63. Li, P.-C. *et al.* In vivo photoacoustic molecular imaging with simultaneous multiple selective targeting using antibody-conjugated gold nanorods. *Opt. Express* **16**, 18605–15 (2008).
64. Desai, N. *et al.* Increased Antitumor Activity, Intratumor Paclitaxel Concentrations, and Endothelial Cell Transport of Cremophor-Free, Albumin-Bound Paclitaxel, ABI-007, Compared with Cremophor-Based Paclitaxel. *Clin. Cancer Res.* **12**, 1317–1324 (2006).
65. Chen, Y., Chen, S., Kawazoe, N. & Chen, G. Promoted Angiogenesis and Osteogenesis by Dexamethasone-loaded Calcium Phosphate Nanoparticles/Collagen Composite Scaffolds with Microgroove Networks. *Sci. Rep.* **8**, 14143 (2018).
66. Tenkumo, T. *et al.* Prolonged release of bone morphogenetic protein-2 in vivo by gene transfection with DNA-functionalized calcium phosphate nanoparticle-loaded collagen scaffolds. *Mater. Sci. Eng. C* **92**, 172–183 (2018).
67. Wang, Y. *et al.* Polymeric nanoparticles promote macrophage reversal from M2 to M1 phenotypes in the tumor microenvironment. *Biomaterials* **112**, 153–163 (2017).
68. Castro, F. *et al.* Pro-inflammatory chitosan/poly(γ -glutamic acid) nanoparticles modulate human antigen-presenting cells phenotype and revert their pro-invasive capacity. *Acta Biomater.* **63**, 96–109 (2017).
69. Amoozgar, Z. & Goldberg, M. S. Targeting myeloid cells using nanoparticles to improve cancer immunotherapy. *Adv. Drug Deliv. Rev.* **91**, 38–51 (2015).
70. Prego, C. *et al.* Chitosan-based nanoparticles for improving immunization against hepatitis B infection. *Vaccine* **28**, 2607–2614 (2010).
71. Kostadinova, A. I. *et al.* PLGA nanoparticles loaded with beta-lactoglobulin-derived peptides modulate mucosal immunity and may facilitate cow's milk allergy prevention. *Eur. J. Pharmacol.* **818**, 211–220 (2018).
72. Chen, Y. *et al.* Targeted delivery of antigen to intestinal dendritic cells induces oral tolerance and prevents autoimmune diabetes in NOD mice. *Diabetologia* **61**, 1384–1396 (2018).
73. Rahman, M. *et al.* Liposome-Based Nanomedicine Therapeutics for Rheumatoid

- Arthritis. *Crit. Rev. Ther. Drug Carrier Syst.* **34**, 283–316 (2017).
74. Xue, X. & Liang, X.-J. Overcoming drug efflux-based multidrug resistance in cancer with nanotechnology. *Chin. J. Cancer* **31**, 100–9 (2012).
75. Merisko-Liversidge, E. M. & Liversidge, G. G. Drug Nanoparticles: Formulating Poorly Water-Soluble Compounds. *Toxicol. Pathol.* **36**, 43–48 (2008).
76. Yang, T. *et al.* Enhanced solubility and stability of PEGylated liposomal paclitaxel: In vitro and in vivo evaluation. *Int. J. Pharm.* **338**, 317–326 (2007).
77. Kennedy, P. J. *et al.* Fab-conjugated PLGA nanoparticles effectively target cancer cells expressing human CD44v6. *Acta Biomater.* (2018). doi:10.1016/j.actbio.2018.09.043
78. Fader, A. N. & Rose, P. G. Abraxane for the Treatment of Gynecologic Cancer Patients With Severe Hypersensitivity Reactions to Paclitaxel. *Int. J. Gynecol. Cancer* **19**, 1281–1283 (2009).
79. Wang, D. *et al.* Erythrocyte–Cancer Hybrid Membrane Camouflaged Hollow Copper Sulfide Nanoparticles for Prolonged Circulation Life and Homotypic-Targeting Photothermal/Chemotherapy of Melanoma. *ACS Nano* **12**, 5241–5252 (2018).
80. Nishiyama, N. *et al.* Enhanced photodynamic cancer treatment by supramolecular nanocarriers charged with dendrimer phthalocyanine. *J. Control. Release* **133**, 245–251 (2009).
81. Neshastehriz, A., Khosravi, Z., Ghaznavi, H. & Shakeri-Zadeh, A. Gold-coated iron oxide nanoparticles trigger apoptosis in the process of thermo-radiotherapy of U87-MG human glioma cells. *Radiat. Environ. Biophys.* **57**, 405–418 (2018).
82. Maeda, H., Wu, J., Sawa, T., Matsumura, Y. & Hori, K. Tumor vascular permeability and the EPR effect in macromolecular therapeutics: a review. *J. Control. Release* **65**, 271–84 (2000).
83. Kim, D., Lee, E. S., Oh, K. T., Gao, Z. G. & Bae, Y. H. Doxorubicin-loaded polymeric micelle overcomes multidrug resistance of cancer by double-targeting folate receptor and early endosomal pH. *Small* **4**, 2043–50 (2008).
84. Huang, R. K., Steinmetz, N. F., Fu, C.-Y., Manchester, M. & Johnson, J. E. Transferrin-mediated targeting of bacteriophage HK97 nanoparticles into tumor cells. *Nanomedicine (Lond)*. **6**, 55–68 (2011).
85. Corsi, F. *et al.* HER2 Expression in Breast Cancer Cells Is Downregulated Upon

- Active Targeting by Antibody-Engineered Multifunctional Nanoparticles in Mice. *ACS Nano* **5**, 6383–6393 (2011).
86. Byeon, H. J. *et al.* Doxorubicin-loaded nanoparticles consisted of cationic- and mannose-modified-albumins for dual-targeting in brain tumors. *J. Control. Release* **225**, 301–313 (2016).
87. Green, A. E. & Rose, P. G. Pegylated liposomal doxorubicin in ovarian cancer. *Int. J. Nanomedicine* **1**, 229–39 (2006).
88. Perez, A. T., Domenech, G. H., Frankel, C. & Vogel, C. L. Pegylated liposomal doxorubicin (Doxil) for metastatic breast cancer: the Cancer Research Network, Inc., experience. *Cancer Invest.* **20 Suppl 2**, 22–9 (2002).
89. van Luijn, M. M. *et al.* Impaired antigen presentation in neoplasia: basic mechanisms and implications for acute myeloid leukemia. *Immunotherapy* **2**, 85–97 (2010).
90. Juneja, V. R. *et al.* PD-L1 on tumor cells is sufficient for immune evasion in immunogenic tumors and inhibits CD8 T cell cytotoxicity. *J. Exp. Med.* **214**, 895–904 (2017).
91. Hahn, S. A. *et al.* A key role of GARP in the immune suppressive tumor microenvironment. *Oncotarget* **7**, 42996–43009 (2016).
92. Strauss, L. *et al.* A Unique Subset of CD4⁺CD25^{high}Foxp3⁺ T Cells Secreting Interleukin-10 and Transforming Growth Factor-1 Mediates Suppression in the Tumor Microenvironment. *Clin. Cancer Res.* **13**, 4345–4354 (2007).
93. Qian, Y. *et al.* Molecular-Targeted Immunotherapeutic Strategy for Melanoma via Dual-Targeting Nanoparticles Delivering Small Interfering RNA to Tumor-Associated Macrophages. *ACS Nano* **11**, 9536–9549 (2017).
94. Zhang, C. *et al.* Targeted antigen delivery to dendritic cell via functionalized alginate nanoparticles for cancer immunotherapy. *J. Control. Release* **256**, 170–181 (2017).
95. Stone, G. W. *et al.* Nanoparticle-Delivered Multimeric Soluble CD40L DNA Combined with Toll-Like Receptor Agonists as a Treatment for Melanoma. *PLoS One* **4**, e7334 (2009).
96. Wilson, J. T. *et al.* pH-Responsive Nanoparticle Vaccines for Dual-Delivery of Antigens and Immunostimulatory Oligonucleotides. *ACS Nano* **7**, 3912–3925 (2013).

97. Mockey, M. *et al.* mRNA-based cancer vaccine: prevention of B16 melanoma progression and metastasis by systemic injection of MART1 mRNA histidylated lipopolyplexes. *Cancer Gene Ther.* **14**, 802–814 (2007).
98. Cao, J. *et al.* DNA vaccines targeting the encoded antigens to dendritic cells induce potent antitumor immunity in mice. *BMC Immunol.* **14**, 39 (2013).
99. Steinman, R. M. & Cohn, Z. A. Identification of a novel cell type in peripheral lymphoid organs of mice. I. Morphology, quantitation, tissue distribution. *J. Exp. Med.* **137**, 1142–62 (1973).
100. Steinman, R. M. Dendritic cells: Understanding immunogenicity. *Eur. J. Immunol.* **37**, S53–S60 (2007).
101. Sharpe, A. H. & Freeman, G. J. The B7–CD28 superfamily. *Nat. Rev. Immunol.* **2**, 116–126 (2002).
102. Averbek, M. *et al.* Early cytoskeletal rearrangement during dendritic cell maturation enhances synapse formation and Ca²⁺ signaling in CD8⁺ T cells. *Eur. J. Immunol.* **34**, 2708–2719 (2004).
103. Sozzani, S. *et al.* Differential regulation of chemokine receptors during dendritic cell maturation: a model for their trafficking properties. *J. Immunol.* **161**, 1083–6 (1998).
104. Yu, J. S. *et al.* Vaccination of malignant glioma patients with peptide-pulsed dendritic cells elicits systemic cytotoxicity and intracranial T-cell infiltration. *Cancer Res.* **61**, 842–7 (2001).
105. Berard, F. *et al.* Cross-priming of naive CD8 T cells against melanoma antigens using dendritic cells loaded with killed allogeneic melanoma cells. *J. Exp. Med.* **192**, 1535–44 (2000).
106. van de Loosdrecht, A. A. *et al.* A novel allogeneic off-the-shelf dendritic cell vaccine for post-remission treatment of elderly patients with acute myeloid leukemia. *Cancer Immunol. Immunother.* **67**, 1505–1518 (2018).
107. Dziubla, T. D., Karim, A. & Muzykantov, V. R. Polymer nanocarriers protecting active enzyme cargo against proteolysis. *J. Control. Release* **102**, 427–439 (2005).
108. Zhang, C. *et al.* Targeted antigen delivery to dendritic cell via functionalized alginate nanoparticles for cancer immunotherapy. *J. Control. Release* **256**, 170–181 (2017).

109. Arosio, D. *et al.* Effective Targeting of DC-SIGN by α -Fucosylamide Functionalized Gold Nanoparticles. *Bioconjug. Chem.* **25**, 2244–2251 (2014).
110. Morse, M. A. *et al.* Phase I study utilizing a novel antigen-presenting cell-targeted vaccine with Toll-like receptor stimulation to induce immunity to self-antigens in cancer patients. *Clin. Cancer Res.* **17**, 4844–53 (2011).
111. Lee, Y.-R. *et al.* Biodegradable nanoparticles containing TLR3 or TLR9 agonists together with antigen enhance MHC-restricted presentation of the antigen. *Arch. Pharm. Res.* **33**, 1859–1866 (2010).
112. Inaba, K. *et al.* Tissue distribution of the DEC-205 protein that is detected by the monoclonal antibody NLDC-145. I. Expression on dendritic cells and other subsets of mouse leukocytes. *Cell. Immunol.* **163**, 148–56 (1995).
113. Wollenberg, A. *et al.* Expression and Function of the Mannose Receptor CD206 on Epidermal Dendritic Cells in Inflammatory Skin Diseases. *J. Invest. Dermatol.* **118**, 327–334 (2002).
114. Harms, G., Dijkstra, C. D. & Hardonk, M. J. Glycosyl receptors in macrophage subpopulations of rat spleen and lymph node. A comparative study using neoglycoproteins and monoclonal antibodies ED1, ED2 and ED3. *Cell Tissue Res.* **262**, 35–40 (1990).
115. Shepherd, V. L., Campbell, E. J., Senior, R. M. & Stahl, P. D. Characterization of the mannose/fucose receptor on human mononuclear phagocytes. *J. Reticuloendothel. Soc.* **32**, 423–31 (1982).
116. Jiang, W. *et al.* The receptor DEC-205 expressed by dendritic cells and thymic epithelial cells is involved in antigen processing. *Nature* **375**, 151–155 (1995).
117. Bühler, J. *et al.* Selective Uptake of Cylindrical Poly(2-Oxazoline) Brush-AntiDEC205 Antibody-OVA Antigen Conjugates into DEC-Positive Dendritic Cells and Subsequent T-Cell Activation. *Chem. - A Eur. J.* **20**, 12405–12410 (2014).
118. Shen, L. *et al.* Protein corona-mediated targeting of nanocarriers to B cells allows redirection of allergic immune responses. *J. Allergy Clin. Immunol.* **142**, 1558–1570 (2018).
119. Scherer, M. *et al.* Functionalization of Active Ester-Based Polymersomes for Enhanced Cell Uptake and Stimuli-Responsive Cargo Release. *Biomacromolecules* **17**, 3305–3317 (2016).

120. Mohr, N. *et al.* Targeting cells of the immune system: mannosylated HPMA–LMA block-copolymer micelles for targeting of dendritic cells. *Nanomedicine* **11**, 2679–2697 (2016).
121. Weber, B. *et al.* PeptoSomes for Vaccination: Combining Antigen and Adjuvant in Polypept(o)ide-Based Polymersomes. *Macromol. Biosci.* **17**, 1700061 (2017).
122. Birke, A., Ling, J. & Barz, M. Polysarcosine-containing copolymers: Synthesis, characterization, self-assembly, and applications. *Prog. Polym. Sci.* **81**, 163–208 (2018).
123. Lau, K. H. A. *et al.* Surface-Grafted Polysarcosine as a Peptoid Antifouling Polymer Brush. *Langmuir* **28**, 16099–16107 (2012).
124. Talelli, M., Rijcken, C. J. F., van Nostrum, C. F., Storm, G. & Hennink, W. E. Micelles based on HPMA copolymers. *Adv. Drug Deliv. Rev.* **62**, 231–239 (2010).
125. Bauer, M. *et al.* Poly(2-ethyl-2-oxazoline) as Alternative for the Stealth Polymer Poly(ethylene glycol): Comparison of in vitro Cytotoxicity and Hemocompatibility. *Macromol. Biosci.* **12**, 986–998 (2012).
126. Ostuni, E., Chapman, R. G., Holmlin, R. E., Takayama, S. & Whitesides, G. M. A Survey of Structure-Property Relationships of Surfaces that Resist the Adsorption of Proteins. *Langmuir* **17**, (2001).
127. Bühler, J. *et al.* Selective Uptake of Cylindrical Poly(2-Oxazoline) Brush-AntiDEC205 Antibody-OVA Antigen Conjugates into DEC-Positive Dendritic Cells and Subsequent T-Cell Activation. *Chem. - A Eur. J.* **20**, 12405–12410 (2014).
128. Niikura, K. *et al.* Gold Nanoparticles as a Vaccine Platform: Influence of Size and Shape on Immunological Responses *in Vitro* and *in Vivo*. *ACS Nano* **7**, 3926–3938 (2013).
129. Jia, J. *et al.* Interactions Between Nanoparticles and Dendritic Cells: From the Perspective of Cancer Immunotherapy. *Front. Oncol.* **8**, 404 (2018).
130. Oyewumi, M. O., Kumar, A. & Cui, Z. Nano-microparticles as immune adjuvants: correlating particle sizes and the resultant immune responses. *Expert Rev. Vaccines* **9**, 1095–1107 (2010).
131. Xiang, S. D. *et al.* Pathogen recognition and development of particulate vaccines: Does size matter? *Methods* **40**, 1–9 (2006).

132. Joshi, V. B., Geary, S. M. & Salem, A. K. Biodegradable Particles as Vaccine Delivery Systems: Size Matters. *AAPS J.* **15**, 85–94 (2013).
133. Reddy, S. T. *et al.* Exploiting lymphatic transport and complement activation in nanoparticle vaccines. *Nat. Biotechnol.* **25**, 1159–1164 (2007).
134. Fromen, C. A. *et al.* Nanoparticle surface charge impacts distribution, uptake and lymph node trafficking by pulmonary antigen-presenting cells. *Nanomedicine* **12**, 677–687 (2016).
135. Park, B. S. & Lee, J.-O. Recognition of lipopolysaccharide pattern by TLR4 complexes. *Exp. Mol. Med.* **45**, e66 (2013).
136. Rutz, M. *et al.* Toll-like receptor 9 binds single-stranded CpG-DNA in a sequence- and pH-dependent manner. *Eur. J. Immunol.* **34**, 2541–2550 (2004).
137. Kawai, T. *et al.* Lipopolysaccharide stimulates the MyD88-independent pathway and results in activation of IFN-regulatory factor 3 and the expression of a subset of lipopolysaccharide-inducible genes. *J. Immunol.* **167**, 5887–94 (2001).
138. Yamamoto, M. *et al.* Role of Adaptor TRIF in the MyD88-Independent Toll-Like Receptor Signaling Pathway. *Science (80-.).* **301**, 640–643 (2003).
139. Klinman, D. M. Immunotherapeutic uses of CpG oligodeoxynucleotides. *Nat. Rev. Immunol.* **4**, 249–259 (2004).
140. Sparwasser, T. *et al.* Bacterial DNA and immunostimulatory CpG oligonucleotides trigger maturation and activation of murine dendritic cells. *Eur. J. Immunol.* **28**, 2045–2054 (1998).
141. Tsujimura, H. *et al.* Toll-like receptor 9 signaling activates NF-kappaB through IFN regulatory factor-8/IFN consensus sequence binding protein in dendritic cells. *J. Immunol.* **172**, 6820–7 (2004).
142. Chen, G., Shaw, M. H., Kim, Y.-G. & Nuñez, G. NOD-Like Receptors: Role in Innate Immunity and Inflammatory Disease. *Annu. Rev. Pathol. Mech. Dis.* **4**, 365–398 (2009).
143. Paßlick, D. *et al.* Delivering all in one: Antigen-nanocapsule loaded with dual adjuvant yields superadditive effects by DC-directed T cell stimulation. *J. Control. Release* **289**, 23–34 (2018).
144. Shen, L. *et al.* Vaccination with trifunctional nanoparticles that address CD8+dendritic cells inhibits growth of established melanoma. *Nanomedicine* **11**, 2647–2662 (2016).

145. Liu, C. *et al.* Encapsulation of Poly I:C and the natural phosphodiester CpG ODN enhanced the efficacy of a hyaluronic acid-modified cationic lipid-PLGA hybrid nanoparticle vaccine in TC-1-grafted tumors. *Int. J. Pharm.* **553**, 327–337 (2018).
146. Salem, A. K. A promising CpG adjuvant-loaded nanoparticle-based vaccine for treatment of dust mite allergies. *Immunotherapy* **6**, 1161–1163 (2014).
147. Lv, S. *et al.* Nanoparticles encapsulating hepatitis B virus cytosine-phosphate-guanosine induce therapeutic immunity against HBV infection. *Hepatology* **59**, 385–394 (2014).
148. Gursel, M., Gursel, I., Mostowski, H. S. & Klinman, D. M. CXCL16 influences the nature and specificity of CpG-induced immune activation. *J. Immunol.* **177**, 1575–80 (2006).
149. Smedsrød, B., Melkko, J., Araki, N., Sano, H. & Horiuchi, S. Advanced glycation end products are eliminated by scavenger-receptor-mediated endocytosis in hepatic sinusoidal Kupffer and endothelial cells. *Biochem. J.* **322 (Pt 2)**, 567–73 (1997).
150. WATANABE, J., HABA, M., URANO, K. & YUASA, H. Uptake Mechanism of Fractionated (3H)Heparin in Isolated Rat Kupffer Cells: Involvement of Scavenger Receptors. *Biol. Pharm. Bull.* **19**, 581–586 (1996).
151. Knuschke, T., Eppe, M. & Westendorf, A. M. The type of adjuvant strongly influences the T-cell response during nanoparticle-based immunization. *Hum. Vaccin. Immunother.* **10**, 164–169 (2014).
152. Shen, L. *et al.* Protein corona-mediated targeting of nanocarriers to B cells allows redirection of allergic immune responses. *J. Allergy Clin. Immunol.* 1–13 (2018). doi:10.1016/j.jaci.2017.08.049
153. Drickamer, K. C-type lectin-like domains. *Curr. Opin. Struct. Biol.* **9**, 585–90 (1999).
154. Figdor, C. G., Kooyk, Y. Van & Adema, G. J. C-Type Lectin Receptors on. *Immunology* **2**, (2002).
155. Guan, J. *et al.* Enhanced immunocompatibility of ligand-targeted liposomes by attenuating natural IgM absorption. *Nat. Commun.* **9**, 2982 (2018).
156. Sharma, R., Mody, N., Kushwah, V., Jain, S. & Vyas, S. C-Type lectin receptor(s)-targeted nanoliposomes: an intelligent approach for effective cancer

- immunotherapy. *Nanomedicine* **12**, 1945–1959 (2017).
157. Hartung, E. *et al.* Induction of Potent CD8 T Cell Cytotoxicity by Specific Targeting of Antigen to Cross-Presenting Dendritic Cells In Vivo via Murine or Human XCR1. *J. Immunol.* **194**, 1069–1079 (2015).
158. Cruz, L. J. *et al.* Targeting nanoparticles to CD40, DEC-205 or CD11c molecules on dendritic cells for efficient CD8+T cell response: A comparative study. *J. Control. Release* **192**, 209–218 (2014).
159. Dufresne, I. *et al.* Targeting lymph nodes with liposomes bearing anti-HLA-DR Fab' fragments. *Biochim. Biophys. Acta* **1421**, 284–94 (1999).
160. Lahoud, M. H. *et al.* Targeting Antigen to Mouse Dendritic Cells via Clec9A Induces Potent CD4 T Cell Responses Biased toward a Follicular Helper Phenotype. *J. Immunol.* **187**, 842–850 (2011).
161. den Haan, J. M., Lehar, S. M. & Bevan, M. J. CD8(+) but not CD8(-) dendritic cells cross-prime cytotoxic T cells in vivo. *J. Exp. Med.* **192**, 1685–96 (2000).
162. Schreibelt, G. *et al.* The C-type lectin receptor CLEC9A mediates antigen uptake and (cross-)presentation by human blood BDCA3+ myeloid dendritic cells. *Blood* **119**, 2284–2292 (2012).
163. Bonifaz, L. C. *et al.* In Vivo Targeting of Antigens to Maturing Dendritic Cells via the DEC-205 Receptor Improves T Cell Vaccination. *J. Exp. Med.* **199**, 815–824 (2004).
164. Birkholz, K. *et al.* Targeting of DEC-205 on human dendritic cells results in efficient MHC class II-restricted antigen presentation. *Blood* **116**, 2277–2285 (2010).
165. Meixlsperger, S. *et al.* CD141+ dendritic cells produce prominent amounts of IFN- after dsRNA recognition and can be targeted via DEC-205 in humanized mice. *Blood* **121**, 5034–5044 (2013).
166. Kato, M. *et al.* Expression of human DEC-205 (CD205) multilectin receptor on leukocytes. *Int. Immunol.* **18**, 857–869 (2006).
167. Small, M. & Kraal, G. In vitro evidence for participation of DEC-205 expressed by thymic cortical epithelial cells in clearance of apoptotic thymocytes. *Int. Immunol.* **15**, 197–203 (2003).
168. Kato, M. *et al.* Expression of multilectin receptors and comparative FITC-dextran uptake by human dendritic cells. *Int. Immunol.* **12**, 1511–9 (2000).

169. Cao, L., Shi, X., Chang, H., Zhang, Q. & He, Y. pH-Dependent recognition of apoptotic and necrotic cells by the human dendritic cell receptor DEC205. *Proc. Natl. Acad. Sci. U. S. A.* **112**, 7237–42 (2015).
170. Mahnke, K. *et al.* The dendritic cell receptor for endocytosis, DEC-205, can recycle and enhance antigen presentation via major histocompatibility complex class II-positive lysosomal compartments. *J. Cell Biol.* **151**, 673–84 (2000).
171. Wadwa, M., Klopffleisch, R., Buer, J. & Westendorf, A. M. Targeting antigens to DEC-205 on dendritic cells induces immune protection in experimental colitis in mice. *Eur. J. Microbiol. Immunol.* **6**, 1–8 (2016).
172. Manolova, V. *et al.* Nanoparticles target distinct dendritic cell populations according to their size. *Eur. J. Immunol.* **38**, 1404–1413 (2008).
173. Perche, F. *et al.* Enhancement of dendritic cells transfection in vivo and of vaccination against B16F10 melanoma with mannosylated histidylated lipopolyplexes loaded with tumor antigen messenger RNA. *Nanomedicine Nanotechnology, Biol. Med.* **7**, 445–453 (2011).
174. Picco, G., Beatson, R., Taylor-Papadimitriou, J. & Burchell, J. M. Targeting DNGR-1 (CLEC9A) with antibody/MUC1 peptide conjugates as a vaccine for carcinomas. *Eur. J. Immunol.* **44**, 1947–1955 (2014).
175. Bonifaz, L. C. *et al.* In vivo targeting of antigens to maturing dendritic cells via the DEC-205 receptor improves T cell vaccination. *J. Exp. Med.* **199**, 815–24 (2004).
176. Fossum, E. *et al.* Vaccine molecules targeting Xcr1 on cross-presenting DCs induce protective CD8⁺ T-cell responses against influenza virus. *Eur. J. Immunol.* **45**, 624–635 (2015).
177. Bonifaz, L. C. *et al.* In vivo targeting of antigens to maturing dendritic cells via the DEC-205 receptor improves T cell vaccination. *J. Exp. Med.* **199**, 815–24 (2004).
178. Kroczyk, R. A. & Henn, V. The Role of XCR1 and its Ligand XCL1 in Antigen Cross-Presentation by Murine and Human Dendritic Cells. *Front. Immunol.* **3**, 14 (2012).
179. Saluja, S. S. *et al.* Targeting human dendritic cells via DEC-205 using PLGA nanoparticles leads to enhanced cross-presentation of a melanoma-associated antigen. *Int. J. Nanomedicine* **9**, 5231–46 (2014).

180. Caminschi, I., Maraskovsky, E. & Heath, W. R. Targeting dendritic cells in vivo for cancer therapy. *Front. Immunol.* **3**, 1–13 (2012).
181. Poulin, L. F. *et al.* Characterization of human DNGR-1⁺ BDCA3⁺ leukocytes as putative equivalents of mouse CD8 α ⁺ dendritic cells. *J. Exp. Med.* **207**, 1261–1271 (2010).
182. Crozat, K. *et al.* The XC chemokine receptor 1 is a conserved selective marker of mammalian cells homologous to mouse CD8 α ⁺ dendritic cells. *J. Exp. Med.* **207**, 1283–1292 (2010).
183. Kronin, V., Wu, L., Gong, S., Nussenzweig, M. C. & Shortman, K. DEC-205 as a marker of dendritic cells with regulatory effects on CD8 T cell responses. *Int. Immunol.* **12**, 731–735 (2000).
184. Gurka, S., Hartung, E., Becker, M. & Kroczeck, R. A. Mouse Conventional Dendritic Cells Can be Universally Classified Based on the Mutually Exclusive Expression of XCR1 and SIRP \pm . *Front. Immunol.* **6**, 35 (2015).
185. Yamazaki, C. *et al.* Conservation of a chemokine system, XCR1 and its ligand, XCL1, between human and mice. *Biochem. Biophys. Res. Commun.* **397**, 756–761 (2010).
186. Schreiberl, G. *et al.* The C-type lectin receptor CLEC9A mediates antigen uptake and (cross-)presentation by human blood BDCA3⁺ myeloid dendritic cells. *Blood* **119**, 2284–2292 (2012).
187. Betting, D. J. *et al.* Enhanced immune stimulation by a therapeutic lymphoma tumor antigen vaccine produced in insect cells involves mannose receptor targeting to antigen presenting cells. *Vaccine* **27**, 250–259 (2009).
188. Glaffig, M., Stergiou, N., Hartmann, S., Schmitt, E. & Kunz, H. A Synthetic MUC1 Anticancer Vaccine Containing Mannose Ligands for Targeting Macrophages and Dendritic Cells. *ChemMedChem* **13**, 25–29 (2018).
189. Keler, T., Ramakrishna, V. & Fanger, M. W. Mannose receptor-targeted vaccines. *Expert Opin. Biol. Ther.* **4**, 1953–1962 (2004).
190. Stahl, P. D., Rodman, J. S., Miller, M. J. & Schlesinger, P. H. Evidence for receptor-mediated binding of glycoproteins, glycoconjugates, and lysosomal glycosidases by alveolar macrophages. *Proc. Natl. Acad. Sci. U. S. A.* **75**, 1399–403 (1978).
191. Cochand, L., Isler, P., Songeon, F. & Nicod, L. P. Human Lung Dendritic Cells

- Have an Immature Phenotype with Efficient Mannose Receptors. *Am. J. Respir. Cell Mol. Biol.* **21**, 547–554 (1999).
192. Sallusto, F., Cella, M., Danieli, C. & Lanzavecchia, A. Dendritic cells use macropinocytosis and the mannose receptor to concentrate macromolecules in the major histocompatibility complex class II compartment: downregulation by cytokines and bacterial products. *J. Exp. Med.* **182**, 389–400 (1995).
193. Hubbard, A. L., Wilson, G., Ashwell, G. & Stukenbrok, H. An electron microscope autoradiographic study of the carbohydrate recognition systems in rat liver. I. Distribution of ¹²⁵I-ligands among the liver cell types. *J. Cell Biol.* **83**, 47–64 (1979).
194. Takahashi, K., Donovan, M. J., Rogers, R. A. & Ezekowitz, R. A. B. Distribution of murine mannose receptor expression from early embryogenesis through to adulthood. *Cell Tissue Res.* **292**, 311–323 (1998).
195. Lee, S. J. *et al.* Mannose Receptor-Mediated Regulation of Serum Glycoprotein Homeostasis. *Science (80-.)*. **295**, 1898–1901 (2002).
196. Shepherd, V. L. & Hoidal, J. R. Clearance of Neutrophil-derived Myeloperoxidase by the Macrophage Mannose Receptor. *Am. J. Respir. Cell Mol. Biol.* **2**, 335–340 (1990).
197. van Liempt, E. *et al.* Specificity of DC-SIGN for mannose- and fucose-containing glycans. *FEBS Lett.* **580**, 6123–6131 (2006).
198. Lee, R. T. *et al.* Survey of immune-related, mannose/fucose-binding C-type lectin receptors reveals widely divergent sugar-binding specificities. *Glycobiology* **21**, 512–520 (2011).
199. Salvati, A. *et al.* Transferrin-functionalized nanoparticles lose their targeting capabilities when a biomolecule corona adsorbs on the surface. *Nat. Nanotechnol.* **8**, 137–143 (2013).
200. Ritz, S. *et al.* Protein Corona of Nanoparticles: Distinct Proteins Regulate the Cellular Uptake. *Biomacromolecules* **16**, 1311–1321 (2015).
201. Maiolo, D., Del Pino, P., Metrangolo, P., Parak, W. J. & Baldelli Bombelli, F. Nanomedicine delivery: does protein corona route to the target or off road? *Nanomedicine* **10**, 3231–3247 (2015).
202. Bros, M. *et al.* The Protein Corona as a Confounding Variable of Nanoparticle-Mediated Targeted Vaccine Delivery. *Front. Immunol.* **9**, 1760 (2018).

203. Chinen, A. B., Guan, C. M., Ko, C. H. & Mirkin, C. A. The Impact of Protein Corona Formation on the Macrophage Cellular Uptake and Biodistribution of Spherical Nucleic Acids. *Small* **13**, 1603847 (2017).
204. Cruz, L. J. *et al.* Comparison of antibodies and carbohydrates to target vaccines to human dendritic cells via DC-SIGN. *Biomaterials* **33**, 4229–4239 (2012).
205. Kanbe, E. *et al.* Novel synthesized trimannose conjugate induces endocytosis and expression of immunostimulatory molecules in monocytic leukemia cells. *Int. J. Hematol.* **74**, 309–15 (2001).
206. He, C., Hu, Y., Yin, L., Tang, C. & Yin, C. Effects of particle size and surface charge on cellular uptake and biodistribution of polymeric nanoparticles. *Biomaterials* **31**, 3657–3666 (2010).
207. Choi, H. S. *et al.* Renal clearance of quantum dots. *Nat. Biotechnol.* **25**, 1165–70 (2007).
208. Almeida, J. P. M., Chen, A. L., Foster, A. & Drezek, R. *In vivo* biodistribution of nanoparticles. *Nanomedicine* **6**, 815–835 (2011).
209. Zhang, Y.-N., Poon, W., Tavares, A. J., McGilvray, I. D. & Chan, W. C. W. Nanoparticle–liver interactions: Cellular uptake and hepatobiliary elimination. *J. Control. Release* **240**, 332–348 (2016).
210. Blanco, E., Shen, H. & Ferrari, M. Principles of nanoparticle design for overcoming biological barriers to drug delivery. *Nat. Biotechnol.* **33**, 941–951 (2015).
211. Sadauskas, E. *et al.* Kupffer cells are central in the removal of nanoparticles from the organism. *Part. Fibre Toxicol.* **4**, 10 (2007).
212. Arora, S., Jain, J., Rajwade, J. M. & Paknikar, K. M. Interactions of silver nanoparticles with primary mouse fibroblasts and liver cells. *Toxicol. Appl. Pharmacol.* **236**, 310–318 (2009).
213. MacPhee, P. J., Schmidt, E. E. & Groom, A. C. Intermittence of blood flow in liver sinusoids, studied by high-resolution *in vivo* microscopy. *Am. J. Physiol. Liver Physiol.* **269**, G692–G698 (1995).
214. Tsoi, K. M. *et al.* Mechanism of hard-nanomaterial clearance by the liver. *Nat. Mater.* **15**, 1212–1221 (2016).
215. Mirshafiee, V., Mahmoudi, M., Lou, K., Cheng, J. & Kraft, M. L. Protein corona significantly reduces active targeting yield. *Chem. Commun. (Camb)*. **49**, 2557–9

- (2013).
216. Stang, E., Kindberg, G. M., Berg, T. & Roos, N. Endocytosis mediated by the mannose receptor in liver endothelial cells. An immunocytochemical study. *Eur. J. Cell Biol.* **52**, 67–76 (1990).
 217. Schlesinger, P. H. *et al.* Plasma clearance of glycoproteins with terminal mannose and N-acetylglucosamine by liver non-parenchymal cells. Studies with beta-glucuronidase, N-acetyl-beta-D-glucosaminidase, ribonuclease B and agalacto-orosomucoid. *Biochem. J.* **176**, 103–9 (1978).
 218. Bashirova, A. A. *et al.* A dendritic cell-specific intercellular adhesion molecule 3-grabbing nonintegrin (DC-SIGN)-related protein is highly expressed on human liver sinusoidal endothelial cells and promotes HIV-1 infection. *J. Exp. Med.* **193**, 671–8 (2001).
 219. Reuter, K. G. *et al.* Targeted PRINT Hydrogels: The Role of Nanoparticle Size and Ligand Density on Cell Association, Biodistribution, and Tumor Accumulation. *Nano Lett.* **15**, 6371–6378 (2015).
 220. Gu, F. *et al.* Precise engineering of targeted nanoparticles by using self-assembled biointegrated block copolymers. *Proc. Natl. Acad. Sci.* **105**, 2586–2591 (2008).
 221. Wang, J., Tian, S., Petros, R. A., Napier, M. E. & Desimone, J. M. The complex role of multivalency in nanoparticles targeting the transferrin receptor for cancer therapies. *J. Am. Chem. Soc.* **132**, 11306–13 (2010).
 222. Lu, L. *et al.* Liver-derived DEC205+B220+CD19- dendritic cells regulate T cell responses. *J. Immunol.* **166**, 7042–52 (2001).
 223. Pietrzak-nguyen, A. *et al.* Enhanced in vivo targeting of murine non-parenchymal liver cells with monophosphoryl lipid A functionalized microcapsules Enhanced in vivo targeting of murine non-parenchymal liver cells with monophosphoryl lipid A functionalized microcapsules. (2014). doi:10.1021/bm5006728
 224. Thomson, A. W. & Knolle, P. A. Antigen-presenting cell function in the tolerogenic liver environment. *Nat. Rev. Immunol.* **10**, 753–766 (2010).
 225. Breous, E., Somanathan, S., Vandenberghe, L. H. & Wilson, J. M. Hepatic regulatory T cells and Kupffer cells are crucial mediators of systemic T cell tolerance to antigens targeting murine liver. *Hepatology* **50**, 612–21 (2009).
 226. Zeng, Z. *et al.* Interferon- γ facilitates hepatic antiviral T cell retention for the

- maintenance of liver-induced systemic tolerance. *J. Exp. Med.* **213**, 1079–93 (2016).
227. Wu, J. *et al.* Toll-like receptor-induced innate immune responses in non-parenchymal liver cells are cell type-specific. *Immunology* **129**, 363–74 (2010).
228. Beck, S. *et al.* Site-Specific DBCO Modification of DEC205 Antibody for Polymer Conjugation. *Polymers (Basel)*. **10**, 141 (2018).
229. Tonigold, M. *et al.* Pre-adsorption of antibodies enables targeting of nanocarriers despite a biomolecular corona. *Nat. Nanotechnol.* **13**, 862–869 (2018).
230. Linehan, S. A. *et al.* Enhanced expression of the mannose receptor by endothelial cells of the liver and spleen microvascular beds in the macrophage-deficient PU.1 null mouse. *Histochem. Cell Biol.* **123**, 365–376 (2005).
231. Magnusson, S. & Berg, T. Extremely rapid endocytosis mediated by the mannose receptor of sinusoidal endothelial rat liver cells. *Biochem. J.* **257**, 651–6 (1989).
232. Lozach, P.-Y. *et al.* DC-SIGN and L-SIGN Are High Affinity Binding Receptors for Hepatitis C Virus Glycoprotein E2. *J. Biol. Chem.* **278**, 20358–20366 (2003).
233. Paßlick, D. *et al.* Delivering all in one: Antigen-nanocapsule loaded with dual adjuvant yields superadditive effects by DC-directed T cell stimulation. *J. Control. Release* **289**, 23–34 (2018).
234. Tuettenberg, A. *et al.* Induction of strong and persistent MelanA/MART-1-specific immune responses by adjuvant dendritic cell-based vaccination of stage II melanoma patients. *Int. J. Cancer* **118**, 2617–2627 (2006).
235. Bloom, M. B. *et al.* Identification of tyrosinase-related protein 2 as a tumor rejection antigen for the B16 melanoma. *J. Exp. Med.* **185**, 453–9 (1997).

5. APPENDIX

5.1 Publication 1

Selective uptake of cylindrical poly(2-oxazoline) brush-antiDEC205 antibody-OVA antigen conjugates into DEC-positive dendritic cells and subsequent T-cell activation

Published in: Chemistry A European Journal, 2014, 22;20(39):12405-10

Reprinted (adapted) with permission from (Bühler, J. *et al.* Selective Uptake of Cylindrical Poly(2-Oxazoline) Brush-AntiDEC205 Antibody-OVA Antigen Conjugates into DEC-Positive Dendritic Cells and Subsequent T-Cell Activation. *Chem. - A Eur. J.* **20**, 12405–12410 (2014)). Copyright (2014) John Wiley and Sons.

Cancer Therapy

Selective Uptake of Cylindrical Poly(2-Oxazoline) Brush-AntiDEC205 Antibody-OVA Antigen Conjugates into DEC-Positive Dendritic Cells and Subsequent T-Cell Activation

Jasmin Bühler,^[a, b] Sabine Gietzen,^[a] Anika Reuter,^[a, c] Cinja Kappel,^[e] Karl Fischer,^[a] Sandra Decker,^[a] David Schäffel,^[d] Kaloian Koynov,^[d] Matthias Bros,^{*,[e]} Ingrid Tubbe,^[e] Stephan Grabbe,^{*,[c, e]} and Manfred Schmidt^{*,[a, b, c]}

Abstract: To achieve specific cell targeting by various receptors for oligosaccharides or antibodies, a carrier must not be taken up by any of the very many different cells and needs functional groups prone to clean conjugation chemistry to derive well-defined structures with a high biological specificity. A polymeric nanocarrier is presented that consists of a cylindrical brush polymer with poly(2-oxazoline) side chains carrying an azide functional group on each of the many side chain ends. After click conjugation of dye and an anti-DEC205 antibody to the periphery of the cylindrical brush polymer, antibody-mediated specific binding and uptake into DEC205⁺-positive mouse bone marrow-derived dendritic cells (BMDC) was observed, whereas binding and uptake by DEC205⁻ negative BMDC and non-DC was essentially absent. Additional conjugation of an antigen peptide yielded a multifunctional polymer structure with a much stronger antigen-specific T-cell stimulatory capacity of pretreated BMDC than application of antigen or polymer-antigen conjugate.

The ideal nanocarrier for biomedical applications is not cytotoxic, has a size between 10 and 100 nm, and does not form aggregates in blood serum that are due to strong interactions with the numerous proteins and enzymes present in the complex biological fluids.^[1] Poly(2-oxazoline)s are excellent candidates for this purpose,^[2] because they are known for their low cytotoxicity,^[3] biocompatibility,^[4,5] stealth behavior,^[6,7] and low protein adsorption from human blood.^[8]

Cylindrical polymer brushes have become increasingly popular because of their anisotropic character and the recent results on shape dependent endocytosis.^[9-12] Furthermore, polymeric brushes may offer a multiplicity of functional groups which are advantageous for conjugation of biologically active compounds.

Several publications report cylindrical brushes with poly(2-oxazoline) side chains prepared by "grafting from"^[13,14] and "grafting through"^[15-17] techniques. Recently our group published the synthesis of cylindrical brushes with poly(2-isopropyl-2-oxazoline) side chains by grafting through with unprecedented high main chain degrees of polymerization.^[18] All of the cylindrical brushes with poly(2-oxazoline) side chains reported to date do not contain functional groups for further conjugation experiments except for one work in which functionalized polymers were prepared though with a main-chain degree of polymerization as low as only 13.^[19] However, azide functionalized linear poly(2-oxazoline)s have been described.^[20-24]

To assess the suitability of the cylindrical brushes described herein to serve as nanocarriers for immuno-therapeutic approaches, their binding and uptake by DC was analyzed, because DC represent an important immune cell population. In their activated state, DC constitute the most potent antigen-presenting cells of the immune system that are solely able to initiate primary immune responses.^[25] Of the several DC subpopulations known, CD8⁺ DC that co-express the C-type lectin receptor DEC205 bear the highest potential to activate cytotoxic T lymphocytes.^[26] Conjugation of anti-DEC205 with antigen and adjuvant resulted in partial loss of targeting activity,^[27] whereas conjugation of an antigen only was shown to main-

[a] Dr. J. Bühler,⁺ S. Gietzen,⁺ Dr. A. Reuter, Dr. K. Fischer, S. Decker, Dr. M. Schmidt
Institute for Physical Chemistry, University of Mainz
Jakob-Welder Weg 11, 55099 Mainz (Germany)
E-mail: mschmidt@uni-mainz.de

[b] Dr. J. Bühler,⁺ Dr. M. Schmidt
Graduate School Materials Science
Staudinger Weg 9, 55128 Mainz (Germany)

[c] Dr. A. Reuter, Dr. S. Grabbe, Dr. M. Schmidt
Max Planck Graduate Center
Staudinger Weg 9, 55128 Mainz (Germany)

[d] D. Schäffel, Dr. K. Koynov
Max Planck Institute for Polymer Research
Ackermannweg 10, 55128 Mainz (Germany)

[e] C. Kappel, Dr. M. Bros, I. Tubbe, Dr. S. Grabbe
Department of Dermatology
University Medical Center of the Johannes Gutenberg
University Mainz
Langenbeckstrasse 1, 55131 Mainz (Germany)
E-mail: mbros@uni-mainz.de
stephan.grabbe@unimedizin-mainz.de

[*] These authors contributed equally to this work.

Supporting information for this article is available on the WWW under <http://dx.doi.org/10.1002/chem.201403942>.

tain DEC205 receptor mediated binding and uptake of antigen by this DC subpopulation.^[28,29]

Polymer–antibody rather than polymer–antibody fragment conjugates are less frequently reported.^[30–32] Antithymocyte globuline,^[33] polyclonal human immunoglobulin, and monoclonal anti-RAGE antibody^[34] were successfully conjugated to linear flexible hydroxypropylmethacrylate (HPMA) chains with no or little loss of antibody activity. Also polymeric capsules of a few μm in size were decorated by a few hundred thousand humanized A33 monoclonal antibodies were reported to selectively address human colorectal cancer cells.^[35,36]

Herein, the binding and uptake properties of bare cylindrical brushes were investigated in comparison to cylindrical brushes conjugated with a DEC205-specific antibody, when co-incubated with DC.

The synthesis is summarized in Scheme 1. The synthesis of the azide-functionalized poly(2-oxazoline) macromonomers was performed similar to the poly(2-isopropyl-2-oxazoline) macromonomer synthesis published recently^[18] and is described in some detail in the Supporting Information. Three different azide-functionalized macromonomers were synthesized and characterized by NMR and IR spectroscopy, GPC, and MALDI-TOF spectrometry (Supporting Information, Figures S1–S11). The results are summarized in Table 1.

Table 1 reveals the molar masses determined by MALDI-TOF and NMR to be similar. The ratio of the 2-ethyl-2-oxazoline block to 2-isopropyl-2-oxazoline block of the N_3 -poly(2-ethyl-2-isopropyl-2-oxazoline) macromonomer was determined by ^1H NMR to be 60% to 40%. MALDI-TOF was not measured for the block co-macromonomer as there would be different distri-

Table 1. Characterization of the macromonomers.

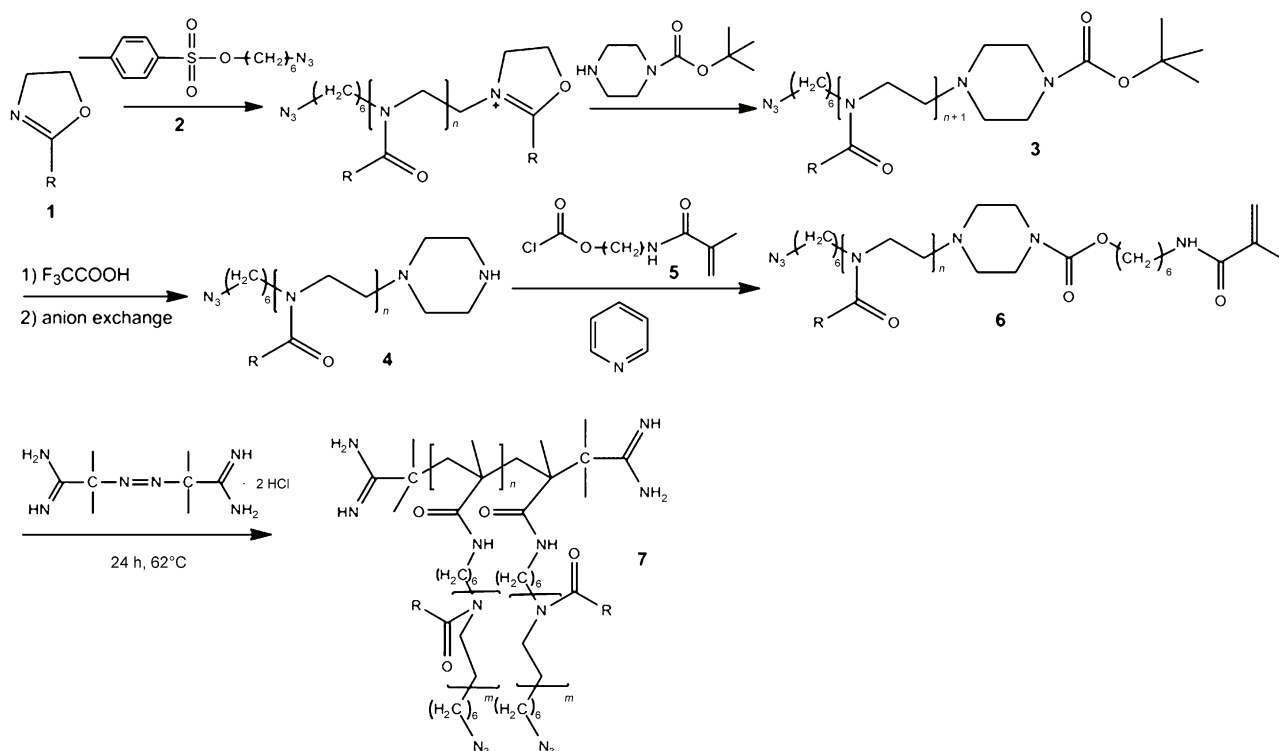
	N_3 -PiPrOx	N_3 -PEtOx	N_3 -PEtOx-b-PiPrOx
M_w/M_n (MALDI/GPC)	1.12/1.13	1.20/1.16	–/1.1
M_n (MALDI) [g mol^{-1}]	4707	3623	–
M_n (GPC) [g mol^{-1}]	14800 ^[a]	13400 ^[a]	18900*
M_n (^1H NMR) [g mol^{-1}]	4946	3694	5869
M_w (MALDI) [g mol^{-1}]	5292	4330	–
P_n	40	33	61

[a] GPC with PMMA calibration yields values that are too large.

butions owing to the different block lengths. For further discussion we will use the ^1H NMR-determined molar masses.

All the three azide-functionalized macromonomers were polymerized in highly concentrated aqueous solutions at 62°C . The IR spectra of all azide end-functionalized brushes show the characteristic band at 2100 cm^{-1} (Supporting Information, Figure S12). After reduction with tris(2-carboxyethyl)phosphine, the azide bands disappeared (Supporting Information, Figure S13).

Polymerization of block co-macromonomers leads to core-shell cylindrical brushes;^[37] that is, polymerization of N_3 -poly(2-ethyl-2-isopropyl-2-oxazoline) macromonomers yields a core-shell structure with a core consisting of slightly hydrophobic poly(2-isopropyl-oxazoline) chains and a corona of hydrophilic poly(2-ethyl-oxazoline) chains. Representative DLS and SLS measurements of the cylindrical brushes with N_3 -poly(2-ethyl-2-isopropyl-2-oxazoline) side chains are shown in Figure 1 (for Zimm plots of the other cylindrical bushes, see the Supporting



Scheme 1. Synthesis of azide-functionalized poly(2-oxazoline)s.

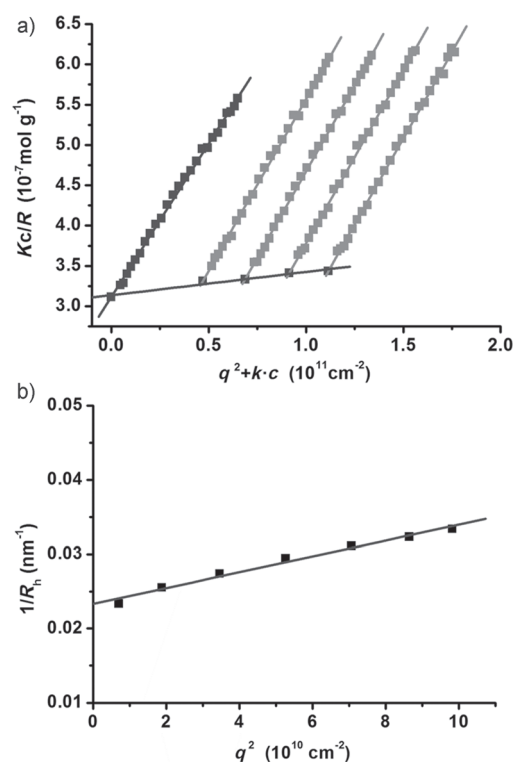


Figure 1. a) Zimm plot and b) reciprocal hydrodynamic radius of the azide end-functionalized cylindrical core-shell brush N_3 -poly(2-ethyl-block-2-isopropyl-2-oxazoline) in methanol with 5 mM added LiBr at 20 °C.

Table 2. Light scattering characterization including the degree of polymerization P_w of the azide end-functionalized brush polymers with poly(2-oxazoline) side chains.

	R_g [nm]	R_h [nm]	$\rho = R_g/R_h$	M_w (LS) [g mol ⁻¹]	dn/dc [cm ³ g ⁻¹]	P_w (LS)	M_w/M_n (GPC)
N_3 -PiPrOx-brush	37.4	26	1.44	$1.3 \cdot 10^6$	0.163	254	2.2
N_3 -PEtOx-brush	32.3	21	1.54	$6.2 \cdot 10^5$	0.177	167	1.7
N_3 -PEtOx- <i>b</i> -PiPrOx-brush	60.5	42	1.44	$3.2 \cdot 10^6$	0.177	547	2.4

Information, Figure S14). The results are summarized in Table 2. GPC calibrated by PMMA standards revealed polydispersities $M_w/M_n \approx 2$ for all samples, as expected (Supporting Information, Figure S11).

AFM (Figure 2; Supporting Information, Figure S15) illustrates the expected worm-like structures in qualitative agreement with the results obtained by static and dynamic light scattering. The N_3 -poly(2-ethyl-2-oxazoline) brush shows besides worm-like structures a multiplicity of spherical particles resulting in the much lower molecular weight compared to the other two brushes.

None of the cylindrical brush polymers exerted inhibitory effects on the metabolic activity of both human HEK293 and mouse BMDCs to any cell-type specific extent, that is, the 50% cell survival concentration was determined to be well above $1 \mu\text{g} \mu\text{L}^{-1}$ (Supporting Information, Table S3).

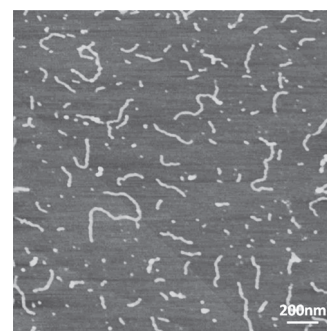


Figure 2. AFM image (height) of azide end-functionalized core-shell poly(2-oxazoline) brush N_3 -poly(2-ethyl-block-2-isopropyl-2-oxazoline) spin-cast onto mica from aqueous solution at $c = 0.1 \text{ g L}^{-1}$.

Recently our group developed a method that allows the determination of aggregation behavior of nanoparticles in human blood serum by dynamic light scattering.^[38] The correlation function of nanoparticles or polymers in serum solution, $g_1(t)_{\text{mix}}$ should be well-fitted the adequate weighted sum of known correlation functions measured from the polymer in isotonic solution, $g_1(t)_p$ and of undiluted serum, $g_1(t)_s$:

$$g_1(t)_{\text{mix}} = a_p g_1(t)_p + a_s g_1(t)_s + (a_A g_1(t)_A) \quad (1)$$

where a_p and a_s represent the amplitudes as the only fit parameters.

In the case of aggregation, a third correlation function describing the aggregate, $g_1(t)_A$, has to be added:

$$g_1(t)_{\text{mix}} = a_p g_1(t)_p + a_s g_1(t)_s + a_A g_1(t)_A \quad (2)$$

Figure 3 shows the autocorrelation function of the mixture of serum and N_3 -PiPrOx brush (a) as well as the mixture of serum and N_3 -PEtOx-*b*-PiPrOx brush (b). For the latter sample, the data points of the mixture are well-described by the force fit with the sum of individual correlation functions of serum and polymer brush, meaning no or negligible aggregation has taken place. Similar results were obtained for the N_3 -PEtOx brush (data not shown).

In contrast, the autocorrelation function of the mixture of serum and N_3 -PiPrOx-brush could not be perfectly fitted by the force fit with the sum of individual correlation functions of serum and polymer brush (Eq. (1); Figure 3 black line). A third correlation function is necessary to achieve a perfect fit (Eq. (2); Figure 3, gray line) and indicates a significant amount of aggregates of 360 nm radius to be present, which may be caused by the higher hydrophobicity of the N_3 -PiPrOx-brush. Hydrophobic proteins such as lipoproteins may interact with the polymer brush, leading to aggregation, although the extent of aggregation is quite small in view of the "intensity weighting" of DLS.

The data above reveal that the N_3 -EtOx and the N_3 -PEtOx-*b*-PiPrOx brushes do not form aggregates in concentrated blood serum, which could provoke unwanted uptake by macrophages and negatively influence the circulation time for later in vivo experiments.

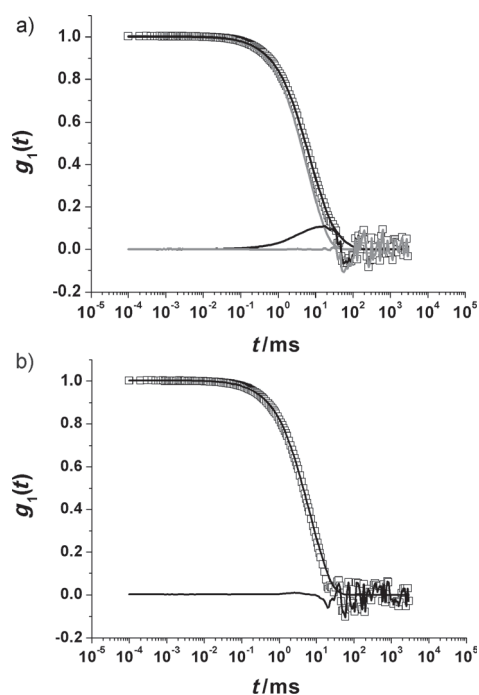


Figure 3. Autocorrelation functions of a) N_3 -PiPrOx and b) N_3 -PEtOx-*b*-PiPrOx brushes in human blood serum; gray lines represent the force fits with the sum of the individual correlation functions of serum and polymer brush according to Eq. (1); black lines represent the fits according to Eq. (2) accounting for the presence of aggregates; scattering angle 30° .

Dibenzocyclooctyne-modified antiDEC205 antibody was conjugated to the N_3 -poly(2-ethyl-2-isopropyl-2-oxazoline) brush utilizing copper-free 1–3 dipolar cycloaddition chemistry (Supporting Information, Scheme S2).^[39] According to UV/Vis spectroscopy, approximately 8 to 10 antibodies were bound to one cylindrical brush polymer (Supporting Information, Figure S17). No free antibody could be detected in the conjugate by gel electrophoresis (Supporting Information, Figure S18).

Fluorescence-activated cell sorting (FACS) showed that 29% of the $CD11^+$ BMDC population co-expressed DEC205, while 33% of the $CD11^+$ BMDC populations lacked DEC205 expression, and 37% of the cells were $CD11^+$ negative; that is, were no DCs (Figure 4a). The mean fluorescence intensity (MFI) of either $CD11^+$ BMDC population as well as of non-DC co-incubated with N_3 -PEtOx-*b*-PiPrOx-brushes for 4 h was rather low, as shown by the dotted lines in Figure 4b–d. When co-incubated with the polymer–antibody conjugate, a three-fold higher MFI was observed for $DEC205^+CD11^+$ BMDC (solid line in Figure 4b). In contrast, neither $DEC205^-CD11^+$ BMDC nor non-DC showed any considerable increase in polymer binding (solid lines in Figure 4c,d). Confocal laser scanning microscopy (CLSM) images confirmed this result and revealed polymer and antibody to be co-localized inside of $DEC205^+CD11^+$ BMDCs (Figure 4e,f). The corresponding FACS data and CLSM pictures for BMDC co-incubated with unconjugated polymer brushes are given in the Supporting Information, Figure S21.

After 4 h, 73% of the $DEC205^+$ BMDCs had engaged conjugate. It should be noted that cellular engagement of polymer antibody conjugates was blocked, if the BMDCs were incubat-

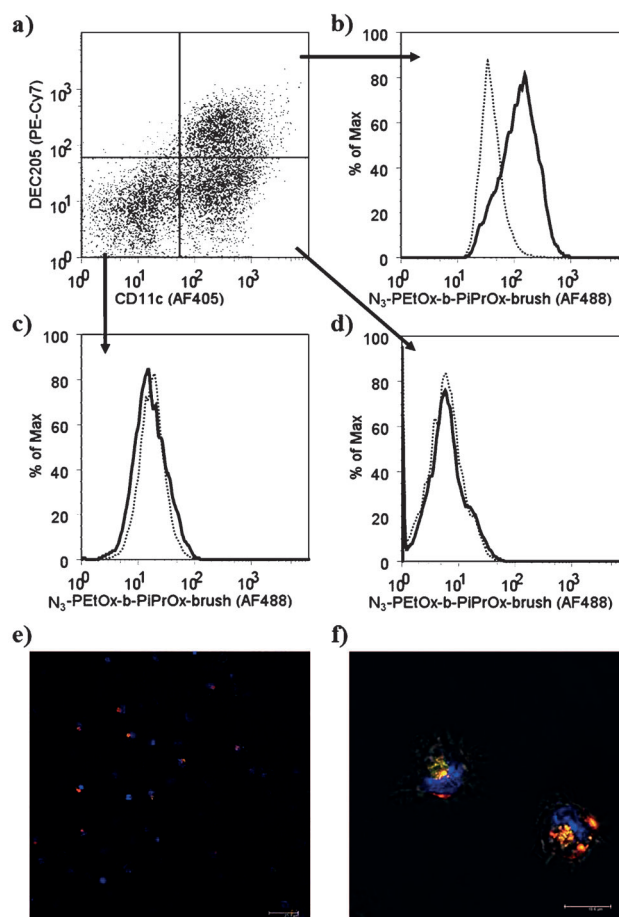


Figure 4. Binding and uptake of N_3 -poly(2-ethyl-block-2-isopropyl-2-oxazoline) brush-antiDEC205 conjugates by BMDC. Unstimulated BMDC were co-incubated for 4 hours in parallel with Carboxy-Rhodamine110-labeled N_3 -PEtOx-*b*-PiPrOx-brush, unconjugated or conjugated with anti-DEC205 antibody (10^{12} particles per 5×10^5 cells). a) BMDCs were double-stained with DEC205 and CD11c specific antibodies. The dot plot shows the distribution of the different subpopulations of BMDC co-incubated with anti-DEC205 antibody conjugated polymer. b–d) Curves show different evaluations of one experiment and indicate cellular binding of anti-DEC205 antibody conjugated (thick solid line) and unconjugated polymer (thin dotted line) by the different cell populations. The corresponding MFI are given in brackets: b) $CD11^+DEC205^+$ (MFI: 152.6 versus 44.6), c) $CD11^+DEC205^-$: (MFI: 20.1 vs. 19.5), and d) $CD11^-$ non-DCs (MFI: 8.1 vs. 7.2). Graphs are representative of 10 experiments. e), f) CLSM pictures of the polymer-DEC205 conjugates taken up by DCs. The polymer is labeled by Carboxyrhodamin (green), the DEC205 by AF647 (red). The orange color shows superposition of polymer and DEC205, that is, the intact conjugate. Hoechst 33342 (blue) was utilized to label cell nuclei. Scale bars 25.3 μm (e) and 10.6 μm (f).

ed with native anti-DEC205 antibody at large excess prior to addition of polymer antibody conjugates (Supporting Information, Figure S22).

To demonstrate a potential biological application of the cylindrical brush conjugates, the SIINFEKL-sequence of the OVA-antigen was additionally conjugated to the cylindrical brush polymer. As described in detail in the Supporting Information, Scheme S3, the AF546-labeled C-SGLEQLS-SIINFEKL oligopeptide (AG, derived from the ovalbumine antigen) was conjugated to the N_3 -poly(2-ethyl-block-2-isopropyl-2-oxazoline) cylindrical brush (CB) first, followed by conjugation of DBCO-func-

tionalized anti-DEC205 antibody (sample CB-AG-aDEC205). The trailer sequence SGLEQLE is known to be enzymatically cleavable by cells^[40] and cysteine was added for the conjugation reaction. On average, the final conjugate contained 17 antigen fragments and 7.5 anti-DEC205 molecules (Supporting Information, Figures S19 and S20).

The suitability of CB-AG-aDEC205 to confer efficient uptake of antigen into BMDCs was monitored by a proliferation of peptide (or SIINFEKL) reactive CD8⁺ T-cells. As shown in Figure 5, BMDC pre-incubated for 4 h with the CB-AG-aDEC205 conjugate (no. 4) induced much stronger proliferation of sub-

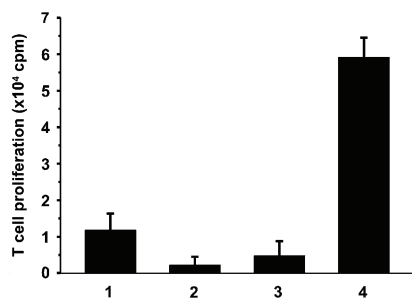


Figure 5. Antigen-specific CD8⁺ T-cell stimulatory capacity of BMDCs pre-incubated with the cylindrical brush conjugate CB-AG-aDEC205. In parallel assays, unstimulated BMDCs (each 5×10^5 cells) were incubated for 4 h with C-SGLEQLE-SIINFEKL peptide (1), with non-conjugated N3-poly(2-ethyl-block-2-isopropyl-2-oxazoline cylindrical brushes (2), with cylindrical brush-antigen conjugate (3), and with CB-AG-aDEC205 carrying both aDEC205 and C-SGLEQLE-SIINFEKL (4), at equimolar concentration of antigen (no. 1, 3, and 4; 10^{12} peptide molecules) or equal number of cylindrical brush polymer chains (no. 2 and 4).

sequently co-cultured peptide-reactive CD8⁺ T-cells than BMDCs pretreated with either antigen alone (no. 1) or polymer-antigen conjugate without aDEC205 (no. 3). The cylindrical brush polymer alone served as a negative control (no. 2).

Thus the azide functionalized polymer brushes with 2-ethyl-2-oxazoline and 2-ethyl-block-2-isopropyl-2-oxazoline side chains seem to be promising candidates for the application as nanocarriers for an antibody mediated specific targeting of cells as it is used in the immune cancer therapy.^[41–45] Although biodegradable the particles utilized so far were spherical in shape with sizes well above 100 nm up to 1 μ m. Thus, they might be taken up by macrophages by unspecific phagocytosis. Although the presented polymer brushes also exhibit high molar masses (Table 2) it should be noted that size rather than molar mass should be the relevant property for body circulation and recognition by macrophages. In this respect, the small size of the cylindrical brush polymers well below 100 nm in combination with their anisotropic shape makes them interesting candidates to study in vivo distribution in future experiments. As compared to antibody conjugates with antigen and/or adjuvant as reported recently^[27–29] the very large number of chemically accessible functional groups (that is, more than 100 azide groups per polymer) may allow particles to be produced with ten and more antibodies which may enhance cell-type-specific targeting.^[27] Furthermore, these particles may contain

several tens of antigen and/or adjuvant molecules to yield a higher quantity of cargo delivered on a per cell base. The applied click chemistry yields almost quantitative conjugation results and allows for the attachment of a predictable number of even different peptide antigens, which may serve to induce both CD4⁺ and CD8⁺ T-cell responses at the same time. Likewise, conjugation with different adjuvants that trigger distinct signaling pathways may serve to exert synergistic effects in terms of DC activation, and therefore the extent of subsequent T-cell stimulation.^[46]

Acknowledgements

Financial support by the DFG graduate school MAINZ (J.B.), by the Max Planck Graduate Center, Mainz, and by the German Science Foundation (SFB625, SFB1066) is gratefully acknowledged. CLSM measurements were performed at the Institute for Molecular Biology, Mainz. Some dye labeling experiments were conducted by Meike Schinnerer, Institute of Physical Chemistry, University Mainz, which is gratefully acknowledged.

Keywords: brush polymers · cancer therapy · dendritic cells · nanocarriers · T-cells

- [1] D. Weller, A. Medina-Oliva, H. Claus, S. Gietzen, K. Mohr, A. Reuter, D. Schäffel, S. Schöttler, K. Koynov, M. Bros, *Macromolecules* **2013**, *46*, 8519–8527.
- [2] R. Luxenhofer, Y. Han, A. Schulz, J. Tong, Z. He, A. V. Kabanov, R. Jordan, *Macromol. Rapid Commun.* **2012**, *33*, 1724.
- [3] R. Luxenhofer, G. Sahay, A. Schulz, D. Alakhova, T. K. Bronich, R. Jordan, A. V. Kabanov, *J. Controlled Release* **2011**, *153*, 73–82.
- [4] P. Goddard, L. E. Hutchinson, J. Brown, L. J. Brookman, *J. Controlled Release* **1989**, *10*, 5–16.
- [5] F. C. Gaertner, R. Luxenhofer, B. Blechert, R. Jordan, M. Essler, *J. Controlled Release* **2007**, *119*, 291–300.
- [6] M. C. Woodle, C. M. Engbers, S. Zalipsky, *Bioconjugate Chem.* **1994**, *5*, 493–496.
- [7] S. Zalipsky, C. B. Hansen, J. M. Oaks, T. M. Allen, *J. Pharm. Sci.* **1996**, *85*, 133–137.
- [8] R. Konradi, B. Pidhatika, A. Mühlebach, M. Textor, *Langmuir* **2008**, *24*, 613–616.
- [9] Y. Geng, P. Dalhaimer, S. Cai, R. Tsai, M. Tewari, T. Minko, D. E. Discher, *Nat. Nano* **2007**, *2*, 249–255.
- [10] J. Champion, S. Mitragotri, *Pharm. Res.* **2009**, *26*, 244–249.
- [11] S. Cai, K. Vijayan, D. Cheng, E. Lima, D. Discher, *Pharm. Res.* **2007**, *24*, 2099–2109.
- [12] J. L. Perry, K. G. Reuter, M. P. Kai, K. P. Herlihy, S. W. Jones, J. C. Luft, M. Napier, J. E. Bear, J. M. DeSimone, *Nano Lett.* **2012**, *12*, 5304–5310.
- [13] N. Zhang, S. Huber, A. Schulz, R. Luxenhofer, R. Jordan, *Macromolecules* **2009**, *42*, 2215–2221.
- [14] N. Zhang, R. Luxenhofer, R. Jordan, *Macromol. Chem. Phys.* **2012**, *213*, 1963–1969.
- [15] C. Weber, C. Remzi Becer, W. Guenther, R. Hoogenboom, U. S. Schubert, *Macromolecules* **2009**, *42*, 160–167.
- [16] C. Weber, A. Krieg, R. M. Paulus, H. M. L. Lambermont-Thijs, C. R. Becer, R. Hoogenboom, U. S. Schubert, *Macromol. Symp.* **2011**, *308*, 17–24.
- [17] C. Weber, S. Rogers, A. Vollrath, S. Hoepfener, T. Rudolph, N. Fritz, R. Hoogenboom, U. S. Schubert, *J. Polym. Sci. A: Polym. Chem.* **2013**, *51*, 139–148.
- [18] J. Bühler, S. Muth, K. Fischer, M. Schmidt, *Macromol. Rapid Commun.* **2013**, *34*, 588–594.
- [19] C. Weber, J. A. Czaplowska, A. Baumgaertel, E. Altuntas, M. Gottschaldt, R. Hoogenboom, U. S. Schubert, *Macromolecules* **2012**, *45*, 46–55.

- [20] G. Volet, T.-X. Lav, J. Babinot, C. Amiel, *Macromol. Chem. Phys.* **2011**, *212*, 118–124.
- [21] W. H. Binder, H. Gruber, *Macromol. Chem. Phys.* **2000**, *201*, 949–957.
- [22] T.-X. Lav, P. Lemechko, E. Renard, C. Amiel, V. Langlois, G. Volet, *React. Funct. Polym.* **2013**, *73*, 1001–1008.
- [23] C. Guis, H. Cheradame, *Eur. Polym. J.* **2000**, *36*, 2581–2590.
- [24] K. Kempe, R. Hoogenboom, M. Jaeger, U. S. Schubert, *Macromolecules* **2011**, *44*, 6424–6432.
- [25] O. Joffre, M. A. Nolte, R. Spörri, C. R. e. Sousa, *Immunol. Rev.* **2009**, *227*, 234–247.
- [26] P. M. Domínguez, C. Ardavín, *Immunol. Rev.* **2010**, *234*, 90–104.
- [27] M. Kreutz, B. Giquel, Q. Hu, R. Abuknesha, S. Uematsu, S. Akira, F. O. Nestle, S. S. Diebold, *PLoS ONE* **2012**, *7*, e40208 EP.
- [28] L. Bonifaz, D. Bonnyay, K. Mahnke, M. Rivera, M. C. Nussenzweig, R. M. Steinman, *J. Exp. Med.* **2002**, *196*, 1627–1638.
- [29] T. S. Johnson, K. Mahnke, V. Storn, K. Schönfeld, S. Ring, D. M. Nettelbeck, H. J. Haisma, F. Le Gall, R. E. Kontermann, A. H. Enk, *Clin. Cancer Res.* **2008**, *14*, 8169–8177.
- [30] M. C. Garnett, *Adv. Drug Delivery Rev.* **2001**, *53*, 171–216.
- [31] J. Kopeček, P. Kopečková, *Adv. Drug Delivery Rev.* **2010**, *62*, 122–149.
- [32] J. Kopeček, *Adv. Drug Delivery Rev.* **2013**, *65*, 49–59.
- [33] K. Ulbrich, T. Etrych, P. Chytil, M. Jelínková, B. Říhová, *J. Controlled Release* **2003**, *87*, 33–47.
- [34] K. Tappertzhofen, V. V. Metz, M. Hubo, M. Barz, R. Postina, H. Jonuleit, R. Zentel, *Macromol. Biosci.* **2013**, *13*, 203–214.
- [35] A. P. R. Johnston, M. M. J. Kamphuis, G. K. Such, A. M. Scott, E. C. Nice, J. K. Heath, F. Caruso, *ACS Nano* **2012**, *6*, 6667–6674.
- [36] M. M. J. Kamphuis, A. P. R. Johnston, G. K. Such, H. H. Dam, R. A. Evans, A. M. Scott, E. C. Nice, J. K. Heath, F. Caruso, *J. Am. Chem. Soc.* **2010**, *132*, 15881–15883.
- [37] R. Djalali, N. Hugenberg, K. Fischer, M. Schmidt, *Macromol. Rapid Commun.* **1999**, *20*, 444–449.
- [38] K. Rausch, A. Reuter, K. Fischer, M. Schmidt, *Biomacromolecules* **2010**, *11*, 2836–2839.
- [39] E. M. Sletten, C. R. Bertozzi, *Acc. Chem. Res.* **2011**, *44*, 666–676.
- [40] R. J. Binder, P. K. Srivastava, *Proc. Natl. Acad. Sci. USA* **2004**, *101*, 6128–6133.
- [41] Y. J. Kwon, E. James, N. Shastri, J. M. J. Fréchet, *Proc. Natl. Acad. Sci. USA* **2005**, *102*, 18264–18268.
- [42] A. Bandyopadhyay, R. L. Fine, S. Demento, L. K. Bockenstedt, T. M. Fahmy, *Biomaterials* **2011**, *32*, 3094–3105.
- [43] A. C. Shirali, M. Look, W. Du, E. Kassis, H. W. Stout-Delgado, T. M. Fahmy, D. R. Goldstein, *Am. J. Transplant.* **2011**, *11*, 2582–2592.
- [44] J. Park, W. Gao, R. Whiston, T. B. Strom, S. Metcalfe, T. M. Fahmy, *Mol. Pharm.* **2011**, *8*, 143–152.
- [45] L. J. Cruz, P. J. Tacken, F. Bonetto, S. I. Buschow, H. J. Croes, M. Wijers, I. J. de Vries, C. G. Figdor, *Mol. Pharm.* **2011**, *8*, 520–531.
- [46] M. Krummen, S. Balkow, L. Shen, S. Heinz, C. Loquai, H. C. Probst, S. Grabbe, *J. Leukocyte Biol.* **2010**, *88*, 189–199.

Received: June 12, 2014

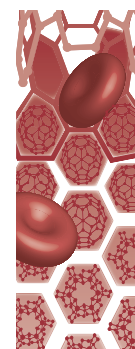
Published online on August 8, 2014

5.2 Publication 2

Targeting cells of the immune system: mannosylated HPMA-LMA block-copolymer micelles for targeting of dendritic cells

Published in: Nanomedicine, 2016, 11(20):2679-2697

(no permission required)



Targeting cells of the immune system: mannosylated HPMA–LMA block-copolymer micelles for targeting of dendritic cells

Background: Successful tumor immunotherapy depends on the induction of strong and sustained tumor antigen-specific immune responses by activated antigen-presenting cells (APCs) such as dendritic cells (DCs). Since nanoparticles have the potential to codeliver tumor-specific antigen and DC-stimulating adjuvant in a DC-targeting manner, we wanted to assess the suitability of mannosylated HPMA-LMA block polymers for immunotherapy. **Materials & methods:** Fluorescence-labeled block copolymer micelles derived from P(HPMA)-block-P(LMA) copolymers and according statistical copolymers were synthesized via RAFT polymerization, and loaded with the APC activator L18-MDP. Both types of copolymers were conjugated with D-mannose to target the mannose receptor as expressed by DCs and macrophages. The extent and specificity of micelle binding and activation of APCs was monitored using mouse spleen cells and bone marrow-derived DC (BMDC). **Results:** Nontargeting HPMA-LMA statistical copolymers showed strong unspecific cell binding. HPMA-LMA block copolymers bound DC only when conjugated with mannose, and in a mannose receptor-specific manner. Mannosylated HPMA-LMA block copolymers were internalized by DC. DC-targeting HPMA-LMA block copolymers mediated DC activation when loaded with L18-MDP. **Conclusion:** Mannosylated HPMA-LMA block copolymers are a promising candidate for the development of DC-targeting nanovaccines.

Nicole Mohr^{*,1}, Cinja Kappel^{*,2}, Stefan Kramer¹, Matthias Bros^{*,2}, Stephan Grabbe^{*,2} & Rudolf Zentel^{***,1}

¹Institute of Organic Chemistry, Johannes Gutenberg-University Mainz, Duesbergweg 10-14, 55099 Mainz, Germany

²Department of Dermatology, University Medical Center, Johannes Gutenberg-University Mainz, Obere Zahlbacher Straße 63, 55131 Mainz, Germany

*Author for correspondence: mbros@uni-mainz.de

**Author for correspondence: stephan.grabbe@unimedizin-mainz.de

***Author for correspondence: zentel@uni-mainz.de

[†]Authors contributed equally

First draft submitted: 17 April 2016; Accepted for publication: 15 July 2016; Published online: 15 September 2016

Keywords: dendritic cell • HPMA block copolymer • immune system • mannose as targeting ligand

While vaccination against infectious diseases has revolutionized human healthcare in the last century, it is still difficult to transfer this strategy to diseases derived from the body's own tissue as in cancer. Here the immune system is usually 'somehow silenced' to these 'autopathogens', since also immune tolerance mechanisms are involved in cancer. Thus, to activate the immune system against cancer, it is necessary to activate it strongly and to eliminate tolerance mechanisms at the same time. In this respect, nanoparticles have a great potential as carriers (Figure 1):

- Nanoparticles are attractive to the

immune system because they are in the same size range (nm) as viruses and fragments of bacteria. The immune system evolved to care about these pathogens. Interestingly, a sort-of 'passive' delivery effect for nanoparticles also exists within the immune system: Reddy *et al.* demonstrated that after intradermal injection nanoparticles accumulate in the lymph nodes over time [2]. The interstitial flow is able to transport, especially, rather small nanoparticles with sizes around 25 nm through the lymphatic capillaries into the draining lymph nodes, where these particles can be taken up by antigen-presenting

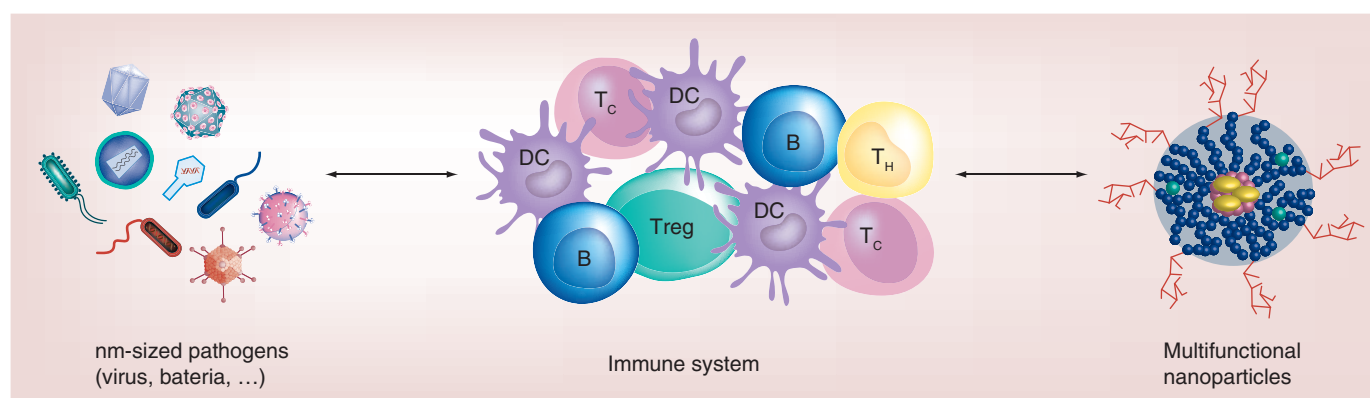


Figure 1. Pathogenic fragments in the nanosize range are attracted by the immune system as well as well-defined nanoparticles engineered for (targeted) (co-)delivery of immune modulators to certain immune cells [1].

immune cells without further targeting ligands [3]. To that respect, the immune system itself seems to attract nanosized materials (comparable to nanosized pathogen (fragments) derived from viruses or bacteria): ‘the immune system likes nanotechnology’ [1,4]. Thus, the potential of nanoparticles for immunotherapy has recently been summarized under medical aspects [5].

- Nanoparticulate carriers are able to co-deliver bioactive compounds. This is important for an optimal activation of the immune system, because this requires the co-delivery of antigens and activation signals to the desired subpopulations of specialized immune cells at the time point when they are most sensitive (otherwise, it is most likely that the opposite behavior can be induced, in particular, immune tolerance) [6]. To that respect, nanoparticles can effectively protect and shield biologically sensitive molecules (e.g., antigen-bearing peptides or immunostimulatory oligonucleotides) from degradation, increase their half-life in the body and minimize their systemic toxicity [7].
- Nanocarriers can further be equipped with homing devices for targeted delivery to desired immune cell subpopulations. This is, on one hand, required to stimulate, for example, dendritic cells (DCs; as the most potent immune stimulatory cells) without losing the majority of the cargo ‘somewhere.’ It is even more necessary, when immunosuppressive activities have to be turned off in only certain subpopulations.

In recent work, we could demonstrate that nanodimensional antigen presentation plays a key role in the immune system: multifunctional HPMA (N-[2-hydroxypropyl]methacrylamide)-based homo and block copolymers [8] were equipped with tumor-associated MUC1 glycopeptides as cancer cell surface antigens

and applied as antitumor vaccine in mice. Interestingly, only those glycopeptide–polymer conjugates bearing a nanostructure promoting, self-assembling poly(lauryl methacrylate [LMA]) domain were able to induce antibodies of highest tumor affinity [9]. Thus, a nanoparticle-promoting multivalent presentation of poorly immunogenic antigens seems to play a pivotal role during immunization, as soluble MUC1 glycopeptides without any nanostructural presentation cannot induce antibodies, as shown in another study independently [10].

As carrier, poly-HPMA has been developed for many nanomedicines during the last years [11–13]. This is due to its nontoxic and nonimmunogenic features and based on the contributions of Duncan [14], Kopecek and Kopecková [15]. Poly-HPMA polymers functionalized with LMA as a hydrophobic comonomer can self-assemble into polymeric micelles in water [16,17]. Such a core–shell structure [18] is advantageous for shielding the cargo in the core and for a multivalent presentation of targeting units in the periphery in analogy to Figure 1. It is, however, very important in this context to remember that statistical and block copolymers from the hydrophilic HPMA and LMA behave rather differently in the biological context [19,20]. In block copolymers, hydrophilic and hydrophobic segments separate well into an inner core and the pure hydrophilic poly-HPMA corona. Thus, these polymeric micelles get stealth like [17,19,21] and show very little unspecific interactions with plasma proteins and cell membranes. However, this is not the case for the statistical copolymers [22]. Because of unspecific interactions of hydrophobic groups statistically distributed in the corona of the particle with hydrophobic parts of cell membranes they interact with some serum proteins [22], they show unspecific uptake in leucocytes [20] and get able to mediate drug delivery over biological barriers [23]. Because of strong unspecific interactions with cell membranes, the statistical copolymers are thus not desirable for a tar-

geted delivery to subpopulations of leucocytes [20], but the block copolymers are.

To prepare such a narrowly distributed well-defined HPMA–LMA block copolymer, the reversible addition-fragmentation chain-transfer (RAFT) polymerization of pentafluorophenylmethacrylate (PFPMMA) with a subsequent postpolymerization modification offers an elegant method to achieve polymers with narrow chain length distributions [8,16,24]. In combination with LMA as the hydrophobic component amphiphilic HPMA–LMA structures can be easily synthesized. Another advantage of this reactive ester route is the possibility of introducing simultaneously different markers for *in vitro* visualization as well as the targeting structures for specific cell targeting.

For targeting subpopulations of leucocytes like DCs, besides antibodies [25] carbohydrates can also be used, for example, mannose, which binds to the mannose receptor present on DCs [26]. Suitable carbohydrates offer here the advantage that they are much smaller than antibodies (typically 6–7 nm) and lead thus only to a minor modification of the polymeric micelles. In addition, they are more tolerant to heat and chemical reagents and generally more easy to handle than the peptidic, high-molecular-weight antibodies. Generally, carbohydrates play an essential role in nature due to their involvement in many biological recognition processes, for example, in cell–cell interaction and inflammation [27]. For this reason, biocompatible and especially ‘stealth-like’ polymers conjugated with sugar moieties on the surface, show a high potential as carrier systems for active targeting in the field of polymer therapeutics [28]. In general, the interaction between carbohydrates and the corresponding lectin is relatively weak ($K_d \sim 10^3\text{--}10^6$ mol/l) [29]. This binding force can, however, be tremendously increased by a multivalent binding between the ligand and the receptor [29–37]. Linking mannose to hydrophilic corona of polymeric micelles offers a route for multivalent targeting of DCs or macrophages, which are an interesting target to trigger and modify immune response [38,39]. By interaction with transmembrane proteins like the transferrin receptor [40,41] or the mannose-binding receptors (e.g., measles–mumps–rubella family, DC-SIGN) [42] expressed on the cell surface of DCs or macrophages clathrin-mediated endocytosis occurs. This leads to an enhanced cell specific internalization, which could be clearly demonstrated in studies on cell uptake kinetics, intracellular distribution and pathway specificity of virus particles [43,44].

Regarding this, we aimed at a carrier system, which shows so little unspecific interaction that it has the potential for selective active targeting to DCs. For this purpose, mannosylated HPMA–LMA block polymers were synthesized and investigated with regard to DC

targeting and regarding activation of DCs based on the cargo in the core of the polymeric micelle.

Materials & methods

Materials

All reagents and solvents were purchased from Acros Organics (Nidderau, Germany), Sigma Aldrich (Munich, Germany), Roth (Karlsruhe, Germany) or Fluka (Munich, Germany) and used without further purification if not mentioned otherwise. Solvents with technical grade were distilled before and solvents p.a. (pro analysis) were used as received. Dichloromethane and chloroform were distilled from CaH_2 . THF, hexane, diethyl ether and 1,4-dioxane were distilled from Na/K with benzophenone as an indicator. Water-free DMSO was stored in a septum sealed bottle over activated molecular sieve (3 Å). Dimethylformamide (DMF) was purchased from VWR (Darmstadt, Germany), dried over BaO and subsequently distilled *in vacuo* onto predried molecular sieves (3 Å). 2,2'-azobis(4-methoxy-2,4-dimethylvaleronitrile) (V-70) was purchased from Wako Chemicals (Neuss, Germany). Oregon Green 488 cadaverine was purchased from Invitrogen (Neuss).

Characterization

The 300-MHz ^1H -NMR (nuclear magnetic resonance) spectra were recorded on a Bruker (MA, USA) Avance II 300. The 400-MHz ^1H -NMR and 19F-NMR spectra were recorded on a Bruker Avance II 400. ^1H – ^1H COSY, HSQC and DOSY NMR measurements were performed on a Bruker Avance III HD 400. Inverse gated ^{13}C spectra were obtained at 100.7 and 75.48 MHz, respectively using a Fourier transform spectrometer from Bruker and analyzed. All spectra were recorded at room temperature and analyzed with MestReNova software. The polymers were dried at 40°C overnight under vacuum and afterward submitted to gel permeation chromatography (GPC). GPC was performed in tetrahydrofuran (THF) or hexafluoroisopropanol (HFIP) as the solvent and with following parts: pump PU 1580, auto sampler AS 1555, UV-detector UV 1575, RI-detector RI 1530 from Jasco (Groß-Umstadt, Germany) and miniDAWN Tristar light scattering detector from Wyatt (Dernbach, Germany). Columns were used from MZ-Analyzentechnik: MZ-Gel SDplus 10^2 Å, MZ-Gel SDplus 10^4 Å, MZ-Gel SDplus 10^6 Å. HPMA polymers were analyzed by HFIP as solvent containing 3g/l potassium trifluoroacetate. For HFIP GPC, a pump PU 2080+, an autosampler AS1555 and an RI detector RI2080+ from Jasco were used. The elution diagrams were analyzed using the WinGPC Uni Chrom. Calibration was done using polystyrene (PS) for THF or poly methyl

methacrylate (PMMA) for HFIP standards. The flow rate was 1 ml/min at a temperature of 25°C (THF) and 40°C (HFIP). HPMA polymers and the polymer micelles were purified by water GPC from Jasco using a preparative Sephadex column G-25 (HiTrap™ Desalting column, Sephadex G-25, superfine, 0.9% NaCl), an HPLC pump of type PU 2080+ and the detectors UV 2077+ and RI 2031+. The flow rate was between 0.5 and 1.0 ml/min and Milli-Q (Merck Millipore, Darmstadt, Germany) water was used as the solvent. The UV/VIS detectors were set to wavelengths of 488 and 235 nm and the data were analyzed using WinGPC Unichrome 8.00 (Build 994) from Polymer Standard Services.

UV/VIS spectroscopy was performed with a UV/VIS spectrometer from Jasco, model V-630 and the spectra were analyzed by the Spectra Manager Version 2.04 software using a quartz cell with a thickness of 10 mm.

ESI-MS was performed on a Navigato-Instrument from Thermo Electron (Langensfeld, Germany). The concentration was 0.1 mg/ml using methanol/ acetonitrile and/or water as the solvent. The flow rate was set on 0.75 ml/min with a cone voltage of 35–70 V and a nitrogen flow of 300 l/min.

For dynamic light scattering (DLS) experiments micelle solutions were prepared with concentrations as described. After transfer to a dust-free flow box, all samples were filtered (Millex HV 0.45 µm) into dust-free cylindrical scattering cells (Suprasil, 20 mm diameter, Hellma, Mühlheim, Germany). Then, DLS measurements were performed using a Uniphase He/Ne Laser ($\lambda = 632.8$ nm, 22 mW), a ALV-SP125 Goniometer, an ALV/High QE APD-Avalanche photodiode with fiber optical detection, an ALV 5000/E/PCI correlator and a Lauda RC-6 thermostat unit at 20°C. Angular-dependent measurements of typically 15° steps were carried out in the range $30^\circ \leq \varphi \leq 150^\circ$. For data evaluation experimental intensity correlation functions were transformed into amplitude correlation functions applying the Siegert relation extended to include negative values after baseline subtraction by calculation $g_1(t) = \text{SIGN}(G_2(t)) \cdot \text{SQRT}(\text{ABS}((G_2(t) - A)/A))$. All field correlation functions usually showed monomodal decay and were fitted by a sum of two exponentials $g_1(t) = a \cdot \exp(-t/b) + c \cdot \exp(-t/d)$ to take polydispersity into account. Average apparent diffusion coefficients D_{app} were calculated by applying $q^2 \cdot D_{\text{app}} = (a \cdot b - 1 + c \cdot d - 1)/(a + c)$ resulting in an angular-dependent diffusion coefficient D_{app} or reciprocal hydrodynamic radius $\langle 1/R_h \rangle_{\text{app}}$, according to formal application of the Stokes–Einstein law. By extrapolation of $\langle 1/R_h \rangle_{\text{app}}$ to $q=0$ z-average hydrodynamic radii $R_h = \langle 1/R_h \rangle_z^{-1}$ were obtained (uncorrected for c-dependency).

FACS analysis was performed on an FACS Canto II flow cytometer equipped with BD FACS Diva software (both from BD Biosciences, CA, USA). Data were analyzed using FlowJo software (FLOWJO, OR, USA). Confocal laser scanning microscopy was performed using an LSM510-UV (Zeiss, Jena, Germany) equipped with a Plan-Apochromat 63/1.40 Oil DIC M27 objective.

Methods & experimental protocols

Tetraethylene glycol monotosylate [45]

To a mixture of 4.11 g (103 mmol) sodium hydroxide in 23 ml of water and 23 ml of THF tetraethylene glycol was added. The solution was cooled to 0°C and a mixture of 12.15 g (65 mmol) p-toluenesulfonic acid in 100 ml THF was added dropwise. The reaction mixture was stirred for 2 h at 0°C. After stirring for 2 h at room temperature, the mixture was poured into ice-cold water and extracted with dichloromethane (4 × 150 ml). The organic layers were washed with water (2 × 75 ml) and dried over magnesium sulfate. Rotary evaporation gave a pale yellow oil which was used in the next reaction step without further purification. Yield: 22 g (63 mmol, 97%), Lit.: 90% [38]. Rf = 0.24 (cyclohexane:EtOAc, 1:4).

¹H-NMR (300 MHz, CDCl₃): δ [ppm] = 7.77 (2H, d, J = 8.5 Hz, -SO₂-o-Ar-H), 7.32 (2H, d, J = 8.5 Hz, -SO₂-m-Ar-H), 4.14 (2H, t, J = 4.5 Hz, -CH₂-OTos), 3.71–3.51 (14H, m, -CH₂-CH₂-O), 2.42 (3H, s, -CH₃).

ESI-MS [*m/z*]: = 371.13 ([M+Na]⁺, ber.: 371.11).

C₁₅H₂₄O₇S (348.41 g/mol)

N-(11-Hydroxy-3,6,9-trioxaundecyl)phthalimide [45]

A mixture of 22 g (63 mmol) of tetraethylene glycol monotosylate, 14 g (76 mmol) of potassium phthalimide and 3 g of molecular sieve (3 Å) in 160 ml DMF was stirred for 10 h at 150°C and 8 h at room temperature. The suspension was filtered through Celite and washed with DMF. The solvent was evaporated using high vacuum. The crude product was co-distilled with toluene (4 × 70 ml) and purified by column chromatography (eluent: EtOAc) to obtain a pale yellow oil. Yield: 18.2 g (56 mmol, 89%), Lit.: 57% [38]. Rf = 0.34 (EtOAc).

¹H-NMR (300 MHz, CDCl₃): δ [ppm] = 7.85–7.81 (2H, m, Ar-H), 7.72–7.68 (2H, m, Ar-H), 3.88 (2H, t, J = 5.5 Hz, NPhth-CH₂-CH₂-O-), 3.73 (2H, t, J = 5.8 Hz, NPhth-CH₂-CH₂-O-), 3.75–3.52 (m, 12H, -CH₂-CH₂-O-).

ESI-MS [*m/z*]: 346.14 ([M+Na]⁺, ber.: 346.13).

C₁₆H₂₁NO₆ (348.41 g/mol)

1,2,3,4,6-Penta-O-acetyl-D-mannopyranoside [46]

To a solution of 5 g (27.7 mmol) D-mannose in 200 ml pyridine, 39 ml (415 mmol) of acetic anhydride was added and stirring was continued overnight at room temperature. After coevaporation with toluene (3 × 40 ml), the residue was taken up in 200-ml ethyl acetate, washed with 2N HCl (3 × 50 ml), water (1 × 40 ml), saturated sodium bicarbonate (3 × 50 ml) and brine (1 × 40 ml). The organic layers were dried with Na₂SO₄ and rotary evaporation gives a α,β mixture as a pale yellow oil, which was used in the next reaction without further purification. Yield: 10 g (25.6 mmol, 92%). Lit.: 100% [40]. R_f = 0.57 (n-hexane:EtOAc, 1:1).

¹H-NMR (300 MHz, CDCl₃): δ [ppm] = 6.06 (1H, d, J = 1.8 Hz, 1 α), 5.84 (1H, d, J = 1.2 Hz, 1 β), 5.46 (1H, dd, J = 1.1 Hz, 3.3 Hz, 2 β), 5.24–5.34 (3H, m, 2 α , 3 α , 4 α), 5.12 (1H, dd, J = 3.3 Hz, 9.9 Hz, 3 β), 4.23–4.32 (2H, m, 4 β , 5 α), 4.12–4.02 (4H, m, 6 $\alpha\alpha$, 6 $\alpha\beta$, 6 $\beta\beta$), 3.78 (1H, ddd, J = 2.4 Hz, 5.3 Hz, 9.8 Hz, 5 β), 2.19–1.94 (5s, 15H, -CH₃).

ESI-MS [*m/z*]: 413.52 ([M+Na]⁺, ber.: 413.11), 803.24 ([M-M+Na]⁺, ber.: 803.23).

C₁₆H₂₂O₁₁ (390.12 g/mol)

2,3,4,6-Tetra-O-acetyl-D-mannopyranosyl bromide [46]

About 10 g (25.6 mmol) of 1,2,3,4,6-penta-O-acetyl-D-mannopyranoside was dissolved in 25 ml dichloromethane and stirred at room temperature under argon. About 20 ml of 33% HBr/acetic acid was added via syringe and the reaction was stirred at room temperature for 2 h. About 100 ml of dichloromethane was added and the reaction mixture was extracted with ice-cold water (3 × 200 ml). The organic layer was neutralized by a saturated sodium bicarbonate solution, washed with brine, dried over sodium sulfate and concentrated under reduced pressure to give a yellow oil which was used in the next reaction without further purification. Yield: 9.8 g (24 mmol, 93%). Lit.: 81% [40]. R_f = 0.3 (n-hexane/EtOAc (6:4)).

¹H-NMR (300 MHz, CDCl₃): δ [ppm] = 6.26 (1H, d, J = 1.1 Hz, 1), 5.67 (1H, dd, J = 3.4 Hz, 10.2 Hz, 3), 5.40 (1H, dd, J = 1.6 Hz, 3.4 Hz, 2), 5.31 (1H, t, J = 10.1 Hz, 4), 4.29 (1H, dd, J = 4.8 Hz, 12.4 Hz, 5), 4.18 (1H, ddd, J = 1.9 Hz, 4.9 Hz, 10.1 Hz, 6a), 4.09 (1H, dd, J = 2.1 Hz, 12.4 Hz, 6b), 2.23–2.03 (12H, 4s, -CH₃).

ESI-MS [*m/z*]: 412.16 ([M+H]⁺, ber.: 412.20).

C₁₄H₁₉O₅Br (411.20 g/mol)

11-(N-Phthalimide)-3,6,9-trioxaundecan-2,3,4,6-tetra-O-acetyl- β -D-mannopyranoside

About 2.0 g (4.9 mmol) of 1,2,3,4,6-penta-O-acetyl-D-mannopyranosyl bromide and 2.4 g (7.3

mmol) of 1 N-(11-hydroxy-3,6,9-trioxaundecyl) phthalimide were dissolved in 100 ml dichloromethane. About 3 g of molecular sieve (3 Å) was added and the reaction mixture was stirred for 30 min at -20°C and under argon atmosphere in the absence of light. About 1.9 g (7.5 mmol) of silver trifluoromethane sulfonate was added and the reaction was stirred at room temperature overnight. After neutralizing with triethylamine (pH = 8), the mixture was filtered through Celite, washed with dichloromethane and dried over MgSO₄. The solvent was removed by rotary evaporation and the crude product was purified by column chromatography to obtain a pale yellow oil. Yield: 2.0 g (3.1 mmol, 63%). R_f = 0.4 (EtOAc/cHex, 4:1).

¹H-NMR (300 MHz, CDCl₃): δ [ppm] = 7.84 (2H, m, Ar-H), 7.72 (2H, m, Ar-H), 5.35 (1H, dd, J = 3.2 Hz, 10 Hz, 4), 5.28 (1H, d, J = 9.6 Hz, 3), 5.25 (1H, t, J = 1.6 Hz, 2), 4.85 (1H, d, J = 1.6, 1), 4.28 (1H, dd, J = 5.2 Hz, 12 Hz, 5), 4.13–4.04 (2H, 6a, 6b), 3.9 (2H, t, J = 5.9 Hz, N-CH₂-CH₂-O), 3.78 (1H, m, Man-CHH-CH₂-O), 3.74 (2H, t, J = 5.9 Hz, N-CH₂-CH₂-O), 3.68–3.58 (11H, m, -CH₂-CH₂-O-), 2.13 (3H, s, -CH₃), 2.08 (3H, s, -CH₃), 2.02 (3H, s, -CH₃), 1.97 (3H, s, -CH₃).

ESI-MS [*m/z*]: 676.21 ([M+Na]⁺, ber.: 676.21).

C₃₀H₄₃NO₁₅ (653.23 g/mol)

11-Amino-3,6,9-trioxaundecyl- α -D-mannopyranoside

About 1.7 g (2.6 mmol) of 11-(N-phthalimide)-3,6,9-trioxaundecan-2,3,4,6-tetra-O-acetyl- β -D-mannopyranoside was dissolved in 35 ml methanol and 0.95 ml of hydrazine hydrate (65%) was added. The reaction mixture was stirred for 3 days at room temperature under argon atmosphere until a precipitation occurs. The solid was removed by filtration and the resulting filtrate was concentrated under vacuum. Purification by column chromatography (EtOH:NH₃ solution [25%], 4.5:1) yields a colorless oil with high viscosity. Yield: 900 mg (2.5 mmol, 97%). R_f = 0.16 (EtOH:NH₃-solution (25%), 4.5:1). ¹H-NMR [1H-1H-COSY] (400 MHz, D₂O): δ [ppm] = 4.87 (1H, d, ³J_{H1, H2} = 1.7 Hz, 1), 3.94 (1H, dd, ³J_{H2, H3} = 3.4 Hz, ³J_{H2, H1} = 1.7 Hz, 2), 3.88–3.66 (¹⁹H, m, 6a, 6b {3.88–3.83}, 3 {3.79}, -CH₂-CH₂-O {3.75–3.65}, 4 {3.63}, 5 {3.61}, 3.16 (2H, m, -CH₂-NH₂). ¹³C-NMR [HSQC] (100.6 MHz, D₂O): δ [ppm] = 99.96 (C1), 72.75 (C5), 70.51 (C3), 69.89 (C2), 69.61, 69.55, 69.52, 69.44 (O-CH₂-), 66.85 (C4), 66.60 (Man-O-CH₂-CH₂-), 60.83 (C6), 39.21 (CH₂-NH₂).

ESI-MS [*m/z*]: 356.56 [M+H]⁺, ber.: 356.18; 378.18 [M+Na]⁺, ber.: 356.18;

C₁₄H₂₉NO₉ (355.18 g/mol)

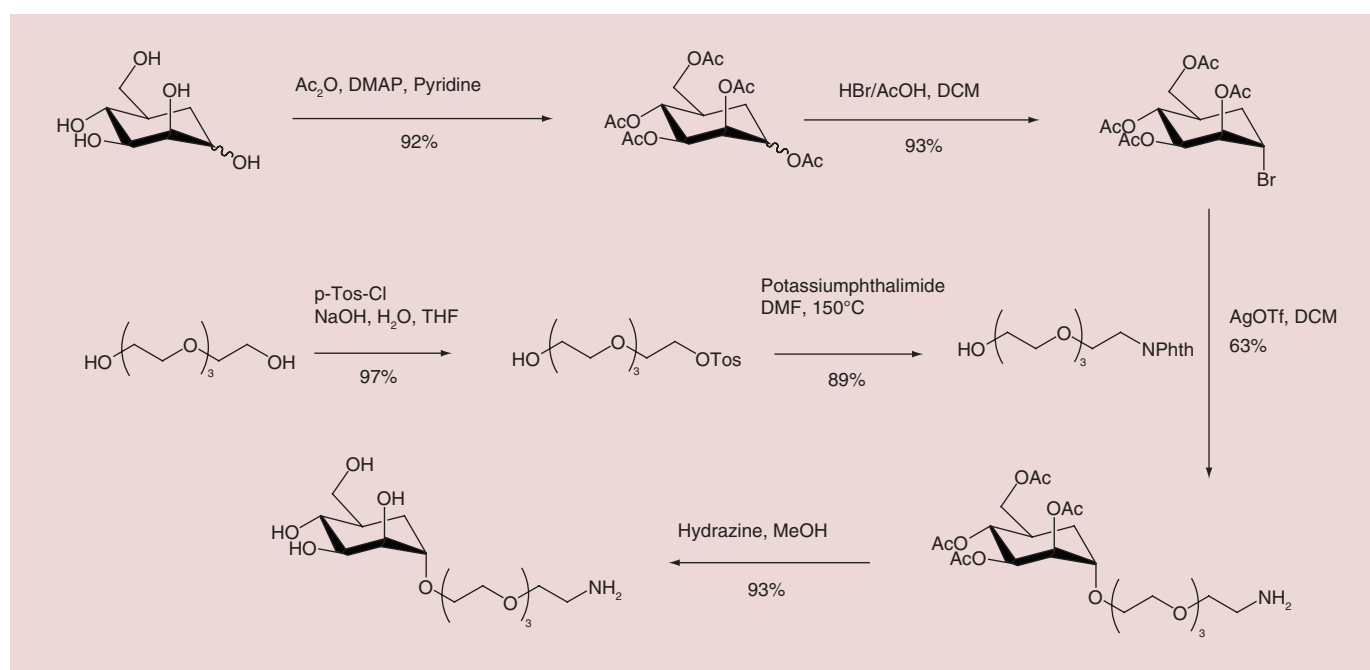


Figure 2. Synthesis of the amine functionalized mannose linker (man4).

Synthesis of the polymers

Synthesis of 4-cyano-4-((thiobenzoyl)sulfanyl)pentanoic acid

The 4-cyano-4-((thiobenzoyl)sulfanyl)pentanoic acid was used as the chain transfer agent (CTA) and synthesized in a three-step reaction according to the literature [47].

Synthesis of PFMA

PFMA was prepared according to the literature [48].

Synthesis of the reactive ester homopolymer (macro-CTA)

First a PFPMA-macro-CTA was synthesized by RAFT polymerization of PFPMA with CTA under Schlenk conditions. The reaction vessel was loaded with 4 g of PFPMA, 40 mg of CTA, 4 mg of ABNDM (2,2-Azobis(2,4-dimethyl)valeronitrile) and 5 ml of absolute dioxane. Following three freeze-vacuum-thaw cycles, the tube was immersed into an oil bath at 40°C and stirred overnight. After the polymerization, the polymer solution was precipitated three-times in n-hexane, isolated by centrifugation and dried overnight under vacuum at 40°C. In the end, a slightly pink powder was obtained. Yield: 1.7 g (43 weight%). ¹H NMR (300 MHz, CDCl₃): δ [ppm] 2.1–2.5 (br, 2H), 1.3–1.6 (m, 3H). ¹⁹F NMR (400 MHz, CDCl₃): δ [ppm] -151.5 to -153.1 (br, 2F), -157.9 to -158.2 (br, 1F), -162.9 to -163.4 (br, 2F).

Synthesis of the reactive ester block copolymer

About 0.5 g of the macro-CTA obtained after homopolymerization of PFPMA was dissolved in 4 ml of abso-

lute dioxane (Supplementary Figure 1). Afterwards, 0.3 g of LMA and 1.4 mg of ABNDM were added and mixed. After three freeze-vacuum-thaw cycles, the tube was immersed into an oil bath at 40°C and stirred for three days. Afterward poly(PFPMA)-b-poly(LMA) precipitated three-times from dioxane into ethanol, isolated by centrifugation and dried overnight under vacuum at 40°C. In the end, a slightly pink powder was obtained. Yield: 0.46 g (92 weight%). ¹H NMR (300 MHz, CDCl₃): δ [ppm] 3.9 (br, 2H), 2.4–0.9 (m, 5H). ¹⁹F-NMR (400 MHz, CDCl₃): δ [ppm] -151.5 to -153.1 (br, 2F), -157.9 to -158.2 (br, 1F), -162.9 to -163.4 (br, 2F) (Supplementary Figures 2 & 3).

Synthesis of a statistical copolymer

RAFT polymerization of PFPMA with LMA by the help of CTA was performed in a schlenk tube. As an example, 4 g of PFPMA dissolved in 5 ml dioxane, LMA, ABNDM and CTA were mixed. The molar ratio of CTA/ABNDM was set to 8:1. After three freeze-vacuum-thaw cycles, the mixture was immersed in an oil bath at 65°C and stirred overnight. Afterwards, poly(PFPMA)-ran-poly(LMA) was precipitated three-times in hexane, centrifuged and dried under vacuum at 40°C overnight. A slightly pink powder was obtained. Yield: 54%. ¹H-NMR (300 MHz, CDCl₃) δ/ppm: 0.84 (br t), 1.20–1.75 (br), 2.00–2.75 (br s). ¹⁹F-NMR (400 MHz, CDCl₃) δ /ppm: -162.01 (br), -156.95 (br), -152 to -150 (br).

Removal of the dithioester end groups

The dithiobenzoate end group was removed accord-

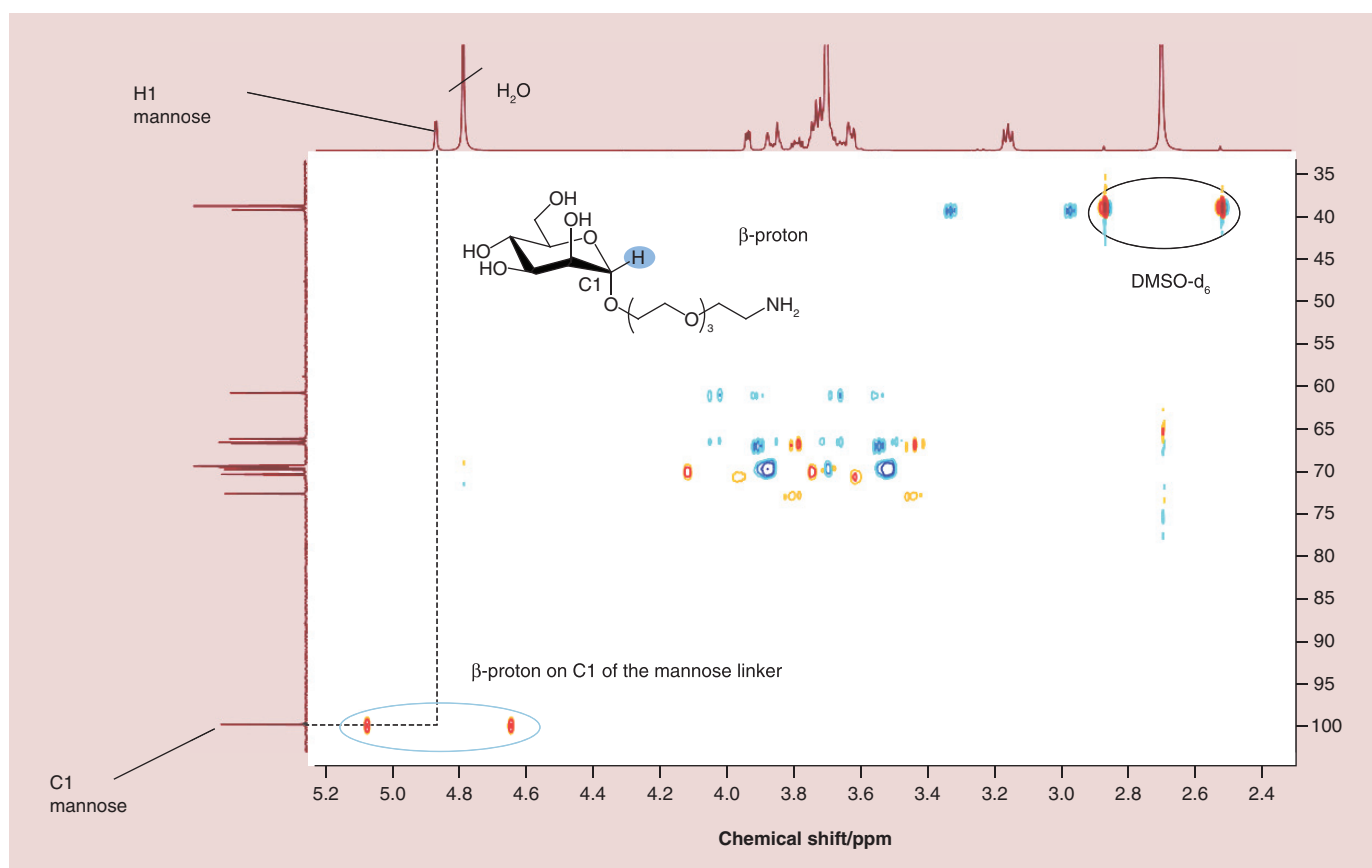


Figure 3. Decoupled HSQC nuclear magnetic resonance spectrum of the amine functionalized mannose linker man4. It proves the α anomeric form and therefore the bioactivity of man4 [50].

ing to literature. As an example, 400 mg of the polymer was dissolved in absolute dioxane and a 40-fold excess of ABNDM in relation to the polymer end group was added. The solution was heated at 40°C until the color vanished. Finally, the copolymer was

precipitated in ethanol and collected by centrifugation. The copolymer was dried under vacuum at 40°C overnight and a colorless powder was obtained. Yield: 380–390 mg (95–98 weight%). The absence of the dithiobenzoate end group was confirmed by

Table 1. Characterization of the synthesized block and random copolymers with and without mannose.

Polymer	Label	Amount of LMA (mol%) [†]	Amount of Man (mol%) [‡]	M_n (g/mol) [§]	$\bar{D}^§$
P(PFPMA)-b-P(LMA)	P1	7.45	–	44.100	1,4
P(PFPMA)-b-P(LMA)	P2	13	–	24.200	1,3
p(HPMA)-b-P(LMA)	P1a	7.5	–	31.400	1,3
p(HPMA)-b-P(LMA)	P2a	13	–	13.700	1,2
p(HPMA)_Man-b-P(LMA)	P1b	7.5	5	26.700	1,3
p(HPMA)_Man-b-P(LMA)	P2b	13	5	16.600	1,2
p(HPMA)-ran-P(LMA)	P3	7	–	28.200	1,4
p(HPMA)_Man-ran-P(LMA)	P4	7	4	28.200	1,3

[†]Calculated by ¹H-NMR spectroscopy in CDCl₃ of the PFPMA precursor polymers.

[‡]Calculated by ¹³C-NMR of the HPMA–LMA block copolymer in D₂O and related to the total number of repeating units in hydrophilic and hydrophobic blocks.

[§]Measured by gel permeation chromatography with hexafluoroisopropanol/tetrahydrofuran as solvent and PMMA/PS standard.

HPMA: N-(2-Hydroxypropyl)methacrylamide; LMA: Lauryl methacrylate; NMR: Nuclear magnetic resonance.

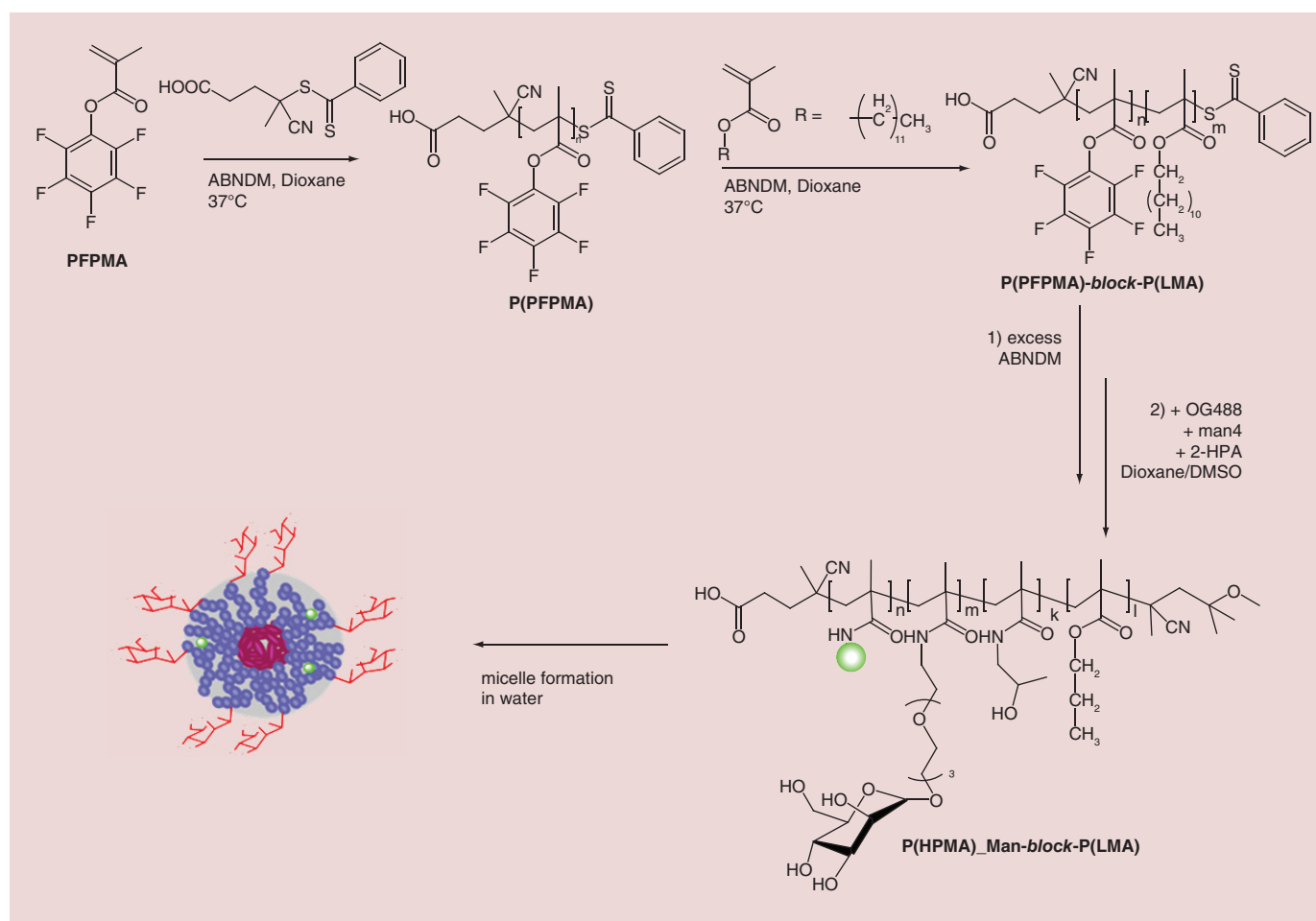


Figure 4. Synthesis of the p(HPMA)-block-P(LMA) copolymers with (P1a, P2a) and without mannose (P1b, P2b) and micelle formation. HPMA: N-(2-Hydroxypropyl)methacrylamide; LMA: Lauryl methacrylate.

UV/VIS spectroscopy by the absence of the peak at 302 nm.

Synthesis of the HPMA–LMA copolymers with & without mannose

As an example, 70.0 mg of the reactive ester precursor polymer poly(PFMA) P1 and 1.65 mg (2.76 μmol, 0.01 eq.) of the fluorescent dye Oregon Green cadaverine were dissolved in 1.5 ml abs. dioxane and 1.5 ml abs. DMF. This solution was stirred at 50°C overnight. Afterwards, 9.9 mg (27.8 μmol, 0.05 eq. regarding to the reactive ester groups) man4 and NEt₃ as base were added to the schlenk tube and stirred for 24 h, for the mannose containing polymers. The bound mannose was afterward quantified by inverse gated ¹³C-NMR spectroscopy. Thereafter, 84.0 μl (83.0 mg, 1.11 mmol, 4.0 eq.) of 2-hydroxyaminopropanol and 192 μl (140 mg, 1.38 mmol, 5.0 eq. regarding to the reactive ester groups) of triethylamine were added and the reaction was stirred for 3 days at 50°C under argon atmosphere.

For purification the polymer solution was diluted with Milli-Q water and dialyzed for 3 days using Spectra/Por membranes (molecular weight cut-off 3500 g/mol) and changing the water every 12 h. The resulting solution was freeze-dried to obtain a yellow powder. Yield: 40.0 mg (2.68 μmol, 97%). ¹H-NMR (400 MHz, MeOD): δ [ppm] = 7.5–7.4 (br, 1H, -NH), 4.8 (br, 1H, -C-OH), 4.6 (br, 1H, -COO-CH₂-), 4.05–3.70 (br, 1H, CH-HPA), 2.22–1.58 (br, 2H, -NH-CH₂-HPA), 1.44–0.76 (br, -CH₂-LMA, -CH₃-LMA, -CH₃-HPA, -CH₃ polymer backbone) (Supplementary Figures 4–6).

¹³C NMR [inverse gated] (100,6 MHz, MeOD): δ [ppm] = 180,10–178,56 (m, O=CNH), 101,72 (C1).

Micelle preparation

About 10 mg of the HPMA–LMA block copolymer was dissolved in 200 μl of abs. DMSO. The polymer solution was added dropwise under vortex in 0.7 ml of Milli-Q water. The polymer solution was purified by water GPC using a Sephadex G-25 column to elimi-

Table 2. Micellar structures of P2a and P2b with and without L18-MDP as cargo measured by dynamic light scattering with $c = 0.1$ g/l.

Polymer	R_h (nm)	μ_2
P2a	40,2	0,12
P2a + L18-MDP	48,1	0,24
P2b	44,2	0,13
P2b + L18-MDP	47,2	0,15

nate free DMSO. The concentration of the polymer solution was calculated by freeze-drying of an aliquot of the purified polymer solution. For the L18-MDP loaded nanoparticle 5 mg of HPMA-LMA block copolymer and 50 μ g of L18-MDP (muramyl dipeptide) (Figure 6) were dissolved in 200 μ L DMSO. The purification took place by GPC as described above.

The size of the micelles was determined by DLS studies (see the 'Characterization' section).

Preparation of blood serum

The human blood serum used for this study was obtained from the University Medical Center Mainz (Germany). It was prepared according to the standard guidelines of the University Medical Center Mainz. Because of the high variation of protein composition of different patients a pool of serum obtained by the mixture of serum of healthy donors was used for all measurements.

Preparation of samples for DLS studies in serum

DLS studies to determine interaction and stability of the micelles in serum were performed as described in [22].

Serum solutions are filtered through Milex GS filters, 220 nm pore size (Millipore). After testing of several filters, concentration losses of serum proteins by filtration with Milex GS filters are negligible. The polymer formulations are prepared by dissolving polymer and L18-MDP in DMSO and shaking the solution for 5 min. The mixture is then added dropwise to the buffer solution and purified by GPC (Sephadex, water) For light scattering the p(HPMA-co-LMA) as well as the p(HPMA-co-LMA) L18-MDP complex is prepared in Dulbecco's phosphate buffered saline buffer solution (GIBCO, Invitrogen). The polymer is filtered through a Milex GHP450-nm filter in the light scattering cuvette. For the measurements of p(HPMA-co-

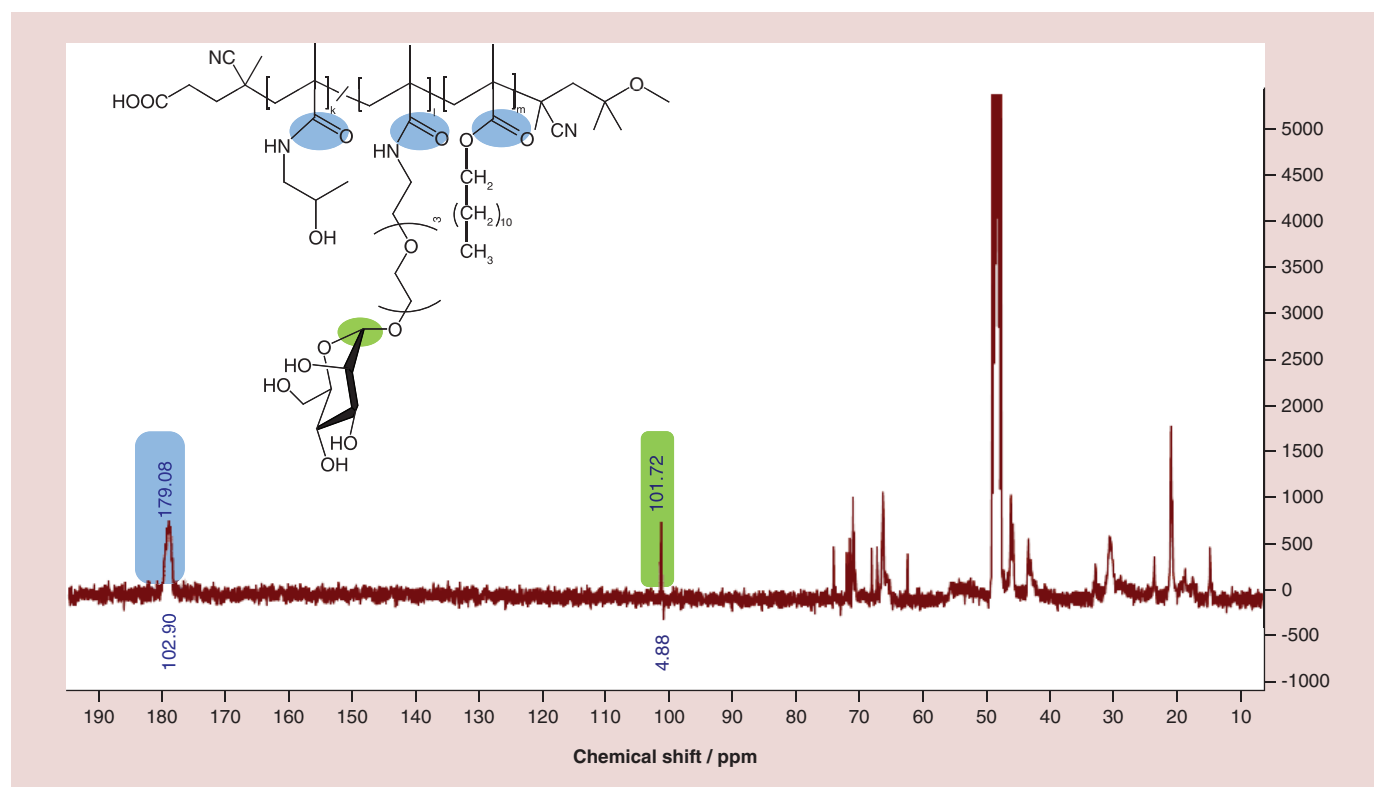


Figure 5. Characterization of the mannose functionalization of blockcopolymer P1b by inverse gated ^{13}C -NMR in MeOD [52]. NMR: Nuclear magnetic resonance.

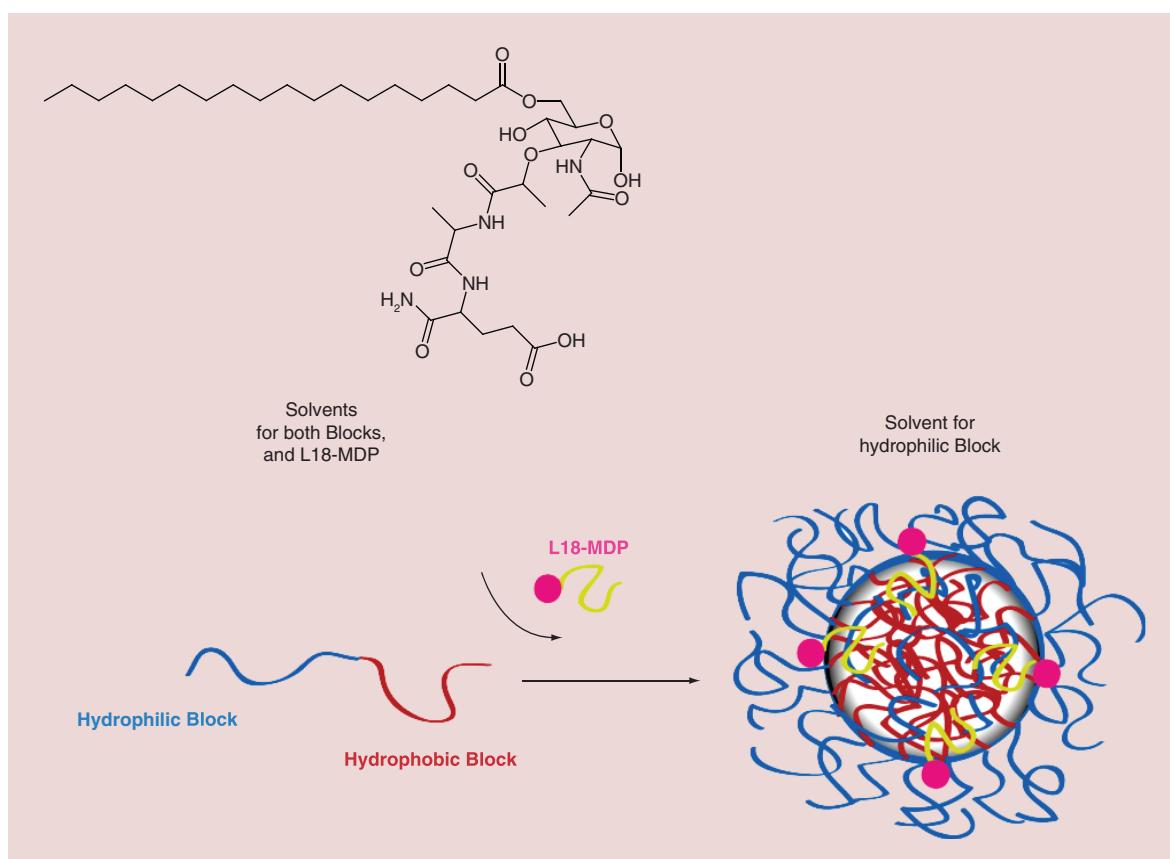


Figure 6. Structure of L18-MDP and illustration of its incorporation into the polymeric nanomicelle.

LMA) with and without L18-MDP, serum and polymer dissolved in Dulbecco's phosphate buffered saline buffer (GIBCO, Invitrogen) are given subsequently into the light scattering cuvette. Then, the cuvettes are incubated for 20 min on a shaker at room temperature before measurement.

Cellular binding of micelles

Bone marrow-derived dendritic cells (BMDCs) were generated with some modifications as described before [49]. In brief, bone marrow cells derived from tibiae and femurs of the mouse were seeded onto flat nontreated 12-well plates (2×10^5 /well) in 1.25 ml medium (Iscove's Modified Dulbecco's Medium supplemented with 5% granulocyte-macrophage colony stimulating factor containing hybridoma supernatant (equivalent to 10 ng/ml of granulocyte-macrophage colony stimulating factor), 5% fetal calf serum (FCS), 1% penicillin/streptavidin (P/S), 1% β -mercaptoethanol and 1% glutamine). Three days after preparation, 500 μ l of fresh medium was added to the wells. On day 6, cells were incubated with varying concentrations of micelles (3–15 μ g/ml) for different periods of time (1–24 h). Samples were harvested by frequent pipetting. The cells were washed with 2%

FCS in phosphate-buffered saline (PBS), incubated with fluorescence-labeled antibodies specific for surface markers (CD11c-PE, CD206-BV421 and CD86-PECy7), fixed with 0.7% paraformaldehyde (PFA) in PBS and subjected to fluorescent-activated cell sorting (FACS) analysis.

Sample preparation for confocal laser scanning microscopy

BMDCs were incubated with 15 μ g/ml micelle solution for 24 h as described above. After washing the cells with PBS, Hoechst dye was added to stain the nucleus with a concentration of 2 μ M. Cells were washed once more with PBS, and the cell membrane was marked with cell mask orange just before taking images.

Blocking studies with mannan

BMDCs were preincubated with mannan (2 mg/ml) for 1 h. Afterwards, micelle solution at different concentrations (3–15 μ g/ml) was added. After 4 h, cells were washed with 2% FCS in PBS, and were incubated with receptor-specific antibodies (anti-CD11c-PE, anti-CD206-BV421, anti-CD205-PECy7 and anti-CD209a-eFluor660), fixed with 0.7% PFA and subjected to flow cytometry.

Stimulation of DC

To assess stimulatory effects of encapsulated NOD2 agonist L18-MDP, BMDCs were incubated in parallel assays with differentially functionalized types of micelles (15 µg/ml) as indicated. After 48 h, BMDCs were harvested, incubated with antibodies (anti-CD11c-PE, anti-CD86-PE-Cy7 and anti-MHCII-Pacific Blue) and subjected to flow cytometric analysis.

Results & discussion

Preparation of the nanomedicine

As targeting core–shell vehicles for DCs, we decided to work with block-copolymer micelles from p(HPMA)-block-P(LMA) copolymers, as they are known to have minimal unspecific interaction with plasma proteins and cell membranes [18,20–21,25]. As targeting moiety we choose mannose, which is known to bind to the mannose receptor expressed on DCs and macrophages [26]. As the ligation of the mannose to the hydrophilic p(HPMA) block is supposed to be done via the reactive ester approach of Barz *et al.* [16] an α -glycosidic functionalized mannose derivative with a hydrophilic spacer and a terminal primary amine group was needed (man⁴), whose synthesis is described in Figure 2. Details can be found in the ‘Materials & methods’ section. It is important in this context that during the transformation of man² to man³ besides the desired α -anomer β -form may also be formed, which is biologically inactive. It is thus necessary to prove the α -form of man⁴, which could be done successfully with a decoupled HSQC-NMR spectrum (see Figure 3).

The block copolymers for micelle formation and ligation with man⁴ were prepared via the reactive ester route to p(HPMA) [16,18,51] according to Figure 4 as described in the ‘Materials & methods’ section. To reduce unspecific interactions with cellular membranes as much as possible, we aimed thereby at a ratio of about 90 mol% of HPMA to 10 mol% LMA [18]. This required the synthesis of reactive ester block copolymers P(PFPMA)-block-P(LMA) with about 90 mol% of reactive ester units (see Figure 4). Thus, we prepared two of those block copolymers (Table 1), both with about 10 mol% of LMA and a molecular weight differing by a factor of 2. Thus they are quiet comparable concerning polymer properties. Both show the narrow dispersity known for these polymers, if prepared under correct RAFT conditions (see ‘Materials & methods’ section).

The aminolysis of the reactive ester to prepare poly-HPMA and to incorporate man⁴ was conducted according to Mohr *et al.* [51] to avoid (partial) hydrolysis. Under these conditions also no side reactions with the hydroxyl groups of mannose could be observed.

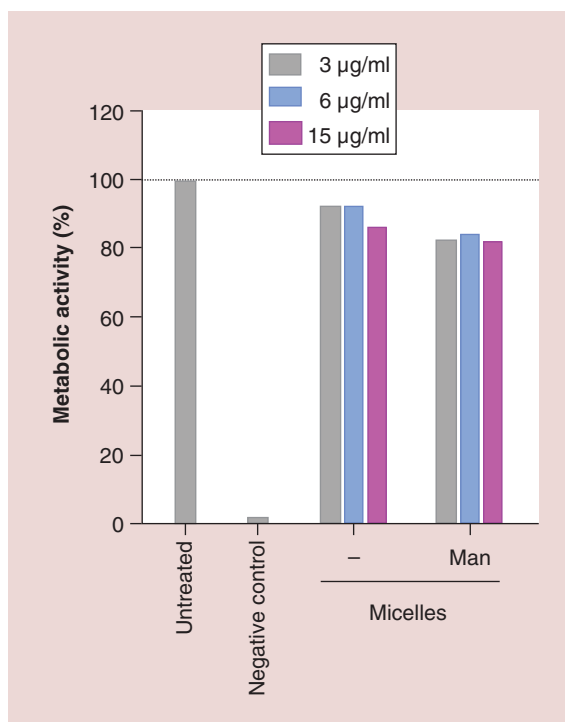


Figure 7. Metabolic activity of bone marrow-derived dendritic cells incubated with HPMA–LMA block-copolymer-based micelles (P1a and P1b). Bone marrow-derived dendritic cells (BMDCs) were incubated with micelles at different concentrations as indicated for 24 h. The metabolic activity of the samples was normalized to untreated BMDCs. As an internal negative control, BMDCs were incubated with DMSO at cytotoxic concentration (10%). HPMA: N-(2-Hydroxypropyl)methacrylamide; LMA: Lauryl methacrylate.

Generally this aminolysis allows a nearly quantitative ligation of man⁴. Here we reduced the reaction time and determined the amount of man⁴ finally incorporated into the hydrophilic block by inverse gated ¹³C-NMR in MeOD (Figure 5). The incorporated amount of man⁴ was slightly lower than the composition of the reaction batch, because we calculated the composition of the reaction batch for 5 mol% of man⁴ per reactive ester unit (90 mol% block), but we incorporated about 5 mol% with respect to the full polymer (100% of repeating units). The values are incorporated into Table 1. GPC measurements are included in the Supplementary Information. They demonstrate slightly different molecular weights (more correctly sizes) for the block copolymers with and without mannose. However, the corresponding polymers have an identical degree of polymerization since they were prepared starting with the identical reactive ester block copolymers.

Micellar aggregates from block copolymers and statistical copolymers of the hydrophilic HPMA

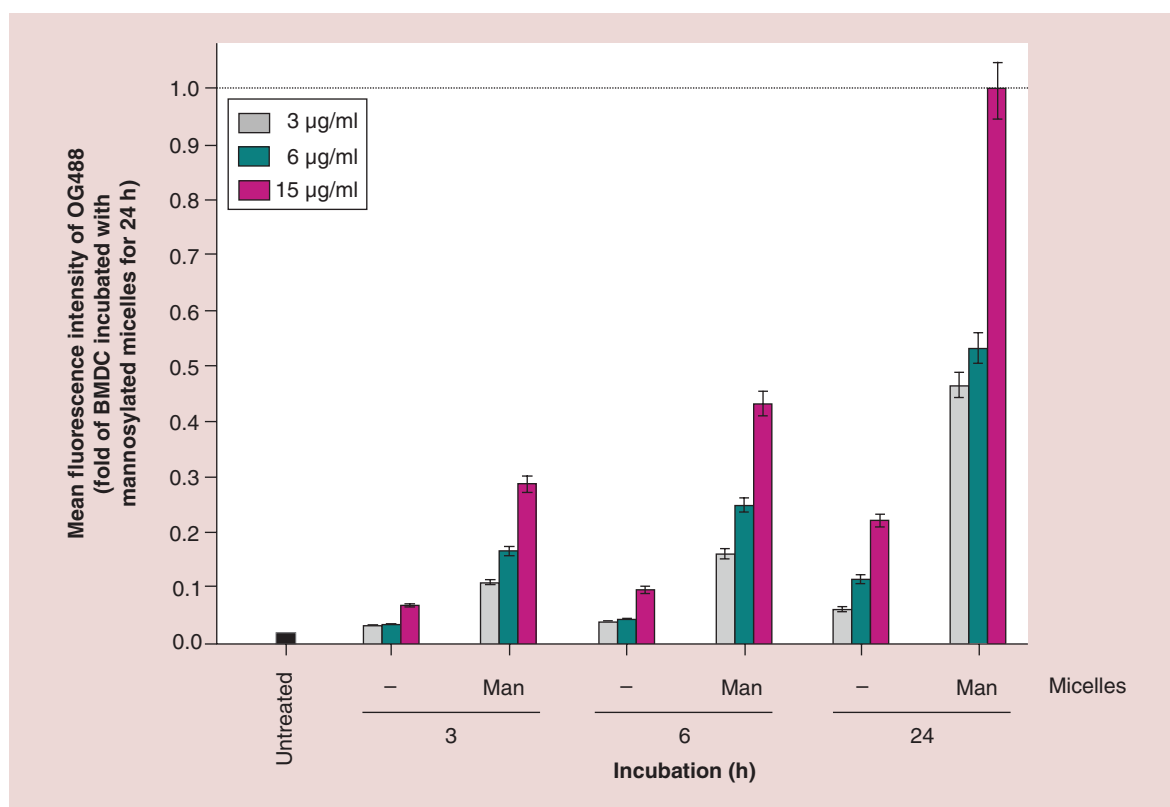


Figure 8. Time and dose kinetic studies of bone marrow-derived dendritic cells incubated with P1a and P1b copolymer-based micelles. BMDCs were incubated in parallel with either type of micelles at the indicated doses and periods of time. Afterwards, samples were incubated with CD11c-specific antibody. Data show the mean \pm standard error of the mean of OG488 fluorescence intensities of CD11c⁺ BMDC ($n = 3$). BMDC: Bone marrow-derived dendritic cell.

and LMA behave rather differently in the biological context [18,20]. While block copolymers show little unspecific interaction [17–18,21] statistical copolymers bind unspecifically to cellular membranes [22]. Thus for comparison also a statistical copolymer P3 with the same amount of LMA and man⁴ was prepared ('Materials & methods' section) and included into the comparison.

All polymers were additionally labeled with Oregon green 488 for detection in the cellular binding experiments. The properties of the resulting block and statistical copolymers are compiled in Table 1.

The critical micelle concentration (CMC) of the block copolymers p(HPMA)-b-P(LMA) was in the range of $6\text{--}7 \times 10^{-4}$ mg/ml in PBS-buffer solution as determined by the pyrene fluorescence technique (see Supplementary Figure 9). This low value assures that the micellar system stays stable in the body. Concerning the value of the CMC it should be noted that we give CMC values determined in PBS buffer, which are typically higher than the values determined in saline solution [18].

These micellar solutions were prepared – as previously reported [16,18,20,22] – by dropping solutions of

the various copolymers in DMSO into Milli-Q water. Afterwards, the micellar solution was purified by water GPC to eliminate free DMSO. The size of the micellar aggregates was characterized by DLS (see Table 2). They are with values of 40 nm (hydrodynamic radius) or a diameter of 80 nm in the size range reported for such micellar aggregates, which correspond more to a 'compound micelle' [53].

As cargo to induce an immune activation after cellular binding, the micellar aggregates were loaded with the hydrophobic L18-MDP (Figure 6). This led to an increase in their size due to the different composition of the nanoaggregate (see Table 2). To determine the stability of the micellar structures in contact with serum, we mixed them with human serum and investigated them by DLS as discussed in [22]. This allows it to determine aggregate formation (see Supplementary Figure 10). These experiments demonstrate that the L18-MPD loaded micelles keep their size and do not lead to aggregation during the first 30 min after mixing. However, after more than an hour some aggregates can be observed, probably caused by some loss of cargo. This indicates that the loaded micelles are stable for – at least – 30 min.

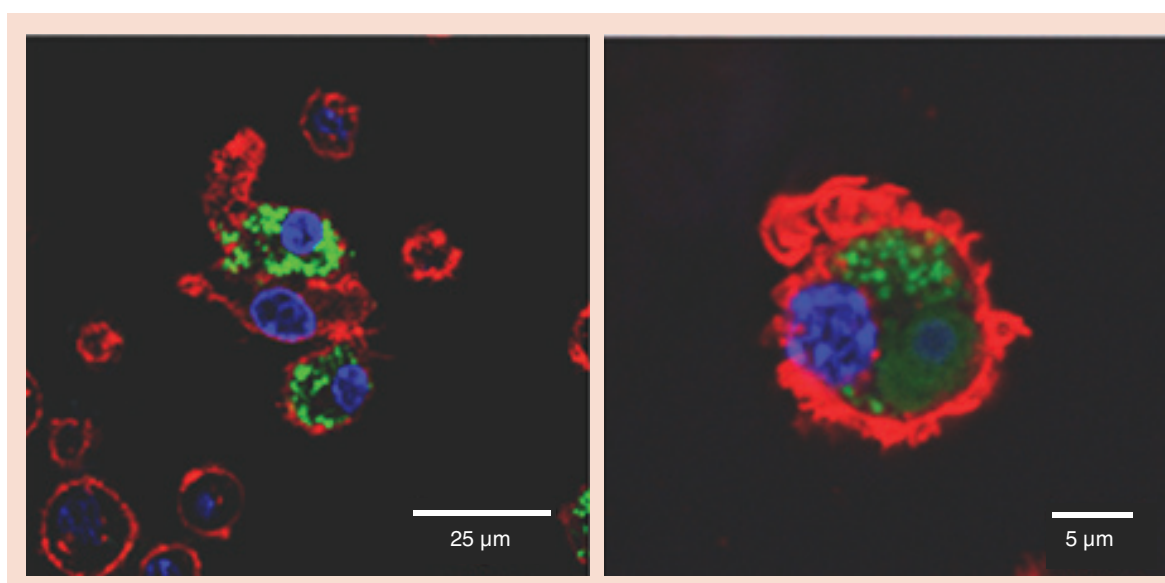


Figure 9. Confocal microscopy of bone marrow-derived dendritic cells incubated with mannosylated HPMA–LMA block-copolymer-based micelles (P1b). Bone marrow-derived dendritic cells were incubated with mannosylated micelles (15 µg/ml) for 24 h, and subjected to confocal laser scanning microscopy analysis. Green: OG488-labeled micelles, red (cell membrane): cell mask orange, blue (nucleus): Hoechst 33342. Magnifications are indicated. HPMA: N-(2-Hydroxypropyl)methacrylamide; LMA: Lauryl methacrylate.

Biological evaluation of the functionalized micelles

At first we checked the micellar aggregates regarding toxicity. As depicted in Figure 7, HPMA–LMA block

copolymers had no detrimental effect on the metabolic activity of BMDC.

Next we investigated the binding of micellar aggregates of the block copolymers with and without man-

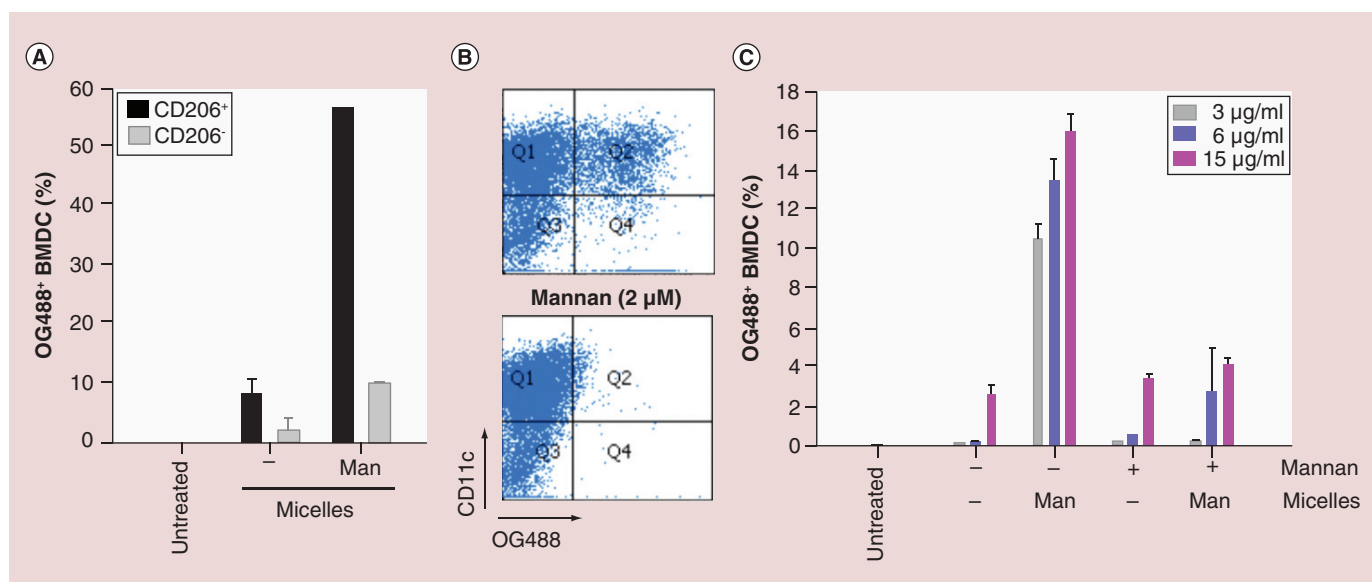


Figure 10. Assessment of mannose receptor-specific binding of mannosylated micelles (P1a and P1b). In parallel setting, bone marrow-derived dendritic cells (BMDCs) were incubated with mannan (2 µM) for 1 h or left untreated prior to addition of OG488-labeled p(HPMA)-b-P(LMA) block-copolymer-based micelle formulations at (A & B) 15 µg/ml or (C) at concentrations as indicated. After 4 h, all samples were incubated with CD11c-specific and (A) CD206-specific antibodies. All samples were assayed by flow cytometry. (A) Graphs indicate frequencies of OG488+ CD11c+ BMDC within the CD206+ and CD206- BMDC subpopulations. (B) Dot blots show the frequencies of OG488+ CD11c+ BMDC obtained after incubation with mannosylated micelles in the presence or absence of mannan. (C) Quantification of OG488+ CD11c+ BMDC after incubation with OG488-labeled micelle populations in the absence or presence of mannan. (A & C) Data denote mean ± standard error of the mean of three experiments each. (B) Representative of three experiments.

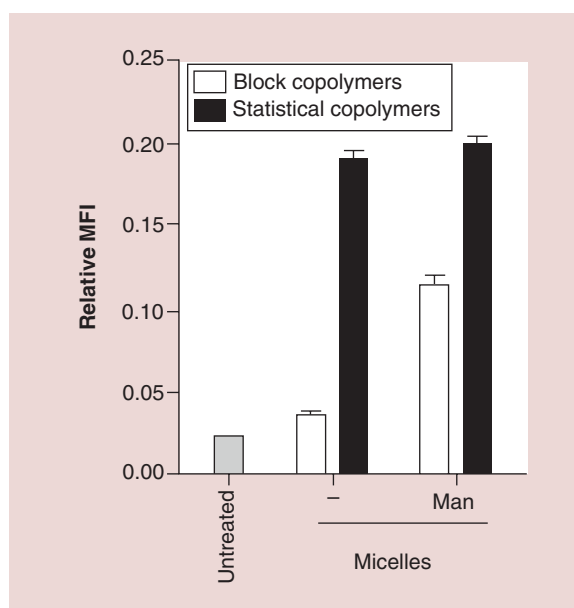


Figure 11. Differential binding behavior of micelles based on block (P1a and P1b) and statistical (P3 and P4) copolymers. Bone marrow-derived dendritic cells (BMDCs) were incubated in parallel with micelles derived from nonfunctionalized and mannoseylated block and statistical copolymers (each 3 $\mu\text{g}/\text{ml}$) for 3 h. Data show the mean \pm standard error of the mean of OG488 fluorescence intensities of CD11c⁺ BMDC. Relative MFIs are given as fold of BMDC incubated for 24 h with mannoseylated micelles derived from block copolymers (see Figure 6). Values shown for block copolymers correspond to those given in Figure 6 (n = 3). MFI: Mean fluorescence intensity.

nose to DCs. Coincubation of BMDC with nonfunctionalized HPMA–LMA block -copolymer-based micelles at different concentrations (3–15 $\mu\text{g}/\text{ml}$) yielded neglectable binding only (Figure 8). In contrast, mannoseylated micelles considerably bound BMDC in a time- and dose-dependent manner. These observations show that mannoseylation is critical for binding of HPMA–LMA block copolymers to BMDC. Similar results were obtained in binding assays using primary spleen cells. As shown in Supplementary Figure 11, DC and macrophages, which are known to express the mannose receptor, displayed stronger binding of mannoseylated than of nonmannoseylated micelles [26]. In contrast, T cells that lack the mannose receptor displayed only very low binding of either micelle formulation. Confocal microscopy confirmed cellular uptake of mannoseylated micelles by BMDC as a consequence of binding (Figure 9).

Mannoseylated micelles predominantly bound BMDC that expressed the mannose receptor CD206, while binding to CD206⁻ BMDC was low (Figure 10A). Nonmannoseylated micelles engaged either BMDC subpopulation at low extent only. To confirm the

essential role of mannose binding receptors for binding of mannoseylated HPMA–LMA block-copolymer-based micelles, BMDCs were preincubated with mannan as a competitor. As depicted in Figure 10B, and quantitatively assessed in Figure 10C, binding of mannoseylated micelles to BMDC was strongly inhibited in the presence of mannan. On the contrary, low-level binding of nonmannoseylated micelles to BMDC was not affected. These findings confirm that mannoseylated micelles bind BMDC specifically via mannose binding receptors.

To verify the importance of the molecular structure for active targeting, we investigated the micellar aggregates of the statistical copolymers. In this case, the presence of mannose did not improve binding to DCs (Figure 11). The main reason for this is the high level of unspecific binding of the statistical, not-mannoseylated copolymers, which is in full agreement with earlier observations on statistical copolymers [18,20,22]. In addition, here the exposure of the bound mannose to the outside – the mannose receptor – may be smaller in the micellar structures, which differ from the micellar structures of the block copolymers [18,22].

Based on the selective DC-targeting properties of mannoseylated micelles from the block copolymers, we asked for their potential to mediate their stimulation. For this, we encapsulated L18-MDP which constitutes a lipophilic immunostimulatory ligand of the NOD2 receptor [54]. Mannoseylated HPMA–LMA block-copolymer-based micelles encapsulated with L18-MDP showed the same BMDC binding properties as nonloaded mannoseylated micelles (Figure 12A). On the contrary, encapsulation of L18-MDP into nonmannoseylated micelles had no effect on their low potential to bind BMDC. As compared with untreated BMDC, incubation with L18-MDP loaded mannoseylated micelles moderately enhanced expression of the DC activation markers CD86 and major histocompatibility complex II (MHCII) by a BMDC subset (Figure 12B).

Discussion

In this study, p(HPMA)-block-P(LMA) polymer-based micelles were synthesized and assayed in cellular studies to evaluate their potential for immunotherapeutic applications. Because of the prominent role of DC as the most potent antigen presenting cell (APC) population [55], we focused our analysis on the DC binding and uptake properties of these micelle formulations. Flow cytometry measurements showed that nonmannoseylated micelles scarcely bound BMDC in agreement with previous studies [20]. In contrast, for other types of nanoparticles, passive targeting to myeloid cells including DC was demonstrated as mediated by scavenger receptors [56]. Therefore, p(HPMA)-

block-P(LMA) block-copolymer-based micelles as used in this study bear the advantage of low unspecific binding. This raises the possibility of conferring active targeting of DC by conjugation of the corresponding ligands that engage receptors on DC.

For this, we modified block copolymers with D-mannose, which binds both the mannose receptor CD206 as expressed by macrophages and DC, and DC-SIGN (CD209a), which is specific for DC [57]. We observed strongly enhanced binding of mannosylated micelles to CD206⁺ BMDC or to other cells known to express the mannose receptor and not to, for example, T cells. This binding was effectively blocked in the presence of the competitor mannan [58]. Similar findings were reported for other types of mannose-conjugated nanoparticles intended to target DC [59] or macrophages [60,61].

In our study, mannosylated micelles exerted no intrinsic immunomodulatory effects on BMDC as reflected by unaltered expression of MHCII and CD86. In contrast, polyanhydride nanoparticles modified with dimannose [56] and mannosylated micelles composed of DOTAP (liposomal transfection reagent) and α -mannose-conjugated lipid [61] activated their target cells. Of note, while mannose was reported to initiate an anti-inflammatory program in DC and macrophages via CD206, the polymannose mannan was shown to mediate CD206-dependent activation of both cell types [62]. It is tempting to speculate that the struc-

tural arrangement of mannose on the nanoparticle surface, and the physicochemical properties of the carrier system itself may determine immunomodulatory effects of mannosylated nanoparticles. Anyway, an inert targeting carrier system, as represented by mannosylated HPMA–LMA block-copolymer-based micelles, may be more feasible for immunotherapeutic approaches since it allows to encapsulate adjuvants with defined stimulatory properties [63]. By this, the activation of targeted APC may be directed toward an immunophenotype that mediates specific T-cell polarization [64].

We confirmed that mannosylated p(HPMA)-block-P(LMA) polymer-based micelles were internalized by BMDC. In a number of studies, exogenous material internalized by endocytotic activity of CD206 was demonstrated to result in endosomal localization and release into the cytoplasm [26]. Therefore, mannosylated p(HPMA)-block-P(LMA) polymer-based micelles may be loaded with adjuvants that bind to danger receptors localized in endosomal membranes, like nucleic-acid-sensing toll-like receptors (TLRs) [7,65]. Additionally, adjuvants that engage cytoplasmic danger receptors, like NOD receptors and the inflammasome, may be employed [66]. These different classes of danger receptors transmit stimulatory signals via different pathways that converge to mediate cell activation. We and others have shown that parallel engagement of different stimulator receptors may result in strong synergistic

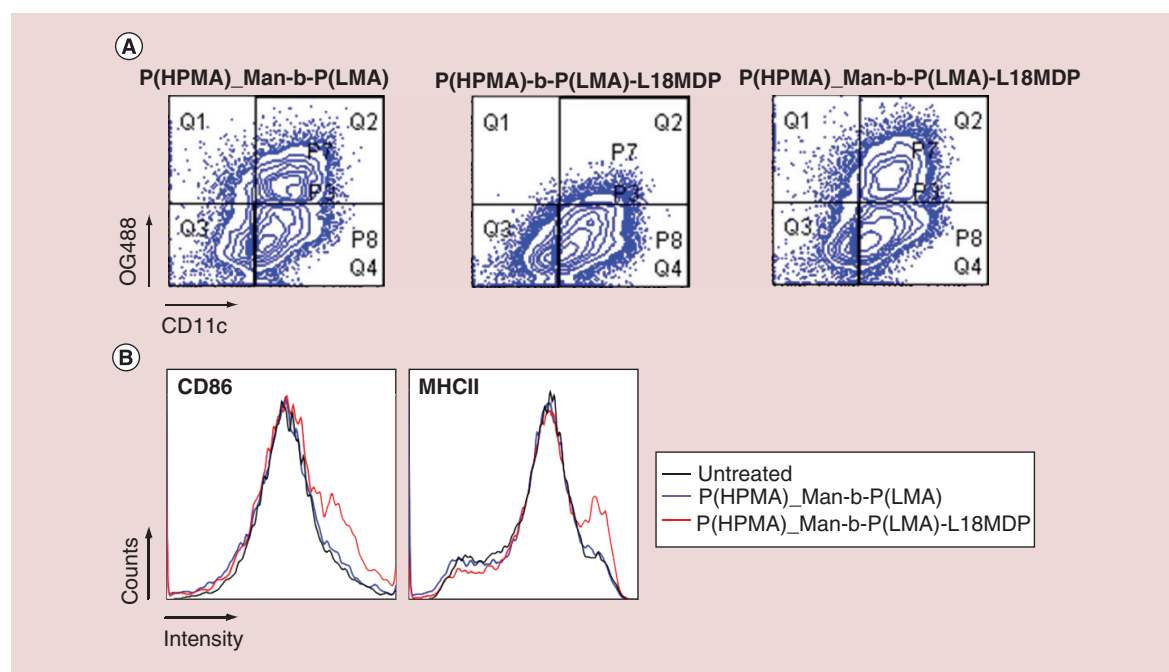


Figure 12. Stimulatory effects of L18-MDP loaded mannosylated micelles from P2a and P2b. Bone marrow-derived dendritic cells (BMDCs) were incubated in parallel with different types of micelles (15 μ g/ml) for 48 h. **(A)** Binding of OG488-labeled micelles to CD11c⁺ BMDC was assayed after 48 h of incubation. **(B)** Stimulatory effects of empty and L18-MDP-loaded (300 ng per sample) mannosylated micelles on BMDC pregated for CD11c⁺ cells were monitored by flow cytometry.

effects [67]. Both the loading capacity of a nanoparticle and the number of nanoparticles that are to be internalized by a target cell are limiting factors. To compensate for these limitations and to achieve more potent cell activation, ongoing research is focused to assess the outcome of codelivery of adjuvants that bind distinct receptors by the same nanoparticle [68]. Alternatively, adjuvants that engage different danger receptors [69] may be used. So far, many micelle formulations bear a hydrophilic core to be loaded, for example, with nucleic acids to activate endosomal TLR [7,70–71]. In contrast, mannosylated HPMA–LMA block-copolymer-based micelles bear a hydrophobic core and therefore are most suitable to assess the efficacy of lipophilic adjuvants. As a proof of concept, we show that loading of micelles with L18-MDP as a ligand of the cytoplasmic NOD2 receptor [54] resulted in activation of a subset of BMDC, which confirmed on functional level release of that cargo into the cytoplasm. Similar results were obtained for human-monocyte-derived DC treated with L18-MDP loaded poly(lactic-co-glycolic acid) nanoparticles [72]. Ongoing studies are focused on comparative testing of more recently developed lipophilic adjuvants which activate NOD or TLR receptors like CL075 [73] or receptors of both types in parallel as exemplified by CL429 [69] to exploit potential synergistic effects.

Furthermore, uptake of mannosylated proteins by CD206 was shown to result in cross presentation of derived antigens [74]. Cross presentation of antigen via MHC I (major histocompatibility complex) enables APC

to stimulate CD8⁺ T cells which differentiate to cytotoxic T cells that kill antigen-expressing tumor cells [75]. We currently assess strategies to conjugate oligopeptide antigens to the surface of mannosylated HPMA–LMA block copolymers to enable the induction of antigen-specific immune responses. Taken together, we aim to develop this promising nanocarrier system to obtain nanovaccines that target myeloid APC via mannose, and codeliver antigen and adjuvants to achieve presentation of tumor-specific antigens and consequently strong T-cell-mediated antitumor immune responses.

Supplementary data

To view the supplementary data that accompany this paper please visit the journal website at: www.futuremedicine.com/doi/full/10.2217/nnm-2016-0167

Acknowledgements

The authors acknowledge the help of I Alberg to characterize the micellar aggregates by dynamic light scattering.

Financial & competing interests disclosure

The authors acknowledge funding by the SFB 1066 (DFG), especially projects B4 and B5. The authors have no other relevant affiliations or financial involvement with any organization or entity with a financial interest in or financial conflict with the subject matter or materials discussed in the manuscript apart from those disclosed.

No writing assistance was utilized in the production of this manuscript.

Executive summary

Background

- Successful tumor immunotherapy depends on the induction of strong and sustained tumor antigen-specific immune responses by activated antigen presenting cells (APC) like dendritic cells (DCs).
- Since nanoparticles have the potential to codeliver tumor-specific antigen and DC-stimulating adjuvant in a DC-targeting manner we wanted to assess the suitability of mannosylated N-(2-hydroxypropyl) methacrylamide (HPMA)–lauryl methacrylate (LMA) block polymers for immunotherapy.

Materials & methods

- Fluorescence-labeled block-copolymer micelles derived from p(HPMA)-block-P(LMA) copolymers and corresponding statistical copolymers were synthesized via RAFT polymerization and loaded with the APC activator L18-MDP.
- Both types of copolymers were conjugated with D-mannose to target the mannose receptor as expressed by DC and macrophages.
- The extent and specificity of micelle binding and activation of APC was monitored using mouse spleen cells and bone marrow-derived DCs.

Results

- Nontargeting HPMA–LMA statistical copolymers showed strong unspecific cell binding.
- HPMA–LMA block copolymers bound DC only when conjugated with mannose, and in a mannose receptor-specific manner.
- Mannosylated HPMA–LMA block copolymers were internalized by DC.
- DC-targeting HPMA–LMA block copolymers mediated DC activation when loaded with L18-MDP.

Conclusion

- Mannosylated HPMA–LMA block copolymers are a promising candidate for the development of DC-targeting nanovaccines.

References

Papers of special note have been highlighted as: • of interest;

•• of considerable interest

- 1 Lepeltier E, Nuhn L, Lehr CM, Zentel R. Not just for tumor targeting. Unmet medical needs and opportunities for nanomedicine. *Nanomedicine* 10(20), 3147–3166 (2015).
- 2 Reddy ST, Rehor A, Schmoekel HG, Hubbell JA, Swartz MA. *In vivo* targeting of dendritic cells in lymph nodes with poly(propylene sulfide) nanoparticles. *J. Control. Release* 112(1), 26–34 (2006).
- 3 Reddy ST, van der Vlies AJ, Simeoni E, O’Neil CP, Swartz MA, Hubbell JA. Exploiting lymphatic transport and complement activation in nanoparticle vaccines. *Nat. Biotechnol.* 25, 1159–1164 (2007).
- **First article using nanoparticles as vaccine platform by targeting lymph node residing dendritic cells via interstitial flow and activating these cells by *in situ* complement activation.**
- 4 Toth I, Skwarczynski M. The immune system likes nanotechnology. *Nanomedicine (Lond.)* 9(17), 2607–2609 (2014).
- **Foreword of a special focus issue in Nanomedicine (Lond.) with highlights, reviews and research articles about ‘Nanotechnology for Vaccine Development’.**
- 5 Shao K, Singha S, Clemente-Casares X, Tsai S, Yang Y, Santamaria P. Nanoparticle-based immunotherapy for cancer. *ACS Nano* 9(1), 16–30 (2015).
- 6 Van Parijs L, Abbas AK. Homeostasis and self-tolerance in the immune system: turning lymphocytes off. *Science* 280(5361), 243–248 (1998).
- 7 Hartmann S, Nuhn L, Palitzsch B *et al.* CpG-loaded multifunctional cationic nanohydrogel particles as self-adjuncting glycopeptide antitumor vaccines. *Adv. Healthc. Mater.* 4(4), 522–527 (2015).
- **First article using glycopeptide nanogel conjugates as antitumor vaccines for co-delivery of tumor-associated MUC1 glycopeptide antigens together with immunostimulatory CpG.**
- 8 Nuhn L, Barz M, Zentel R. New perspectives of HPMA-based copolymers derived by post-polymerization modification. *Macromol. Biosci.* 14(5), 607–618 (2014).
- 9 Nuhn L, Hartmann S, Palitzsch B *et al.* Water-soluble polymers coupled with glycopeptide antigens and T-cell epitopes as potential antitumor vaccines. *Angew. Chem. Int. Ed. Engl.* 52(40), 10652–10656 (2013).
- **First article describing novel glycopeptide polymer conjugates as antitumor vaccines for the codelivery of tumor-associated MUC1 glycopeptide antigens together with a T-helper cell epitope.**
- 10 Cai H, Chen MS, Sun ZY, Zhao YF, Kunz H, Li YM. Self-adjuncting synthetic antitumor vaccines from MUC1 glycopeptides conjugated to T-cell epitopes from tetanus toxoid. *Angew. Chem. Int. Ed. Engl.* 52(23), 6106–6110 (2013).
- 11 Duncan R, Vicent MJ. Do HPMA copolymer conjugates have a future as clinically useful nanomedicines? A critical overview of current status and future opportunities. *Adv. Drug Deliv. Rev.* 62(2), 272–282 (2010).
- 12 Duncan R. Soluble synthetic polymers for targeting and controlled release of anticancer agents, particularly anthracycline antibiotics. *J. Bioact. Compat. Polym.* 3(1), 4–15 (1988).
- 13 Willner D, Trail PA, Hofstead SJ *et al.* (6-Maleimidocaproyl) hydrazone of doxorubicin – a new derivative for the preparation of immunoconjugates of doxorubicin. *Bioconjug. Chem.* 4(6), 521–527 (1993).
- 14 Duncan R. The dawning era of polymer therapeutics. *Nat. Rev. Drug Discov.* 2(5), 347–360 (2003).
- **Major review and prospect of polymeric nanoparticles as versatile part of future pharmaceuticals, covering topics such as polymer–drug and –protein conjugates, polymeric micelles with covalently bound drugs and polyplexes for DNA delivery.**
- 15 Kopecek J, Kopecková P. HPMA copolymers: origins, early developments, present, and future. *Adv. Drug Deliv. Rev.* 62(2), 122–149 (2010).
- **Comprehensive summary on the development and prospects of HPMA (N-[2-hydroxypropyl]methacrylamide) polymers with a focus on the development of macromolecular therapeutics for the treatment of cancer and musculoskeletal diseases.**
- 16 Barz M, Tarantola M, Fischer K *et al.* From defined reactive diblock copolymers to functional HPMA-based self-assembled nanoaggregates. *Biomacromolecules* 9(11), 3114–3118 (2008).
- 17 Allmeroth M, Moderegger D, Biesalski B *et al.* Modifying the body distribution of HPMA-based copolymers by molecular weight and aggregate formation. *Biomacromolecules* 12(7), 2841–2849 (2011).
- 18 Talelli M, Barz M, Rijcken CJF, Kiessling F, Hennink WE, Lammers T. Core-crosslinked polymeric micelles: principles, preparation, biomedical applications and clinical translation. *Nano Today* 10(1), 93–117 (2015).
- 19 Barz M, Luxenhofer R, Zentel R, Kabanov A V. The uptake of N-(2-hydroxypropyl)-methacrylamide based homo, random and block copolymers by human multi-drug resistant breast adenocarcinoma cells. *Biomaterials* 30(29), 5682–5690 (2009).
- 20 Weilbacher M, Allmeroth M, Hemmelmann M *et al.* Interaction of N-(2-hydroxypropyl) methacrylamide based homo, random and block copolymers with primary immune cells. *J. Biomed. Nanotechnol.* 9, 1–11 (2013).
- 21 Allmeroth M, Moderegger D, Gündel D *et al.* PEGylation of HPMA based block copolymers enhances tumor accumulation *in vivo*: a quantitative study using radiolabeling and positron emission tomography. *J. Control. Release* 172, 77–85 (2013).
- 22 Hemmelmann M, Mohr K, Fischer K, Zentel R, Schmidt M. Interaction of pHPMA–pLMA copolymers with human blood serum and its components. *Mol. Pharm.* 10, 3769–3775 (2013).
- 23 Hemmelmann M, Knoth C, Schmitt U *et al.* HPMA based amphiphilic copolymers mediate central nervous effects

- of domperidone. *Macromol. Rapid Commun.* 32(9–10), 712–717 (2011).
- 24 Klok H, Gibson MI, Froehlich E. postpolymerization modification of poly(pentafluorophenyl methacrylate): synthesis of a diverse water-soluble polymer library. *Polym. Chem.* 47, 4332–4345 (2009).
- 25 Tappertzshofen K, Bednarczyk M, Koynov K, Bros M, Grabbe S, Zentel R. Toward anticancer immunotherapeutics: well-defined polymer–antibody conjugates for selective dendritic cell targeting. *Macromol. Biosci.* 14, 1444–1457 (2014).
- **Showing selective uptake of multifunctional HPMA (N-[2-hydroxypropyl]methacrylamide) polymer systems into CD8⁺ dendritic cells via antiDEC205 antibodies in the presence of phagocytosing macrophages.**
- 26 Martinez-Pomares L. The mannose receptor. *J. Leukoc. Biol.* 6, 1177–1186 (2012).
- 27 Zhao H, Li Y, Hu Y. Nanotechnologies in glycoproteomics. *Clin Proteomics* 11(21), 1–10 (2014).
- 28 Kramer JR, Deming TJ. Recent advances in glycopolymer synthesis. *Polym. Chem.* 5(3), 671–682 (2014).
- 29 Spain SG, Cameron NR. A spoonful of sugar: the application of glycopolymers in therapeutics. *Polym. Chem.* 2(1), 60–68 (2011).
- 30 Ting SRS, Chen G, Stenzel MH. Synthesis of glycopolymers and their multivalent recognitions with lectins. *Polym. Chem.* 1, 1392–1412 (2010).
- 31 Lundquist JJ, Toone EJ. The cluster glycoside effect. *Chem. Rev.* 102, 555–578 (2002).
- 32 Ercolani G, Schiaffino L. Allosteric, chelate, and interannular cooperativity: a mise au point. *Angew. Chemie Int. Ed. Engl.* 50, 1762–1768 (2011).
- 33 Kiessling LL, Gestwicki JE, Strong LE. Synthetic multivalent ligands as probes of signal transduction. *Angew. Chem. Int. Ed. Engl.* 45(15), 2348–2368 (2006).
- 34 Gestwicki JE, Cairo CW, Strong LE *et al.* Influencing receptor–ligand binding mechanisms with multivalent ligand architecture. *J. Am. Chem. Soc.* 124(50), 14922–14933 (2002).
- 35 Sparks MA, Williams KW, Whitesides GM. Neuraminidase-resistant hemagglutination inhibitors: acrylamide copolymers containing a c-glycoside of N-acetylneuraminic acid. *J. Med. Chem.* 36, 778–783 (1993).
- 36 Mammen M, Dahmann G, Whitesides GM. Effective inhibitors of hemagglutination by influenza virus synthesized from polymers having active ester groups. Insight into mechanism of inhibition. *J. Med. Chem.* 38, 4179–4190 (1995).
- 37 Papp I, Dervede J, Enders S *et al.* Multivalent presentation of mannose on hyperbranched polyglycerol and their interaction with concanavalin A lectin. *ChemBiochem* 8, 1075–1083 (2011).
- 38 Qian X, Metallo SJ, Choi IS, Wu H, Liang MN, Whitesides GM. Arrays of self-assembled monolayers for studying inhibition of bacterial adhesion. *Anal. Chem.* (14), 1805–1810 (2002).
- 39 Ponader D, Wojcik F, Beceren-braun F, Dervede J, Hartmann L. Sequence-defined glycopolymer segments presenting mannose: synthesis and lectin binding affinity. *Biomacromolecules* 13, 1845–1852 (2012).
- 40 Qian ZM, Li H, Sun H, Ho K. Targeted drug delivery via the transferrin receptor. *Pharmacol. Rev.* 54, 561–587 (2002).
- 41 Li H, Qian ZM. Transferrin/Transferrin receptor-mediated drug delivery. *Med. Res. Rev.* 22, 225–250 (2002).
- 42 Irache JM, Salman HH, Gamazo C *et al.* Mannose-targeted systems for the delivery of therapeutics. *Expert Opin. Drug Deliv.* 5, 703–724 (2008).
- 43 Cureton DK, Massol RH, Saffarian S, Kirchhausen TL, Sean PJ. Vesicular stomatitis virus enters cells through vesicles incompletely coated with clathrin that depend upon actin for internalization. *PLoS Pathog.* 5, 5–15 (2009).
- 44 Pelkmans L, Kartenbeck J, Helenius A. Caveolar endocytosis of simian virus 40 reveals a new two-step vesicular-transport pathway to the ER. *Nat. Cell Biol.* 3, 473–484 (2001).
- 45 Xie H, Braha O, Gu L, Cheley S, Bayley H. Single-molecule observation of the catalytic subunit of cAMP-dependent protein kinase binding to an inhibitor peptide. *Chem. Biol.* 12, 109–120 (2005).
- 46 Nobrega C, Vazquez J. Conformational study of the hydroxymethyl group in alpha – D-mannose derivatives. *Tetrahedron Asymmetry.* 14, 2793–2801 (2003).
- 47 Moad G, Rizzardo E, Thang SH. Radical addition–fragmentation chemistry in polymer synthesis. *Polymers* 49(5), 1079–1131 (2007).
- 48 Eberhardt M, Mruk R, Zentel R, Théato P. Synthesis of pentafluorophenyl(meth)acrylate polymers: new precursor polymers for the synthesis of multifunctional materials. *Eur. Polym. J.* 41(7), 1569–1575 (2005).
- 49 Balkow S, Krux F, Loser K, Becker JU, Grabbe S, Dittmer U. Friend retrovirus infection of myeloid dendritic cells impairs maturation, prolongs contact to naive T cells, and favors expansion of regulatory T cells. *Blood* 110, 3949–3959 (2007).
- 50 Gunther W, Kunz H. Synthesis of /beta-D-mannosides from P-D-glucosides via an intramolecular SN2 reaction at C-2. *Carbohydr. Res.* 228, 217–241 (1992).
- 51 Mohr N, Barz M, Forst R, Zentel R. A deeper insight into the postpolymerization modification of poly(penta fluorophenyl methacrylates) to poly(N-(2-hydroxypropyl)methacrylamide). *Macromol. Rapid Commun.* 35, 1522–1527 (2014).
- 52 Zhang J, Liu W, Nakano T, Okamoto Y. Stereospecific radical polymerization of N-methyl methacrylamide. *Polym. J.* 32(8), 694–699 (2000).
- 53 Mai Y, Eisenberg A. Self-assembly of block copolymers. *Chem. Soc. Rev.* 41(18), 5969–5985 (2012).
- 54 Sato T, Shikama Y, Shimauchi H, Endo Y, Takada H. Analgesic effects of chemically synthesized NOD1 and NOD2 agonists in mice. *Innate Immun.* 17(1), 54–59 (2011).
- 55 Schraml BU, Reise Sousa C. Defining dendritic cells. *Curr. Opin. Immunol.* 32, 13–20 (2015).
- 56 Shannahan JH, Bai W, Brown JM. Implications of scavenger receptors in the safe development of nanotherapeutics. *Receptors Clin. Investig.* 2(3), e811 (2015).

- 57 Frenz T, Grabski E, Durán V *et al.* Antigen presenting cell-selective drug delivery by glycan-decorated nanocarriers. *Eur. J. Pharm. Biopharm.* 95(Pt A), 13–17 (2015).
- 58 Sallusto F, Cella M, Danieli C, Lanzavecchia A. Dendritic cells use macropinocytosis and the mannose receptor to concentrate macromolecules in the major histocompatibility complex class II compartment: downregulation by cytokines and bacterial products. *J. Exp. Med.* 182(2), 389–400 (1995).
- 59 Carrillo-Conde B, Song EH, Chavez-Santoscoy A *et al.* Mannose-functionalized ‘pathogen-like’ polyanhydride nanoparticles target C-type lectin receptors on dendritic cells. *Mol. Pharm.* 8(5), 1877–1886 (2011).
- 60 Chavez-Santoscoy AV, Roychoudhury R, Pohl NL, Wannemuehler MJ, Narasimhan B, Ramer-Tait AE. Tailoring the immune response by targeting C-type lectin receptors on alveolar macrophages using ‘pathogen-like’ amphiphilic polyanhydride nanoparticles. *Biomaterials* 33(18), 4762–4772 (2012).
- 61 Fukuda I, Mochizuki S, Sakurai K. Macrophage-targeting gene delivery using a micelle composed of mannose-modified lipid with triazole ring and dioleoyl trimethylammonium propane. *Biomed. Res. Int.* 2015, 350580 (2015).
- 62 Tong C, Cui Z, Sun X *et al.* Mannan derivatives instruct dendritic cells to induce Th1/Th2 cells polarization via differential mitogen-activated protein kinase activation. *Scand. J. Immunol.* 83(1), 10–17 (2016).
- 63 Pearce EJ, Kane CM, Sun J. Regulation of dendritic cell function by pathogen-derived molecules plays a key role in dictating the outcome of the adaptive immune response. *Chem. Immunol. Allergy* 90, 82–90 (2006).
- 64 Gi M, Im W, Hong S. Dendritic cells as danger-recognizing biosensors. *Sensors* 9(9), 6730–6751 (2009).
- 65 Brown J, Wang H, Hajishengallis GN, Martin M. TLR-signaling networks: an integration of adaptor molecules, kinases, and cross-talk. *J. Dent. Res.* 90(4), 417–427 (2011).
- 66 Cui J, Chen Y, Wang HY, Wang RF. Mechanisms and pathways of innate immune activation and regulation in health and cancer. *Hum Vaccin. Immunother.* 10(11), 3270–3285 (2014).
- 67 Krummen M, Balkow S, Shen L *et al.* Release of IL-12 by dendritic cells activated by TLR ligation is dependent on MyD88 signaling, whereas TRIF signaling is indispensable for TLR synergy. *J. Leukoc. Biol.* 88(1), 189–199 (2010).
- 68 Tada H, Aiba S, Shibata K, Ohteki T, Takada H. Synergistic effect of Nod1 and Nod2 agonists with toll-like receptor agonists on human dendritic cells to generate interleukin-12 and T helper Type 1 cells. *Infect. Immun.* 73(12), 7967–7976 (2005).
- 69 Pavot V, Rochereau N, Rességuier J *et al.* Cutting edge: new chimeric NOD2/TLR2 adjuvant drastically increases vaccine immunogenicity. *J. Immunol.* 193(12), 5781–5785 (2014).
- 70 Karlsten K, Korsholm KS, Mortensen R *et al.* A stable nanoparticulate DDA/MMG formulation acts synergistically with CpG ODN 1826 to enhance the CD4⁺ T-cell response. *Nanomedicine* 9(17), 2625–2638 (2014).
- 71 Rahimian S, Fransen MF, Kleinovink JW *et al.* Polymeric nanoparticles for co-delivery of synthetic long peptide antigen and poly IC as therapeutic cancer vaccine formulation. *J. Control. Release* 203, 16–22 (2015).
- 72 Pavot V, Rochereau N, Primard C *et al.* Encapsulation of Nod1 and Nod2 receptor ligands into poly(lactic acid) nanoparticles potentiates their immune properties. *J. Control. Release* 167(1), 60–67 (2013).
- 73 Gorden KB, Gorski KS, Gibson SJ *et al.* Synthetic TLR agonists reveal functional differences between human TLR7 and TLR8. *J. Immunol.* 174(3), 1259–1268 (2015).
- 74 Rauen J, Kreer C, Paillard A *et al.* Enhanced cross-presentation and improved CD8⁺ T cell responses after mannosylation of synthetic long peptides in mice. *PLoS One* 9(8), e103755 (2014).
- 75 Zaric M, Lyubomska O, Poux C *et al.* Dissolving microneedle delivery of nanoparticle-encapsulated antigen elicits efficient cross-priming and Th1 immune responses by murine Langerhans cells. *J. Invest. Dermatol.* 135(2), 425–434 (2015).

5.3 Publication 3

Functionalization of Active Ester-Based Polymersomes for Enhanced Cell Uptake and Stimuli-Responsive Cargo Release

Published in: *Biomacromolecules*, 2016, 17(10):3305-3317

Reprinted (adapted) with permission from (Scherer, M. *et al.* Functionalization of Active Ester-Based Polymersomes for Enhanced Cell Uptake and Stimuli-Responsive Cargo Release. *Biomacromolecules* **17**, 3305–3317 (2016)). Copyright (2016) ACS publications.

Functionalization of Active Ester-Based Polymersomes for Enhanced Cell Uptake and Stimuli-Responsive Cargo Release

Martin Scherer,[†] Cinja Kappel,[‡] Nicole Mohr,[†] Karl Fischer,[§] Philipp Heller,[†] Romina Forst,[†] Frank Depoix,^{||} Matthias Bros,[‡] and Rudolf Zentel^{*,†}

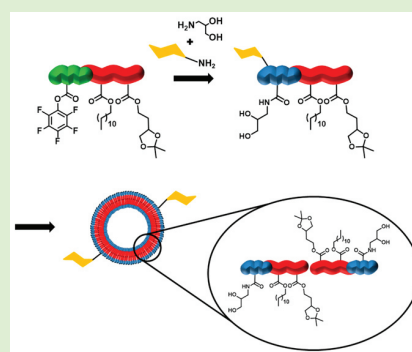
[†]Institute of Organic Chemistry, Johannes Gutenberg-University Mainz, Duesbergweg 10-14, 55128 Mainz, Germany

[‡]Department of Dermatology, University Medical Center, Johannes Gutenberg-University Mainz, Obere Zahlbacher Straße 63, 55131 Mainz, Germany

[§]Institute of Physical Chemistry, Johannes Gutenberg University Mainz, Jakob-Welder-Weg 11, 55099 Mainz, Germany

^{||}Institute of Zoology, Johannes Gutenberg University Mainz, J.-J.-Becher-Weg 7, 55128 Mainz, Germany

ABSTRACT: Poly(2,3-dihydroxypropyl methacrylamide) (P(DHPMA))-based amphiphilic block copolymers have recently proven to form polymer vesicles (polymersomes). In this work, we further expand their potential by incorporating (i) units for pH-dependent disintegration into the hydrophobic membrane and (ii) mannose as targeting unit into the hydrophilic block. This last step relies on the use of an active ester prepolymer. We confirm the stability of the polymersomes against detergents like Triton X-100 and their low cytotoxicity. The incorporation of 2-(2,2-dimethyl-1,3-dioxolane-4-yl)ethyl methacrylate into the hydrophobic block (lauryl methacrylate) allows a pH-responsive disintegration for cargo release. Efficient decomposition of the polymersome structure is monitored by dynamic light scattering. It is thus possible to include an active enzyme (glucose oxidase), which gets only active (is set free) after vesicle disintegration. In addition, the introduction of mannose as targeting structure allows enhanced and selective targeting of dendritic cells.



INTRODUCTION

Nanosized block copolymer vesicles (polymersomes) with an aqueous core are currently investigated as potential drug carriers.^{1–7} Their prominent advantage compared to many other types of nanoparticles is the ability to serve as universal carriers for both hydrophilic and hydrophobic cargo without requiring any substance-specific ligation chemistry. Compared to liposomes—their small-molecule counterparts—most types of polymersomes exhibit a superior mechanical stability, and their membranes are less fluid and permeable. The key factor contributing to this phenomenon is the high molecular weight of the membrane-forming hydrophobic block.⁸ The average molecular weight of the entire amphiphilic polymer chains can exceed the mass of common phospholipids by up to 2 orders of magnitude.⁵ The high molecular weight of such block copolymers results in a decreased exchange rate and critical assembly concentration, a hampered lateral diffusion and membrane thicknesses of about 10 to 50 nm.⁹ Furthermore, the bulky outer hydrophilic block can lead to a decreased interaction with biological media such as serum proteins (stealth-like effect), as long as no net charges are present.^{10–13}

For many years, polyethylene glycol (PEG) has been the hydrophilic material to be employed most often for colloidal stabilization and shielding of nanoparticles including polymersomes.^{14–16} It can be synthesized to yield narrow dispersities over a broad range of molecular weight and can therefore be

tuned precisely to fit the respective application. Furthermore, due to the absence of surface charges, the aforementioned stealth-like effect is particularly strong. However, the further functionalization of PEG-based nanoparticles is hampered by the lack of sites for modification. The $-\text{CH}_2-\text{CH}_2-\text{O}-$ repeating unit is inert to selective functionalization, and thus only the hydroxyl end group is left for modification. Hence, no multivalent functionalization and simultaneous attachment of different labels are possible.

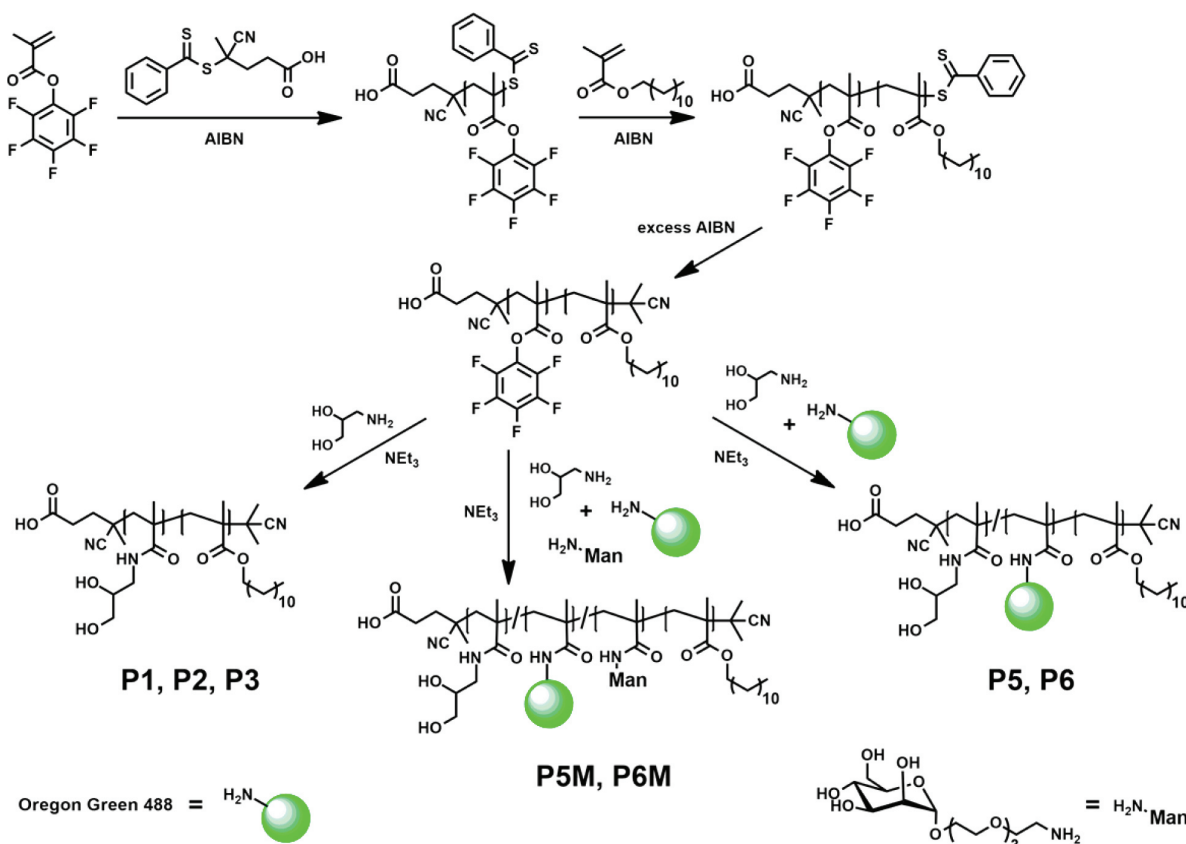
We have recently presented a way to prepare polymersomes from amphiphilic block copolymers with poly(2,3-dihydroxypropyl methacrylamide) (P(DHPMA)) as the hydrophilic block.¹⁷ P(DHPMA) is similar to the biocompatible polymer poly(2-hydroxypropyl methacrylamide) (P(HPMA)). Additionally, as in the case of P(HPMA), this hydrophilic polyamide can be synthesized via the conversion of an activated ester polymer precursor with a suitable amine (here 2,3-dihydroxypropylamine). Thus, the addition of further amines during the aminolysis of the activated ester polymer enables a versatile and multivalent functionalization of the hydrophilic block. This can give rise to a broad range of applications.^{18–24}

Received: July 15, 2016

Revised: September 12, 2016

Published: September 27, 2016

Scheme 1. Synthesis of P(DHPMA)-b-P(LMA)-Based Block Copolymers by RAFT Polymerization



^aFor the acid degradable analogous polymer see [Scheme 3](#).

Employing the process of dual centrifugation (DC)—hitherto known in liposome formation²⁵—we were able to form vesicles from these amphiphilic P(DHPMA)-based block copolymers and load them with water-soluble molecules such as hydrophilic dyes and siRNA. High encapsulation efficiencies of about 30% were achieved. This makes the new polymers promising candidates as nanosized drug carriers.

However, there are more requirements that polymersomes have to meet to be used as drug carriers. This includes active targeting and a stimulus-responsive release of cargo. Active targeting becomes especially important if special cells of the immune system like dendritic cells are to be addressed.²⁶ Synthetic routes via active ester intermediates facilitate the attachment of targeting ligands for receptor-mediated cell uptake. Such a ligand facilitates selective and enhanced cellular uptake into the desired cell population once the particle has reached the target tissue by passive diffusion-controlled mechanisms (EPR, passive targeting).^{27,28} The other important factor is the stimulus-responsive release of cargo. Since the thick polymersome membrane is an effective barrier to separate the inner compartment from the outer aqueous phase, it is tough for the cargo—especially substances of higher molecular weight such as oligonucleotides or even proteins—to escape from the vesicle within an appropriate time frame (hours).

Here we describe the double functionalization of these amphiphilic block copolymers both within the hydrophilic P(DHPMA) corona and the hydrophobic part. To make the hydrophobic part acid-degradable, ketal-containing monomers

are incorporated. Alternatively, mannose is incorporated into the hydrophilic block via active ester chemistry for the targeting of dendritic cells.

■ MATERIALS AND METHODS

All reagents and solvents were purchased from Acros Organics, Carl Roth, eBioscience, Fisher and Sigma-Aldrich and used without further purification unless stated otherwise. Cyclohexane, 1,4-dioxane, tetrahydrofuran (THF), and triethylamine were purified and dried according to standard procedures prior to use.

Lauryl methacrylate (LMA) was subjected to vacuum distillation prior to use to remove the stabilizer.

2,2'-Azobis(isobutyronitrile) (AIBN) was recrystallized from diethyl ether and stored at $-20\text{ }^{\circ}\text{C}$.

Sephadex CL-2B/4B was stored in 20% ethanol and flushed with phosphate-buffered saline (PBS, Dulbecco's phosphate-buffered saline, ThermoFisher) prior to use.

Characterization. NMR spectra were recorded using Bruker Avance III HD 300 (300 MHz ¹H NMR), Avance III HD 300 (300 MHz ¹H NMR) and Avance II 400 (400 MHz ¹H NMR; 100 MHz ¹³C NMR; 377 MHz ¹⁹F-NMR) spectrometers. Measurements were performed at room temperature and analyzed with MestReNova 9.0.0 software.

Gel permeation chromatography (GPC) was performed using tetrahydrofuran as an eluent. For molecular weight determination, a setup from Jasco was employed, consisting of a HPLC pump PU 1850, an autosampler AS 1555 and detectors UV 1575 (UV-detection, $\lambda = 254\text{ nm}$) and RI 1530 (refractive index-detection). The column was packed with cross-linked styrene-divinylbenzene copolymers of pore sizes 102, 104, and 106 Å. For calibration, polystyrene standards by PSS Polymer Standards Service were used. The sample concentration

Table 1. Reaction Batches Homopolymers H1–H4 and Statistical Copolymer SC

polymer	monomer [mol]	CTA [mol]	AIBN [mol]	yield [g]	M_n [g·mol ⁻¹]	\bar{D}
H1 (P(PFPMA) ₂₃)	7.92×10^{-3}	3.91×10^{-4}	3.96×10^{-5}	1.09	6100	1.31
H2 (P(PFPMA) ₃₁)	1.75×10^{-2}	7.36×10^{-4}	6.42×10^{-5}	3.02	8100	1.34
H3 (P(PFPMA) ₃₃)	1.20×10^{-2}	5.04×10^{-4}	4.40×10^{-5}	1.67	8400	1.29
H4 (P(LMA) ₁₃)	1.18×10^{-2}	6.36×10^{-4}	6.33×10^{-5}	1.01	3500	1.08
SC (P(LMA) ₁₆ -stat-(DDEMA) ₆)	3.93×10^{-3} (LMA) + 1.68×10^{-3} (DDEMA)	1.65×10^{-4}	2.75×10^{-5}	0.55	6200	1.13

Table 2. Reaction Batches PFPMA-*b*-LMA Block Copolymers

polymer	homopolymer [mol]	2nd monomer [mol]	AIBN [mol]	yield [g]	M_n [g·mol ⁻¹]	\bar{D}
BC1 (P(PFPMA) ₂₃ - <i>b</i> -P(LMA) ₂₁)	4.57×10^{-5} (H1)	1.14×10^{-4}	5.97×10^{-6}	0.48	11500	1.23
BC2 (P(PFPMA) ₁₅ - <i>b</i> -P(LMA) ₁₃)	1.24×10^{-4} (H4)	1.84×10^{-3}	1.20×10^{-5}	0.69	7200	1.20
BC3 (P(PFPMA) ₃₁ - <i>b</i> -P(LMA) ₁₆)	1.10×10^{-4} (H2)	2.26×10^{-3}	1.38×10^{-5}	1.24	12100	1.16
BC4 (P(PFPMA) ₃₃ - <i>b</i> -P(LMA) ₂₈)	1.43×10^{-4} (H3)	7.12×10^{-3}	1.46×10^{-5}	2.51	15500	1.21

was set to 2 mg/mL. As an internal standard, toluene (0.2%) was added to each sample. The flow rate was adjusted to 1 mL/min.

For dynamic light scattering (DLS) experiments, colloidal dispersions in PBS buffer were prepared and filtered into dust free cylindrical scattering cells (Suprasil, 20 mm diameter, Hellma, Mühlheim, Germany) in a dust free flow box using Millex LCR 0.45 μ m filters.

DLS measurements were performed using a Uniphase He/Ne Laser ($\lambda = 632.8$ nm, 25 mW), an ALV-SP125 goniometer, an ALV/High QE APD Avalanche photo diode with fiber optical detection, an ALV 5000/E/PCI correlator, and a Lauda RC-6 thermostat unit at 20 °C. Angular dependent measurements were carried out in the range of 30°–150° at steps of 15°. Experimental intensity correlation functions were transformed into amplitude correlation functions applying the Siegert relation extended to include negative values after baseline subtraction by calculation $g_i(t) = \text{SIGN}(G_2(t)) \cdot \text{SQRT}(\text{ABS}(G_2(t) - A)/A)$, with A the measured baseline and $G_2(t)$ the experimental intensity correlation function. The field correlation functions were fitted by a sum of two exponentials $g_i(t) = a \cdot \exp(-t/b) + c \cdot \exp(-t/d)$ to take polydispersity into account. Average apparent diffusion coefficients D_{app} were obtained by applying $q^2 \cdot D_{\text{app}} = (a \cdot b - 1 + c \cdot d - 1)/(a + c)$ resulting in an angular-dependent diffusion coefficient or reciprocal hydrodynamic radius $(1/R_h)_{\text{app}}$. The z -average hydrodynamic radii R_h were obtained by extrapolation of $(1/R_h)_{\text{app}}$ to $q = 0$. The normalized second cumulant μ_2 was calculated using a cumulant fit at 90°.

UV/vis spectra and absorption and transmission measurements were recorded using a V-630 (Jasco) spectrometer. The quartz glass cuvettes (Hellma Analytics) had a light path of 10 mm. The spectrometer was kept at a temperature of $T = 20$ °C using a Jasco ETC-717 Peltier element. Data analysis was performed using the Jasco Spectra Manager 2.04 software.

Monomer Synthesis. Pentafluorophenyl methacrylate (PFPMA) was synthesized according to a procedure published by Eberhardt et al.²⁹

2-(2,2-Dimethyl-1,3-dioxolane-4-yl)ethyl methacrylate (DDEMA) was synthesized in a one-step nucleophilic substitution via the Schotten–Baumann method: 4-(2-Hydroxyethyl)-2,2-dimethyl-1,3-dioxolane ($m = 5.0$ g; 34.2 mmol) was dissolved in 100 mL of anhydrous dichloromethane under an argon atmosphere together with 4.15 g (41.0 mmol; 1.2 equiv) triethylamine. The flask content was cooled to 0 °C and 3.93 g of methacryloyl chloride (37.6 mmol; 1.1 equiv) were added dropwise while stirring. The mixture was allowed to warm up to room temperature and stirred for another 15 h. The colorless precipitate was filtered off, and the organic phase was washed with 3x 50 mL of water and dried with magnesium sulfate. After concentration using a rotary evaporator, the slightly yellow liquid was purified via column chromatography (eluent: cyclohexane/ethyl acetate, 6:1 v/v). DDEMA was yielded as a colorless oil; $m = 4.28$ g (20.0 mmol; 58.4%).

¹H NMR (400 MHz, CDCl₃): δ [ppm] = 6.12 (s, 1H, C=CH₂-cis); 5.59 (s, 1H, C=CH₂-trans); 4.32 (m, 1H, -O-CH-CH₂-);

4.22 (m, 2H, -COO-CH₂-); 4.10 (dd, $J_1 = 7.0$ Hz; $J_2 = 1,1$ Hz, 1H, -O-CH₂-CH-); 3.62 (dd, $J_1 = 7.0$ Hz; $J_2 = 1.1$ Hz, 1H, -O-CH₂-CH-); 2.06–1.89 (m, 2H, -COO-CH₂-CH₂-); 1.97 (s, 3H, CH₃-C(C H₂)-); 1.43 (s, 3H, CH₃-C(C H₃)-O); 1.38 (s, 3H, CH₃-C(CH₃)-O-).

Synthesis of the Mannose Linker. The mannose linker H₂N-Man (Scheme 1) was synthesized according to a procedure developed by Mohr.³⁰

Polymer Synthesis. The synthesis of PFPMA-based amphiphilic block copolymers was performed using a modification of the procedure published by Barz et al.³¹

In a first step, the homopolymers H1–H4 were produced from PFPMA or LMA via reversible addition–fragmentation chain transfer (RAFT) polymerization to serve as macromolecular chain transfer agents for the generation of diblock copolymers. The respective amounts of monomer and 4-Cyano-4-((thiobenzoyl)sulfanyl)pentanoic acid as a chain transfer agent (CTA) were dissolved in anhydrous dioxane in a Schlenk tube. A solution of AIBN in anhydrous dioxane was added before the tube was sealed and instantly immersed into liquid nitrogen. The total amount of dioxane corresponded to 1.5 mL per gram of monomer. The reaction mixture was submitted to three freeze–pump–thaw cycles and then stirred in vacuo at 65 °C for 19 h. The reaction was quenched by precipitation of the homopolymer in cold hexane, followed by centrifugation (4000 rpm, 15 min) and resolution in anhydrous dioxane. After two more precipitation steps, the polymers were dried in vacuo (40 °C, 16 h) to yield a pink-colored solid (H1–H3) or viscous oil (H4) (Table 1).

To synthesize a statistical copolymer SC containing LMA and DDEMA, the monomers were mixed at a given ratio (Table 1). All other steps were conducted according to the procedure for homopolymer synthesis.

H1–H3. ¹H NMR (400 MHz, CDCl₃): δ [ppm] = 2.55–1.90 (br, 2H, -CH₂-); 1.65–1.18 (br, 3H, -CH₃).

¹⁹F-NMR (377 MHz, CDCl₃): δ [ppm] = -151.30 to -153.50 (br, 2F, *o*-ArF); -157.60 to -158.60 (br, 1F, *p*-ArF); -162.65 to -163.70 (br, 2F, *m*-ArF).

H4. ¹H NMR (400 MHz, CDCl₃): δ [ppm] = 4.02–3.78 (br, 2H, -COO-CH₂-); 1.96–0.83 (br, 23H, -CH₂-, -CH₃-).

SC. ¹H NMR (400 MHz, CDCl₃): δ [ppm] = 4.37–4.25 (br, 1H, -O-CH-CH₂-); 4.12–3.86 (br, 7.38H, -COO-CH₂- LMA, -O-CH₂-CH-); 3.85–3.73 (br, 2.09H, -COO-CH₂- DDEMA); 2.65–0.82 (br, 84.71H, -C(CH₃)₂-, -CH₂ (LMA side chain), -COO-CH₂-CH₂- (DDEMA), -CH₂- (backbone DDEMA/LMA), -CH₃ (backbone DDEMA/LMA), -CH₃ (LMA)).

P(PFPMA)-*b*-P(LMA) block copolymers were synthesized by employing the homopolymers H1–H4 as macro-chain transfer agents in combination with the respective second monomer (Table 2).

The homopolymers were dissolved in anhydrous dioxane and transferred into a Schlenk tube together with the second monomer, and AIBN, dissolved in further dioxane, was added (total amount of solvent: 4 mL per gram of polymer). The reaction mixture was submitted to three freeze–pump–thaw cycles and then stirred in

Table 3. Reaction Batch DDEMA-Containing Block Copolymer BS

polymer	stat. copolymer [mol]	PFPMA [mol]	AIBN [mol]	yield [g]	M_n [g·mol ⁻¹]	\bar{D}
BS (P(PFPMA) ₂₁ - <i>b</i> -P(LMA ₁₆ - <i>stat</i> -DDEMA ₆))	4.80×10^{-5}	1.05×10^{-3}	6.09×10^{-6}	0.41	10,700	1.11

Table 4. Reaction Batches of Nonfunctionalized Block Copolymers P1–P3 and Acid-Labile P4

polymer	block copolymer [mol]	DHPA [mol]	NEt ₃ [mol]	yield [mg]	M_n [g·mol ⁻¹]	hydrophilic weight fraction <i>f</i>
P1 (P(DHPMA) ₂₃ - <i>b</i> -P(LMA) ₂₁)	9.13×10^{-6} (BC1)	4.17×10^{-4}	8.34×10^{-4}	73.0	9100	0.398
P2 (P(DHPMA) ₁₅ - <i>b</i> -P(LMA) ₁₃)	2.48×10^{-5} (BC2)	7.40×10^{-4}	1.48×10^{-3}	126.1	5600	0.420
P3 (P(DHPMA) ₃₃ - <i>b</i> -P(LMA) ₂₈)	3.31×10^{-5} (BC4)	4.31×10^{-3}	8.61×10^{-3}	353.1	12 200	0.415
P4 (P(PFPMA) ₂₁ - <i>b</i> -P(LMA ₁₆ - <i>stat</i> -DDEMA ₆))	1.35×10^{-5} (BS)	4.39×10^{-4}	8.80×10^{-4}	110.0	8800	0.348

Table 5. Reaction Batches of Mannose- and Dye-Functionalized Polymers

polymer	block copolymer [mol]	mannose [mol]	OG488 [mol]	DHPA [mol]	NEt ₃ [mol]	yield [mg]	M_n [g·mol ⁻¹]	hydrophilic weight fraction <i>f</i>
P5 P(DHPMA- <i>stat</i> -OG) ₃₁ - <i>b</i> -P(LMA) ₁₆	6.25×10^{-6}	-	1.95×10^{-6}	7.78×10^{-4}	1.56×10^{-3}	56.3	8900	0.554
P5M P(DHPMA- <i>stat</i> -Mann- <i>stat</i> -OG) ₃₁ - <i>b</i> -P(LMA) ₁₆	6.06×10^{-6}	1.50×10^{-5}	1.88×10^{-6}	7.52×10^{-4}	1.05×10^{-3}	52.7	"	"
P6 P(DHPMA- <i>stat</i> -OG) ₃₃ - <i>b</i> -P(LMA) ₂₈	1.28×10^{-5}	-	4.01×10^{-6}	1.60×10^{-3}	3.21×10^{-3}	144.4	12 200	0.415
P6M P(DHPMA- <i>stat</i> -Mann- <i>stat</i> -OG) ₃₃ - <i>b</i> -P(LMA) ₂₈	1.29×10^{-5}	3.25×10^{-5}	4.07×10^{-6}	1.63×10^{-3}	3.26×10^{-3}	103.6	"	"

vacuo at 65 °C for 55 h. The reaction was quenched by precipitation of the polymer in cold methanol, followed by centrifugation (4000 rpm, 30 min) and resolution in anhydrous dioxane. After two more precipitation steps, the polymers were dried in vacuo (40 °C, 16 h) to yield pink-colored solids of rubber-like texture.

¹H NMR (400 MHz, CDCl₃): δ [ppm] = 3.96–3.68 (br, 2H, –O–CH₂–CH₂–); 2.70–0.78 (br, 33.57H (BC1)/34.34H (BC2)/38.67H (BC3)/33.89H (BC4), –CH₂– (backbone PFPMA/LMA), –CH₃ (backbone PFPMA/LMA), –CH₂– (LMA side chain), –CH₃ (backbone PFPMA/LMA)).

¹⁹F-NMR (377 MHz, CDCl₃): δ [ppm] = –151.30 to –153.50 (br, *o*-ArF); –157.60 to –158.60 (br, *p*-ArF); –162.65 to –163.70 (br, *m*-ArF).

The statistical copolymer SC was used as a macro-CTA to produce a PFPMA-containing block copolymer structure BS (Table 3). The synthesis was performed analogue to the P(PFPMA)-*b*-P(LMA) copolymers except that the mixture was stirred at 70 °C for 72 h.

¹H NMR (400 MHz, CDCl₃): δ [ppm] = 4.37–4.25 (br, 1H, –O–CH–CH₂–); 4.12–3.86 (br, 7.33H, –COO–CH₂– LMA, –O–CH₂–CH–); 3.85–3.73 (br, 2.15H, –COO–CH₂– DDEMA); 2.65–0.82 (br, 103.81H, –C(CH₃)₂–, –CH₂– (LMA side chain), –COO–CH₂–CH₂– (DDEMA), –CH₂– (backbone DDEMA/LMA/PFPMA), –CH₃ (backbone DDEMA/LMA/PFPMA), –CH₃ (LMA)).

The substitution of the block copolymers' reactive dithiobenzoate groups was achieved by substitution with AIBN via the Perrier method.³² The polymers were dissolved in anhydrous dioxane and stirred together with a 30× molar excess of AIBN at 65 °C under an argon atmosphere until the characteristic UV absorption band of the dithiobenzoate group at $\lambda_{\text{abs}} = 310$ nm could no more be detected (usually around 5 h). After three precipitation steps analogue to the block copolymer synthesis, the end group-substituted polymers were yielded as colorless solids of rubber-like texture.

The P(PFPMA)-*b*-P(LMA) polymers were converted into the amphiphilic P(DHPMA)-*b*-P(LMA) block copolymers P1–P3 by polymer–analogue conversion of the reactive pentafluorophenyl (PFP) ester with 2,3-dihydroxypropylamine (DHPA) (Table 4).

The respective PFPMA-based prepolymer was dissolved in dioxane in a Schlenk tube under Argon (10 mL per gram of polymer). Two equivalents of DHPA and 4 equiv of triethylamine per PFPMA repeating unit, dissolved in DMSO (4 mL per gram of polymer), were added, and the mixture was stirred at 50 °C. After 17 h, a second identical charge of DHPA and triethylamine in DMSO was added, and

the mixture was stirred for 24 h. Then the Schlenk tube was cooled to room temperature and the solvents were removed by dialysis against Milli-Q water and subsequent lyophilization. The polymers P1–P3 were obtained as fluffy, colorless substances.

The conversion of BS into the corresponding amphiphilic block copolymer P4 (Table 4) was conducted analogously to the procedure described for the synthesis for P1, P2, and P3.

In order to determine the block compositions by ¹H NMR spectroscopy, data obtained from the P(PFPMA)-*b*-P(LMA) precursor polymers BC1–BC4 were used because of the overlapping broad signals of the hydroxyl groups that were introduced in the final synthetic step during the active ester conversion to P1–P4. Because of this overlap, no reliable information could be obtained from the final amphiphilic polymers and no integrals are given for the corresponding signals. To determine the block compositions, the integral of the α -methylene group of LMA (BC1–BC4) was defined as $I = 2$. The signals of the CTA protons could be disregarded in good approximation. The signals belonging to the remaining lauryl ester protons as well as the polymer backbone were summarized and subtracted by $I = 28$ accounting for the other protons of the LMA repeating unit. The residue gave the integral corresponding to the 5 protons of the PFPMA repeating unit and enabled the calculation of the molar ratio of PFPMA and LMA. After the conversion of PFPMA into hydrophilic DHPMA, the hydrophilic weight fraction f was obtained by multiplication of the relative molar ratio of DHPMA with the molecular mass of the DHPMA repeating unit and division by the sum of the relative molar contents of DHPMA and LMA, each weighted by their individual molecular mass ($M_{\text{DHPMA}} = 159.18$ g/mol; $M_{\text{LMA}} = 254.41$ g/mol).

P1–P3. ¹H NMR (400 MHz, CDCl₃/MeOH-*d*₄): δ [ppm] = 3.95–3.68 (br, –O–CH₂–CH₂–); 3.35–3.05 (br, O=CNH–CH₂–); 2.96–2.66 (br, –CHOH–CH₃); 2.59–0.51 (br, –CH₂– (backbone DHPMA/LMA), –CH₃ (backbone DHPMA/LMA), –CH₂– (LMA side chain)).

¹³C NMR (100 MHz, CDCl₃/MeOH-*d*₄): δ [ppm] = 177.99 (–CON–); 177.68 (–COO–); 77.43 (–NH–CH₂–COH–); 65.14 (HO–CH₂–); 64.32 (COO–CH₂–); 54.32 (–CH₂– backbone); 54.16 (–CH₂– backbone); 45.14 (–NH–CH₂–); 44.90 (C_{quat} backbone); 44.75 (C_{quat} backbone); 31.93 (COO–CH₂–CH₂–); 29.63/29.60/29.53/29.33/28.21/28.10 (–CH₂– side chain); 26.06 (CH₃–CH₂–CH₂–); 22.68 (CH₃–CH₂–); 18.38 (CH₃ backbone); 16.45 (CH₃ backbone); 14.01 (CH₃–CH₂–).

P4. ^1H NMR (400 MHz, $\text{DMSO}-d_6$): δ [ppm] = 4.95–4.72 (br, $-\text{CHOH}-$); 4.67–4.40 (br, $-\text{CH}_2\text{OH}$); 3.90–3.45 (br, $-\text{COO}-\text{CH}_2-$ LMA, $-\text{COO}-\text{CH}_2-$ DDEMA, $-\text{NH}-\text{CH}_2-$); 2.95–0.27 (br, $-\text{C}(\text{CH}_3)_2$, $-\text{CH}_2$ (LMA side chain), $-\text{COO}-\text{CH}_2-\text{CH}_2-$ (DDEMA), $-\text{CH}_2-$ (backbone DDEMA/LMA/DHPMA), $-\text{CH}_3$ (backbone DDEMA/LMA/DHPMA), $-\text{CH}_3$ (LMA)).

The polymers **BC3** and **BC4** were converted into mannose-containing amphiphilic polymers **PSM** and **P6M** and their non-mannosylated equivalents **P5** and **P6** in an analogue reaction. Additionally, all these four polymers were labeled with Oregon Green 488 (OG488) for fluorescence-based detection (Table 5).

For dye labeling, a solution of OG488 cadaverine in anhydrous DMSO was added to the polymer solution together with 5 μL of triethylamine. After 5 h of stirring under argon at 35 $^\circ\text{C}$, the conversion of the remaining PFPMA repeating units with DHPA was conducted according to the aforementioned protocol (see preparation of **P1–P4**). For additional mannose labeling, the mannose linker was dissolved in anhydrous DMSO and added to the polymer solution together with 5 μL of trimethylamine prior to the addition of OG488. After stirring at 50 $^\circ\text{C}$ (**P5**: 8 h; **P6**: 24 h), the further procedure for dye labeling was conducted as described above.

^{13}C NMR (100 MHz, inverse gated, CDCl_3): δ [ppm] = 179.3–176.2 (m, $\text{O}=\text{CNH}-$); 100.4–100.0 (m, C_1 -mannose).

Vesicle Preparation. Vesicle formation for cytotoxicity evaluation and cell uptake studies was achieved by the solvent switching method. 4.5 mg of the respective Polymers **P1/P2/P5/PSM/P6/P6M** were dissolved in 0.5 mL of DMSO by 3 h of agitation using a ThermoMixer (Eppendorf) at 800 rpm (30 $^\circ\text{C}$). While stirring, these solutions were infused with 2 mL of PBS buffer at a rate of 0.03 mL/h using a PHD 2000 syringe pump (Harvard Apparatus). The obtained highly turbid vesicle dispersions were dialyzed against PBS to remove the organic solvent.

For preparation via dual centrifugation, 2 mg of the respective lyophilized powders were weighed into 0.2 mL Eppendorf vials and incubated with 8 μL of the aqueous phase (PBS or a PBS-based solution of the cargo to be encapsulated) at room temperature for 30 min. 47 mg of ceramic beads ($\varnothing = 0.3$ –0.4 mm) were added, and the samples were homogenized for 2×16 min in a Rotanda 400 centrifuge (Hettich/Tuttligen) at a rotating velocity of 2500 rpm. Afterward, 19.1 μL of further aqueous phase (PBS) were added and the samples were centrifuged for another 2×2 min.

Detergent-Based Stability Assay. Vesicle dispersions of **P3** in PBS were produced by solvent switching as described above and extruded 21x through a polycarbonate membrane (Whatman Nuclepore Track-Etched Membranes, $d = 200$ nm) to yield narrowly distributed polymersomes of $R_h = 100$ nm. In an analogous fashion, liposomes from 1,2-dipalmitoyl-*sn*-glycero-3-phosphocholine (DPPC) were produced as control. Concentrations were adjusted to $c = 10$ mg/mL. After an initial DLS measurement of the pure vesicle dispersions (performed as described above), rising amounts of Triton X-100 were added (see Figure 2). In order to avoid dilution effects, the concentrations of the detergent solutions were chosen not to dilute the original dispersion by more than 20% after the maximum amount of detergent was reached.

Glucose Oxidase Assay. In order to test the permeability of the membrane of **P4** vesicles for high molecular weight substances such as enzymes, an assay based on the enzymatic determination of the blood glucose concentration was set up. Glucose oxidase (GOx, from *Aspergillus niger*, 200 U/mg; Sigma-Aldrich) was loaded into vesicles. Loading was achieved by dual centrifugation (DC). Two milligrams of lyophilized powders of **P4** or DPPC, respectively, was weighed into 0.2 mL Eppendorf vials and incubated with 8 μL of a GOx solution (0.15 mg/mL) in PBS at room temperature for 30 min. Forty-seven milligrams of ceramic beads ($\varnothing = 0.3$ –0.4 mm) was added, and the samples were homogenized for 2×16 min in a Rotanda 400 centrifuge (Hettich/Tuttligen) at a rotating velocity of 2500 rpm. Afterward, 19.1 μL of pure PBS buffer were added and the samples were centrifuged for another 2×2 min. The nonencapsulated enzyme was separated by size exclusion chromatography using Sepharose CL-2B. Separation was carried out in a flow box employing 7 μL batches of

the raw vesicle dispersions. The encapsulation efficiency and therefore the GOx content in the vesicle dispersions was quantified via the separately performed encapsulation of Alexa Fluor 647 SE fluorescent dye and quantification of the amount of dye separated from the vesicles via Beer–Lambert law by measuring the transmission of the separated liquid phase at $\lambda = 650$ nm via UV/vis spectrometry. Encapsulation efficiencies of **EE (P4)** = 18.8% and **EE (DPPC)** = 26.8% were yielded that corresponded to the order of magnitude previously reported.¹⁷

After removal of the free enzyme, the vesicle dispersions were added to a solution of D-(+)-glucose, horseradish peroxidase (HRP) and 2,2'-azino-bis(3-ethylbenzthiazoline-6-sulfonic acid) (ABTS) in PBS. Additionally, a sample containing this solution and an equivalent amount of nonencapsulated GOx was prepared as a control. The final GOx-concentration in each sample was 2.5 $\mu\text{g}/\text{mL}$ while the samples contained 25.0 $\mu\text{M}/\text{L}$ glucose, 18.8 $\mu\text{g}/\text{mL}$ HRP, and 50.0 $\mu\text{g}/\text{mL}$ ABTS. Total volumes were adjusted to $V = 2.0$ mL. The absorption of the samples at $\lambda_{\text{abs}} = 415$ nm was determined via UV/vis spectrometry from the respective directly measured transmission data, starting immediately after sample preparation. A detector fluctuation of $\Delta T = 0.03$ was used to calculate the uncertainty of the absorption values. In the case of GOx encapsulated in polymersomes, an excess of Triton X-100 detergent ($V = 20$ μL) was added after 1456 min to disintegrate the vesicles and release the encapsulated GOx.

Vesicle Degradation. The pH-dependent degradation of the vesicles was studied using vesicles prepared from **P4** and **P5** via the solvent switching method. The vesicles were prepared in Milli-Q water containing 5 mM NaCl and were extruded 21x through a polycarbonate membrane (Whatman Nuclepore Track-Etched Membranes, $d = 200$ nm) to yield narrowly distributed polymersomes of $R_h = 100$ nm. The vesicle dispersions were aliquoted and the pH of the samples was adjusted to pH 6.5 and pH 4.5 using hydrochloric acid. The final polymer concentration was set to 10 mg/L. The samples were incubated at 37 $^\circ\text{C}$ for 48 h/53 h and examined via DLS.

Cell Viability. The influence of P(DHPMA)-*b*-P(LMA)-based and DDEMA-modified polymersomes on the viability of HEK293T cells was tested using a CellTiter96 Non-Radioactive Cell Proliferation Assay (MTT) Kit (Promega). The cells were seeded in a 96-well plate (12 500 cells/well) and were incubated with vesicle dispersions of **P1/P2/P4** in PBS buffer, contained in a total volume of 100 μL . The concentration range tested was 0.01–0.1 mg/mL and the assay was performed using hexaplicates of each sample. The samples were incubated at 37 $^\circ\text{C}$ for 24 h before 30 μL of the MTT substrate solution were added to each aliquot and the cells were incubated for another 4 h. 100 μL of the “solubilization solution/stop mix” were added. After 1 h, the absorption at $\lambda_{\text{abs}} = 570$ nm was measured.

Particle Uptake. In order to examine the relative cell uptake of vesicles from **P5** and **P6** and their mannosylated counterparts **PSM** and **P6M**, murine bone marrow-derived dendritic cells (BMDCs) were seeded into 12-well plates (250,000/well) after isolation and 1.25 mL of FACS medium (Iscove’s modified Dulbecco’s medium (IMDM), containing 5% fetal calf serum (FCS), 5% granulocyte macrophage colony-stimulating factor, 1% penicillin/streptavidin, 1% glutamine, and 1% β -mercaptoethanol) were added. On the third day of incubation, 500 μL of the culture medium were substituted for 500 μL of fresh medium. On the seventh day, the culture volume was reduced to 750 μL and 750 μL of the respective vesicle dispersion were added at a total polymer concentration of 3 $\mu\text{g}/\text{mL}$. The cells were incubated with the particles for 24 h at 37 $^\circ\text{C}$ before they were washed with PBS buffer containing 2% FCS to removed particles that had not been taken up. After harvesting for data acquisition, the cells were distributed to FACS tubes (BD, #352008, 0.2–0.5x 10^6 cells per tube) and incubated with surface marker α -ms CD206-BV421 (2.5 μL , eBioscience) at 0 $^\circ\text{C}$ for 20 min. Afterward, the samples were washed with 1 mL of FACS medium, fixed with 0.5 mL 0.7% PFA, and stored in the dark at 4 $^\circ\text{C}$ until measurements were taken. The particle uptake was quantified measuring the fluorescence intensity of the covalently attached Oregon Green 488 dye.

Table 6. Characterization of P(DHPMA)-Based Polymers and Vesicles

polymer	block composition	M_n^a [g·mol ⁻¹]	\bar{D}^a	hydrophilic weight fraction, f^b	R_h [nm] ^c	μ_2
P1	P(DHPMA) ₂₃ - <i>b</i> -P(LMA) ₂₁	9100	1.23	0.40	101	0.15
P2	P(DHPMA) ₁₅ - <i>b</i> -P(LMA) ₁₃	5600	1.20	0.42	98	0.16
P3	P(DHPMA) ₃₃ - <i>b</i> -P(LMA) ₂₈	12 200	1.21	0.42	175	0.17
P4	(P(PFPMA) ₂₁ - <i>b</i> -P(LMA ₁₆ - <i>stat</i> -DDEMA ₆))	8800	1.27	0.35	105 ^d /84 ^e	0.11 ^d /0.16 ^e
P5	P(DHPMA- <i>stat</i> -OG) ₃₁ - <i>b</i> -P(LMA) ₁₆	8900	1.16	0.55	134	0.11
P5M	P(DHPMA- <i>stat</i> -Mann- <i>stat</i> -OG) ₃₁ - <i>b</i> -P(LMA) ₁₆	"	1.16	0.55	137	0.13
P6	P(DHPMA- <i>stat</i> -OG) ₃₃ - <i>b</i> -P(LMA) ₂₈	12 200	1.21	0.42	174	0.17
P6M	P(DHPMA- <i>stat</i> -Mann- <i>stat</i> -OG) ₃₃ - <i>b</i> -P(LMA) ₂₈	"	1.21	0.42	181	0.16

^aExamined by THF-GPC from the respective PFPMA-based prepolymer. ^bExamined by ¹H NMR spectroscopy. ^cExamined by DLS ^dPrepared by solvent switching. ^ePrepared by DC.

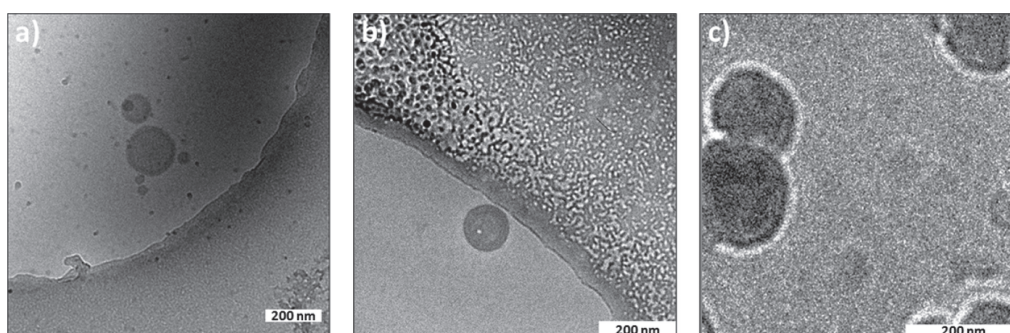


Figure 1. CryoTEM of Polymersomes formed from (a) P1, (b) P2, (c) P4.

RESULTS AND DISCUSSION

Our approach to functionalize the polymersomes for controlled release is the incorporation of an acid-labile comonomer into the hydrophobic block of the amphiphilic polymers. Zhang and Louage used (2,2-dimethyl-1,3-dioxolane-4-yl)methyl acrylate (DMDMA) to synthesize amphiphilic block copolymers that assembled into micelles which decomposed through the hydrolysis of the hydrophobic block.^{33,34} Inspired by their work, we developed a hydrolyzable ketal monomer that is both suitable for RAFT polymerization and will survive the basic reaction conditions of the polymer-analogue PFPMA-conversion without serving as an activated ester itself. We demonstrate the disintegration of vesicles formed from block copolymers that contain this ketal monomer as a part of their hydrophobic block.

Furthermore, we demonstrate the straightforward modification of active ester-based vesicles with a mannose targeting ligand for the enhanced uptake into bone marrow-derived dendritic cells (BMDCs). These cells overexpress mannose-binding lectins on their surface and hence are able to take up particles via receptor-mediated endocytosis. We have recently presented the synthesis of a mannose derivative that was equipped with an amine functional unit through a hydrophilic linker.²⁶ Using this amine group, we were able to link the mannose targeting moiety to an amphiphilic block copolymer via activated ester chemistry. The mannose-labeled polymers assembled into micellar aggregates and were taken up by BMDCs via receptor-mediated endocytosis.²⁶ Here, we apply this technique to label P(DHPMA)-*b*-P(LMA) block copolymer vesicles.

The synthesis of P(DHPMA)-*b*-P(LMA) in block compositions suitable for vesicle formation was achieved as reported previously (see Scheme 1).¹⁷

Starting from either PFPMA or LMA, homopolymers were produced by RAFT polymerization that were still bearing the active dithiobenzoate end group and could therefore be used as macro initiators to synthesize P(PFPMA)-*b*-P(LMA) block copolymers. After the dithiobenzoate groups were substituted with AIBN following the Perrier method,³² the final amphiphilic copolymers were obtained by the aminolysis of the activated PFP ester functional units with DHPA. The amphiphilic block copolymers P1, P2, and P3 were obtained, ranging from $M_n = 5600$ – $12\,200$ g/mol and exhibiting hydrophilic weight fractions around $f = 0.4$. The dispersities were around $\bar{D} = 1.2$, which is typical of PFPMA-derived block copolymers prepared via RAFT polymerization (Table 6).³⁵ In addition, pH degradable (P4, Scheme 3) and mannose-functionalized block copolymers (P5M/P6M, Scheme 1) were prepared. They will be discussed later.

We previously examined the critical aggregation concentration (CAC) values of such polymers and found values in the 10^{-8} mol/L range. For example, P2 has a CAC of 4.1×10^{-8} mol/L (determined via the pyrene method).³⁶

These polymers were used to prepare vesicles via the solvent switching method. Solutions of the polymers in DMSO were infused with PBS buffer as a selective solvent for the P(DHPMA) block in order to induce vesicle formation. After the organic solvent was removed by dialysis, the vesicles dispersed in pure PBS were yielded as confirmed by cryogenic transmission electron microscopy (Figure 1). The vesicle size was determined by DLS measurements, revealing that P1 and P2 formed vesicles of almost identical hydrodynamic radius (98 nm vs 101 nm) and moderate dispersities around $\mu_2 = 0.15$, while the P3 vesicles were significantly larger (175 nm).

In order to verify the superior stability of the P(DHPMA)-based polymersomes, their resistance toward dissolution by a nonionic detergent was tested and compared to liposomes from DPPC. Vesicle dispersions of P3 and DPPC were produced via

solvent switching and subsequent homogenization by extrusion through a 200 nm membrane. Then they were mixed with rising amounts of Triton X-100 and examined via DLS (Figure 2).

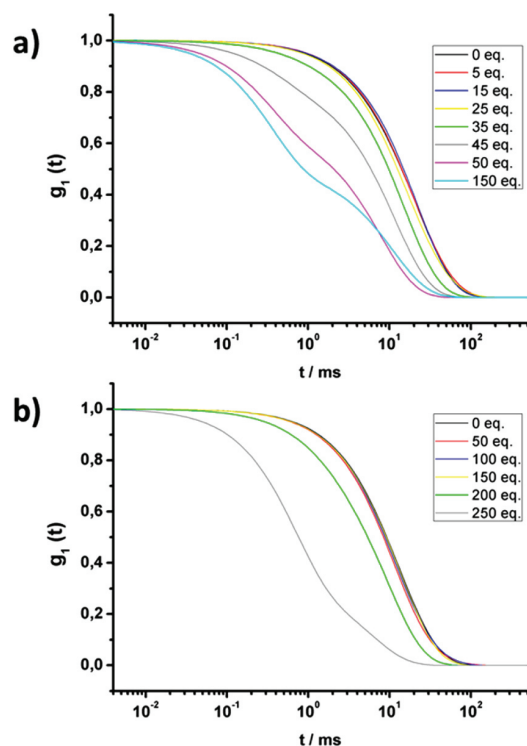


Figure 2. DLS-based disaggregation assay of vesicles by adding rising concentrations of Triton X-100 (ACF-Fit, 30°). (a) DPPC liposomes; (b) polymersomes from P3.

In the case of lipid vesicles (Figure 2a), no pronounced effect on the autocorrelation function (ACF) was detected up to a 25-fold molar excess. Further addition of detergent caused a shift toward shorter correlation times, indicating that smaller structures than the initial vesicles ($R_h = 100$ nm) were present. At an excess larger than 45-fold, a bimodal size distribution was clearly detected, going along with a largely reduced fraction of scattering intensity caused by the liposomes. Due to the addition of Triton X-100, the liposomes were dissolved and the DPPC molecules were solubilized by the detergent to form aggregates of compound-micellar size ($R_h \sim 50$ nm).³⁷ At even higher contents of Triton X-100 (>50 equiv), the vesicles were dissolved completely and the ACF was primarily determined by the lipid/detergent mixed micelles and pure detergent micelles due to their high concentration.

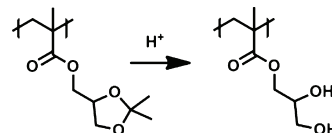
Figure 2b shows the analogue experiment when vesicles formed from P3 ($M_n = 12200$ g/mol) were employed. Up to a 150-fold detergent excess, which had entirely dissolved the lipid vesicles, no effect on the ACF was detected at all. Only when the ratio reached 200 equiv, a pronounced shift toward structures of $R_h = 85$ nm did occur. After addition of another 50 equiv, a sudden shift toward much smaller structures ($R_h < 20$ nm) was detected. Obviously, a more than 150-fold molar excess initially caused a shrinking of the vesicles, which had an original hydrodynamic radius of 100 nm. The radius was first decreased to 85 nm before the vesicles finally collapsed. These findings are in good agreement with the mechanism for

membrane solubilization of polymer vesicles postulated by Discher et al.³⁸ They state that above a certain threshold level (detergent-content in the membrane), the tension caused by the asymmetric packing of detergent molecules into the outer part of the membrane is released by the diffusion of the molecules toward the inner surface. This causes a detachment of polymer/detergent mixed micelles, followed by a complete disintegration when a second threshold value is reached. The observation that the polymer-based mixed micelles are smaller than DPPC/Triton X-100 mixed micelles can be attributed to the fact that the aggregation number in polymer/detergent mixed micelles is usually lower than in small molecule micelles.

Via this detergent-based assay, we could prove the superior stability of P(DHPMA)-based vesicles compared to liposomes.

On the other side, the release of cargo gets more difficult because of their increased stability. Thus, the controlled permeabilization of polymersomes—at the site of action—is a key issue to their application as drug carriers.^{4,39} Hence, to efficiently release the cargo, different ways to destabilize polymersomes have been developed.^{3,4,40–54} In order to destabilize P(DHPMA)-*b*-P(LMA) polymersomes, we chose an acid-degradable monomer since the conditions the polymer is subjected to during the polymer analogue conversion (aminolysis) are incompatible with many chemical moieties such as disulfides. As such a repeating unit, 2,2-dimethyl-1,3-dioxolan-4-yl)methyl methacrylate (DMDMA) has been investigated. The polymerization and hydrolysis of DMDMA has first been described by Beinert.⁵⁵ At acidic pH, the ketal structure is cleaved (Scheme 2), leading to the deprotection of the hydroxyl groups and a significant increase in hydrophilicity.

Scheme 2. Hydrolysis of P(DMDMA)



This mechanism has recently been exploited by Zhang and Louge for the acid-induced degradation of micelles, employing the respective acrylate as a comonomer.^{33,34} Based on their work, we developed a modified version of DMDMA which has been adapted to the alkaline environment of the polymer-analogue PFP-conversion. Due to the electronegative oxygen atom in direct proximity to the α -carbon of the ester, DMDMA is a moderately activated ester itself. Hence, the aminolysis of the DMDMA repeating units can occur as a side reaction. To circumvent this problem, we have synthesized 2-(2,2-dimethyl-1,3-dioxolane-4-yl)ethyl methacrylate (DDEMA) as a variant of the DMDMA monomer, extended by an additional methylene group (Figure 3).

The synthesis of an amphiphilic block copolymer P4, containing DDEMA as a pH-responsive repeating unit was achieved using the same RAFT chain transfer agent and reaction conditions analogue to the synthesis of P1–P3 (Scheme 3).

Starting from a mixture of LMA and DDEMA at a molar ratio of 7:3, the statistical copolymer SC (Table 1) was obtained at a mean degree of polymerization $X_n = 22$ and a DDEMA content of 27%. SC was then used as a macro chain transfer agent in the block copolymerization of PFPMA to yield the P(PFPMA)-*b*-P(LMA-*stat*-DDEMA) block copolymer BS.

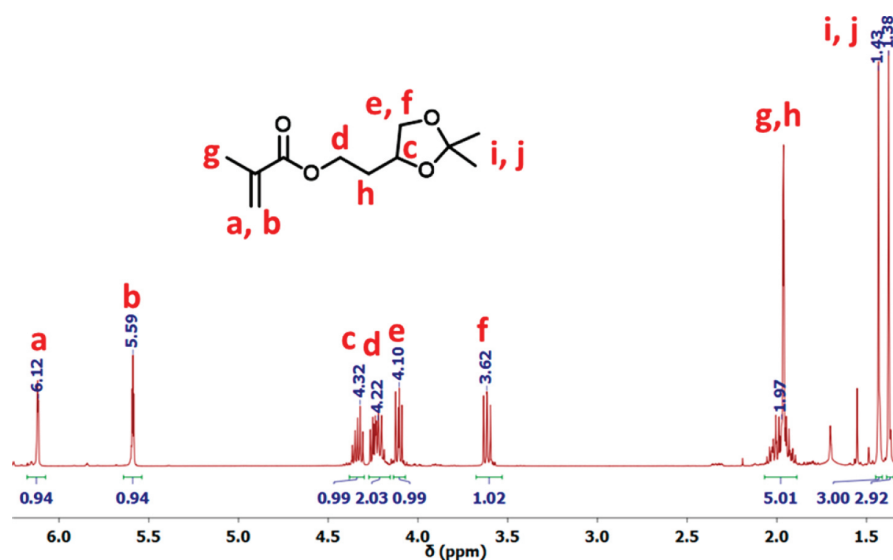


Figure 3. ^1H NMR spectrum of DDEMA (CDCl_3 , 400 MHz).

Scheme 3. Synthesis of the DDEMA-Modified Block Copolymer P4

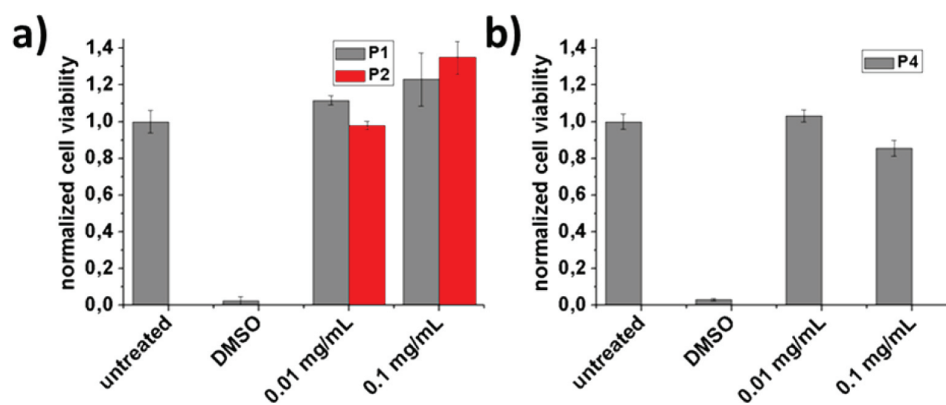
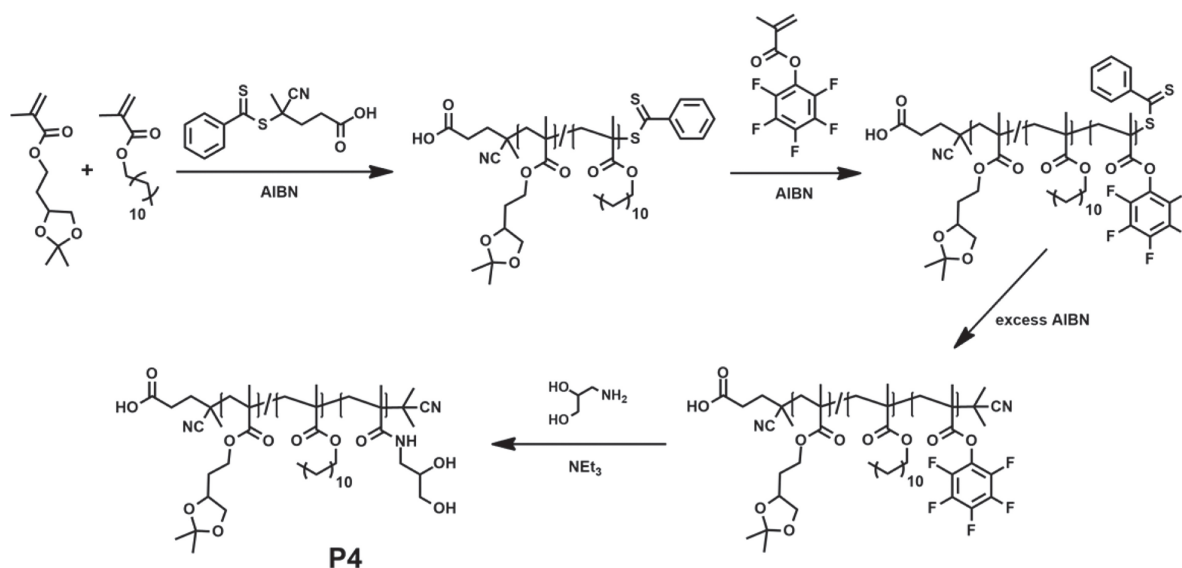


Figure 4. MTT Assay: (a) P(DHPMA)-*b*-P(LMA) vesicles (P1: gray, P2: red; $n = 6$), (b) P(DHPMA)-*b*-P(LMA-*stat*-DDEMA) vesicles (P4; $n = 3$).

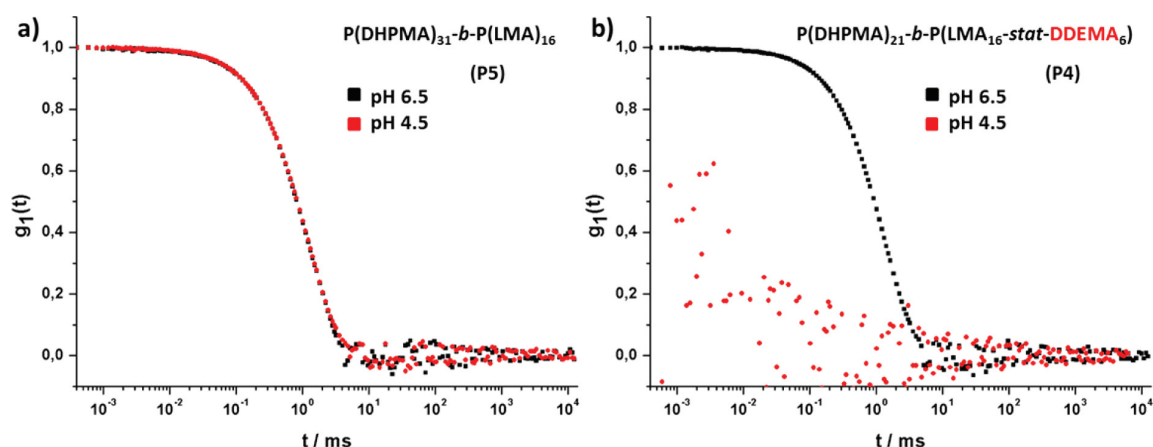


Figure 5. Examination of the influence of lowered pH on vesicles from P4 and P5 (a) ACF of unmodified vesicles from P5 at pH 6.5 (black) and pH 4.5 (red) (b) ACF of DDEMA-modified vesicles from P4 at pH 6.5 (black) and pH 4.5 (red). Scattering angle: $\alpha = 90^\circ$.

After the substitution of the dithiobenzoate group with AIBN, the PFP activated ester groups were converted to DHPMA via the aminolysis with DHPA. The amphiphilic block copolymer P(DHPMA)₂₁-*b*-P(LMA₁₆-*stat*-DDEMA₆) (P4, Table 6) was yielded, exhibiting a molecular weight of $M_n = 8800$ g/mol with a hydrophilic weight fraction of 34.8%. The ability of this polymer to form vesicles was confirmed by cryogenic transmission electron microscopy (Figure 1c). The vesicles formed via the solvent switching method exhibited a hydrodynamic radius of $R_h = 105$ nm ($\mu_2 = 0.11$), while they were significantly smaller and exhibited a broader size distribution ($R_h = 84$ nm; $\mu_2 = 0.16$) when prepared via dual centrifugation.

Previous toxicity studies revealed that P(DHPMA) has a very low effect on cell viability,¹⁷ comparable to P(HPMA), which is generally considered as nontoxic.^{56–58} Based on these experiments, we assessed the cytotoxicity of vesicles formed from P(DHPMA)-*b*-P(LMA) block copolymers P1 and P2 and the pH-degradable P4 via an MTT assay using HEK293T cells. In this assay, the metabolic activity of the cells was monitored via the conversion of the yellow tetrazole 3-(4,5-dimethylthiazol-2-yl)-2,5-diphenyltetrazolium bromide (MTT) to its purple formazan which was quantified photometrically and interpreted as a measure of cell viability and therefore cytotoxicity.

The cells were incubated together with different concentrations of vesicles formed from P1, P2, and P4 for 24 h before the absorption was measured. The results are displayed in Figure 4, together with the untreated reference (pure PBS) and the toxic solvent DMSO as controls. The polymers were tested at concentration ranges relevant in drug delivery studies (0.01–0.1 mg/mL). High cell viabilities >0.8 were observed and therefore no cytotoxic effects did occur. The differences between the three polymers were marginal and within the standard deviation of the measured data determined from hexaplicates. As was to be expected from the low effect of P(DHPMA) homopolymers on cell viability, vesicles from P(DHPMA)-*b*-P(LMA) and the pH degradable copolymer P4 also demonstrate a very low cytotoxicity. This is due to the high hydrophilicity of the DHPMA repeating units, which creates a strongly bound hydration shell, effectively restraining the interaction of the vesicles with their surrounding media. Hence, P(DHPMA)-based polymersomes are well-suited nanosized drug carriers in this regard.

The details of the disintegration of vesicles from the pH-responsive polymer P4 were studied by DLS. The vesicles were

prepared in a 5 mM NaCl dispersion and extruded through a 200 nm polycarbonate membrane to yield a uniform hydrodynamic radius of $R_h = 100$ nm. Vesicles from the DDEMA-free polymer P5, which has a molecular weight very similar to P4 (M_n (P4) = 8800 g/mol; M_n (P5) = 8900 g/mol) served as a reference sample. The vesicle dispersions were aliquoted and the pH was adjusted to pH 6.5 and pH 4.5. Before and after an incubation period of 48 h ($T = 37^\circ\text{C}$), the samples were examined via DLS.

The plots in Figure 5a show the experimentally obtained autocorrelation functions (ACF) of vesicles from the non-modified polymer P5. Upon lowering the pH to 4.5, the ACF did not change during the incubation period of 48 h and remained entirely congruent with the data at pH 6.5. The decreased pH did not have any effect on the vesicles. The initial ACF of the vesicles from the DDEMA-modified polymer P4, too, was found to be nearly congruent with the sample from P5, as was to be expected due to the extrusion process (Figure 5b). However, after 48 h of incubation, a dramatic decline in scattering intensity was observed ($I_{\text{pH } 6.5} = 85.4$ kHz vs $I_{\text{pH } 4.5} = 1.2$ kHz at scattering angle $\alpha = 90^\circ$) and an ACF could no longer be determined.

This observation is the result of a vesicle disintegration caused by the hydrolysis of the ketal structures, which leads to a deprotection of the hydroxyl groups and makes the DDEMA repeating unit highly hydrophilic. Given its molar ratio in the formerly hydrophobic block of the polymer of approximately 30%, a complete hydrolyzation of the ketal structures leads to an increase in the overall hydrophobic weight fraction f from $f = 0.348$ to $f > 0.5$. Accordingly, the membrane collapses due to the hydrophilic/hydrophobic imbalance as result of molecular solvation of the individual polymer chains. This can be concluded, because supramolecular structures of a higher aggregation number such as micelles would have been detected due to their significantly higher scattering intensity. In contrast, due to the molecular solvation, the scattering intensity was too low to examine an ACF, even though the total number of polymer molecules remained unchanged.

To study the vesicle disintegration in more detail, we conducted a kinetic study and investigated the decrease of scattering intensity in more detail. These studies were conducted at a scattering angle of $\alpha = 50^\circ$ and at a higher laser power leading to a higher overall scattering intensity ($I_{\text{P4}, T=0} = 392.7$ kHz) in order to detect potential aggregates

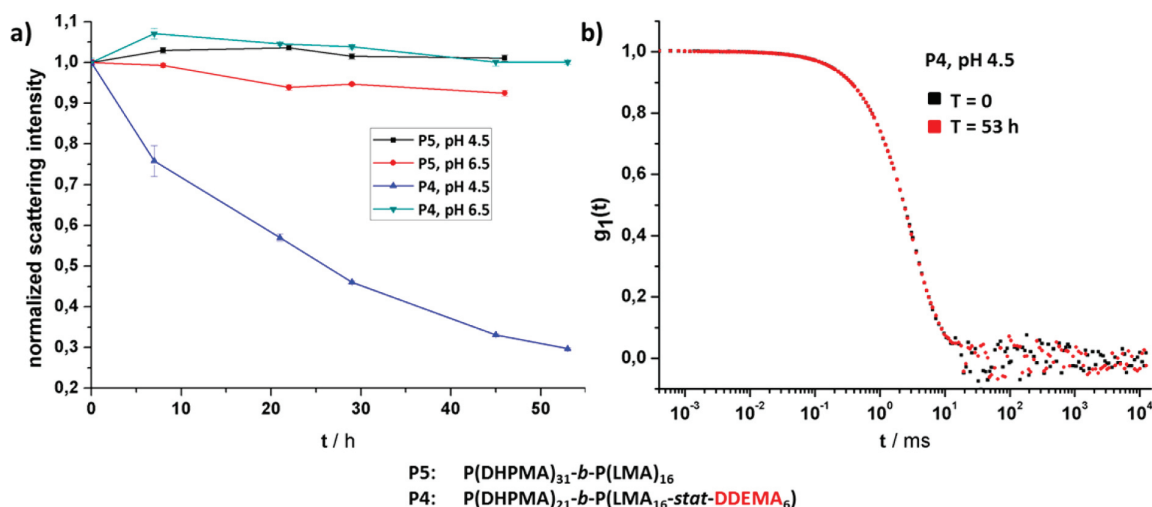


Figure 6. Kinetic studies of the vesicle disintegration by DLS. (a) time-dependent observation of the scattering intensities of polymersomes from P4 (with acid-labile modification) and P5 (not acid degradable, no DDEMA). (b) ACF of P4 polymersomes after sample preparation ($T = 0$) and after 53 h of incubation at 37 °C. Scattering angle: $\alpha = 50^\circ$.

different from the original vesicles more accurately. We used again polymersomes from the DDEMA-modified acid-labile polymer P4 and the nonmodified P5 as a control (Figure 6a). During a 53 h period of incubation at 37 °C, no significant changes in scattering intensity were detected both for P5 (pH 6.5 and pH 4.5) and for P4 at pH 6.5. In contrast, P4 showed a constant decrease in scattering intensity at pH 6.5 down to <30% of the initial value, as shown in Figure 6a. However, in this more sensitive experimental setup, we could detect an ACF for the whole time period (see Figure 6b). This ACF remained perfectly unchanged, which gives proof that the polymersomes remained intact until their complete solvation.

In summary, the aim to functionalize the hydrophobic domain of the P(DHPMA)-*b*-P(LMA) block copolymers with an acid-labile structure was reached by the copolymerization of LMA with DDEMA. The vesicles assembled from this polymer could be disintegrated at pH 4.5 due to the hydrolysis of the ketal structure, while nonfunctionalized vesicles from a polymer of similar molecular weight remained intact. This is an important result regarding the applicability of the polymer vesicles as drug carriers since the cargo release is substantially facilitated.

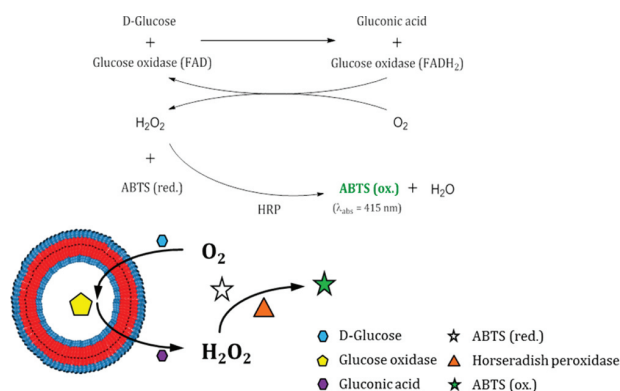
Next, the ability of these vesicles to safely encapsulate large molecules was compared to lipid vesicles formed from low molecular weight DPPC. As a model substance, Glucose oxidase (GOx) was used. The setup of this assay was based on the quantification of glucose as applied to determine the blood glucose level.

The corresponding mechanism is shown in Scheme 4.

GOx was encapsulated into vesicles from P4 by dual centrifugation and GOx-loaded liposomes from DPPC served as a control. Then the reaction kinetics of the conversion of D-glucose by equal amounts of GOx encapsulated into polymersomes and liposomes as well as free GOx were studied (Figure 7). Concentrations were assessed via the encapsulation efficiency of Alexa Fluor 647 as a model substance.

In the case of free GOx, a rapid linear increase in absorption was detected as was to be expected since the accessibility of the nonencapsulated enzyme by the glucose substrate was not hindered by any means. The encapsulation of GOx with DPPC

Scheme 4. Principle of the Glucose Oxidase Assay



^aD-Glucose is oxidized to Gluconic Acid under the catalytic influence of GOx. The generated hydrogen peroxide then converts a colorless redox indicator (ABTS) into its green oxidized species which allows the quantification of the reaction process.

led to a slower increase, with time. Here, the reaction kinetic is limited by the diffusion of glucose through the lipid bilayer. However, the encapsulation of GOx in the aqueous interior of the polymersomes lead to an enormous decrease of the oxidation rate of the redox indicator. It took around 24 h with polymersomes as GOx-carriers to reach a degree of absorption that was observed after only 30 min in the case of lipid vesicles. Additionally, a slightly declining slope was observed after 20 h. This demonstrates the tightness of the polymer membrane against both glucose (the substrate) and the enzyme GOx. After 25 h, the polymer vesicles were dissolved by the addition of an excess amount of the detergent Triton X-100, which resulted in an abrupt increase in absorption, comparable to the free GOx. This observation confirms the still perfectly functional catalytic activity of the enzyme as well as the presence of significant amounts of glucose even after the flattening of the absorption curve. Hence, the decay in reaction kinetics is due to the extremely low permeability of the polymersome membrane at moderate osmotic differences.

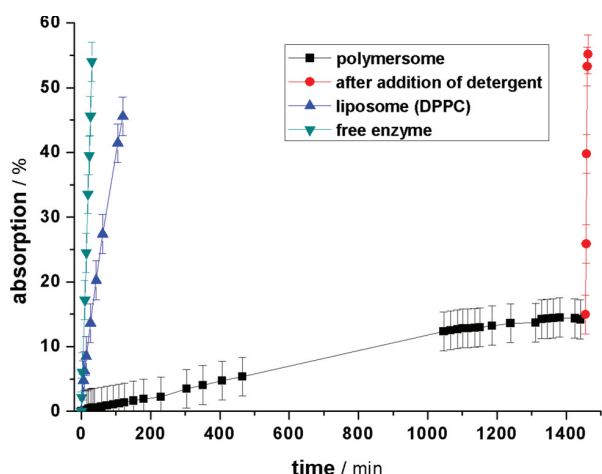


Figure 7. Quantification of the absorption ($\lambda_{\text{abs}} = 415 \text{ nm}$) of GOx-containing glucose solutions. Black: GOx-loaded polymersomes (P4). Red: GOx-loaded polymersomes (P4) after addition of Triton X-100 (6800 equiv). Blue: GOx-loaded DPPC vesicles. Green: free GOx.

The observations made in this experiment are of high importance for the loading of activated ester-based polymer vesicles and their application as drug carriers. Beyond the proof of the superior stability and lower permeability of polymersomes (compared to liposomes), the feasibility of the vesicle loading with high molecular weight cargo via the dual centrifugation process is proven as well as the separation of the free (nonencapsulated) protein. If the nonencapsulated fraction of GOx had not been completely removed by the size exclusion chromatography process or otherwise if the GOx had lost its catalytic activity due to the shear forces in centrifugation, a much stronger initial increase in absorption would have been observed or no increase in absorption would have appeared, respectively.

Regarding active targeting, we examined the influence of mannose ligands on the particle uptake by dendritic cells. For this purpose we linked the mannose derivative $\text{H}_2\text{N-Man}$ (Scheme 1) to the polymers P5M and P6M via activated ester chemistry during the conversion of their precursors BC3 and BC4 with DHPA. In terms of cytotoxicity, it is important that micellar structures with a P(HPMA) corona and the same mannose ligand have shown no cytotoxicity.²⁶ Their non-mannosylated equivalents P5 and P6 were synthesized from the same precursors in order to obtain identical properties apart from the mannosylation. The mannose content was quantified via ^{13}C inverse gated NMR spectroscopy as shown in Figure 8 for polymer P6M.

Degrees of mannosylation of 2.2% (P5M) and 4.3% (P6M) were obtained. We investigated whether the mannosylation of the polymers did enhance the uptake into bone marrow-derived dendritic cells, which present the mannose receptor (DC206) on their surface. This receptor induces a clathrin-dependent endocytosis mechanism that leads to an increased particle uptake. The investigations were conducted using vesicles that were extruded to yield a homogeneous size of $R_h = 100 \text{ nm}$ to exclude the influence of size effects on the internalization.

First, the relative uptake of vesicles from P5/P6 and P5M and P6M was investigated by FACS at a total polymer concentration of $3 \mu\text{g/mL}$ (Figure 9). In this context, it should be mentioned that the binding of nonmannosylated polymersomes was rather low, although this was not quantified. This corresponds to little unspecific uptake (see also ref 26). Next, the relative uptake of vesicles from P5M (degree of mannosylation: 2.2%) and P5 was compared (Figure 9, left). No significant difference between the uptake of mannosylated and nonmannosylated polymersomes was observed here.

However, in the case of the higher degree of mannosylation (P6M/P6), a different result was obtained (Figure 9, right). The mean fluorescence intensity (MFI) of vesicles from P6M showed almost six times the value recorded for P6, corresponding to a much more pronounced particle uptake.

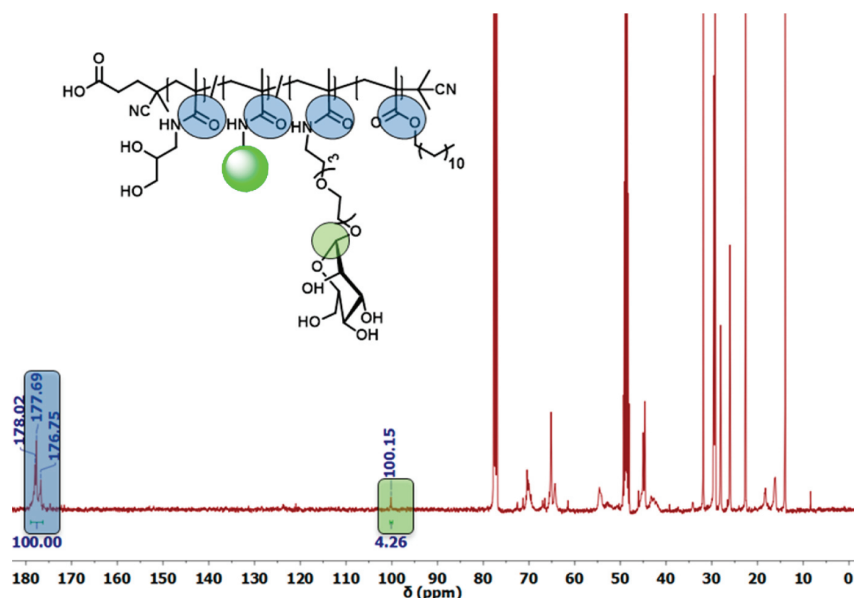


Figure 8. Determination of the mannose content of P6M by ^{13}C inverse gated NMR spectroscopy ($\text{DMSO-}d_6$, 100 MHz). The integral of the mannose C_1 atom was referenced to the total integral of the backbone carbonyl atoms.

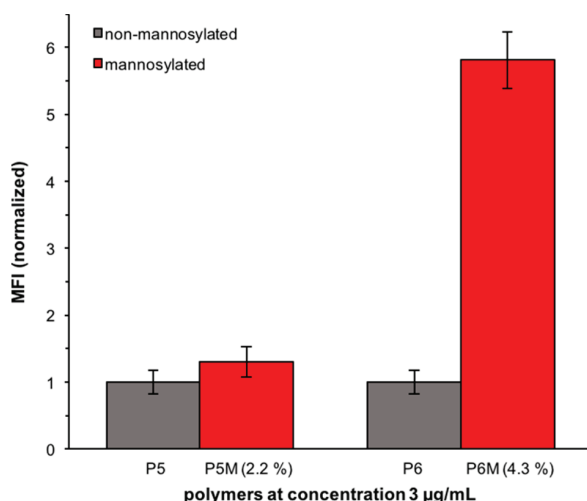


Figure 9. Quantification of the relative uptake of mannosylated (red) and nonmannosylated (gray) polymersomes (incubation time 24 h; $n = 2$). Left: P5/P5M (degree of mannosylation: 2.2%). Right: P6/P6M (degree of mannosylation: 4.3%).

Because of the equal vesicle size and the identical chain length of the hydrophilic domains, which are presented toward the environment, the different uptake behavior can only be caused by the mannosylation. This means that mannose induces binding, but a certain minimum amount is required.

P6M, e.g., exhibits a mannose content of 4.3% (per total repeating units), which corresponds to 8.0% of the hydrophilic repeating units. Hence, about any 12th former PFP ester carries a sugar moiety. This means that on average, 2.7 mannose units are linked to every polymer chain (see the block lengths given in Table 6). By contrast, P5M with the smaller degree of substitution (and the smaller molecular weight) only carries about one mannose unit per hydrophilic block. Hence, in the case of vesicles from P6M, there is a much higher probability for mannose receptor interaction due to multivalent presentation.

CONCLUSIONS

In previous studies, we presented a concept to form polymersomes from readily functionalizable pentafluorophenyl ester-based precursor polymers. Via the aminolysis of this activated ester, amphiphilic polymers are obtained that can be versatilely functionalized and form vesicles at suitable block ratios and preparation conditions. These polymers exhibited low cytotoxicity, and the respective vesicles did not show protein adsorption-induced aggregation in human blood serum.¹⁷

Since polymersome membranes exhibit higher stability and extremely low permeabilities compared to lipid-based membranes, as was demonstrated by a detergent-based and a glucose oxidase assay, a stimuli-responsive unit needed to be introduced that was compatible with the conditions of RAFT polymerization and the polymer-analogue conversion under basic conditions. This issue was solved by the use of DDEMA, an acid-labile monomer that was derived from DMDMA. It could be introduced into the polymersome membrane by copolymerization into the hydrophobic domain of the amphiphilic polymer. The polymersomes formed by DDEMA-functionalized amphiphilic block copolymers proved to be nontoxic as confirmed by MTT assays. They could be degraded through

the hydrophilization of their membrane at pH 4.5 due to the hydrolysis of the ketal structure.

Furthermore, the enhancement of particle uptake by mannosylation of the polymersomes via activated ester chemistry was confirmed. An average degree of substitution of 2.7 mannose units per polymer chain was required for this effect to occur.

These results greatly improve the applicability of P(DHPMA)-based vesicles as nanosized drug carriers.

AUTHOR INFORMATION

Notes

The authors declare no competing financial interest.

ACKNOWLEDGMENTS

The authors would like to thank Prof. Dr. Manfred Schmidt for providing the light scattering equipment and Prof. Dr. Mark Helm for providing access to the dual centrifuge (DC). The dual centrifuge prototype used in this study was kindly provided by Andreas Hettich GmbH, Tuttlingen (Germany). Support by the SFB 1066 is gratefully acknowledged.

REFERENCES

- (1) Meier, W. *Chem. Soc. Rev.* **2000**, *29* (5), 295–303.
- (2) Antonietti, M.; Förster, S. *Adv. Mater.* **2003**, *15* (16), 1323–1333.
- (3) Meng, F.; Zhong, Z.; Feijen, J. *Biomacromolecules* **2009**, *10* (2), 197–209.
- (4) Li, M.-H.; Keller, P. *Soft Matter* **2009**, *5* (5), 927.
- (5) Brinkhuis, R. P.; Rutjes, F. P. J. T.; van Hest, J. C. M. *Polym. Chem.* **2011**, *2* (7), 1449.
- (6) Gaitzsch, J.; Appelhans, D.; Wang, L.; Battaglia, G.; Voit, B. *Angew. Chem., Int. Ed.* **2012**, *51* (18), 4448–4451.
- (7) Palivan, C. G.; Goers, R.; Najer, A.; Zhang, X.; Car, A.; Meier, W. *Chem. Soc. Rev.* **2016**, *45*, 377.
- (8) Discher, D. E.; Ahmed, F. *Annu. Rev. Biomed. Eng.* **2006**, *8* (1), 323–341.
- (9) Bermudez, H.; Brannan, A. K.; Hammer, D. A.; Bates, F. S.; Discher, D. E. *Macromolecules* **2002**, *35*, 8203–8208.
- (10) Wilkins, D. J.; Myers, P. A. *Br. J. Exp. Pathol.* **1966**, *47*, 568–576.
- (11) Schwendener, R. A.; Lagocki, P. A.; Rahman, Y. E. *Biochim. Biophys. Acta, Biomembr.* **1984**, *772* (1), 93–101.
- (12) Tabata, Y.; Ikada, Y. *Biomaterials* **1988**, *9* (4), 356–362.
- (13) Owens, D. E.; Peppas, N. A. *Int. J. Pharm.* **2006**, *307* (1), 93–102.
- (14) Knop, K.; Hoogenboom, R.; Fischer, D.; Schubert, U. S. *Angew. Chem., Int. Ed.* **2010**, *49* (36), 6288–6308.
- (15) Harris, J. M.; Cess, R. B. *Nat. Rev. Drug Discovery* **2003**, *2*, 214–221.
- (16) Barz, M.; Luxenhofer, R.; Zentel, R.; Vicent, M. J. *Polym. Chem.* **2011**, *2* (9), 1900–1918.
- (17) Scherer, M.; Fischer, K.; Depoix, F.; Fritz, T.; Thiermann, R.; Mohr, K.; Zentel, R. *Macromol. Rapid Commun.* **2016**, *37* (1), 60–66.
- (18) Kelsch, A.; Tomcin, S.; Rausch, K.; Barz, M.; Mailander, V.; Schmidt, M.; Landfester, K.; Zentel, R. *Biomacromolecules* **2012**, *13*, 4179.
- (19) Hemmelmann, M.; Knoth, C.; Schmitt, U.; Allmeroth, M.; Moderegger, D.; Barz, M.; Koynov, K.; Hiemke, C.; Rösch, F.; Zentel, R. *Macromol. Rapid Commun.* **2011**, *32* (9–10), 712–717.
- (20) Gauthier, M.; Gibson, M.; Klok, H.-A. *Angew. Chem., Int. Ed.* **2009**, *48* (1), 48–58.
- (21) Tappertzhofen, K.; Bednarczyk, M.; Koynov, K.; Bros, M.; Grabbe, S.; Zentel, R. *Macromol. Biosci.* **2014**, *14* (10), 1444–1457.
- (22) Tappertzhofen, K.; Weiser, F.; Montermann, E.; Reske-Kunz, A.; Bros, M.; Zentel, R. *Macromol. Biosci.* **2015**, *15*, 1159–1173.

- (23) Nuhn, L.; Braun, L.; Overhoff, I.; Kelsch, A.; Schaeffel, D.; Koynov, K.; Zentel, R. *Macromol. Rapid Commun.* **2014**, *35* (24), 2057–2064.
- (24) Nuhn, L.; Barz, M.; Zentel, R. *Macromol. Biosci.* **2014**, *14* (5), 607–618.
- (25) Massing, U.; Cicko, S.; Ziroli, V. J. *Controlled Release* **2008**, *125* (1), 16–24.
- (26) Mohr, N.; Kappel, C.; Kramer, S.; Bros, M.; Grabbe, S.; Zentel, R. *Nanomedicine* **2016**, DOI: [10.2217/nnm-2016-0167](https://doi.org/10.2217/nnm-2016-0167).
- (27) Matsumura, Y.; Maeda, H. *Cancer Res.* **1986**, *46*, 6387–6392.
- (28) Moghimi, S. M.; Hunter, A. C.; Murray, J. C. *Pharmacol. Rev.* **2001**, *53* (2), 283–318.
- (29) Eberhardt, M.; Mruk, R.; Zentel, R.; Théato, P. *Eur. Polym. J.* **2005**, *41* (7), 1569–1575.
- (30) Mohr, N. *Glykopolymere für Biomedizinische Anwendungen: Synthese von mannosylierten N-(2-Hydroxypropyl)methacrylamid Polymersystemen für die Adressierung von Zellen des Immunsystems*; Johannes Gutenberg University: Mainz, Germany, 2015.
- (31) Barz, M.; Tarantola, M.; Fischer, K.; Schmidt, M.; Luxenhofer, R.; Janshoff, A.; Theato, P.; Zentel, R. *Biomacromolecules* **2008**, *9* (11), 3114–3118.
- (32) Perrier, S.; Takolpuckdee, P.; Mars, C. a. *Macromolecules* **2005**, *38* (6), 2033–2036.
- (33) Zhang, D.; Zhang, H.; Nie, J.; Yang, J. *Polym. Int.* **2010**, *59* (7), 967–974.
- (34) Louage, B.; Zhang, Q.; Vanparijs, N.; Voorhaar, L.; Vande Castele, S.; Hennink, W. E.; Van Bocxlaer, J.; Hoogenboom, R.; De Geest, B. G. *Biomacromolecules* **2015**, *16*, 336.
- (35) Eberhardt, M.; Théato, P. *Macromol. Rapid Commun.* **2005**, *26* (18), 1488–1493.
- (36) Kalyanasundaram, J. K.; Thomas, K. *J. Am. Chem. Soc.* **1977**, *99*, 2039–2044.
- (37) Mattei, B.; França, A. D. C.; Riske, K. A. *Langmuir* **2015**, *31*, 378–386.
- (38) Pata, V.; Ahmed, F.; Discher, D. E.; Dan, N. *Langmuir* **2004**, *20* (10), 3888–3893.
- (39) Le Meins, J.-F.; Sandre, O.; Lecommandoux, S. *Eur. Phys. J. E: Soft Matter Biol. Phys.* **2011**, *34* (2), 1–17.
- (40) Napoli, A.; Valentini, M.; Tirelli, N.; Müller, M.; Hubbell, J. A. *Nat. Mater.* **2004**, *3*, 183–189.
- (41) Lomas, H.; Canton, I.; MacNeil, S.; Du, J.; Armes, S. P.; Ryan, A. J.; Lewis, A. L.; Battaglia, G. *Adv. Mater.* **2007**, *19* (23), 4238–4243.
- (42) Onaca, O.; Enea, R.; Hughes, D. W.; Meier, W. *Macromol. Biosci.* **2009**, *9* (2), 129–139.
- (43) Chécot, F.; Lecommandoux, S.; Klok, H.-A.; Gnanou, Y. *Eur. Phys. J. E: Soft Matter Biol. Phys.* **2003**, *10* (1), 25–35.
- (44) Cerritelli, S.; Velluto, D.; Hubbell, J. A. *Biomacromolecules* **2007**, *8* (6), 1966–1972.
- (45) Meng, F.; Hiemstra, C.; Engbers, G. H. M.; Feijen, J. *Macromolecules* **2003**, *36* (9), 3004–3006.
- (46) Ghoroghchian, P. P.; Li, G.; Levine, D. H.; Davis, K. P.; Bates, F. S.; Hammer, D. A.; Therien, M. J. *Macromolecules* **2006**, *39* (5), 1673–1675.
- (47) Hales, M.; Barner-Kowollik, C.; Davis, T. P.; Stenzel, M. H. *Langmuir* **2004**, *20* (25), 10809–10817.
- (48) Rodriguez, A. R.; Kramer, J. R.; Deming, T. J. *Biomacromolecules* **2013**, *14* (10), 3610–3614.
- (49) Qin, S. H.; Geng, Y.; Discher, D. E.; Yang, S. *Adv. Mater.* **2006**, *18*, 2905–2909.
- (50) Tong, X.; Wang, G.; Soldera, A.; Zhao, Y. *J. Phys. Chem. B* **2005**, *109* (43), 20281–20287.
- (51) Zhou, W.; Meng, F.; Engbers, G. H. M.; Feijen, J. *J. Controlled Release* **2006**, *116* (2), 62–64.
- (52) Wang, X.; Liu, G.; Hu, J.; Zhang, G.; Liu, S. *Angew. Chem., Int. Ed.* **2014**, *53* (12), 3138–3142.
- (53) Wang, X.; Hu, J.; Liu, G.; Tian, J.; Wang, H.; Gong, M.; Liu, S. *J. Am. Chem. Soc.* **2015**, *137* (48), 15262–15275.
- (54) Wang, L.; Liu, G.; Wang, X.; Hu, J.; Zhang, G.; Liu, S. *Macromolecules* **2015**, *48* (19), 7262–7272.
- (55) Beinert, G.; Hild, G.; Rempp, P. *Makromol. Chem.* **1974**, *175*, 2069.
- (56) Lammers, T.; Ulbrich, K. *Adv. Drug Delivery Rev.* **2010**, *62* (2), 119–121.
- (57) Říhová, B.; Kovář, M. *Adv. Drug Delivery Rev.* **2010**, *62* (2), 184–191.
- (58) Kopeček, J.; Kopecková, P. *Adv. Drug Delivery Rev.* **2010**, *62* (2), 122–149.

5.4 Publication 4

PeptoSomes for Vaccination: Combining Antigen and Adjuvant in Polypept(o)ide-Based Polymersomes

Published in: *Macromolecular Bioscience*, 2017, doi: 10.1002/mabi.201700061

Reprinted (adapted) with permission from (Weber, B. *et al.* PeptoSomes for Vaccination: Combining Antigen and Adjuvant in Polypept(o)ide-Based Polymersomes. *Macromol. Biosci.* **17**, 1700061 (2017)). Copyright (2017) John Wiley and Sons.

PeptoSomes for Vaccination: Combining Antigen and Adjuvant in Polypept(o)ide-Based Polymersomes

Benjamin Weber, Cinja Kappel, Martin Scherer, Mark Helm, Matthias Bros, Stephan Grabbe, and Matthias Barz*

In this work, the first vaccine is reported based on a PeptoSome, which contains a model antigen (SIINFEKL) and adjuvant (CpG). PeptoSomes are polypept(o)ide-based polymersomes built of a block-copolymer with poly-sarcosine (PSar) as the hydrophilic block ($X_n = 111$) and poly(benzyl-glutamic acid) (PGlu(OBn)) as the hydrophobic one ($X_n = 46$). The polypept(o)ide is obtained with low dispersity index of 1.32 by controlled ring-opening polymerization. Vesicle formation by dual centrifugation technique allows for loading of vesicles up to 40 mol%. PeptoSomes are characterized by multi-angle dynamic light scattering, static light scattering, and cryogenic transmission electron microscopy (cryoTEM). The PeptoSomes have a hydrodynamic radius of 39.2 nm with a low dispersity ($\mu_2 = 0.1$). The ρ -ratio R_g/R_h of 0.95 already indicates that vesicles are formed, which can be confirmed by cryoTEM. Loaded PeptoSomes deliver the antigen (SIINFEKL) and an adjuvant (CpG) simultaneously into dendritic cells (DCs). Upon cellular uptake, dendritic cells are stimulated and activated, which leads to expression of cluster of differentiation CD80, CD86, and MHCII, but induces excretion of proinflammatory cytokines (e.g., TNF α). Furthermore, DC-mediated antigen-specific T-cell proliferation is achieved, thus underlining the enormous potential of PeptoSomes as a versatile platform for vaccination.

vaccines bearing the antigen but lacking the adjuvant can easily induce immune tolerance. Thus, the coadministration of adjuvants and antigen is necessary to achieve protective immunity.^[2-4] Among established adjuvants, CpG-rich oligonucleotides address the toll-like receptor 9 (TLR9), which is expressed in endosomal compartments of dendritic cells (DCs). The fact that it is of crucial importance for effective vaccination, that antigen and adjuvant are codelivered into antigen presenting cells like DCs, creates a rationale for the use of nanoparticle-based codelivery systems.^[5,6] In agreement, Laing et al. showed that vaccination is most efficient, when peptide antigen and TLR agonist are combined within liposomes.^[7] While liposomes are established systems for drug delivery and have already entered clinical practice, these systems possess low stability in complex biological fluids, which is critical for targeted delivery into specific cell populations. Stability can be enhanced and unspecific cell uptake reduced by coformulation of lipopolymers, which can lead to stealth

1. Introduction

Most commonly, vaccines are produced from heat inactivated or live attenuated organisms. Therefore, these vaccines contain antigen and components that serve as adjuvants.^[1] Synthetic

liposomes.^[8,9] Nevertheless, lipopolymers in general possess higher critical micelle concentration (CMC) than amphiphilic block copolymers, which already indicates that the stability of liposomes is limited.^[10] In addition, free amphiphilic lipopolymers can cause immune responses, e.g., accelerated blood clearance, reducing circulation times even of stealth liposomes.^[11,12]


In contrast, polymersomes, which are polymer-based vesicles and thus structural counterparts to liposomes, provide higher stability.^[13] Polymersomes tend to form when the hydrophilic weight fraction of the block copolymer is about 35% (± 10), while micelles form at a hydrophilic weight fraction >45 .^[14] Therefore, amphiphilic block copolymers intrinsically possess a lower CMC, which explains the enhanced stability of polymersomes compared to liposomes or even micelles enabling a plethora of in vivo applications.^[14,15]

In contrast to micelles, polymersomes can be loaded with both hydrophobic drugs as well as hydrophilic molecules, e.g. oligonucleotides.^[13,16] In this respect, the aqueous core enables encapsulation of hydrophilic components while the hydrophobic part of the shell provides a compartment for hydrophobic drugs. Due to this versatility, polymersomes have been widely used in drug delivery.^[17] Lecommandoux and

B. Weber, Dr. M. Scherer, Dr. M. Barz
Institute of Organic Chemistry
Johannes Gutenberg-University Mainz
Duesbergweg 10-14, 55128 Mainz, Germany
E-mail: barz@uni-mainz.de

C. Kappel, Dr. M. Bros, Prof. S. Grabbe
Department of Dermatology
University Medical Center
Johannes Gutenberg-University Mainz
Obere Zahlbacher Straße 63, 55131 Mainz, Germany

Prof. M. Helm
Department of Pharmacy and Biochemistry
Johannes Gutenberg-Universität Mainz
Staudinger Weg 5, 55128 Mainz, Germany

 The ORCID identification number(s) for the author(s) of this article can be found under <https://doi.org/10.1002/mabi.201700061>.

DOI: 10.1002/mabi.201700061

co-workers, for example, introduced different peptide-based polymersomes for cancer therapy.^[18] On the one hand, they used poly(γ -benzyl-L-glutamate-*b*-hyaluronan (PGlu(OBn)-*b*-HyA) for encapsulation of doxorubicine (DOX) to suppress DOX-related side effects and therefore enhance the therapeutic efficacy.^[19] On the other hand, they prepared glycopeptide-based polymersomes by ring-opening polymerization and postpolymerization functionalization via click reaction.^[20] Polypeptoid-based polymersomes have been investigated by Luxenhofer and co-workers.^[21–23] Polypeptide-based polymersomes have been first reported by Kimura and co-workers already in the late 1990s.^[24,25] They employed polysarcosine-*block*-poly(methyl glutamate) copolymers for tumor imaging with a near-infrared dye.^[26] The hydrophilic part, polysarcosine, possesses stealth properties and is used as an alternative for Poly(ethylene glycol) (PEG).^[27]

Polymersomes for vaccine delivery have been reported just recently. Quer et al. used a peptide-based polymersome as a carrier for the antigen influenza hemagglutinin. In this work, the polymersome enhances the immune response, acting as an adjuvant.^[28] Hubbel and co-workers have synthesized polymersomes from PEG-*b*-PPS (Poly(propylene sulfide)) and loaded them with antigen and adjuvant for inducing cell-mediated antigen-specific immune responses,^[29] and compared them to solid nanoparticles^[30] underlining the potential of polymersomes. Interestingly, the use of PeptoSomes (polymersomes from polypeptide-*block*-polypeptoid copolymers)^[31] has so far not been reported for vaccine delivery. In this work we introduce PeptoSomes as novel class of vaccines.

2. Experimental Section

2.1. Synthesis of the Polypept(o)ide

PGlu(OBn)₄₆-*b*-PSar₁₁₁ was synthesized as earlier reported.^[32,33] Chain lengths were adjusted to yield a polymer with a hydrophilic mass fraction of 44 wt%, so that the polymer assembles preferably into polymersomes and not into micelles.

2.2. Preparation of PeptoSomes

The procedure was adapted from literature and modified.^[34] 5.6 mg of the lyophilized polymer were weighed into 0.2 mL Eppendorf vials and incubated with 24 μ L of the aqueous phase (Phosphate buffered saline (PBS)-based solution of the cargo to be encapsulated) at room temperature overnight. 75 mg of ceramic beads ($\varnothing = 0.3$ – 0.4 mm) was added, and the samples were homogenized for 2×16 min in a Rotanda 400 centrifuge (Hettich/Tuttlingen) at a rotating velocity of 2500 rpm. Afterward, 36 μ L of further aqueous phase (PBS) were added and the samples were centrifuged for another 2×2 min. To remove not encapsulated cargo the product was purified via a sepharose column and the fractions were collected.

2.3. Dynamic Light Scattering (DLS)

A solution of the PeptoSome was prepared to yield a concentration of 0.1 mg mL⁻¹ in PBS. After transfer to a dust free flow

box, all samples were filtered (Millipore GHP 0.45 μ m) into dust free cylindrical scattering cells (Suprasil, 20 mm diameter, Hellma, Mühlheim, Germany). DLS measurements were performed using a Uniphase He/Ne Laser ($\lambda = 632.8$ nm, 22 mW), an ALV-SP125 Goniometer, an ALV/high quantum efficiency (QE) APD-avalanche photodiode with fiber optical detection, an ALV 5000/E/PCI-correlator and a Lauda RC-6 thermostat unit at 20 °C. Angular-dependent measurements of typically 15° steps were carried out in the range $30^\circ \leq q \leq 150^\circ$. For data evaluation experimental intensity correlation functions were transformed into amplitude correlation functions applying the Siegert relation extended to include negative values after baseline subtraction by calculation $g_1(t) = \text{SIGN}(G_2(t)) \cdot \text{SQRT}(\text{ABS}((G_2(t) - A)/A))$. All field correlation functions usually showed monomodal decay and were fitted by a sum of two exponentials $g_1(t) = a \cdot \exp(-t/b) + c \cdot \exp(-t/d)$ to take polydispersity into account. Average apparent diffusion coefficients D_{app} were calculated by applying $q^2 D_{\text{app}} = (a \cdot b^{-1} + c \cdot d^{-1}) / (a + c)$ resulting in an angular-dependent diffusion coefficient D_{app} or reciprocal hydrodynamic radius $\langle 1/R_h \rangle_{\text{app}}$, according to formal application of Stokes Einstein law. By extrapolation of $\langle 1/R_h \rangle_{\text{app}}$ to $q=0$ z-average hydrodynamic radii were obtained (uncorrected for c -dependency).

2.4. Static Light Scattering (SLS)

SLS measurements were performed with an ALV-SP86 goniometer, a Uniphase HeNe Laser (25 mW output power at $\lambda = 632.8$ nm wavelength) and ALV/high QE APD avalanche diode fiber optic detection system. The same solution as for DLS was used. The measured Kc/R values for every angle or q^2 were plotted in a Zimm plot and fitted by a linear function. The slope of the fit yielded the z-average of the squared radius of gyration $\langle R_g^2 \rangle_z$ (uncorrected for c -dependency) by applying the Zimm equation $\left(\frac{Kc}{R} = \frac{1}{M} \left(1 + \frac{1}{3} R_g^2 q^2 \right) \right)$.

2.5. Cryogenic Transmission Electron Microscopy (cryoTEM)

5 μ L of the PeptoSome solution (0.1 mg mL⁻¹, in PBS) were applied to freshly glow-discharged carbon grids with a copper 200 mesh (Quantifoil Micro Tools GmbH). Excess fluid was removed by direct blotting (2.5 s) and the grids were individually plunge-frozen in liquid ethane. Grids were cryotransferred in liquid nitrogen using a Gatan cryoholder (model 626 DH) to a Technai T12 transmission electron microscope equipped with a field emission electron source and operating at 120 kV accelerating voltage. Images were recorded using a TemCam-F416 (TVIPS, Gauting, Germany).

2.6. DC Culture and Treatment

Bone marrow cells (2×10^6 cells mL⁻¹) were resuspended in Iscove's Modified Dulbecco's Medium (IMDM) medium (Sigma-Aldrich), supplemented with 5% fetal calf serum (FCS), 2×10^{-3} M L-glutamine, 0.1×10^{-3} M nonessential amino acids,

50 $\mu\text{g mL}^{-1}$ gentamycin (all from PAA Laboratories, Pasing, Austria), 50×10^{-6} M β -mercaptoethanol (Sigma-Aldrich), and 10 ng mL^{-1} recombinant murine granulocyte-macrophage colony-stimulating factor (GM-CSF) (R&D, Wiesbaden, Germany) and were seeded (1 mL per well) into 12-well cell culture plates (BD, Franklin Lakes, NJ). Media were replenished on days 3 and 6 of culture. On days 7 or 8 of culture PeptoSomes and soluble reagents (SIINFEKL peptide, CpG oligodeoxynucleotide, ODN 1826) were applied at the indicated concentrations. On the next day, bone marrow derived dendritic cell (BMDC) was harvested, extensively washed, and subjected to experiments.

2.7. Flow Cytometry

For detection of surface marker expression, BMDC were washed in FACS buffer (PBS, 1% FCS, 0.5×10^{-3} M ethylenediaminetetraacetic acid (EDTA)) and incubated with Fc receptor blocking rat anti mouse CD16/CD32 antibody (clone 2.4G2). Afterward, antibodies specific for CD11c (clone N418; PE-Cy7-conjugated) and CD86 were applied (clone GL1, PE-conjugated) (all antibodies from eBioscience). Samples were analyzed using a BD FACS CANTO II flow cytometer equipped with DIVA software (BD Biosciences). Data were analyzed using FACS DIVA software (BD Biosciences). Cytokine contents of BMDC supernatants were quantified by Cytometric bead array following the manufacturer's instructions (BD Bioscience). Results were analyzed using cytometric bead array (CBA) Analysis Software (BD).

2.8. T-Cell Proliferation

BMDC (1.25×10^3) were cocultured with syngeneic ovalbumin (OVA) peptide-reactive OT-I T cells (each 5×10^4) in triplicates for 3 d. T-cell proliferation was assessed by detecting incorporation of ^3H -thymidine during the last 16 h of coculture as determined by liquid scintillation counting.

3. Results and Discussion

3.1. Synthesis of PeptoSomes

PGLu(OBn)-*b*-PSar copolymer was synthesized via controlled ring-opening polymerization as reported earlier.^[32] Degrees of polymerizations were adjusted to PGLu(OBn)₅₀-*b*-PSar₁₂₀, so

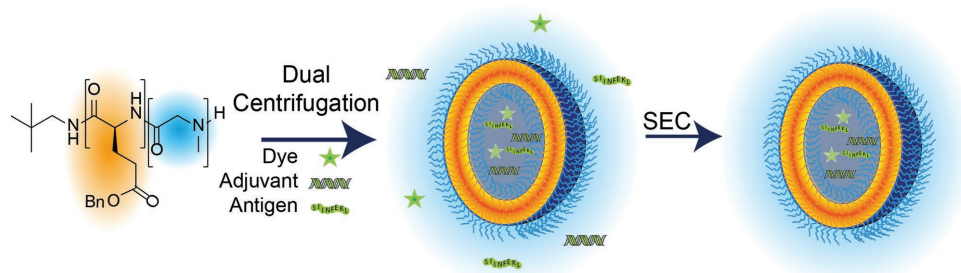
that the final polymer had a ratio of hydrophilic to hydrophobic block of around 44 wt% inducing presumable the formation of polymersomes instead of micelles. The Glu(OBn) N-carboxy anhydride (NCA) was dissolved in dimethylformamide (DMF) containing less than 50 ppm water and $1/n$ equivalents of neopentylamine were added. After full conversion was ensured via Fourier-transformed infrared (FTIR) spectroscopy, the sarcosine NCA (N-alkylated NCA) was added to the macroinitiator. After complete conversion of the NNCA, the polymer was precipitated in cold ether, centrifuged, and lyophilized. The obtained polymer was analyzed with ^1H -NMR, DOSY ^1H -NMR and hexafluoroisopropanol-size exclusion chromatography (HFIP-SEC) (see the Supporting Information). Chain lengths were determined by ^1H -NMR, indicating the formation of PGLu₄₆-*b*-PSar₁₁₁ copolymers.

Polymersomes were prepared by dual centrifugation (see Scheme 1), following the recently reported protocol by Scherer et al.^[16,34] Therefore, the lyophilized polymer was allowed to swell overnight in PBS, ceramic beads were added and the mixture was applied to dual centrifugation.

For the encapsulation of antigen (SIINFEKL) and adjuvant (CpG), solutions of both components were mixed with the polypept(o)ide and also applied to dual centrifugation (see Scheme 1). The gel-like product ($C \approx 100$ g L⁻¹) was diluted to ≈ 20 g L⁻¹ with PBS and purified by size exclusion chromatography (sepharose column) to remove any nonencapsulated components. The final loading efficiency was determined via UV-Vis spectroscopy according to Scherer et al.,^[16,34] assuming that antigen, adjuvant and dye (AF-647) are incorporated into the PeptoSomes in the same ratio as weighed in. The loading efficiencies varied from 35% (adjuvant, antigen, and dye) to 40% (dye only). In comparison to film hydration, the loading efficiencies achieved by dual centrifugation are five to ten times higher. In addition, polymersomes can be synthesized with high reproducibility in size and loading efficiency. Size variations are below 10% between different polymersome batches.

3.2. Physicochemical Characterization of PeptoSomes

PeptoSomes were characterized by multiangle DLS, SLS, and cryoTEM. The combination of DLS and SLS is particularly interesting for the verification of vesicular structures. While DLS measurements determine the hydrodynamic radius R_h , SLS yields the radius of gyration R_g . The ρ -ratio R_g/R_h is indicative for particle morphology. In the case of $\rho = 0.775$,



Scheme 1. Preparation of PeptoSomes and purification by dual centrifuging technique and size exclusion chromatography.

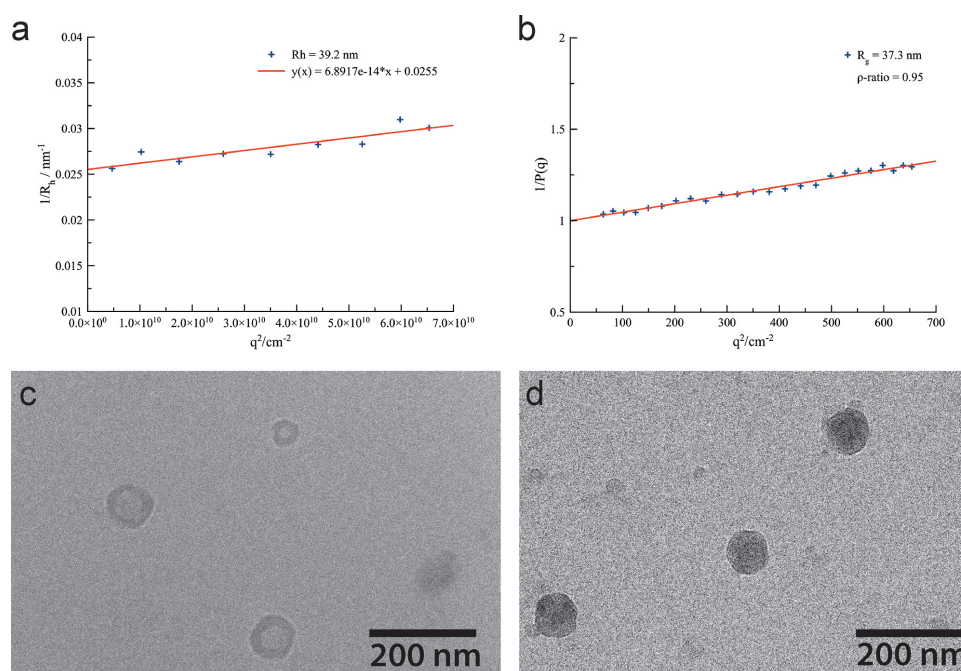


Figure 1. Characterization of the PeptoSomes: a) multiangle dynamic light scattering indicating an $R_h = 39.2$ nm; b) static light scattering experiments display an $R_g = 37.3$ nm yielding a ρ ratio $R_g/R_h = 0.95$; cryogenic TEM images of c) nonloaded and d) loaded PeptoSomes.

the particle is a homogeneous sphere (micellar structure). For a perfect hollow sphere, ρ equals 1. For a hollow sphere with a finite membrane thickness one would expect the ratio to be between 0.95 and 1.^[35] For light scattering experiments, a concentration of 0.1 mg mL^{-1} was chosen. For every angle, an apparent diffusion coefficient D_{app} was obtained. By extrapolation to $q^2 = 0$, a z -average of the diffusion coefficient D_z found to be $5.48 \text{ nm}^2 \text{ s}^{-1}$. Applying Stokes–Einstein equation yielded a hydrodynamic radius of $R_h = 39.2$ nm. However, only a minor angular dependency could be observed, indicating particles with low to moderate dispersity (Figure 1A). Furthermore, by fitting the correlation function using the cumulants method at 90° the μ_2 -parameter could be calculated, which is also an index for dispersity. In our case, the μ_2 parameter equals 0.1, thus verifying that well defined PeptoSomes can be obtained from dual centrifugation even without any extrusion process. R_g , determined by static light scattering via a Zimm plot, is 37.3 nm, leading to a ρ -ratio of 0.95 (Figure 1B), which indicates the formation of polymersomes.

To further validate the formation of polymersomes, cryoTEM imaging was employed. These measurements visualized the formation of vesicular structures for unloaded PeptoSomes with a diameter of about 70 nm, which is in line with the DLS measurements. A comparison of empty and loaded polymersomes confirmed that sizes are comparable, but while empty polymersomes display a core with the expected low scattering contrast combined with a membrane like layer with enhanced contrast, loaded particles display uniform distribution of scattering contrast. The polymersomes visible in the cryoTEM images are of comparable structure and possess similar diameters compared to the polymersomes based on PDHPMA-*b*-LMA,^[16] which also have been prepared by dual centrifugation. The presence of a polymer membrane around the core is not visible anymore (see

Figure 1C,D), which may be due to the enhanced scattering contrast of the cargo, peptide SIINFEKL antigen and CpG (oligonucleotide), loaded into the polymersome. These findings additionally underline the efficient loading by dual centrifugation.

A precise determination of the concentrations of the encapsulated antigen and the adjuvant, however, was not possible by a conventional liquid chromatography-mass spectrometry (LC-MS) and may require more advanced analytical setups.

3.3. Biological Evaluation

After physicochemical characterization the antigen- and adjuvant-loaded PeptoSomes were evaluated in several biological experiments. For this purpose, BMDCs were incubated in parallel with nonloaded PeptoSomes and PeptoSomes loaded with the model antigen (peptide sequence SIINFEKL; AnaSpec, Fremont, CA) and the adjuvant CpG ODN 1826 (Invivogen, San Diego, CA), which binds to the TLR9 inducing DC activation. Incubation of BMDCs with nonloaded PeptoSomes had no effect on the expression of activation markers on the cell surface, e.g., CD80 and CD86 (Figure 2A), nor on the production of the proinflammatory cytokine tumor necrosis factor alpha (TNF- α) (Figure 2B). In contrast, treatment of BMDCs with antigen/adjuvant-loaded PeptoSomes resulted in upregulation of maturation markers and elevated cytokine production, at similar (CD80, CD86) or even stronger (TNF- α) extent as induced by soluble CpG ODN 1826, which was used as an internal control. Due to the strong DC-activating potency of antigen/adjuvant-loaded PeptoSomes, we investigated the antigen presenting capacity of accordingly treated BMDC. The model antigen peptide SIINFEKL when presented by major histocompatibility complex (MHC I) is recognized by CD8⁺ T cells derived

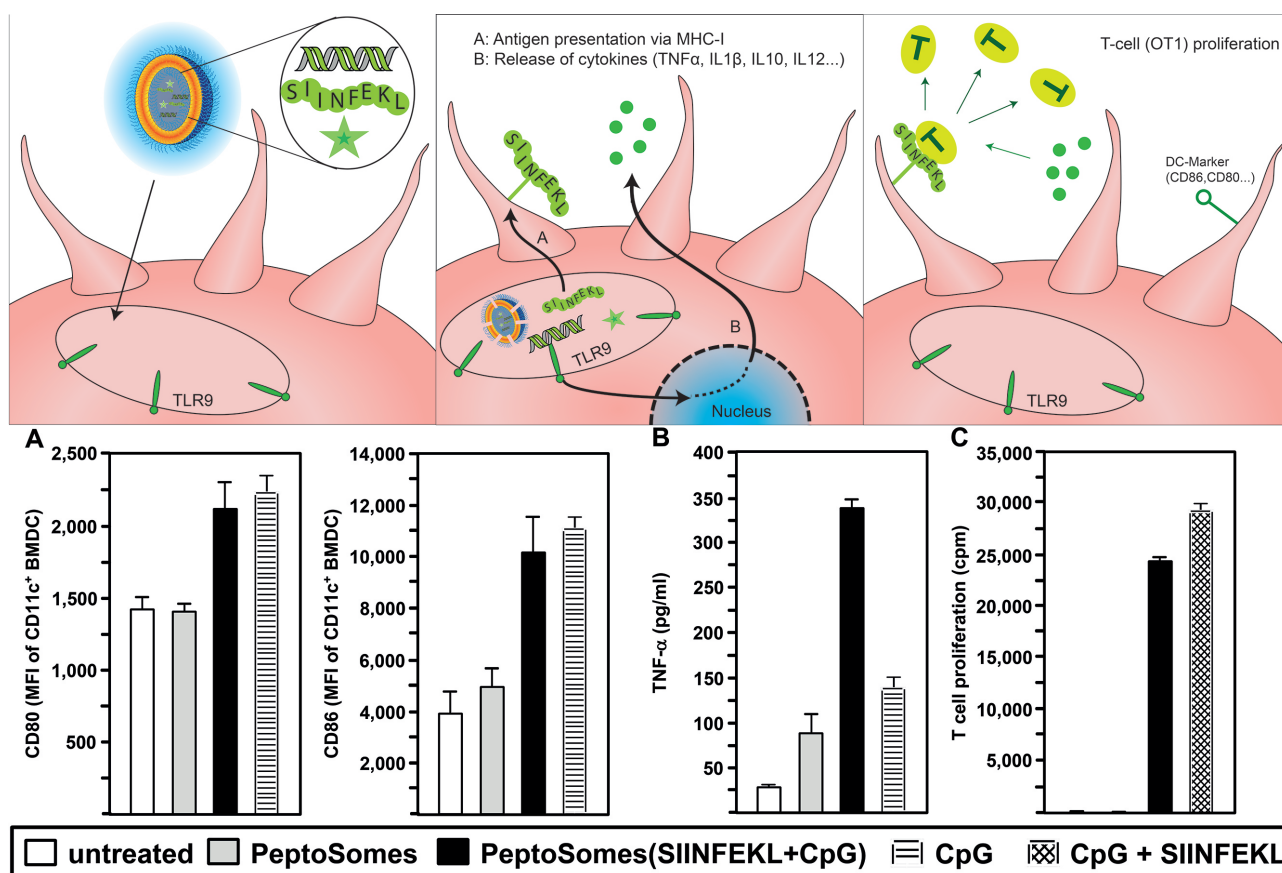


Figure 2. Effects of PeptoSomes on BMDC. BMDC were incubated in parallel with nonloaded or SIINFEKL plus CpG ODN 1826 loaded PeptoSomes (dose equivalent to 100 ng mL⁻¹ CpG a,b) or equivalent to 10 ng mL⁻¹ SIINFEKL c) and either a,b) soluble CpG ODN 1826 (100 ng mL⁻¹) alone or c) plus SIINFEKL peptide (10 ng mL⁻¹). On the next day, expression of a) surface activation markers and b) TNF- α contents in supernatants were determined by flow cytometry. Data denote mean \pm SD of each two independent experiments. c) Differentially pretreated BMDC were cocultured with SIINFEKL-reactive CD8⁺ T cells for 4 d, and T-cell proliferation was determined as uptake of 3H thymidine for the last 16 h of coculture. Data denote mean \pm SD of triplicates of one experiment representative of two independent experiments.

from OVA specific T cell receptor transgenic mice (OT-I mice). BMDC preincubated with antigen/adjuvant-loaded PeptoSomes induced strong T-cell proliferation as observed for BMDC pre-treated with soluble peptide plus CpG as an internal control (Figure 2C). CpG-treated BMDC displayed DC-activation but no T-cell proliferation. As expected, BMDC preincubated with control PeptoSomes (unloaded) did neither induce any activation of BMDCs nor T-cell proliferation (see Figure 2).

4. Conclusions

In summary, a block copolypept(o)ide was synthesized combining a hydrophilic P_{Sar}111 segment with a hydrophobic P_{Glu(OBn)}46 block by controlled sequential ring opening polymerization of the corresponding NCAs. The polypept(o)ide was successfully applied for the preparation of PeptoSomes by dual centrifuging. As indicated by multiangle dynamic light scattering, this method afforded polymersomes with hydrodynamic radii of around 40 nm (PeptoSomes) and enabled us to encapsulate both antigen (SIINFEKL) and adjuvant (CpG) with loading efficiencies of 40%. Upon incubation with loaded PeptoSomes,

BMDCs were activated, leading to an enhanced expression of activation markers and strong cytokine excretion. Furthermore, the antigen was processed inside dendritic cells and presented via the MHC-I complex, which resulted in an antigen specific T-cell proliferation. In contrast, PeptoSomes without antigen and adjuvant did cause neither dendritic cell activation nor T-cell proliferation. Altogether, these results confirm that loaded PeptoSomes can induce potent immune responses in vitro. Therefore, this polymersome based on polypept(o)ides may become a suitable platform for the next generation of polymer-based vaccines.

Supporting Information

Supporting Information is available from the Wiley Online Library or from the author.

Acknowledgements

The authors would like to acknowledge funding from Deutsche Forschungsgesellschaft (DFG) (SFB 1066-1) and the naturwissenschaftliches Forschungszentrum (NMFZ) Mainz. Support

by the Microscopy Core Facility of the Institute of Molecular Biology (IMB) Mainz is gratefully acknowledged. The paper was written through contributions of all authors. All authors have given approval to the final version of the paper.

Conflict of Interest

The authors declare no conflict of interest.

Keywords

peptides, peptoids, polymersomes, polypept(o)ides, vaccines

Received: February 14, 2017

Revised: June 25, 2017

Published online: July 31, 2017

-
- [1] D. W. Dresser, *Nature* **1961**, 191, 1169.
- [2] B. Lemaître, E. Nicolas, L. Michaut, J.-M. Reichhart, J. A. Hoffmann, *Cell* **1996**, 86, 973.
- [3] A. Poltorak, X. He, I. Smirnova, C. Van Huffel, X. Du, D. Birdwell, E. Alejos, M. Silva, C. Galanos, M. Freudenberg, P. Ricciardi-Castagnoli, B. Layton, B. Beutler, *Science* **1998**, 282, 2085.
- [4] H. Shirota, D. Tross, D. Klinman, *Vaccines* **2015**, 3, 390.
- [5] D. M. Klinman, S. Klaschik, T. Sato, D. Tross, *Adv. Drug Delivery Rev.* **2009**, 61, 248.
- [6] S. Grabbe, K. Landfester, D. Schuppan, M. Barz, R. Zentel, *Nanomedicine* **2016**, 11, 2621.
- [7] P. Laing, A. Bacon, B. McCormack, G. Gregoriadis, B. Frisch, F. Schuber, *J. Liposome Res.* **2006**, 16, 229.
- [8] M. L. Immordino, F. Dosio, L. Cattel, *Int. J. Nanomed.* **2006**, 1, 297.
- [9] T. Suzuki, M. Ichihara, K. Hyodo, E. Yamamoto, T. Ishida, H. Kiwada, H. Ishihara, H. Kikuchi, *Int. J. Pharm.* **2012**, 436, 636.
- [10] B. Weber, C. Seidl, D. Schwiertz, M. Scherer, S. Bleher, R. Süss, M. Barz, *Polymers* **2016**, 8, 427.
- [11] K. Shiraishi, K. Kawano, Y. Maitani, T. Aoshi, K. J. Ishii, Y. Sanada, S. Mochizuki, K. Sakurai, M. Yokoyama, *J. Controlled Release* **2016**, 234, 59.
- [12] T. Ishida, M. Harada, X. Y. Wang, M. Ichihara, K. Irimura, H. Kiwada, *J. Controlled Release* **2005**, 105, 305.
- [13] L. Messenger, J. Gaitzsch, L. Chierico, G. Battaglia, *Curr. Opin. Pharmacol.* **2014**, 18, 104.
- [14] D. E. Discher, F. Ahmed, *Annu. Rev. Biomed. Eng.* **2006**, 8, 323.
- [15] C. G. Palivan, R. Goers, A. Najer, X. Zhang, A. Car, W. Meier, *Chem. Soc. Rev.* **2016**, 45, 377.
- [16] M. Scherer, K. Fischer, F. Depoix, T. Fritz, R. Thiermann, K. Mohr, R. Zentel, *Macromol. Rapid Commun.* **2016**, 37, 60.
- [17] P. J. Photos, L. Bacakova, B. Discher, F. S. Bates, D. E. Discher, *J. Controlled Release* **2003**, 90, 323.
- [18] H. De Oliveira, J. Thevenot, S. Lecommandoux, *Wiley Interdiscip. Rev.: Nanomed. Nanobiotechnol.* **2012**, 4, 525.
- [19] K. K. Upadhyay, A. K. Mishra, K. Chuttani, A. Kaul, C. Schatz, J. F. Le Meins, A. Misra, S. Lecommandoux, *Nanomed. Nanotechnol. Biol. Med.* **2012**, 8, 71.
- [20] J. Huang, C. Bonduelle, J. Thévenot, S. Lecommandoux, A. Heise, *J. Am. Chem. Soc.* **2012**, 134, 119.
- [21] C. Fetsch, J. Gaitzsch, L. Messenger, G. Battaglia, R. Luxenhofer, *Sci. Rep.* **2016**, 6, 33491.
- [22] C. Fetsch, S. Flecks, D. Gieseler, C. Marschelke, J. Ulbricht, K.-H. van Pée, R. Luxenhofer, *Macromol. Chem. Phys.* **2015**, 216, 547.
- [23] J. Gaitzsch, K. Karu, G. Battaglia, *Eur. Polym. J.* **2015**, 73, 447.
- [24] Y. Imanishi, K. Fujita, Y. Miura, S. Kimura, *Supramol. Sci.* **1996**, 3, 13.
- [25] K. Fujita, S. Kimura, Y. Imanishi, E. Rump, H. Ringsdorf, *Adv. Biophys.* **1997**, 34, 127.
- [26] H. Tanisaka, S. Kizaka-Kondoh, A. Makino, S. Tanaka, M. Hiraoka, S. Kimura, *Bioconjugate Chem.* **2008**, 19, 109.
- [27] M. Barz, R. Luxenhofer, R. Zentel, M. J. Vicent, *Polym. Chem.* **2011**, 2, 1900.
- [28] C. B. Quer, H. Robson Marsden, S. Romeijn, H. Zope, A. Kros, W. Jiskoot, *Polym. Chem.* **2011**, 2, 1482.
- [29] E. A. Scott, A. Stano, M. Gillard, A. C. Maio-Liu, M. A. Swartz, J. A. Hubbell, *Biomaterials* **2012**, 33, 6211.
- [30] A. Stano, E. A. Scott, K. Y. Dane, M. A. Swartz, J. A. Hubbell, *Biomaterials* **2013**, 34, 4339.
- [31] K. Klinker, M. Barz, *Macromol. Rapid Commun.* **2015**, 36, 1943.
- [32] A. Birke, D. Huesmann, A. Kelsch, M. Weilbacher, J. Xie, M. Bros, T. Bopp, C. Becker, K. Landfester, M. Barz, *Biomacromolecules* **2014**, 15, 548.
- [33] P. Heller, N. Mohr, A. Birke, B. Weber, A. Reske-Kunz, M. Bros, M. Barz, *Macromol. Biosci.* **2015**, 15, 63.
- [34] M. Scherer, C. Kappel, N. Mohr, K. Fischer, P. Heller, R. Forst, F. Depoix, M. Bros, R. Zentel, *Biomacromolecules* **2016**, 17, 3305.
- [35] W. Schärtl, *Light Scattering from Polymer Solutions and Nanoparticle Dispersions*, Springer, Berlin **2007**.

5.5 Publication 5

Protein corona-mediated targeting of nanocarriers to B cells allows redirection of allergic immune responses

Published in: Journal of Allergy and Clinical Immunology, 2018, 142(5):1558-1570. Doi (open access)

Protein corona-mediated targeting of nanocarriers to B cells allows redirection of allergic immune responses



Limei Shen, PhD,^a Stefan Tenzer, PhD,^b Wiebke Storck, MSc,^b Dominika Hobernik, MSc,^a Verena Katherina Raker, PhD,^a Karl Fischer, PhD,^c Sandra Decker, PhD,^c Andrzej Dzionek,^d Susanne Krauthäuser, PhD,^d Mustafa Diken, PhD,^e Alexej Nikolaev,^f Joachim Maxeiner, MSc,^g Petra Schuster,^g Cinja Kappel, MSc,^a Admar Verschoor, PhD,^h Hansjörg Schild, PhD,^{b,*} Stephan Grabbe, MD,^{a,*} and Matthias Bros, PhD^{a,*} Mainz, Bergisch Gladbach, and Lübeck, Germany

Background: Nanoparticle (NP)-based vaccines are attractive immunotherapy tools because of their capability to codeliver antigen and adjuvant to antigen-presenting cells. Their cellular distribution and serum protein interaction (“protein corona”) after systemic administration and their effect on the functional properties of NPs is poorly understood.

Objectives: We analyzed the relevance of the protein corona on cell type-selective uptake of dextran-coated NPs and determined the outcome of vaccination with NPs that codeliver antigen and adjuvant in disease models of allergy.

Methods: The role of protein corona constituents for cellular binding/uptake of dextran-coated ferrous nanoparticles (DEX-NPs) was analyzed both *in vitro* and *in vivo*. DEX-NPs conjugated with the model antigen ovalbumin (OVA) and

immunostimulatory CpG-rich oligodeoxynucleotides were administered to monitor the induction of cellular and humoral immune responses. Therapeutic effects of this DEX-NP vaccine in mouse models of OVA-induced anaphylaxis and allergic asthma were assessed.

Results: DEX-NPs triggered lectin-induced complement activation, yielding deposition of activated complement factor 3 on the DEX-NP surface. In the spleen DEX-NPs targeted predominantly B cells through complement receptors 1 and 2. The DEX-NP vaccine elicited much stronger OVA-specific IgG_{2a} production than coadministered soluble OVA plus CpG oligodeoxynucleotides. B-cell binding of the DEX-NP vaccine was critical for IgG_{2a} production. Treatment of OVA-sensitized mice with the DEX-NP vaccine prevented induction of anaphylactic shock and allergic asthma accompanied by IgE inhibition.

Conclusions: Opsonization of lectin-coated NPs by activated complement components results in selective B-cell targeting. The intrinsic B-cell targeting property of lectin-coated NPs can be exploited for treatment of allergic immune responses. (*J Allergy Clin Immunol* 2018;142:1558-70.)

Key words: Dendritic cells, B cells, complement, antibody, complement factor 3, lectin pathway, IgG_{2a}

From ^athe Department of Dermatology, ^bthe Institute for Immunology, ^fthe Institute for Molecular Medicine, and ^ethe Asthma Core Facility, Research Center for Immunotherapy, University of Mainz Medical Center; ^cthe Department of Physical Chemistry, University of Mainz; ^dMiltenyi Biotec GmbH, Bergisch Gladbach; ^gTRON-Translational Oncology at the University Medical Center of the Johannes Gutenberg University gGmbH, Mainz; and ^hthe Institute for Systemic Inflammation Research, Universität zu Lübeck.

*These authors contributed equally to this work.

L.S. and S.G. were supported by a grant of the Hoffmann Klose Stiftung. W.S., S.T., and H.S. were supported by Stiftung Rheinland-Pfalz (NANOSCH). L.S., W.S., S.T., H.S., S.G., and M.B. were supported by grants from the DFG (SFB 1066).

Disclosure of potential conflict of interest: S. Tenzer has received grants from Stiftung Rheinland-Pfalz (NANOSCH) and the German Research Foundation (SFB1066). W. Storck has received grants from Deutsche Forschungsgesellschaft (SFB1066) and Stiftung Rheinland-Pfalz (NANOSCH). S. Krauthäuser is employed by Miltenyi Biotec GmbH. Hansjörg Schild has received a grant from the German Research Foundation. S. Grabbe has received grants from the German Research Foundation (SFB1066-B04 and SFB1066-B05), Hoffman-Klose Stiftung, and Stiftung Rheinland-Pfalz; has consultant arrangements with AbbVie, Bristol-Myers-Squibb, Roche, Novartis, MSD, Merck-Serono, and Sanofi-Pasteur-MSD; has provided expert testimony for Guidepoint Global advisors and OnkoZert; has received payment for lectures from Bristol-Myers Squibb, MSD, Roche, MedConcept, Beiersdorf, L'Oréal, and Novartis; and has received travel support from Bristol-Myers Squibb, AbbVie, MSD, Merck-Serono, Roche, Novartis, and Takeda. M. Bros has received a grant from the German Research Foundation. The rest of the authors declare that they have no relevant conflicts of interest.

Received for publication January 23, 2017; revised July 26, 2017; accepted for publication August 26, 2017.

Available online January 31, 2018.

Corresponding author: Stephan Grabbe, MD, University Medical Center Mainz, Department of Dermatology, Langenbeckstr 1, Mainz D-55131, Germany. E-mail: stephan.grabbe@unimedizin-mainz.de.

The CrossMark symbol notifies online readers when updates have been made to the article such as errata or minor corrections

0091-6749

© 2018 The Authors. Published by Elsevier Inc. on behalf of the American Academy of Allergy, Asthma & Immunology. This is an open access article under the CC BY-NC-ND license (<http://creativecommons.org/licenses/by-nc-nd/4.0/>).

<https://doi.org/10.1016/j.jaci.2017.08.049>

Abbreviations used

AIT:	Allergen-specific immunotherapy
APC:	Antigen-presenting cell
BCR:	B-cell receptor
C3:	Complement factor 3
CFSE:	Carboxyfluorescein succinimidyl ester
CR:	Complement receptor
DAPI:	4'-6-Diamidino-2-phenylindole dihydrochloride
DC:	Dendritic cell
DEX-NP:	Dextran-coated ferrous nanoparticle
FDC:	Follicular dendritic cell
MBL:	Mannose-binding lectin
NP:	Nanoparticle
ODN:	Oligodeoxynucleotide
OVA:	Ovalbumin
TLR:	Toll-like receptor

protolerogenic state in DCs. As an alternative, T_H2 -dependent allergic reactions were inhibited by redirecting the immune response toward a T_H1 response through coapplication of adjuvants that imprint a T_H1 -promoting capacity in DCs.¹ Therefore multifunctional vaccines hold great promise for AIT.^{7,8} Because of advances in nanotechnology, complex nanoparticulate vaccines are now being explored that contain antigens, immunostimulants, and/or specific cellular targeting moieties.

However, the protein corona that covers the nanovaccine after serum contact can interfere with cell-specific targeting strategies through several mechanisms: (1) targeting moieties can be covered, preventing them from binding to their specific receptors on target cells⁹; (2) components of the serum protein corona of nanovaccines might mediate binding to cellular receptors, such as scavenger receptors¹⁰; and (3) the surface of the nanocarrier can be recognized as foreign by the complement system, triggering its activation and resulting in binding to complement receptors (CRs) highly expressed by APCs and other immune cell types.¹¹

Nonetheless, the functional effect of the nanoparticle (NP) protein corona on its cell-binding properties *in vivo* has not been thoroughly assessed. Knowledge of functional consequences is essential for the design of the surfaces of nanocarriers to ensure their proper cellular targeting and functional efficacy.

In this study we investigated the suitability of dextran-coated ferrous nanoparticles (DEX-NPs), which are widely used in immunologic assays¹² and clinical trials,¹³ to serve as nanovaccines for therapeutic treatment of systemic anaphylaxis and allergic asthma in mouse models. We show that lectin-coated surfaces of DEX-NPs activated the lectin complement pathway. Surface-deposited active complement factor 3 (C3) resulted in predominant targeting to CR1/2-expressing B cells. DEX-NPs coated with ovalbumin (OVA) as a model allergen plus immunostimulatory CpG oligodeoxynucleotides (ODNs) induced strong OVA-specific IgG_{2a} levels. Vaccination of sensitized mice with this model nanovaccine largely prevented allergic symptoms in anaphylaxis and asthma models associated with suppressed IgE levels and increased IgG_{2a} levels. We consider the complement-mediated B-cell targeting properties of lectin-coated NPs as an interesting approach for allergy treatment.

METHODS

Preparation and functionalization of dextran-coated colloidal NPs

Dextran-coated iron oxide NPs were synthesized and functionalized with endotoxin-depleted OVA (Sigma-Aldrich, Deisenhofen, Germany) and CpG ODN 1826 (5'-TCC ATG ACG TTC CTG ACG TT-3'; Metabion, Martinsried, Germany) by Miltenyi Biotec (Bergisch Gladbach, Germany), as previously described.¹² Details on DEX-NP generation are described in the [Methods](#) section in this article's Online Repository at www.jacionline.org. All DEX-NP formulations were labeled with Cy5.

Label-free quantitative proteomic analysis of corona components

NP protein complexes were isolated by means of centrifugation through a sucrose cushion, and the obtained pellets were washed to obtain the hard protein corona, as described previously.¹⁴ Corona constituents were eluted from DEX-NP(OVA) by using 7 mol/L urea, 2 mol/L thiourea, and 2% CHAPS (all from Roth, Karlsruhe, Germany). Label-free quantitative proteomic analysis of protein corona components by using mass spectrometry with ion mobility-enhanced data-independent acquisition was performed, as described in detail previously.^{15,16} The complete proteomic data set with all quantification results is shown in [File E1](#) in this article's Online Repository at www.jacionline.org.

Mice

BALB/c, C57BL/6, and C3^{-/-} (B6;129S4-C3^{tm1Crr/J})¹⁷; mannose-binding lectin (MBL)^{-/-} (B6.129S4-Mbl^{tm1Kata} Mbl2^{tm1Kata/J})¹⁸; and OT-II¹⁹ mice on the C57BL/6 background were bred and maintained in the Central Animal Facility of the Johannes Gutenberg-University Mainz under specific pathogen-free conditions on a standard diet according to the guidelines of the regional animal care committee. Female mice (BALB/c, C57BL/6, C3^{-/-}, and MBL^{-/-} mice: 6 weeks; OT-II mice: 9-12 weeks) were used throughout all experiments. All animal experiments were performed in accordance with national and European (86/609/EEC) legislation. The "Principles of laboratory animal care" (National Institutes of Health publication no. 85-23, revised 1985) were followed.

Immunohistochemistry

Mice were injected intravenously with DEX-NP formulations (each with 2×10^{12} particles), as indicated. In blocking experiments mice were pretreated with 50 μ g of rat anti-mouse CD21/CD35 antibody (clone 7G6; BD Biosciences, San Jose, Calif) or corresponding isotype control antibody (clone RTK4530; BioLegend, San Diego, Calif) 1 hour before application of DEX-NP formulations. Four hours after DEX-NP injection, inner organs were retrieved, and derived cryosections were incubated with 4'-6-diamidino-2-phenylindole dihydrochloride (DAPI; Life Technologies, Carlsbad, Calif) and Alexa Fluor 488-labeled antibodies (BioLegend) to detect immature (GR-1, clone RB6-8C5) and differentiated (CD11b, M1/70) myeloid cells, macrophages (CD68, FA-11), DCs (CD11c, N418), B cells (CD19, 6D5), and follicular dendritic cells (FDCs; FDC-M1). BX61 and IX81 fluorescence microscopes (Olympus, Tokyo, Japan) were equipped with cellF software (Soft Imaging System, Münster, Germany).

Confocal microscopy

Immunosorted (Miltenyi Biotec) and untouched splenic B cells were incubated with Cy5-labeled DEX-NP(OVA-CpG), as indicated; washed with FACS buffer (PBS, 1% FCS, and 0.5 mmol/L EDTA); and transferred onto chamber slides (IBIDI, Martinsried, Germany). Cells were incubated with anti-CD19 antibody (green) and DAPI (blue). The LSM510-UV confocal microscope (Zeiss, Jena, Germany) was used.

NP binding studies

Immunosorted splenic CD19⁺ B cells were seeded into wells of 96-well cell culture plates ($5 \times 10^5/200 \mu\text{L}$). Aliquots of nonfunctionalized DEX-NPs (DEX-NP[−]; 5×10^{11} per sample) were preincubated (for 1 hour at 37°C) with albumin (5 mg/mL; Sigma-Aldrich), mouse total IgG (100 $\mu\text{g/mL}$; BioLegend), or mouse serum (10 μL per sample) and left untreated or heat inactivated (for 30 minutes at 56°C) in a volume of 20 μL . Aliquots of dextran- and starch-coated NPs (each 10 μg) were preincubated with mouse serum, as indicated. In some experiments seeded mouse B cells were preincubated (for 30 minutes at 37°C) with rat anti-mouse CD21/CD35 antibody (5 $\mu\text{g/mL}$). After 4 hours, samples were incubated with Alexa Fluor–labeled anti-mouse CD19 (clone 6D5) antibodies or corresponding isotype control antibodies.

For *in vivo* analysis, DEX-NP formulations were administered intravenously through the tail vein, and spleens were retrieved after 4 or 24 hours. Spleen cell suspensions were incubated with cell type–specific antibodies (see above). Frequencies of DEX-NP(−) binding immune cells were assessed by using flow cytometry (LSR II; BD Biosciences) and analyzed with FlowJo software (FlowJo, Ashland, Ore).

In vivo T-cell proliferation

To assess OVA-specific CD4⁺ T-cell proliferation *in vivo*, we used OT-II mice, which have CD4⁺ T cells that express a transgenic T-cell receptor that recognizes OVA_{323–339} (ISQAVHAAHAEINEAGR) in the context of I-A^b. To this end, splenocytes derived from OT-IIxCD45.1 mice were labeled with 0.5 $\mu\text{mol/L}$ carboxyfluorescein succinimidyl ester (CFSE; Life Technologies) for 10 minutes. CFSE-labeled splenocytes (10^7 in 200 μL of PBS) were transferred intravenously into C57BL/6 mice. After 48 hours, DEX-NP formulations at equivalent doses of OVA (4 μg per mouse) and CpG ODN 1826 (0.4 $\mu\text{g}/\text{mouse}$) were injected intravenously. Four days later, spleens and peripheral lymph nodes were removed, and cell suspensions were analyzed for proliferation of CFSE-labeled T cells by using flow cytometry.

Antibody detection

Mice were bled 14 days after immunization from the retro-orbital plexus, and sera were collected. OVA-specific IgG₁, IgG_{2a}, and IgE levels were quantitated by means of ELISA. For this, plates were coated with OVA (25 mg/mL) and incubated with diluted sera (for IgG₁ detection, 1:10⁵; for IgG_{2a} detection, 1:500; for IgE detection, 1:10). Afterward, IgG class-specific rat anti-mouse antibodies conjugated with horseradish peroxidase were applied (Dianova, Hamburg, Germany).

Cytokine quantification

Cytokine contents (TNF- α and IL-6) in supernatants of spleen cells were detected by using the CBA assay (BD Biosciences), a previously described.²⁰ Samples were analyzed in the FL3 channel of an LSR-II flow cytometer. Results were analyzed by using CBA Analysis software (BD Biosciences).

Anaphylaxis model

In a therapeutic model of systemic anaphylaxis, BALB/c mice were sensitized subcutaneously 3 times (days 0, 7, and 14) with 10 μg of OVA in PBS (10 μg per mouse). One week after the last sensitization, mice were vaccinated intravenously 3 times every other day with different DEX-NP formulations at equivalent doses of OVA (4 μg) or corresponding numbers of DEX-NP(−) in 200 μL of PBS or with PBS as a solvent control alone. At days 14 (before the first vaccination) and 28 (after the third vaccination), blood samples were collected for antibody measurements. One week after the last vaccination, untreated (naive) and differentially pretreated mice were challenged with OVA (25 μg per mouse) by means of intravenous injection, and body temperature was monitored rectally every 15 minutes.

Asthma model

In a therapeutic model of asthma, BALB/c mice were sensitized with 10 μg of OVA emulsified in 1.5 mg of Alum (Pierce, Rockford, Ill) administered intraperitoneally 2 times (days 0 and 7). Mice were vaccinated with DEX-NP formulations (days 10 and 12) at equivalent doses of OVA (4 μg) or with corresponding numbers of DEX-NP(−) in 200 μL of PBS or with PBS alone. Untreated (naive) and differentially treated mice were challenged daily with nebulized OVA (1% in PBS for 20 minutes) 3 times, starting on day 14. Two days after the last challenge, differentially pretreated mice were administered serially increasing doses of methacholine, and airway hyperresponsiveness was measured, as previously described.²¹ Afterward, bronchoalveolar lavage was performed to yield lung-infiltrating immune cells. Bronchoalveolar lavage fluid–derived cells were cytospun (5×10^5 cells per slide) onto microscope slides, stained with Diff-Quick (Dade Behring, Marburg, Germany), and photographed for morphologic analysis. Sections of lung tissue were stained with hematoxylin and eosin to identify inflammatory cells. Lung inflammation was scored (no change, score = 0; mild, score = 1; moderate, score = 2; and severe, score = 3), as previously described.²²

Bioinformatics and statistical analysis

Statistical analysis was performed with GraphPad Prism 4.0 software (GraphPad Software, San Diego, Calif). Results were expressed as means \pm SEMs. Differences among groups were tested by using ANOVA. Data were normally distributed, and variance between groups was not significantly different. Differences between 2 groups were tested by using the paired Student *t* test, assuming significance at a *P* value of less than .05.

RESULTS

Systemically applied DEX-NPs target B cells

Generation of DEX-NP formulations and their physicochemical characterization are described in the Methods section and in Table E1 in this article's Online Repository at www.jacionline.org. Atomic force microscopy showed a spherical shape of DEX-NPs and confirmed limited size variability (see Fig E1 in this article's Online Repository at www.jacionline.org). To assess the suitability of DEX-NPs as vaccines, we first monitored their organ biodistribution and cell type–specific accumulation after intravenous injection into mice. DEX-NP(−) accumulated preferentially in the liver (see Fig E2, A, in this article's Online Repository at www.jacionline.org), where they colocalized with the CD11b⁺ macrophage population (see Fig E2, B). However, a considerable fraction of DEX-NP(−) also accumulated to the spleen. Within the spleen, DEX-NP(−) scarcely colocalized with phagocytic myeloid cells, namely GR-1⁺ immature myeloid cells/neutrophils and CD68⁺ macrophages, but with CD11c⁺ DCs (Fig 1, A). Surprisingly, the vast majority of DEX-NP(−) accumulated within the B-cell areas of the spleen (Fig 1, B, left panel) and colocalized with CD19⁺ B cells (Fig 1, B, right panel). FDCs displayed some engagement of DEX-NP(−) (Fig 1, A).

B-cell targeting by DEX-NPs depends on activation of the lectin complement pathway and deposition of activated C3 on the particle surface

Next, we investigated the mechanism leading to specific B-cell targeting by DEX-NP(−). In contrast to the *in vivo* situation, DEX-NP(−) bound poorly to immunomagnetically sorted CD19⁺ splenic B cells *in vitro* (Fig 2, A), which suggested a critical role for mouse serum components that might form a

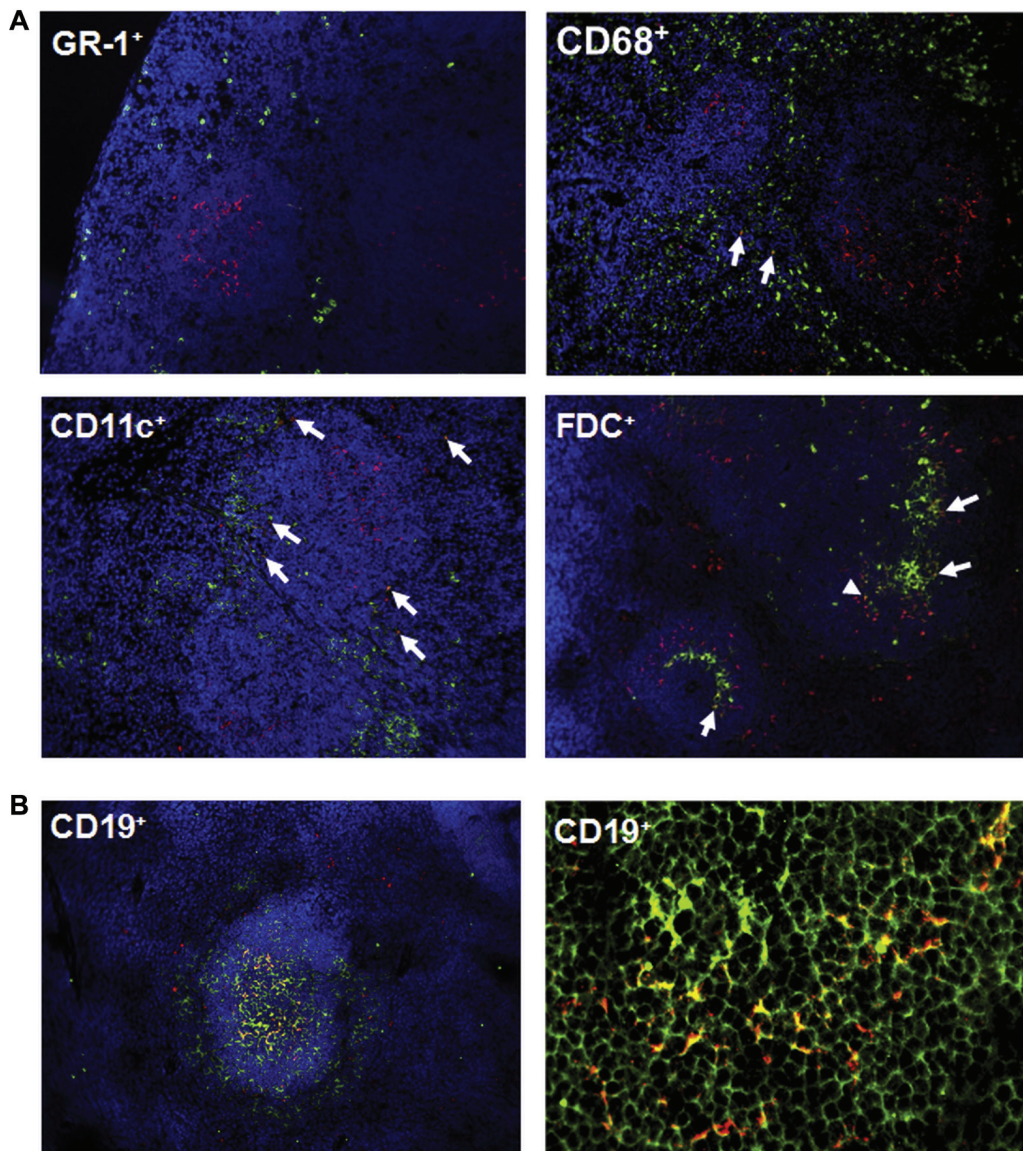


FIG 1. DEX-NPs colocalize with CD19⁺ B cells. Cy5-labeled DEX-NPs (DEX-NP[-]) were administered intravenously into mice. After 4 hours, retrieved spleen sections were incubated with antibodies (green fluorescence) and DAPI (blue) to identify immature myeloid cells/neutrophils (GR-1⁺), macrophages (CD68⁺), DC (CD11c⁺), and FDCs (FDC⁺; arrows denote cells colocalizing with DEX-NP[-]; **A**) and B cells (CD19⁺; **B**). Results are representative of 4 experiments. Fig 1, **A** and **B**, left panel, ×20 magnification; Fig 1, **B**, right panel, ×40 magnification.

protein corona around DEX-NP(-) *in vivo*. However, *in vitro* pretreatment of DEX-NP(-) with known major constituents of protein coronae¹² had no effect on subsequent B-cell binding (Fig 2, A). In contrast, pretreatment of DEX-NP(-) with native mouse serum yielded strong binding and uptake of DEX-NPs by B cells, as confirmed by using confocal microscopy (Fig 2, B). Heat treatment (at 30 minutes for 56°C) of mouse serum before incubation with DEX-NP(-) prevented B-cell binding (Fig 2, A), which suggested a decisive role of complement factors.²³ Indeed, quantitative proteomic analysis of the protein corona of DEX-NP(-) pretreated with native mouse serum identified components of the lectin-activated complement cascade, including MBL-associated proteases 1 and 2 (Table I). Both proteins are recruited and activated by MBL, which recognizes polysaccharides on cell surfaces of pathogens.²⁴ MBL-associated

proteases 1 and 2 can activate C3 convertase, which results in deposition of activated C3b on lectin-coated surfaces. In line with this, C3 was identified as a major constituent of the DEX-NP(-) protein corona (Table I and Fig 2, C). All CRs preferentially bind C3 products.²⁵ Therefore activated C3 constituted a likely candidate for binding of serum-opsonized DEX-NPs to B cells.

Preincubation of DEX-NP(-) with recombinant C3 protein yielded no enhanced B-cell binding (Fig 2, D), which demonstrates that C3 activation on the NP surface is required for subsequent B-cell binding (Fig 2, E). In accordance with this, DEX-NP(-) opsonized with serum derived from C3^{-/-} and MBL^{-/-} mice showed strongly reduced B-cell binding. Serum-pretreated DEX-NP(-) had no effect on overall viability of spleen cells (see Fig E3, A, in this article's Online Repository

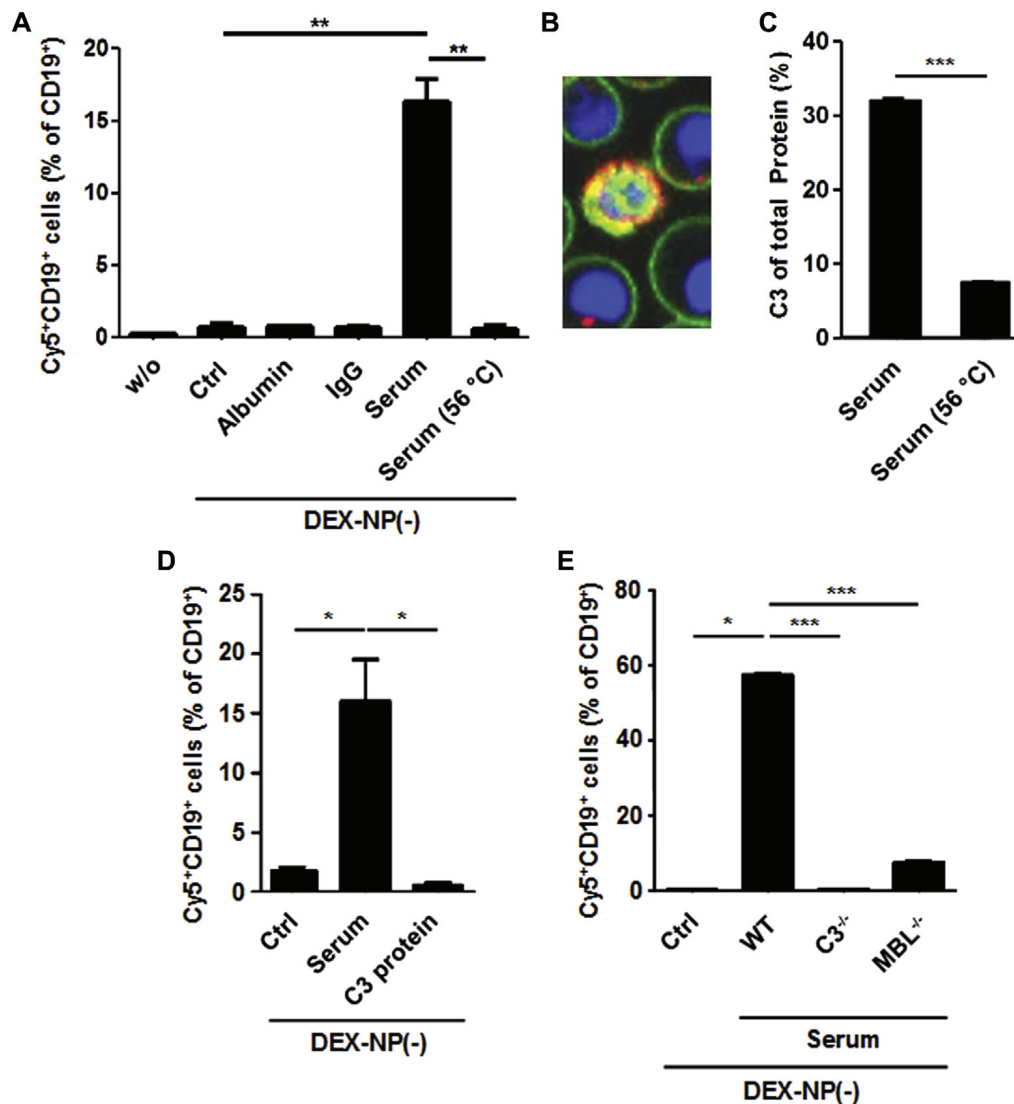


FIG 2. Complement opsonization of DEX-NPs mediates B-cell binding. **A** and **C-E**, Frequencies of B cells (*in vitro*) binding differentially pretreated DEX-NP(-) derived from wild-type (WT; Fig 2, **A** and **D**) or knockout (Fig 2, **E**) mice after 4 hours of coincubation ($n = 3$). **B**, Internalization of DEX-NP(OVA-CpG) by B cells (*in vitro*) after 4 hours. Fig 2, **D**, Complement C3 abundance in the DEX-NP(-) protein corona ($n = 3$). Fig 2, **A** and **C-E**: * $P < .05$, ** $P < .01$, and *** $P < .001$.

at www.jacionline.org) and also did not activate splenic leukocytes, as shown by unaltered cytokine profiles (see Fig E3, **B**), which suggests that complement activation is confined to the DEX-NP(-) surface.

In accordance with our findings for mouse B cells, pretreatment of DEX-NP(-) with human plasma resulted in a strongly enhanced binding to CD19⁺ human B cells, which was abolished by heat inactivation of complement as well (see Fig E4 in this article's Online Repository at www.jacionline.org). Thus our results obtained in mice might be of translational relevance for clinical application in human subjects.

C3-opsonized DEX-NPs bind B cells through CR1/2

Antibody-mediated blockade of CR1/2 (CD21/CD35) on B cells completely prevented binding of serum-pretreated DEX-NP(-) *in vitro* (Fig 3, **A**) and reduced colocalization of DEX-NP(-) with splenic B cells *in vivo* (Fig 3, **B** and **C**).

Other solid-core NP formulations that were coated with starch (Fig 3, **D** and **E**) or dextran (Fig 3, **F**) engaged B cells in a complement-dependent manner as well. In contrast, standard silica NPs, which bound to splenic B cells to a high extent in the absence of serum, displayed strongly reduced B-cell binding after serum preincubation (Fig 3, **G**). This suggests that only lectin-coated NPs bind B cells in a complement-mediated fashion by triggering the lectin pathway of complement activation.

DEX-NPs that codeliver antigen and adjuvant induce APC activation and an antigen-specific CD4⁺ T-cell response

Next, we evaluated the suitability of DEX-NP-derived formulations for B cell-focused vaccinations. DEX-NPs coupled with the model antigen OVA (DEX-NP[OVA]) and with the T_H1-promoting immunostimulatory CpG ODN 1826 (DEX-NP

TABLE I. Top 20 most abundant corona proteins detected after incubation of DEX-NP(OVA) with untreated and heat-inactivated mouse serum*

UniProt accession no.	Protein	Isoelectric point	Molecular weight (kDa)	Reported peptides	Total protein (%)	
					Native serum	Heat-inactivated serum
P01027	Complement C3	6.27	188	125	7.7	3.6
P11276	Fibronectin	5.25	276	111	3.2	3.4
P07724	Serum albumin	5.68	71	51	3.1	4.5
O08677	Kininogen-1	6.05	74	29	3.1	3.1
P06909	Complement factor H	6.60	144	73	3.0	1.9
P35441	Thrombospondin-1	4.54	134	72	2.9	2.4
Q61838	α_2 -Macroglobulin	6.23	167	70	2.7	4.2
P01029	Complement C4-B	7.25	195	82	2.3	2.0
P26262	Plasma kallikrein	7.89	73	41	2.2	0.9
P98064	MBL-associated lectin serine protease 1 (MASP-1)	5.21	82	35	2.2	1.5
Q9ESB3	Histidine-rich glycoprotein	7.33	60	23	2.1	2.2
P19221	Prothrombin	6.00	72	41	2.1	0.6
P28665	Murinoglobulin-1	5.96	167	72	1.9	2.4
Q92111	Serotransferrin	6.85	79	44	1.8	2.2
Q91WP0	MBL-associated serine protease 2 (MASP-2)	5.63	77	34	1.8	0.5
O88783	Coagulation factor V	5.61	248	55	1.7	2.2
Q8VDD5	Myosin-9	5.38	228	26	1.7	2.5
P06684	Complement C5	6.37	191	75	1.6	0.9
P01872	Ig mu chain C region secreted form	6.58	51	24	1.5	1.5
Q61702	Inter- α -trypsin inhibitor heavy chain H1	6.51	102	33	1.4	2.2

*Proteins associated with the lectin pathway of complement activation are shown in boldface. The complete data set is shown in [File E1](#).

[OVA-CpG]) in addition retained their B-cell targeting properties *in vivo* (see [Fig E5](#) in this article's Online Repository at www.jacionline.org). Within the spleen, CpG ODN-coupled DEX-NPs mediated upregulation of CD86 expression by B cells ([Fig 4, A and B](#)), engaged no CD86⁺ macrophages but did engage CD11c⁺ DCs ([Fig 4, C](#)) and activated these ([Fig 4, D](#)). Furthermore, application of DEX-NP(OVA) yielded moderate proliferation of adoptively transferred OT-II CD4⁺ T cells, which were enhanced strongly on coinjection of CpG ODN 1826 ([Fig 4, E and F](#)).

Induction of a T_H1-biased antibody response by antigen/adjuvant-codelivering DEX-NPs depends on B-cell targeting

As expected, only vaccination with DEX-NP(OVA-CpG) mounted very high levels of T_H1-associated OVA-specific IgG_{2a} antibodies but only slightly increased levels of T_H2-associated OVA-specific IgG₁ and IgE ([Fig 5, A](#)). Moreover, DEX-NP-mediated induction of OVA-specific IgG_{2a} was much stronger than application of equimolar amounts of soluble OVA protein plus soluble CpG in parallel experiments ([Fig 5, B](#)).

In accordance with the critical role of activated C3 to mediate B-cell targeting of DEX-NPs, immunization of C3^{-/-} and MBL^{-/-} mice with DEX-NP(OVA-CpG) yielded no or strongly attenuated OVA-specific IgG_{2a} production. Congruently, antibody-mediated blockade of CR1/2 strongly reduced the frequency of splenic CD19⁺ B cells that colocalized with

DEX-NP(OVA-CpG) ([Fig 5, C](#)) and inhibited OVA-specific IgG_{2a} antibody production ([Fig 5, D](#)).

In a therapeutic setting vaccination of mice with antigen/adjuvant-codelivering DEX-NPs prevents IgE-mediated anaphylactic shock

To assess the therapeutic potential of DEX-NPs, we used a model of systemic anaphylaxis ([Fig 6, A](#)). Only vaccination of sensitized mice with the antigen/adjuvant-codelivering NP formulation (DEX-NP[OVA-CpG]) prevented a decrease in body temperature after challenge ([Fig 6, B](#)), which was associated with an inhibition of OVA-specific IgE ([Fig 6, C](#)) but a strong induction of OVA-specific IgG_{2a} antibody production ([Fig 6, D and E](#)). Levels of OVA-specific IgG₁ remained largely unaltered in all groups of mice (see [Fig E6](#) in this article's Online Repository at www.jacionline.org).

Vaccination of mice with antigen/adjuvant-codelivering DEX-NPs prevents asthma in a therapeutic setting

Similarly, in a therapeutic model of allergic asthma ([Fig 7, A](#)), only sensitized mice vaccinated with DEX-NP(OVA-CpG) before challenge with nebulized OVA showed no strong airway hyperresponsiveness in response to pretreatment with higher doses of methacholine ([Fig 7, B](#)), lacked lung-infiltrating eosinophils ([Fig 7, C](#)), and had no increased lung inflammation score ([Fig 7, D](#), and see [Fig E7](#) in this article's Online Repository

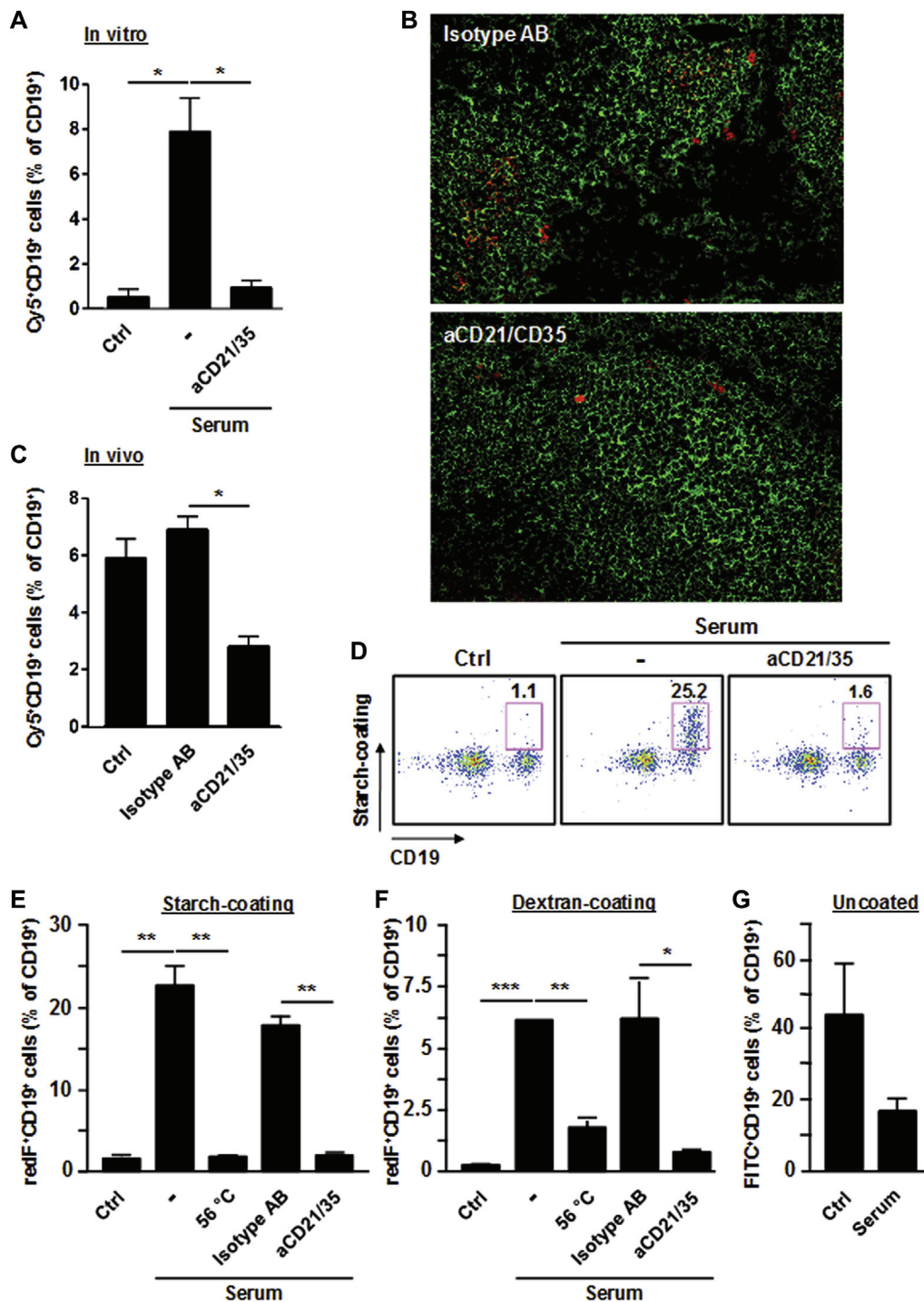


FIG 3. Serum-opsonized NPs bind B cells through CD21/CD35. **A**, Frequencies of B cells (*in vitro*) binding DEX-NP(-) in the presence of neutralizing anti-CD21/CD35 antibody ($n = 3$). **B**, DEX-NPs in spleens of mice pretreated with isotype control or anti-CD21/CD35 antibody assessed 4 hours after injection (3 mice per group, $n = 2$; magnification $\times 10$). **C**, Quantification of NP-binding B cells (300 cells counted per experiment, $n = 2$). **D**, B cells (*in vitro*) binding starch-coated NPs (gated, $n = 3$). **E-G**, Frequencies of B cells binding starch-coated (Fig 3, **E**) and dextran-coated (Fig 3, **F**) NPs ($n = 3$) and carboxylated silica NPs (Fig 3, **G**; $n = 4$). Fig 3, **A**, **C**, and **E-G**: * $P < .05$, ** $P < .01$, and *** $P < .001$.

at www.jacionline.org). In line with this, only these mice showed no induction of OVA-specific IgE (Fig 7, **E**, upper panel) but strongly upregulated OVA-specific IgG_{2a} (Fig 7, **E**, lower panel).

In general, levels of OVA-specific IgG₁ remained largely unaffected (see Fig E8 in this article's Online Repository at www.jacionline.org).

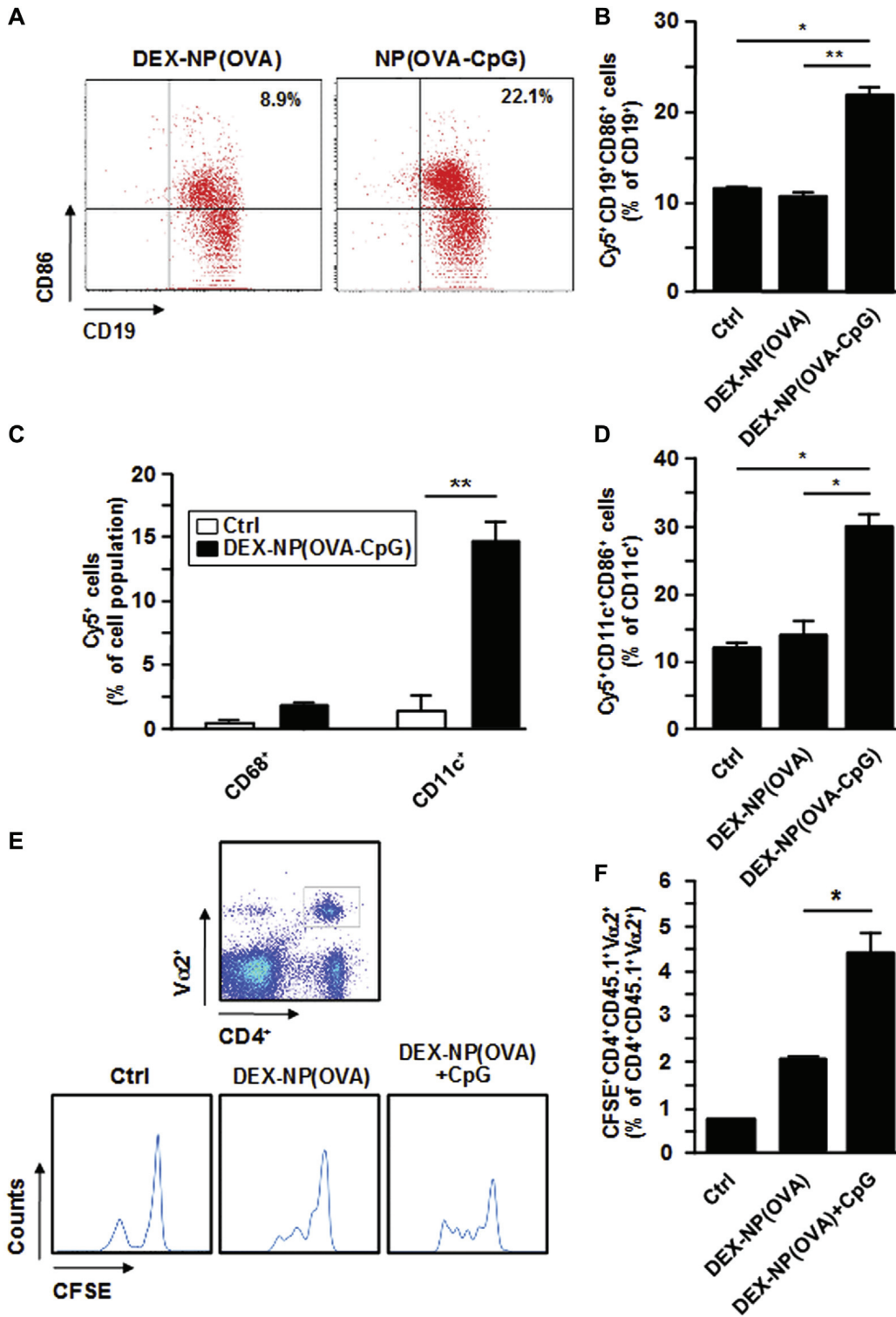


FIG 4. Functionalized DEX-NPs activate B cells and DCs *in vivo* and evoke CD4⁺ T-cell proliferation. **A-D**, Frequencies of activated B cells (24 hours; Fig 4, **A** and **B**), DCs and macrophages (4 hours; Fig 4, **C**), and activated DCs (24 hours; Fig 4, **D**) after intravenous application of DEX-NP formulations (3 mice per group, compiled from n = 2 [total of 6 mice per group]). **E** and **F**, Proliferation of CD4⁺ OT-II T cells assessed 3 days after vaccination with DEX-NP(OVA) and soluble CpG (4 mice per group; representative of 3 experiments; Fig 4, **E**) and according quantification (n = 3; a total of 12 mice per group; Fig 4, **F**). Fig 4, **B-D** and **F**: *P < .05, **P < .01, and ***P < .001.

Altogether, these results confirm that vaccination of sensitized mice with DEX-NP(OVA-CpG) prevents induction of a T_H2-associated humoral immune response, which in turn drives

allergies by promoting T_H1-associated IgG_{2a} antibody switching. Therefore we conclude that lectin-coated NP vaccines, which intrinsically target B cells and codeliver antigen and a

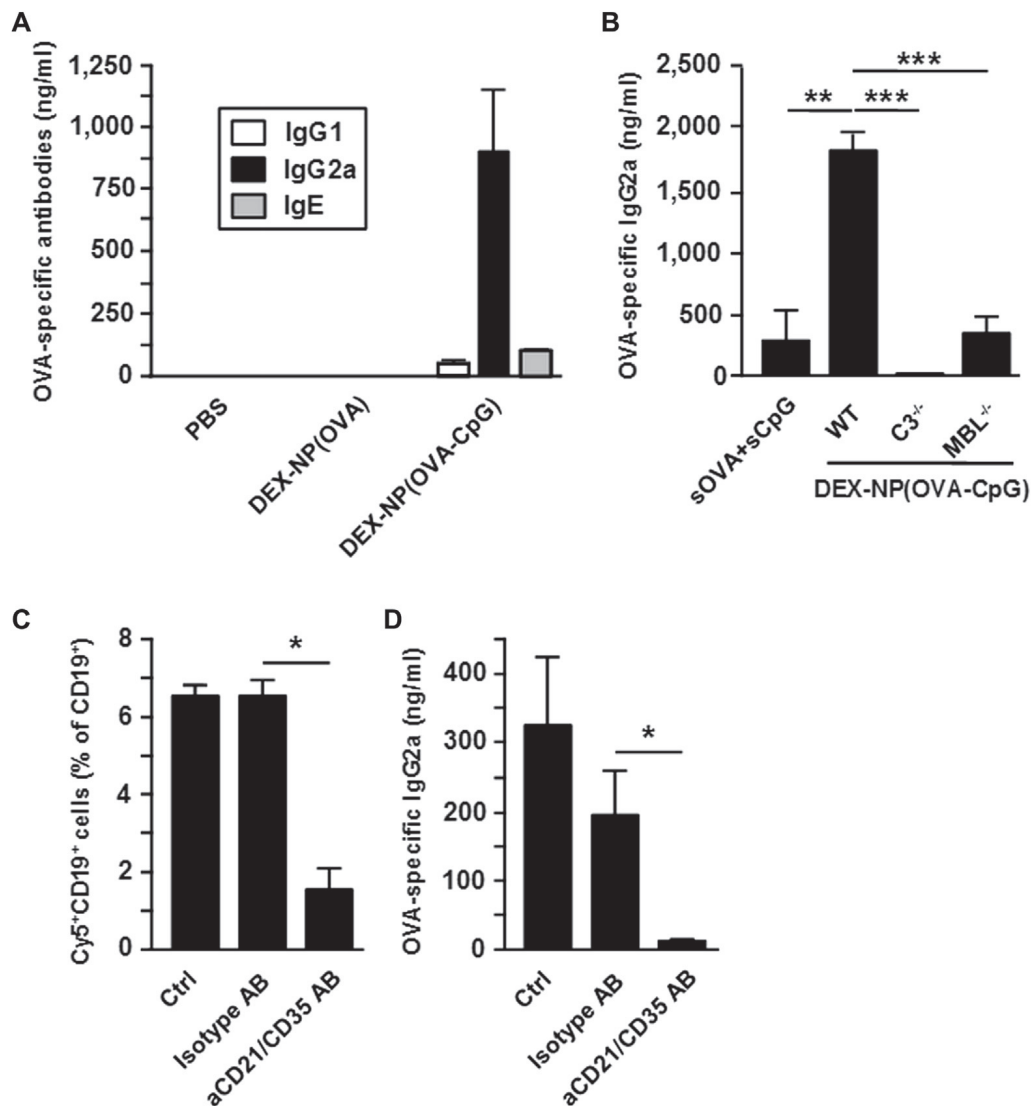


FIG 5. Functionalized DEX-NPs induce profound antibody production dependent on complement activity and binding to CD21/CD35. **A, B, and D,** OVA-specific IgG₁, IgG_{2a}, and IgE in sera of mice obtained 10 (Fig 5, *B* and *D*) or 14 (Fig 5, *A*) days after vaccination with OVA and soluble CpG or DEX-NP formulations or PBS alone (control group) and in the presence of anti-CD21/CD35 or isotype control antibody (Fig 5, *D*). **C,** Frequencies of splenic B cells that colocalized with DEX-NPs 4 hours after application. Fig 5, *A* and *C*, Five mice per group compiled from *n* = 2 (a total of 10 mice per group); Fig 5, *B* and *D*, 3 mice per group compiled from *n* = 3 (a total of 9 mice per group). Fig 5, *A-D*: **P* < .05, ***P* < .01, and ****P* < .001.

T_H1-promoting adjuvant, such as CpG ODN, are suitable candidates for therapeutic treatment of allergies.

DISCUSSION

Here we show that DEX-NPs trigger activation of the lectin pathway of complement activation²⁶ and demonstrate the essential role of active C3 deposited on DEX-NPs to mediate their binding to CD19⁺ B cells through CR1/2. To the best of our knowledge, our study is the first to demonstrate specific B-cell binding of an NP not functionalized with a B-cell targeting antibody but rather because of its intrinsic complement-activating potential. These key findings are summarized in Fig E9 in this article's Online Repository at www.jacionline.org.

Based on the intrinsic B-cell targeting properties of DEX-NPs and their concurrent binding to a fraction of splenic CD11c⁺ DCs

required to induce primary CD4⁺ T-cell responses,⁵ we evaluated the suitability of DEX-NPs to serve as a nanovaccine for the induction and therapeutic modulation of humoral immune responses. We used the model antigen OVA, which is frequently used in mouse allergy models.²⁷ In addition, we used CpG ODN 1826, which binds to TLR9 expressed by splenic DCs and B cells,²⁸ as a T_H1-promoting adjuvant to alter allergy-inducing T_H2 responses, as already reported by others.²⁹ Activation of splenic DCs by CpG ODN-conjugated DEX-NPs *in vivo* is in line with previous reports on endocytotic uptake of CpG ODN-coupled NPs by DCs and hence accessibility of endosomal/lysosomal TLR9.³⁰ Our finding of concurrent B-cell activation indicates that targeted B cells must have internalized at least a fraction of C3-opsonized DEX-NP(OVA-CpG) to trigger TLR9 as well.^{28,31}

The induction of pronounced OVA-specific IgG_{2a} but largely unaltered IgG₁ antibody levels on vaccination with

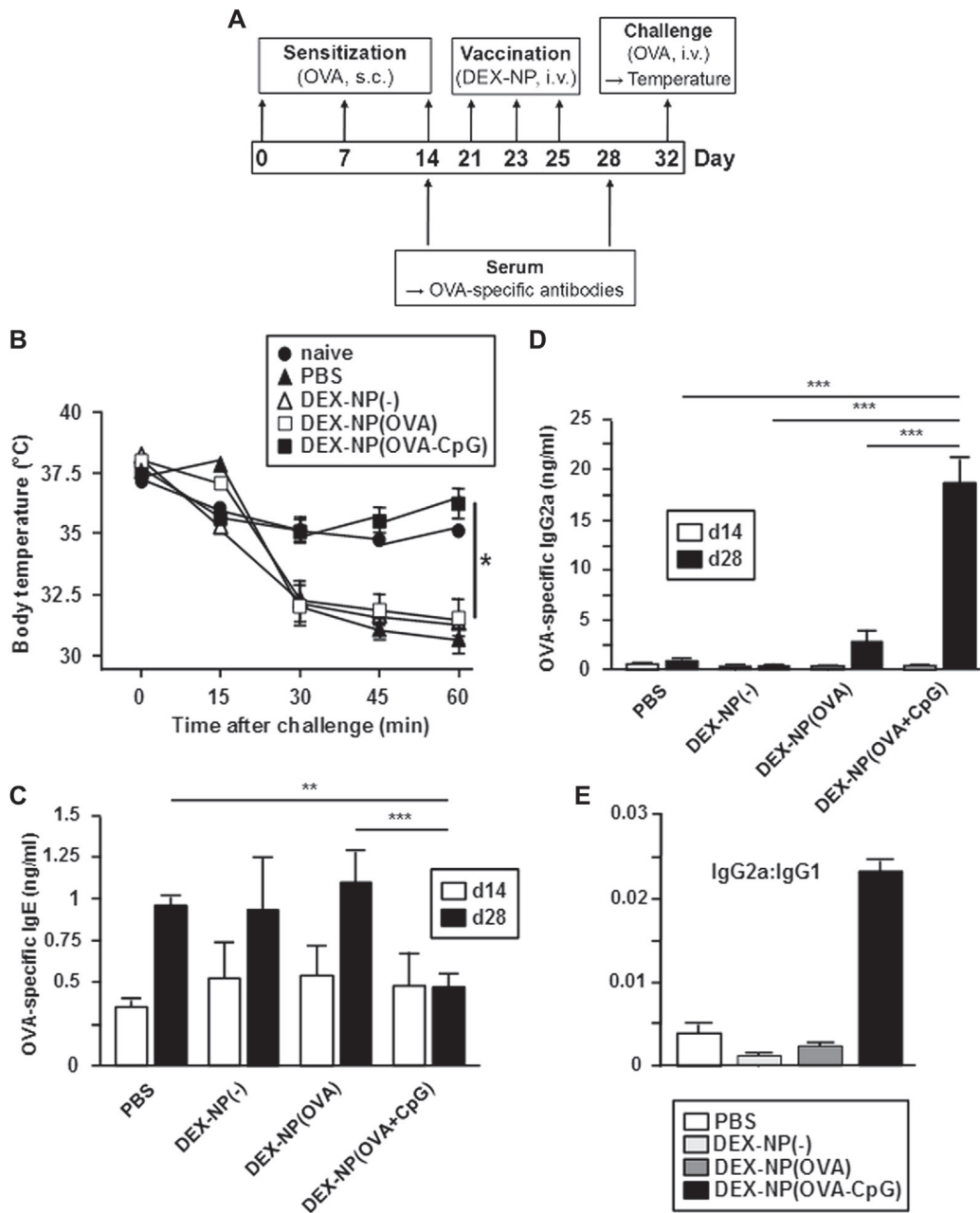


FIG 6. Vaccination of OVA-sensitized mice with OVA CpG-codelivering DEX-NPs prevents IgE induction and inhibits anaphylactic shock. **A**, Experimental design. *i.v.*, Intravenous; *s.c.*, subcutaneous. **B**, Alterations of body temperature after challenge (15 mice per group, compiled from $n = 3$). **C** and **D**, OVA-specific IgE (Fig 6, C) and IgG_{2a} (Fig 6, D) in serum obtained before the first (day 14) and after the last (day 28) vaccination with indicated DEX-NP formulations or PBS alone (control group). **E**, IgG_{2a}/IgG₁ ratio. Fig 6, C-E, Five mice per group; 1 experiment representative of 5. Fig 6, B-E, * $P < .05$, ** $P < .01$, and *** $P < .001$.

DEX-NP(OVA-CpG) is in accordance with the T_H1-skewing properties of the type of CpG ODN used.²⁹ Application of DEX-NP(OVA-CpG) to C3^{-/-} mice yielded no OVA-specific antibody response, which is in agreement with our finding of C3-dependent B-cell targeting of DEX-NP formulations. C3^{-/-} mice in general are characterized by diminished antibody production after protein immunization.^{32,33} However, MBL^{-/-} mice show no such defect¹⁵ but also mounted poor antibody responses after vaccination with DEX-NP(OVA-CpG). These findings underscore the strict requirement for lectin-induced

complement C3 activation on the DEX-NP surface for subsequent B-cell targeting, which in turn is indispensable for induction of antigen-specific antibody responses.

Indeed, it was shown previously that complement opsonization of pathogens and proteins resulted in their binding to CR1/2 on B cells.^{33,34} In case of an antigen-specific B-cell receptor (BCR), concomitant engagement of CR1/2 and the BCR strongly increased uptake of complement-opsonized material and, consequently, antibody production. Nucleic acids applied in soluble form were reported to activate autoreactive B cells.⁴ Therefore soluble CpG,

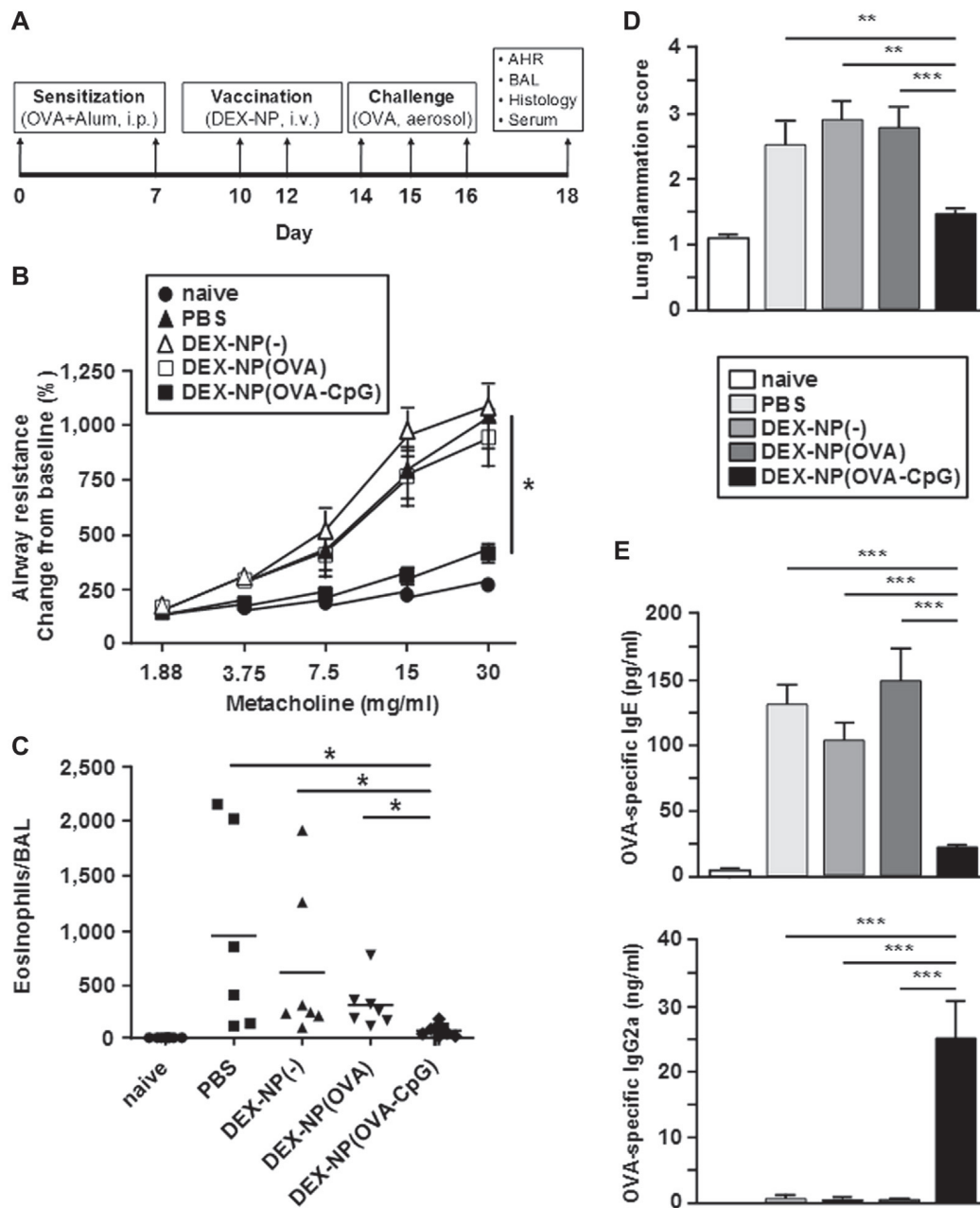


FIG 7. Treatment of OVA-sensitized mice with OVA/CpG-codelivering DEX-NPs prevents asthma. **A**, Experimental design. *i.p.*, Intraperitoneal; *i.v.*, intravenous. **B**, Airway resistance measurements of mice vaccinated with the indicated DEX-NP formulations or PBS alone after challenge and administration of methacholine (6 mice per group, representative of $n = 2$). **C**, Eosinophil numbers in bronchoalveolar lavage fluid (BAL; 300 cells counted per sample; 7 samples per group; compiled from $n = 2$). **D**, Lung inflammation scores (40 sections scored per group; 10-12 mice per group; $n = 2$). **E**, OVA-specific antibodies in sera (10-12 mice per group; compiled from $n = 2$ [a total of 20-24 mice per group]). Fig 7, B-E: * $P < .05$, ** $P < .01$, and *** $P < .001$.

when used as an adjuvant in conventional vaccination, might contribute to the risk of inducing autoimmune diseases. The strategy to use a CpG ODN-carrying nanocarrier with internalization that is not mediated by macropinocytosis, as in case of soluble CpG ODN, but depends on interaction of codelivered allergen with the BCR and of opsonizing C3 with CRI/2 might limit in part unwanted stimulation of autoreactive B cells.

Our finding of low antibody levels in $C3^{-/-}$ and $MBL^{-/-}$ mice immunized with DEX-NP(OVA-CpG) suggests that binding only

through OVA to a specific BCR is insufficient for effective NP uptake by B cells. Our finding of superior antibody induction by vaccination with particulate antigen/adjuvant combinations is in line with previous studies.³⁵ Thus far, this effect was largely attributed to stronger activation and antigen transfer to DCs. However, our results support that B-cell targeting might play a major role because it was previously shown that stimulated B cells that had internalized protein antigen through the BCR exerted potent $CD4^{+}$ T-cell stimulatory activity.³⁶ Therefore we cannot

rule out that in our setting DEX-NP–targeted B cells constitute the dominant APC population and strongly promote T_H1 polarization.

In models of systemic anaphylaxis and asthma, we show that vaccination of sensitized mice with our effective nanovaccine DEX-NP(OVA-CpG) completely inhibited allergic reactions. In both allergy models we observed an inhibition of OVA-specific T_H2 -associated IgG₁ and IgE induction at the expense of strongly upregulated T_H1 -associated IgG_{2a}. After NP therapy, in the anaphylaxis model body temperatures remained unaffected after challenge, and in the asthma model no lung inflammation was observed, probably because of the lack of IgE. In similar approaches poly(lactic-co-glycolic acid)–based NPs loaded with a relevant allergen plus CpG ODN were efficient in the treatment of house dust mite–induced asthma in a preventive setting³⁷ and for therapeutic application in a peanut allergy model.³⁸ Therefore the strategy to prevent or override T_H2 polarization and hence IgE production in favor of T_H1 for allergy treatment is well substantiated.

In these vaccination studies the authors proposed that their nanovaccines acted predominantly on the level of DC activation and antigen transfer to result in T_H1 -biased antibody responses. In this context the importance of B cells as the actual inducers of humoral immune responses was not assessed. Somewhat surprisingly, specific B-cell targeting has thus far been addressed only with regard to the delivery of chemotherapeutics to kill B lymphoma cells.³⁹ Toward this purpose, different types of nanocarriers have been conjugated with antibodies that recognize B cell–specific surface receptors.⁴⁰

In contrast to ongoing vaccination approaches that focus on DCs as critical inducers and regulators of T_H cell responses,³⁵ our work shows that the intrinsic B-cell targeting properties of lectin-coated NPs can be successfully exploited for improvement of AIT and that direct B-cell targeting is actually critical to mount antibody responses. Moreover, DEX-NPs *in vivo* also bound FDCs, which express CR1/2 as well, and serve to retain native antigen for long periods of time.³⁴ It remains to be shown whether binding of C3-opsonized NPs to FDCs yields according long-term effects of vaccination, including B-cell memory.

We show that other types of NPs coated with dextran or starch bound B cells in a complement-dependent manner. We propose that serum complement adsorption might be a general feature of lectin-coated NPs, which suggests that functionalization of nanovaccines with a lectin coating is sufficient to trigger recognition by the complement system and C3-mediated B-cell targeting. We observed complement-dependent targeting of DEX-NPs for human B cells, which suggests clinical relevance of this approach. In addition to lectin-dependent complement activation, other types of NPs can induce distinct pathways of innate immune recognition. Previously, we have shown that various types of polystyrene and silica NPs were opsonized by IgG and the complement component C1q after incubation with human plasma,¹² which is indicative of an activation of the classical complement pathway.⁴¹

We are confident that the strategy to design nanovaccines that mimic pathogens, such as by applying a lectin coat, will allow B cell–focused vaccinations to induce and shape humoral immune responses. In addition, the inherent property of nanocarriers to (co)deliver different kinds of biologicals and drugs can also be exploited to address the whole B-cell compartment (B cells and FDCs) through binding of

C3-opsonized nanocarriers to CR1/2. Further studies are planned to elucidate the potential of C3-mediated targeting of this compartment to yield long-lasting therapeutic effects through induction of B-cell memory, which also requires FDC-dependent long-term storage of native allergen.⁴²

Subsequent studies need to address the therapeutic potential of the B-cell compartment targeting nanovaccines that deliver complex allergens, as required for successful AIT.⁴³ For this, a nanocarrier can be coated with different allergens. Alternatively, nanocarriers are conjugated with one type of recombinant allergen out of a panel and are pooled before administration. In any case, the inherent B-cell targeting property of according nanovaccines might minimize unwanted binding of particulate allergens to IgE receptors, as observed for soluble allergens.

We thank E. von Stebut-Borschitz and B. Lorenz for providing us with $C3^{-/-}$ and $MBL^{-/-}$ mice. We thank I. Bellinghausen for helpful suggestions on the preparation of the manuscript.

Clinical implications: Lectin-coated NPs trigger complement activation, which results in deposition of activated C3 on the NP surface. C3-coated NPs target B cells through CR1/2. This mechanism can be exploited for allergy treatment by using NPs that codeliver an allergen and a T_H1 -promoting adjuvant, as shown in mouse models of anaphylaxis and asthma.

REFERENCES

1. Jutel M, Kosowska A, Smolinska S. Allergen immunotherapy: past, present, and future. *Allergy Asthma Immunol Res* 2016;8:191-7.
2. Gamazo C, Gastaminza G, Ferrer M, Sanz ML, Irache JM. Nanoparticle based-immunotherapy against allergy. *Immunotherapy* 2014;6:885-97.
3. Goldman B, DeFrancesco L. The cancer vaccine roller coaster. *Nat Biotechnol* 2009;27:129-39.
4. Christensen SR, Kashgarian M, Alexopoulou L, Flavell RA, Akira S, Shlomchik MJ. Toll-like receptor 9 controls anti-DNA autoantibody production in murine lupus. *J Exp Med* 2005;202:321-31.
5. Li D, Romain G, Flamar AL, Duluc D, Dullaers M, Li XH, et al. Targeting self- and foreign antigens to dendritic cells via DC-ASGPR generates IL-10-producing suppressive CD4⁺ T cells. *J Exp Med* 2012;209:109-21.
6. Sirvent S, Soria I, Cirauqui C, Cases B, Manzano AI, Diez-Rivero CM, et al. Novel vaccines targeting dendritic cells by coupling allergoids to nonoxidized mannan enhance allergen uptake and induce functional regulatory T cells through programmed death ligand 1. *J Allergy Clin Immunol* 2016;138:558-67.e11.
7. Akdis M, Akdis CA. Mechanisms of allergen-specific immunotherapy: multiple suppressor factors at work in immune tolerance to allergens. *J Allergy Clin Immunol* 2014;133:621-31.
8. Hartwell BL, Antunez L, Sullivan BP, Thati S, Sestak JO, Berkland C. Multivalent nanomaterials: learning from vaccines and progressing to antigen-specific immunotherapies. *J Pharm Sci* 2015;104:346-61.
9. Salvati A, Pitek AS, Monopoli MP, Prapainop K, Bombelli FB, Hristov DR, et al. Transferrin-functionalized nanoparticles lose their targeting capabilities when a biomolecule corona adsorbs on the surface. *Nat Nanotechnol* 2013;8:137-43.
10. Ritz S, Schöttler S, Kotman N, Baier G, Musyanovych A, Kuharev J, et al. Protein corona of nanoparticles: distinct proteins regulate the cellular uptake. *Biomacromolecules* 2015;16:1311-21.
11. Prantner AM, Scholler N. Biological barriers and current strategies for modifying nanoparticle bioavailability. *J Nanosci Nanotechnol* 2014;14:115-25.
12. Miltenyi S, Müller W, Weichel W, Radbruch A. High gradient magnetic cell separation with MACS. *Cytometry* 1990;11:231-8.
13. Keever-Taylor CA, Devine SM, Soiffer RJ, Mendizabal A, Carter S, Pasquini MC, et al. Characteristics of CliniMACS® System CD34-enriched T cell-depleted grafts in a multicenter trial for acute myeloid leukemia-Blood and Marrow Transplant Clinical Trials Network (BMT CTN) protocol 0303. *Biol Blood Marrow Transplant* 2012;18:690-7.
14. Docter D, Distler U, Storck W, Kuharev J, Wünsch D, Hahlbrock A, et al. Quantitative profiling of the protein coronas that form around nanoparticles. *Nat Protoc* 2014;9:2030-44.

15. Tenzer S, Docter D, Kuharev J, Musyanovych A, Fetz V, Hecht R, et al. Rapid formation of plasma protein corona critically affects nanoparticle pathophysiology. *Nat Nanotechnol* 2013;8:772-81.
16. Distler U, Kuharev J, Tenzer S. Biomedical applications of ion mobility-enhanced data-independent acquisition-based label-free quantitative proteomics. *Expert Rev Proteomics* 2014;11:675-84.
17. Wessels MR, Butko P, Ma M, Warren HB, Lage AL, Carroll MC. Studies of group B streptococcal infection in mice deficient in complement component C3 or C4 demonstrate an essential role for complement in both innate and acquired immunity. *Proc Natl Acad Sci U S A* 1995;92:11490-4.
18. Takahashi K, Gordon J, Liu H, Sastry KN, Epstein JE, Motwani M, et al. Lack of mannose-binding lectin-A enhances survival in a mouse model of acute septic peritonitis. *Microbes Infect* 2002;4:773-84.
19. Barnden MJ, Allison J, Heath WR, Carbone FR. Defective TCR expression in transgenic mice constructed using cDNA-based alpha- and beta-chain genes under the control of heterologous regulatory elements. *Immunol Cell Biol* 1998;76:34-40.
20. Shen L, Higuchi T, Tubbe I, Voltz N, Kruppen M, Pektor S, et al. A trifunctional dextran-based nanovaccine targets and activates murine dendritic cells, and induces potent cellular and humoral immune responses in vivo. *PLoS One* 2013;8:e80904.
21. Böhm L, Maxeiner J, Meyer-Martin H, Reuter S, Finotto S, Klein M, et al. IL-10 and regulatory T cells cooperate in allergen-specific immunotherapy to ameliorate allergic asthma. *J Immunol* 2015;194:887-97.
22. Buchweitz JP, Karmaus PW, Harkema JR, Williams KJ, Kaminski NE. Modulation of airway responses to influenza A/PR/8/34 by Delta9-tetrahydrocannabinol in C57BL/6 mice. *J Pharmacol Exp Ther* 2007;323:675-83.
23. Soltis RD, Hasz D, Morris MJ, Wilson ID. Studies on the nature of heat-labile anti-complementary activity in normal human serum. *Clin Exp Immunol* 1979;37:310-22.
24. Pike RN, Wijeyewickrema LC. The molecular switches controlling the interaction between complement proteases of the classical and lectin pathways and their substrates. *Curr Opin Struct Biol* 2013;23:820-7.
25. Ricklin D, Reis ES, Mastellos DC, Gros P, Lambris JD. Complement component C3—the “Swiss army knife” of innate immunity and host defense. *Immunol Rev* 2016;274:33-58.
26. Beltrame MH, Boldt AB, Catarino SJ, Mendes HC, Boschmann SE, Goeldner I, et al. MBL-associated serine proteases (MASPs) and infectious diseases. *Mol Immunol* 2015;67:85-100.
27. Bochner BS, Hamid Q. Advances in mechanisms of allergy. *J Allergy Clin Immunol* 2013;111(suppl):S819-23.
28. Heit A, Huster KM, Schmitz F, Schiemann M, Busch DH, Wagner H. CpG-DNA aided cross-priming by cross-presenting B cells. *J Immunol* 2004;172:1501-7.
29. Creticos PS, Schroeder JT, Hamilton RG, Balcer-Whaley SL, Khattignavong AP, Lindblad R, et al. Immunotherapy with a ragweed-toll-like receptor 9 agonist vaccine for allergic rhinitis. *N Engl J Med* 2006;355:1445-55.
30. Shirota H, Klinman DM. Recent progress concerning CpG DNA and its use as a vaccine adjuvant. *Expert Rev Vaccines* 2014;13:299-312.
31. Kasturi SP, Skountzou I, Albrecht RA, Koutsonanos D, Hua T, Nakaya HI, et al. Programming the magnitude and persistence of antibody responses with innate immunity. *Nature* 2011;470:543-7.
32. Fischer MB, Ma M, Goerg S, Zhou X, Xia J, Finco O, et al. Regulation of the B cell response to T-dependent antigens by classical pathway complement. *J Immunol* 1996;157:549-56.
33. Molina H, Holers VM, Li B, Fung Y, Mariathan S, Goellner J, et al. Markedly impaired humoral immune response in mice deficient in complement receptors 1 and 2. *Proc Natl Acad Sci U S A* 1996;93:3357-61.
34. Gustavsson S, Kinoshita T, Heyman B. Antibodies to murine complement receptor 1 and 2 can inhibit the antibody response in vivo without inhibiting T helper cell induction. *J Immunol* 1995;154:6524-8.
35. Cohn L, Delamarre L. Dendritic cell-targeted vaccines. *Front Immunol* 2014;5:255.
36. Constant S, Schweitzer N, West J, Ranney P, Bottomly K. B lymphocytes can be competent antigen-presenting cells for priming CD4+ T cells to protein antigens in vivo. *J Immunol* 1995;155:3734-41.
37. Joshi VB, Adamcakova-Dodd A, Jing X, Wongrakpanich A, Gibson-Corley KN, Thorne PS, et al. Development of a poly (lactic-co-glycolic acid) particle vaccine to protect against house dust mite induced allergy. *AAPS J* 2014;16:975-85.
38. Srivastava KD, Siefert A, Fahmy TM, Caplan MJ, Li XM, Sampson HA. Investigation of peanut oral immunotherapy with CpG/peanut nanoparticles in a murine model of peanut allergy. *J Allergy Clin Immunol* 2016;138:536-43.
39. Daver N, O'Brien S. Novel therapeutic strategies in adult acute lymphoblastic leukemia—a focus on emerging monoclonal antibodies. *Curr Hematol Malig Rep* 2013;8:123-31.
40. Sullivan-Chang L, O'Donnell RT, Tuscano JM. Targeting CD22 in B-cell malignancies: current status and clinical outlook. *BioDrugs* 2013;27:293-304.
41. Kusaykin M, Bakunina I, Sova V, Ermakova S, Kuznetsova T, Besednova N, et al. Structure, biological activity, and enzymatic transformation of fucoidans from the brown seaweeds. *Biotechnol J* 2008;3:904-15.
42. Heesters BA, Myers RC, Carroll MC. Follicular dendritic cells: dynamic antigen libraries. *Nat Rev Immunol* 2014;14:495-504.
43. Hoffmann HJ, Valovirta E, Pfaar O, Moingeon P, Schmid JM, Skaarup SH, et al. Novel approaches and perspectives in allergen immunotherapy. *Allergy* 2017;72:1022-34.

5.6 Publication 6

Sometimes less is more: Antibody amount determines the biodistribution and dendritic cell uptake of peptobrush nanoparticles in vivo

Submitted (October 2019) for ACS Nano

Sometimes less is more: Antibody amount determines

the biodistribution and dendritic cell uptake

of peptobrush nanoparticles in vivo

Cinja Kappel, †

† Department of Dermatology, University Medical Center of the Johannes Gutenberg
University Mainz, Langenbeckstrasse 1, D-55131 Mainz, Germany

& Institute for Organic Chemistry, Johannes Gutenberg University, Duesbergweg 10-14, D-
55099 Mainz, Germany

‡ Institute for Physical Chemistry, Johannes Gutenberg University, Welder Weg 11, D-55099
Mainz, Germany

TRON–Translational Oncology at the University Medical Center of the Johannes Gutenberg
University GmbH, Freiligrathstr. 12, Mainz 55131, Germany

§ Max Planck Institute for Polymer Research, Ackermannweg 10, 55128 Mainz, Germany

§ Biontech AG, An der Goldgrube 12, 55131, Mainz

Corresponding authors

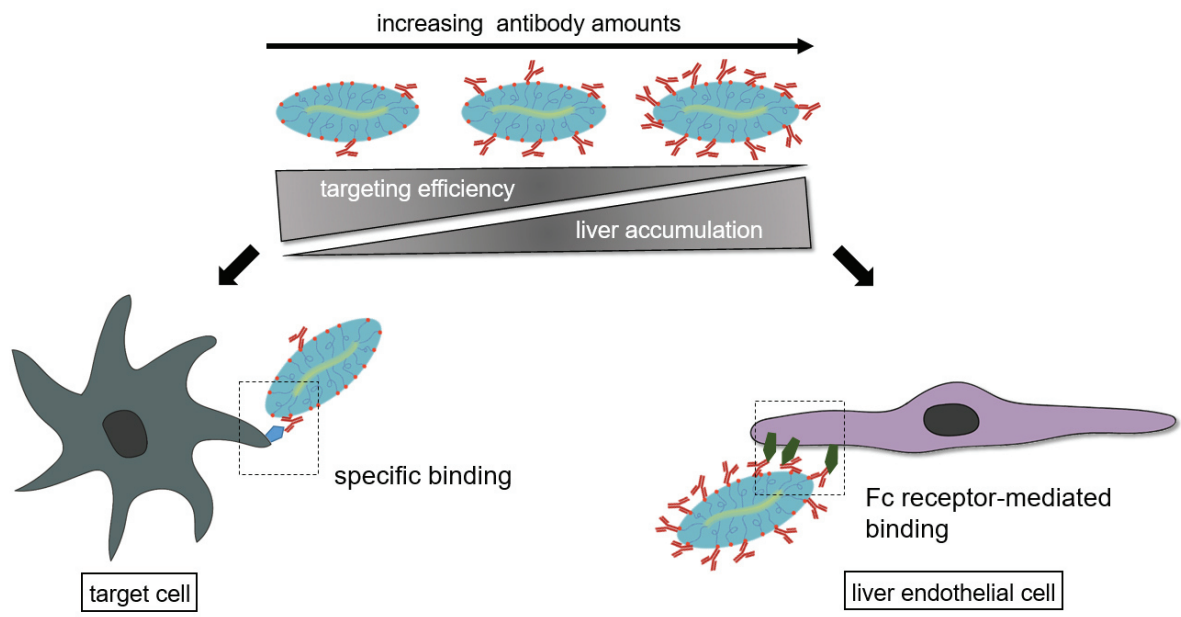
*E-mail: [REDACTED]

*E-mail: [REDACTED]

ABSTRACT

Despite considerable progress in the design of multi-functionalized nanoparticles (NP) to deliver drugs in a cell type-focused manner, their systemic application still often results in unwanted liver accumulation. The exact mechanisms contributing to this general observation have not been fully elucidated yet. Here we asked for the role of cell targeting antibody amount per NP as a determinant of NP liver accumulation. We used sarcosine-based peptobrushes (PB) which in an unconjugated form remain in the circulation for a long time (>24h) due to low unspecific cell binding. PB were labeled with a near infrared dye, and were conjugated with average numbers (2, 6 and 12) of antibodies specific for the dendritic cell (DC) selective surface receptor DEC205. We assessed the time-dependent biodistribution of PB-antibody conjugates by *in vivo/ex vivo* imaging and flow cytometry. We observed that PB-antibody conjugates were trapped in the liver. The extent of liver accumulation of PB-antibody conjugates correlated with the number of attached antibodies. In addition, liver endothelial cells are mostly responsible for retaining aDEC205 coated PB, via their Fc receptors (FcR). Accordingly, PB-antibody conjugates with an average of only two antibodies per brush showed lowest liver entrapment, and engaged DC in spleen and lymph nodes at highest extent. Altogether, our study underlines that liver endothelial cells play a yet scarcely acknowledged role in liver entrapment of antibody-coated NP, and that low antibody numbers on synthetic NP are both necessary to minimize liver accumulation and sufficient for specific cell targeting in other organs *in vivo*.

KEYWORDS nanoparticle, antibody, targeting, biodistribution, liver accumulation, liver endothelial cells, peptobrush



scheme 1, graphical abstract

During the last forty years, nanoparticles (NP) have evolved as carrier systems for tissue- and cell type-directed drug delivery. The first generation of NP developed for tumor targeting, e.g. Doxil, exploited passive accumulation in the vasculature within solid tumors by the enhanced permeability and retention (EPR) effect.¹ In contrast, reprogramming of our body own defense, the immune system, is currently attracting more and more interest. Myeloid cells, such as macrophages (Mph) and dendritic cells (DC), that are specialized to recognize and engulf pathogens² were shown to internalize NP that mimic pathogens in terms of size and may be recognized by innate immune defense mechanisms like the complement system.^{3,4} Mph degrade and internalize material more efficiently than DC, whereas DC potentially process pathogen-derived antigens and present them to T cells as a necessary step to induce antigen-specific T cell responses.⁵ Therefore, the design of NP that actively target DC to minimize unwanted binding/uptake by Mph and other cell types with endocytic and phagocytic capacity are in the focus of research.⁶

Active DC targeting can be achieved by NP-conjugated moieties that bind surface receptors specifically expressed by DC and not by Mph.⁷ These surface receptors need to exert endocytic activity in order to mediate internalization of an engaged NP. Besides derivatives of natural ligands such as carbohydrates⁸ or synthetically designed aptamers⁹, antibodies play a major role in this regard since they show high target affinity and specificity.¹⁰ The attachment of several antibodies per NP increases the overall avidity which may result in enhanced NP uptake, suggesting that an increase in valency of targeting moieties may be a desirable goal of NP design. However, it was also reported that lowered avidity can increase selectivity of cell targeting NP.¹¹ Commonly applied antibody conjugation strategies rely on a random functionalization or direct attachment to lysine moieties in the protein, leading to a non-oriented attachment of the antibody to the NP. If an antibody is attached to the NP in a non-oriented manner, the constant Fc (fragment crystallisable) part may be exposed and facilitate unwanted binding to Fc receptors that are widely expressed in the body.¹² Concerning the design of nano-vaccines for immunotherapeutic applications it remains an important issue to which extent the antibody density of a NP upon systemic application may affect its biodistribution on an organ level and its cell type-specific targeting properties in a time-dependent manner.¹³

So far, it has proven difficult to generate NP that are inert in terms of unspecific binding.⁴ Further, due to methodological problems, it has been a synthetic challenge to generate NP with a defined absolute antibody number¹⁴ or even defined average number in a reproducible and scalable manner.¹⁵ Moreover, so far comparative studies on the biodistribution of antibody-decorated NP have focused either on NP accumulation in distinct organs¹⁶ or on target cell type-specific binding.¹⁷

Therefore, our study aimed to delineate the role of antibody number on NP for their biodistribution on organ and single cell levels, the specificity of cell type targeting, and which non-targeted cell types may compete for NP engagement by which mechanisms. To this end, we employed a polysarcosine-based cylindrical polymer brush that was characterized by very low interaction with cells *in vivo*, resulting in long plasma circulation half-life.^{18,19,20,21,22} NP were conjugated with defined numbers of antibodies, namely 2, 6, and 12, targeting the surface receptor DEC205 (CD205), a type I cell surface protein predominantly expressed by DC.²³ Using these antibody-coated peptobrushes, we analysed their biodistribution by *in vivo* and *ex vivo* imaging and flow cytometry of liver, spleen and lymph node cells generating detailed on organ and cellular distribution of NPs related to the number of antibodies attached to their surface.

RESULTS

Polysarcosine-based peptobrushes can be precisely functionalized with an average numbers of antibodies

For synthesis of the polysarcosine-based cylindrical brush polymers, termed peptobrushes (PB), the backbone pLys₂₅₀ was used as a macroinitiator for the controlled-living ring-opening polymerization of sarcosine *N*-carboxy anhydride yielding polysarcosine side chains (Figure 1A). End group functionalization was achieved using azido-butyric acid pentafluorophenylester to obtain quantitative azide functionality allowing antibody conjugation. The hydrophilicity of the polysarcosine side chains provides a high biocompatibility, enzymatic, and oxidative biodegradability of the PB.²⁴ Furthermore, PB of different sizes were shown to display long circulation half-lives of up to 7 days in zebrafish embryos and in BALB/c mice.²²

CD8 α^+ conventional DC type 1 are characterized by expression of the C-type lectin receptor DEC205 (CD205) and are capable to cross-present antigen of exogenous origin via MHC-I to CD8 $^+$ T cells.²⁵ We and others have previously shown that antigen targeted to DEC205 by specific antibodies results in endocytic uptake by DC and efficient antigen presentation.^{17,23} Therefore, to address DC as a suitable target cell type for nano-vaccines, we used an anti-DEC205 antibody (aDEC205) for conjugation with PB. aDEC205 was modified with a DBCO linker to allow for chemoselective bioconjugation to azide groups on the peptobrush by strain promoted azide-alkyne cycloaddition (SPAAC), a well-established protocol for the attachment of antibodies to nanoparticles.²⁶ The conjugation to the brush, however, results in a more or less random manner since the reactive ester reacts with the primary amine of lysines within the antibody. As a consequence of this non-directive antibody conjugation to the NP surface, some of the NP-bound antibodies likely have an outward orientation of their Fc region, which may enable Fc receptor (FcR) mediated binding. Since antibody conjugation is performed according to established protocols at physiological temperature and pH, the structural integrity of the antibody is maintained. Moreover, purely by

stoichiometry a distinct average number of antibodies, namely 2, 6, and 12, were conjugated to PB (Figure 1B). Western blot analysis revealed complete conjugation of introduced antibodies (Figure 1C). UV-Vis spectroscopy confirmed conjugation of the desired numbers of antibodies per PB (Figure 1D). Multiangle dynamic light scattering (DLS) analysis demonstrated similar sizes of all PB formulations (Figure 1E). For detection of the PB in subsequent analysis the near infrared dye CW800 was conjugated by SPAAC.

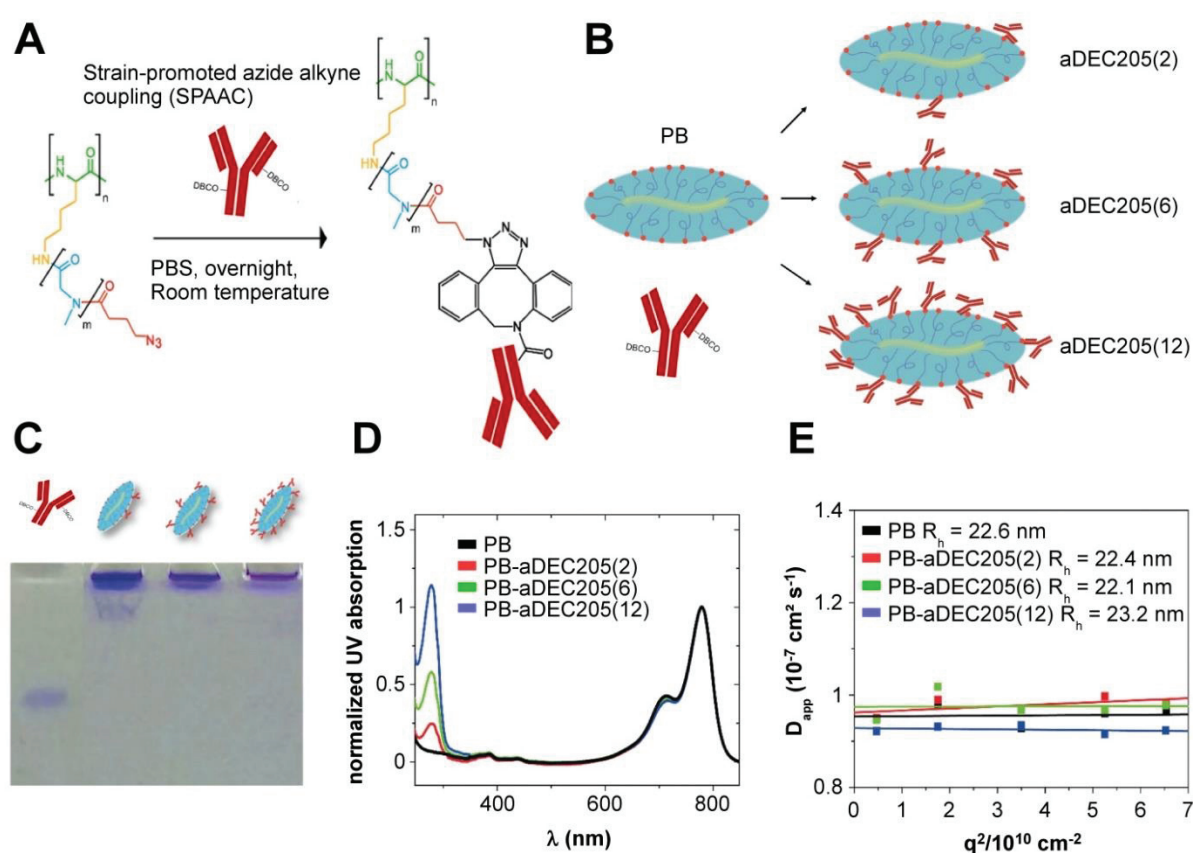


Figure 1. Synthesis and characterization of PB-antibody conjugates: A) scheme of strain-promoted azide-alkyne cycloaddition (SPAAC) reaction employed for antibody conjugation, B) schematic illustration of PB-aDEC205 antibody conjugates, C) Western blot and D) UV-VIS analysis of the effectivity of antibody conjugation, E) multi angle DLS analysis of PB-aDEC205 antibody conjugates.

The antibody number of PB correlates with their accumulation in the liver, and inversely correlates with their blood circulation time

We used the different PB-antibody conjugates with the three different antibody numbers to investigate the impact of increasing antibody density per PB on their pharmacokinetics and biodistribution after intravenous injection. For this, *in vivo* imaging was combined with *ex vivo* analysis of blood and internal organs. As expected, PB w/o antibody displayed a half life exceeding 24 h in blood (Figure 2A). All PB-antibody conjugates exhibited reduced blood circulation times which inversely correlated with the number of attached antibodies. This effect was most pronounced in case of PB conjugated with the highest number of antibodies (PB-aDEC205[12]). In accordance with the stealth-like properties, polysarcosine PB formulations w/o conjugated antibodies were scarcely detectable in any of the monitored internal organs at 24 h post injection (hpi) (Figure 2B, C). In contrast, all PB-antibody conjugates accumulated in the liver. The extent of liver deposition was lowest in case of PB conjugated with 2 antibodies (PB-aDEC205[2]), whereas PB with intermediate (PB-aDEC205[6]) and high (PB-aDEC205[12]) antibody numbers per brush accumulated at higher extent (almost 2-fold for PB-aDEC205[12]).

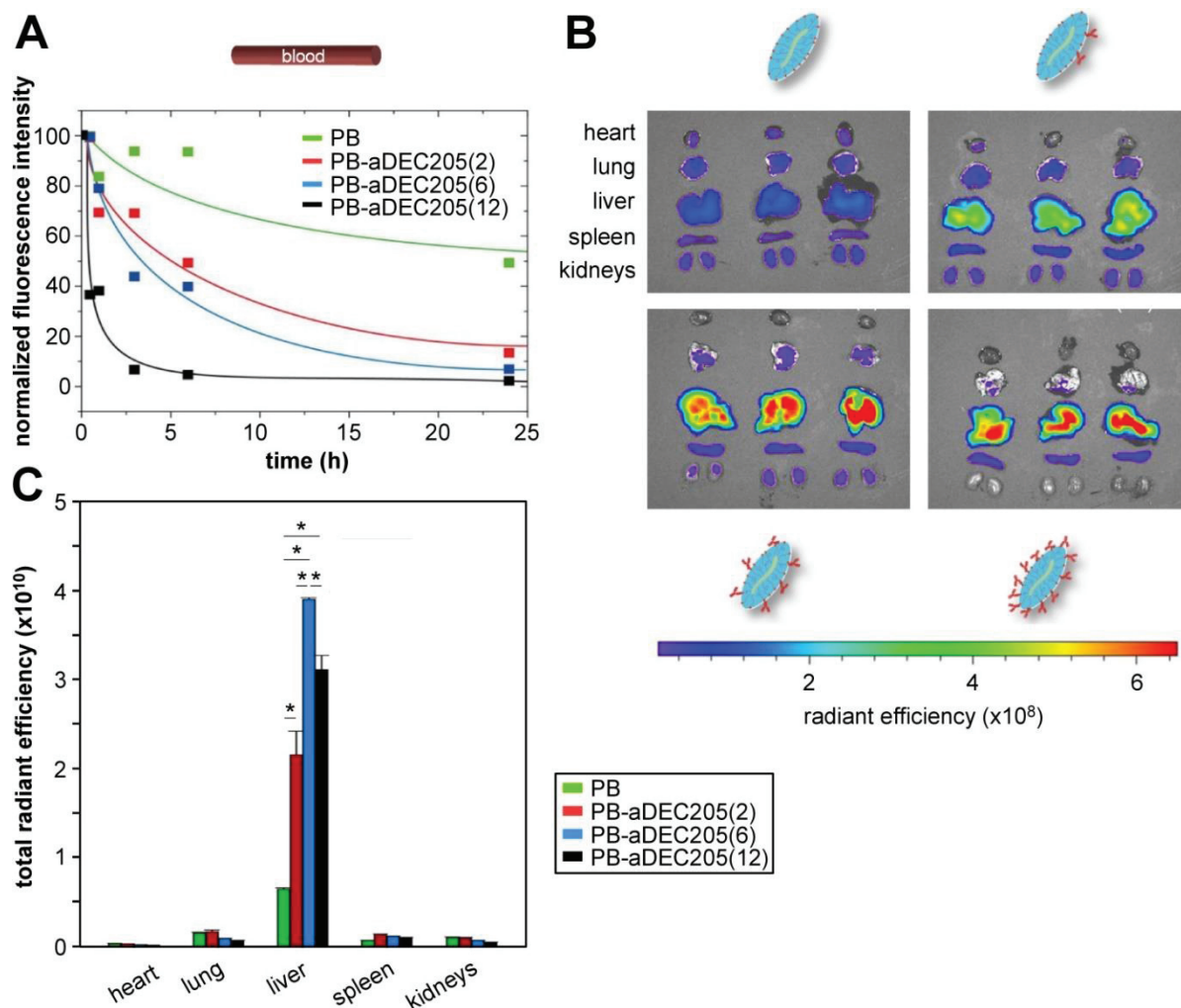


Figure 2. Intravenously injected PB-antibody conjugates accumulate in the liver in correlation with their antibody density: CW800-labeled PB formulations were systemically injected into mice. A) Blood was retrieved at the time points indicated, and contents of PB formulations were quantified by measurement of fluorescence intensities. Data indicate the mean of 3 samples per group and time point), B) fluorescence imaging of organs retrieved from mice 24 hpi of PB formulations, C) quantification of organ-specific fluorescence (see B). Data denote the mean \pm SEM of 6-8 samples per group (compiled from 2-3 experiments; one way ANOVA, significance: * $p < 0.001$).

To elucidate which cell populations within the liver engaged the various PBs, liver cell suspensions were subjected to flow cytometric analysis. Here we focused on non-parenchymal cell (NPC) types previously shown to interact with different types of NP.^{27,28} In accordance

with the imaging results we observed that the mean fluorescence intensity (MFI) of total liver NPC increased in correlation with PB antibody density at 3 hpi (Figure 3B, upper left panel).

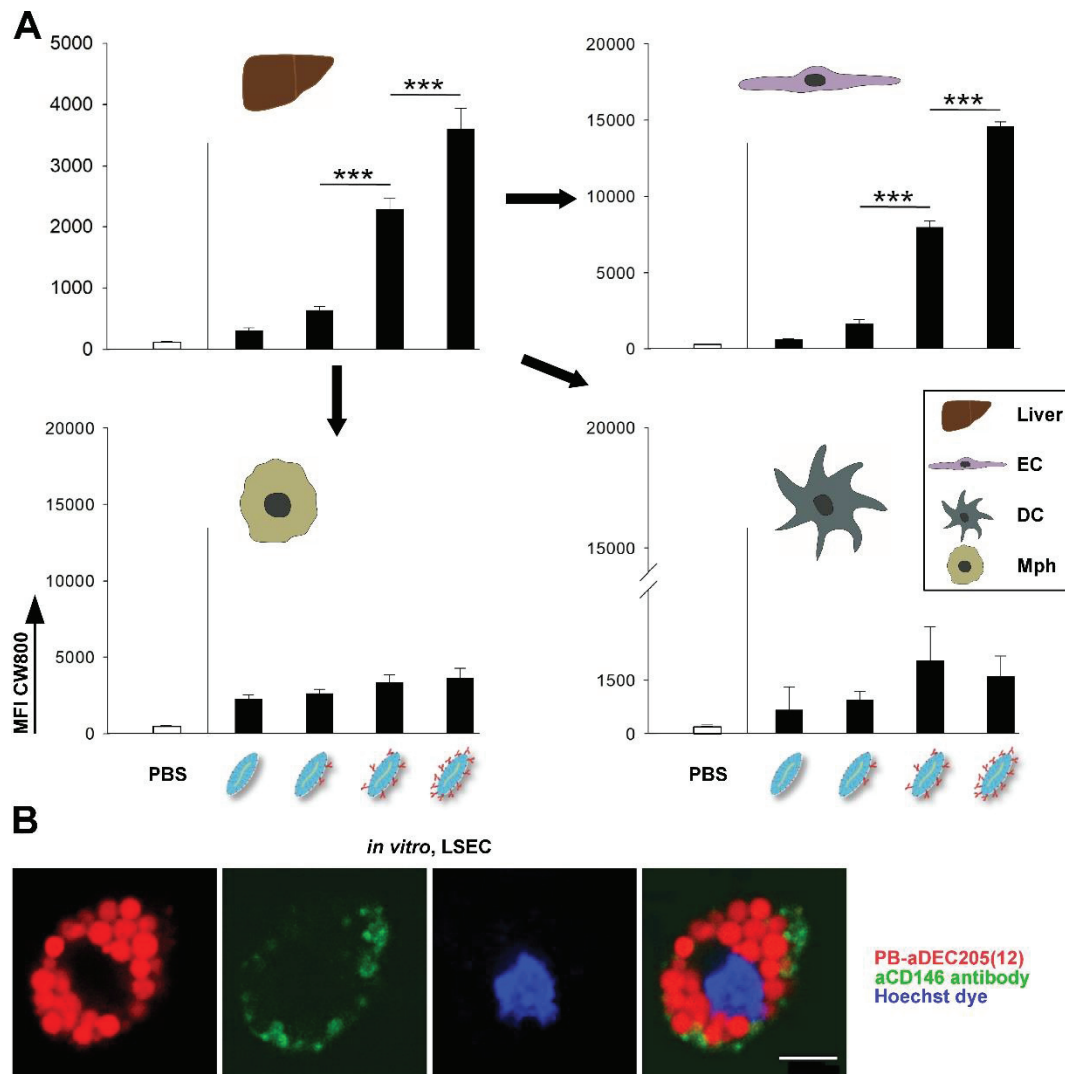


Figure 3. Liver endothelial cells bind PB-antibody conjugates in correlation with antibody density: A) Flow cytometric analyses of liver non-parenchymal cell (NPC) populations at various time points after systemic application of different PB formulations (3 hpi). Liver NPC of mice differentially treated with CW800-labeled PB formulations were prepared and incubated with antibodies to differentiate liver endothelial cells (EC: CD45⁻CD31⁺), macrophages (Mph: CD45⁺F4/80⁺), and dendritic cells (DC: CD45⁺CD11c⁺). Upper left panel: total liver NPC, upper right panel: liver endothelial cells, lower left panel: liver Mph, lower right panel: liver DC. Data denote the CW800 mean fluorescence intensities (MFI) of either NPC population (mean±SEM, n= 6-8 obtained from 2-3 experiments; one way ANOVA, ***p<0.001), B) confocal laser scanning microscopy image of a liver endothelial cell incubated

with PB-aDEC205(12) conjugate for 1h *in vitro*. Cells were incubated with anti-CD146 antibodies to identify liver sinusoidal endothelial cells (LSEC: CD45⁻CD31⁺CD146⁺), and Hoechst dye for nuclear staining. Scale bar: 10 μ m.

Further analysis of distinct liver NPC populations revealed that PB with intermediate/high antibody numbers were largely associated with liver endothelial cells (EC) (Figure 3). On the contrary, the antibody number of PBs had no major effect on engagement by liver macrophages (Mph) and DCs, as measured by MFI, which correlates to the number of NP per cell (Figure 3A) in the applied concentration range. In agreement, at 3 hpi the numbers of PB-positive liver NPC and EC correlated with the number of antibodies per PB, in contrast to Mph and DC (see Supp Figure 1). Application of PB with intermediate antibody numbers already resulted in maximal liver NPC and EC binding frequencies. However, as mentioned before for PB with high versus intermediate antibody density, a higher PB density per cell was observed in case of liver NPC and EC (see Figure 3).

These observations indicate that, the overall avidity as conferred by an intermediate number of antibodies per PB was sufficient to engage all liver EC (see Supp Figure 1). Second, the increase in the avidity of PB-antibody conjugates carrying a high versus intermediate number of antibodies per PB conjugate resulted in binding of more PB per EC. Due to prominent engagement of PB-antibody conjugates by liver EC we asked whether these NP were internalized. Within the EC population, liver sinusoidal endothelial cells (LSEC) have been reported to engulf NP.¹⁶ As depicted in Figure 3B, PB-aDEC205(12) were readily internalized *in vitro* by CD146⁺ LSEC after coincubation for 1h and accumulated in discrete intracellular vesicle-like structures.

Altogether, these findings indicate that at low antibody numbers per PB the unwanted side effect of liver accumulation is rather limited, whereas an intermediate antibody density was sufficient to confer predominant deposition of PB in the liver. Surprisingly, EC exerted a

stronger PB-antibody conjugate binding capacity than Mph (and DC), both in terms of numbers of PB-engulfing cells and the number of PB engaged per cell (MFI).

Liver EC engage PB-antibody conjugates via Fc γ receptors

LSEC have been demonstrated to play an important immunological role by internalizing immune complexes via different types of surface receptors including the Fc γ receptor IIb (Fc γ RIIb)²⁹ which is not expressed by other EC populations and largely confined to immune cells.³⁰ Since aDEC205 antibodies were conjugated to PB in a more or less random manner, the Fc part of a fraction of these may be accessible for binding. We tested the potential role of Fc/Fc γ RIIb interaction for the observed binding and uptake of PB-antibody conjugates by liver EC in blocking studies. To this end, isolated primary liver NPC were preincubated with an anti-Fc γ RIIb/FcRIII specific antibody known to block binding of the Fc part, and subsequently incubated with the different PB formulations. PB w/o antibody showed no cellular interaction at the applied concentration (number of nanoparticles). As observed before, the frequencies of EC and Mph that engaged PB-antibody conjugates correlated with increasing antibody number (Figure 4A). Again, each PB-antibody conjugate was bound by a higher fraction of EC than by Mph. In contrast, liver DC engaged all PB-antibody conjugates at comparable extent. Interestingly, *in vitro* blockade of Fc receptors (FcR) almost completely abrogated the binding of subsequently applied PB-antibody conjugates to EC and Mph whereas their binding to DC remained unaltered, suggesting that liver DC mostly bound the NP via specific interaction of the aDEC205 antibodies with their target, DEC205, whereas liver EC and Mph bound PB via surface Fc γ receptors. This observation indicates that within the liver EC population LSEC are largely responsible for binding of PB-antibody conjugates.

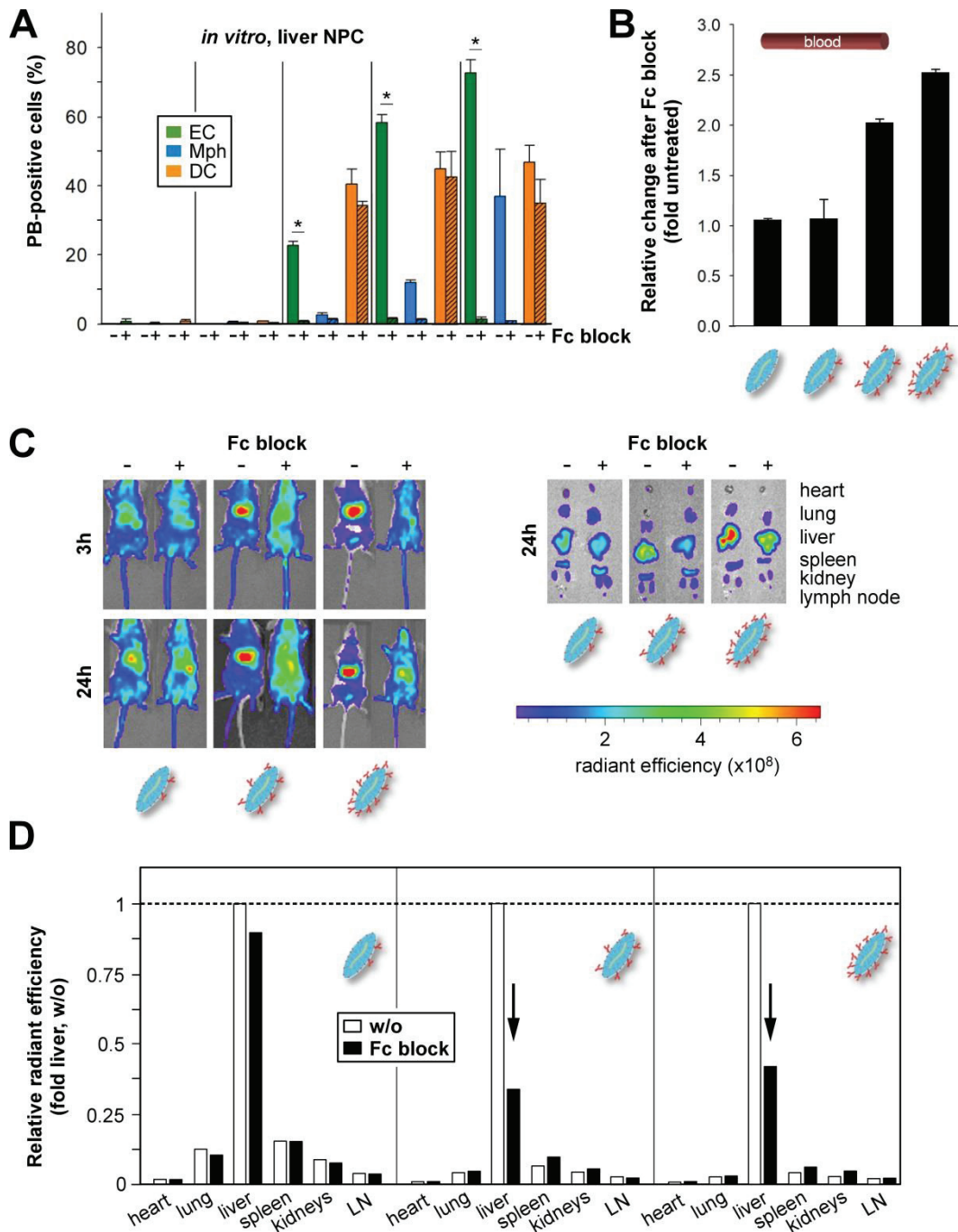


Figure 4. Blockade of Fc receptors reduces accumulation of PB-antibody conjugates in the liver. A), Isolated liver NPC were preincubated with a Fc γ RII/III blocking antibody (Fc block), followed by incubation with PB formulations for 1 h. Data denote the frequencies of PB-positive cells of the different NPC populations as assessed by flow cytometry (see legend of Figure 3A) and represent the mean \pm SEM (n= 3; one way ANOVA, *p<0.001), B-D), Mice were pretreated with Fc block, followed by systemic application of PB formulations, B) Blood was retrieved 6 hpi, and contents of PB formulations were quantified (mean \pm SEM, n= 2 per group). Blood contents of PB formulations in samples derived from mice subjected to Fc block

were normalized to the levels obtained w/o Fc block, C) Fluorescence imaging of mice at 3 and 24 hpi (left panel) and of organs retrieved 24 hpi (right panel), D) quantification of organ-specific fluorescence at 24 hpi (see C, right panel). Data denote the mean±SEM of 3 samples per group (one way ANOVA, significance: *p<0.001). LN: lymph node.

To confirm the role of FcR-mediated accumulation of antibody-decorated PB in the liver we injected the FcγRIIb/FcγRIII-blocking antibody prior to systemic application of PB formulations to block the FcR *in vivo*. While FcR blockade had no effect on the amount of circulating PB w/o antibody and in PB-aDEC205(2), significantly more PB-aDEC205(6) (2-fold) and PB-aDEC205(12) (2.5-fold) conjugates circulated in blood at 6 hpi (Figure 4B). In agreement, FcR blockade had no effect on liver deposition of the PB conjugates with no and low antibody content, but drastically reduced liver accumulation of PB-antibody conjugates with intermediate and high antibody contents at 3 (Figure 4C, left panel) and 24 hpi (Figure 4C, right panel, D). Notably, we observed no considerable increases of PB-antibody conjugate levels in other organs after FcR blockade.

Flow cytometric *ex vivo* analysis confirmed the FcR blockade-dependent decrease of binding of PB with intermediate/high antibody numbers to liver NPC (Figure 5, left upper panel, Supp Figure 2, left panel, Supp Figure 3A). Interestingly, Fc blockade strongly reduced binding of all PB-antibody conjugates to EC (Figure 5 and Supp Figure 2, Supp Figure 3B) Binding of PB-antibody conjugates to DC and Mph was somewhat affected, albeit below statistical significance (Figure 5, Supp Figure 2). Similar results were observed also at 24 hpi (Supp Figure 4).

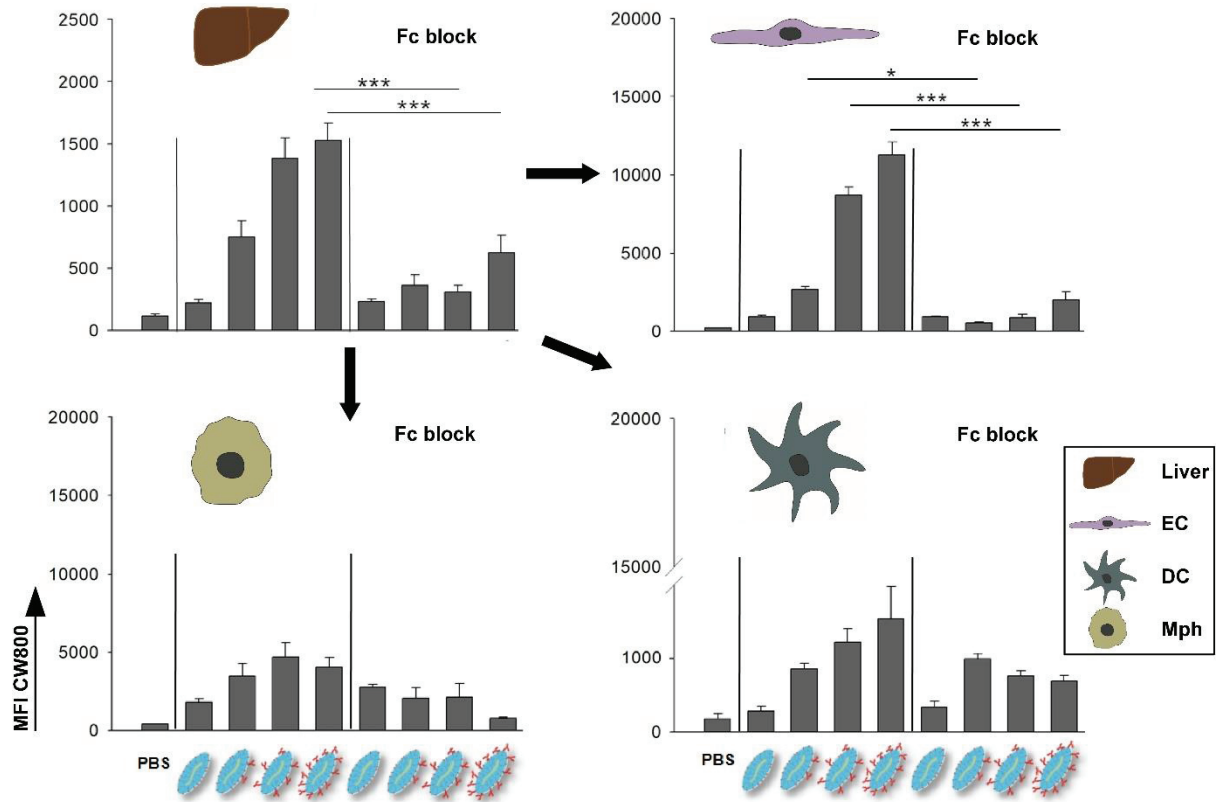


Figure 5: Blockade of Fc receptors diminishes binding of PB-antibody conjugates to liver EC. Mice were treated with Fc block and PB formulations as described in the legend of Figure 4. Liver NPC were prepared 3 hpi, and the MFI of CW800 of either NPC population was assessed by flow cytometry (see legend of Figure 3A). Upper left panel: total liver NPC, upper right panel: liver EC, lower left panel: liver Mph, lower right panel: liver DC. Data denote the mean \pm SEM (n= 6-8 obtained from 2-3 experiments; one way ANOVA, *p<0.05, ***p<0.001).

Taken together, these *in vivo* results indicate that also within the liver EC population LSEC are mostly responsible for the retention of NP decorated with intermediate/high numbers of antibodies in the liver by FcR-mediated binding of the antibodies' Fc part. This effect can be counter-acted by prior application of an FcR blocking antibody.

PB-antibody conjugates with low, but not with intermediate/high DC-targeting antibody number enrich in secondary lymphoid organs

An important prerequisite of NP-based immunotherapeutic approaches that target antigen presenting cells is that the NP reach secondary lymphoid organs, especially lymph nodes (LN) and spleen. Therefore, we next assessed at which extent intravenously injected PB that were functionalized with different amounts of antibodies were detectable in spleen and LN on a single cell level in a time-dependent manner.

As also shown before (see Figure 2C), more PB-antibody conjugates were trapped in the liver when functionalized with 6 or 12 antibodies per NP (PB-aDEC205[6], PB-aDEC205[12]) than with 2 antibodies per NP (PB-aDEC205[2]) (Figure 6, left panel). In general, the frequencies of PB-positive NPC were lower at 24 hpi versus 3 hpi. In spleen, 0.1-0.5% of *ex-vivo* isolated whole spleen cells were PB-positive for either PB-antibody formulation applied. Similar to liver NPC, the frequency of PB-positive spleen cells decreased over time. Only few LN cells engaged either PB-antibody conjugate when assessed at 3 hpi, whereas a significant percentage of LN cells had acquired PB at 24 hpi when these had been functionalized with low amounts of antibodies (PB-aDEC205(2)). Importantly, LN accumulation of PB decreased dramatically with increasing amounts of antibody per PB (Figure 6, right panel). Taken together, these observations suggest that in liver and spleen a fraction of PB-antibody conjugates is engaged by cells in a transient manner only, and that only PB with the low antibody number of 2, but not those with high antibody amounts of 6 and 12 accumulate at their target cells later on.

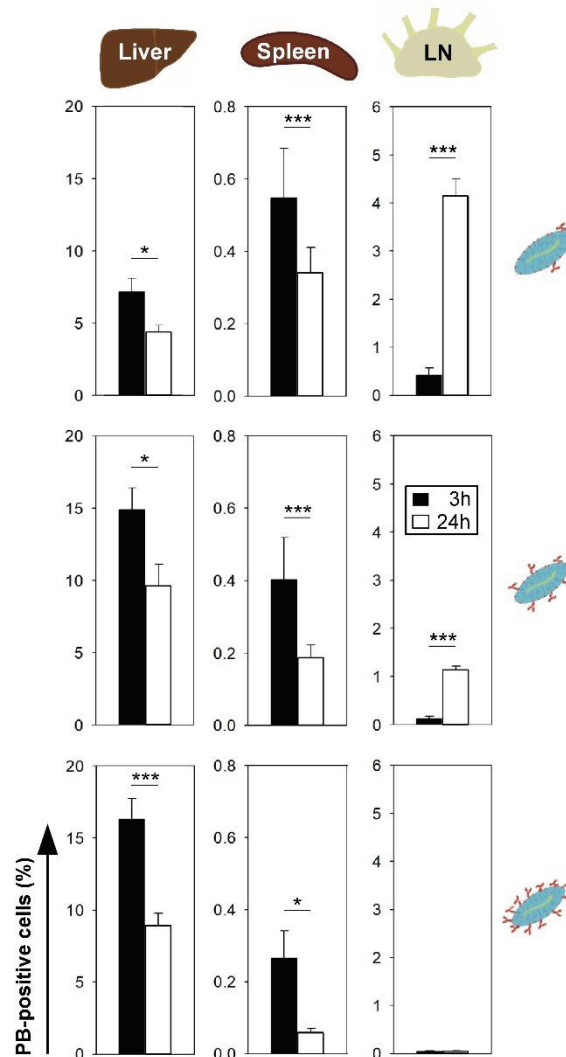


Figure 6: Liver accumulation of PB-antibody conjugates decreases over time, paralleled by increased levels in lymph nodes in case of low/intermediate PB antibody density. Mice were intravenously injected with PB formulations as described in the legend of Figure 2. After 3 hpi (black bars) and 24 hpi (white bars), liver, spleen and LN were retrieved. The fractions of PB-positive cells of the according cell suspensions (liver NPC, total spleen and LN cells) were assessed by flow cytometry. Data denote the mean±SEM (n=6-8, obtained from 2-3 experiments; one way ANOVA, *p<0.05, ***p<0.001).

The effectiveness of DC targeting inversely correlates with antibody number on the PB

We showed that in the liver the extent of accumulation of PB correlated directly with the number of attached antibodies (see Figure 3 and 5). In a complementary manner, the frequencies of PB-positive spleen (Figure 7) and LN cells (Supp Figure 5, upper panel) and even more

obviously their overall MFI (LN: Supp Figure 5, lower panel, spleen cells: Supp Figure 6) inversely correlated with the PB antibody density as assessed at 24 hpi. FcR blockade exerted no significant increase in frequencies of PB-positive cells or their MFI in either organ, indicating that PB primarily bound to cells in lymphatic organs via specific interactions of the aDEC205 antibody with its cellular target DEC205.

In spleen, DEC205⁺ DC co-express CD8a^{31,23}. Thus, within the total DC population, CD8a⁺ but not CD8a⁻ DC were specifically addressed by aDEC205-coated PB (Figure 7B). Notably, in both spleen and LN the extent of DC binding inversely correlated with the number of attached antibodies, presumably due to quantitative accumulation of PB with intermediate/high antibody numbers during first path effects in the liver. Notably, more than 8% of the CD8a⁺ DC, compared to less than 1% of CD8a⁻ DC in spleen took up significant amounts of PB that were coated with an average of 2 aDEC205 antibodies, thus proving the high efficacy of the DC targeting approach presented here.

In conclusion, PB with a low antibody number are superior to those with intermediate/high densities for targeting of DC in secondary lymphoid organs, since antibody-coated PB with >2 antibodies per PB are trapped by LSEC in the liver in a FcR-mediated fashion, preventing them from reaching their target cells. PB with low amounts of aDEC205 antibodies per NP effectively target DC in secondary lymphoid organs. Due to their long circulation half-life of around 6h, minimal entrapment in the liver, and effective binding to their target cells, these PB-antibody conjugates are an excellent platform for the development of DC-targeting nano-vaccines for systemic applications.

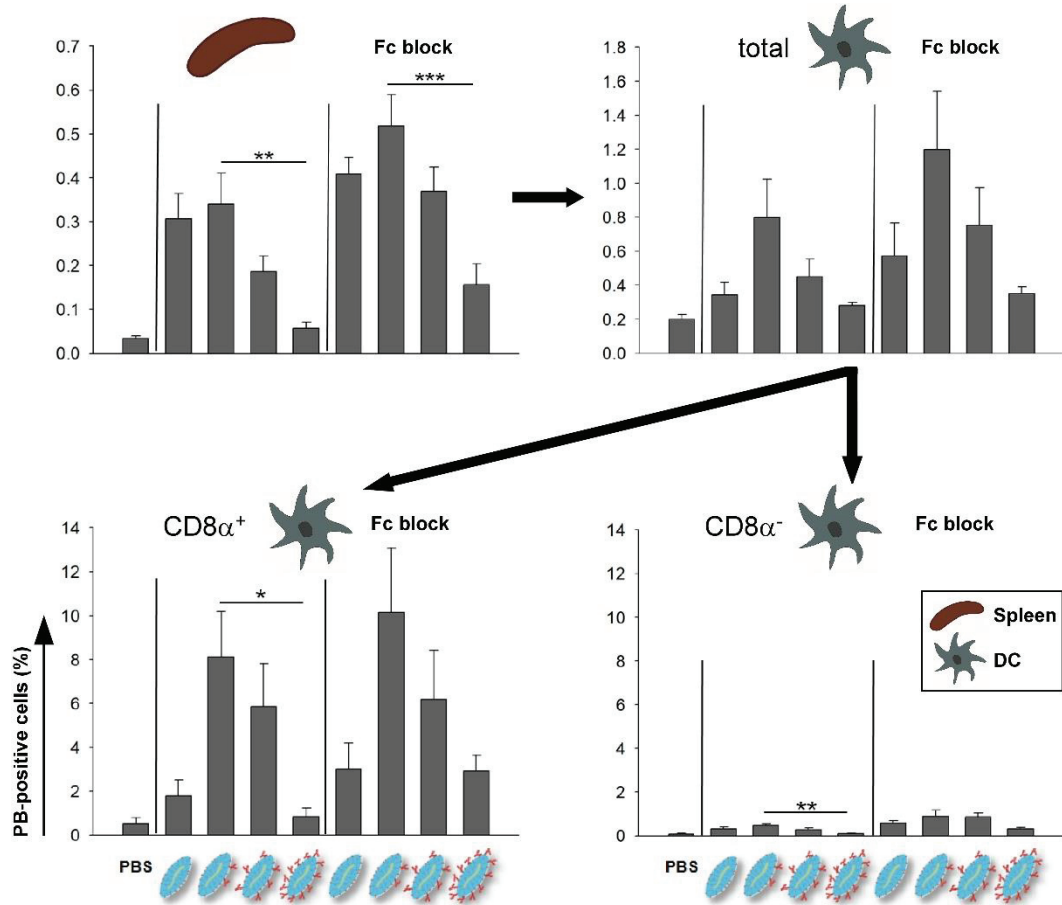


Figure 7: PB-antibody conjugates with low antibody density address DC most efficiently. Mice were treated with Fc block before i.v. injection of PB formulations as described in the legend of Figure 4. Spleens were retrieved at 24 hpi, and frequencies of PB-positive spleen cells, total DC and the CD8 α^+ versus CD8 α^- DC within the splenic leukocyte population were delineated by flow cytometry. A, B) Data denote the mean \pm SEM (n=6-8, obtained from 2-3 experiments; one way ANOVA, *p<0.05, **p<0.01, ***p<0.001).

Discussion

Liver entrapment is a common outcome of systemic NP application,²⁸ both in non-functionalized NP formulations^{32,33} and in those that are surface-functionalized with antibodies.^{34,35} Our study aimed to delineate the role of the number of a cell type-specific antibody per NP as a determinant of unwanted liver accumulation versus the desired antibody-mediated target cell specificity in secondary lymphoid organs. For this, we employed PB that are characterized by minimal cellular interactions and subsequently long plasma circulation half-life^{24,22} and allow fine tunable attachment of antibodies at lysine residues in a well reproducible manner. We chose a very common method of antibody attachment that comprises the reactions between an amine on the antibody surface and a reactive ester DBCO conjugate, which does not require complex modification of the antibody. It will, however, lead to an unspecific modification of the antibody and thus may lead to an exposure of FC domain upon attachment to nanoparticles.³⁶ As an alternative mode of antibody attachment, Kedmi and coworkers reported the use of peptides specifically binding the Fc region of antibodies for the modification of liposomes.³⁷ Moreover, Mailänder and coworkers have recently shown that polystyrene NP preadsorbed with an anti-CD63 antibody retained receptor-specific targeting *ex vivo*.³⁸ However, so far this concept is based on the interaction of an antibody with a hydrophobic NP surface, which may limit its application to other nanoparticles. By the robust synthesis approach³⁶ chosen in this study we generated PB-antibody formulations with adjustable average antibody numbers as an important prerequisite for comparative analysis. The polymer brushes used for the synthesis of different PB-antibody conjugates as well as the number of the near infrared dyes used for *in vivo* and *ex vivo* tracking were identical for all the different systems, enabling an unbiased comparative analysis. We show that PB conjugated with an average of only two antibodies on one hand displayed only moderate liver accumulation, and on the other hand efficiently addressed DC in secondary lymphatic organs.

So far, in most studies the liver-resident Mph population, termed Kupffer cells, has been described as the main NP binding cell population in the liver.^{27,39} In contrast, the contribution of LSEC in this regard is just becoming to be elucidated.^{16,40} We demonstrate that liver endothelial cells contribute at much higher extent to liver entrapment of antibody-coated PB formulations than Mph.

Our blocking studies suggest that LSEC and Mph via FcR bind the Fc part of aDEC205 antibodies attached to PB in a random manner. FcR blockade *in vitro* using isolated liver NPC almost abolished binding of PB-antibody conjugates to LSEC and Mph, and *in vivo* FcR blockade also potently reduced liver entrapment of PB-antibody conjugates.

Within the group of liver EC the subpopulation of CD146⁺ LSEC is specialized in uptake of exogenous material,⁴¹ and engaged PB-antibody conjugates most probably via FcγRIIB since LSEC express only this FcR.²⁹ LSEC are also equipped with various pattern recognition receptors e.g. of the C-type lectin family like the mannose receptor⁴² and L-SIGN⁴³ as well as different scavenger receptors.^{44,45} These sets of surface receptors enable efficient binding and uptake of a vast array of exogenous material by LSEC. Therefore, LSEC may considerably contribute to the frequently observed liver entrapment of different types of NP coated with antibodies³⁴ or carbohydrates⁴⁶ intended to address immune cells. Moreover, we show that LSEC phagocytose antibody-decorated PB. This finding is in line with the strong clearance rate of various kinds of particles by LSEC, both by endocytosis as shown e.g. for HIV-like particles⁴⁷ and phagocytosis as reported for allogeneic platelets.⁴⁸

A growing body of evidence has revealed the immunological role of LSEC to promote antigen-specific T cell tolerance by inducing regulatory CD4⁺ and CD8⁺ T cells specific for antigens derived from internalized material.^{41,49,50,51} The potency of LSEC to induce antigen-specific tolerance *de novo* has been demonstrated most recently by Liu and co-workers using PLGA-based NP that delivered a model antigen and were conjugated with ligands targeting the

mannose and scavenger receptors.⁵² In a model of allergic airway diseases, vaccination of mice with such NP attenuated allergic symptoms. Similar to LSEC, Kupffer cells also express numerous pattern recognition receptors⁵³ and were repeatedly shown to confer tolerance induction under homeostatic conditions⁵⁴ and to support a chronic disease course in virus-induced hepatitis.^{55,56} Nano-vaccines developed to induce and shape antigen-specific adaptive immune responses are intended to co-deliver antigen and adjuvant to antigen presenting cells like DC in order to promote stimulation of T cells.⁵⁷ Therefore, uptake of nanovaccines into LSEC and Kupffer cells should be circumvented for anticancer vaccines.

In light of the default state of LSEC and Kupffer cells to promote tolerance, the liver should not be perceived as an inert 'sponge' due to unwanted binding of a nano-vaccine to LSEC and Mph. Rather, the potency of LSEC and Mph to internalize nano-vaccines via their pattern recognition receptors and to actively counter-act the induction of adaptive immune responses by promoting tolerance should be considered in the design of nano-vaccines.

In our study, the specificity of aDEC205 antibody-mediated binding of PB to DEC205⁺ DC apparent in liver⁵⁸ and in the spleen²³ is confirmed by the observation that FcR blockade in isolated liver NPC *in vitro* and *in vivo* did not affect binding of PB antibody formulations to DC, whereas it blocked binding to LSEC and Mph. In mouse spleen about 1-2% of all leukocytes constitute CD11c⁺ DC.⁵⁹ Of these, only about 25% co-express CD8a and DEC205.⁶⁰ We show that PB-antibody conjugates specifically engaged CD8a⁺ DC cells in spleen since a remarkable amount of 8 % of this subpopulation were PB-positive, while engagement of CD8a⁻ DC was neglectable (Figure 7). Since resident DEC205⁺ DC in spleen, but not in LN, are known to co-express CD8a³¹, this demonstrates the high target specificity of the aDEC205-coated PB *in vivo*. The extent of PB binding to DC was highest in case of low antibody density (PB-aDEC205[2]) in spleen and LN, most probably due to stronger entrapment of PB-antibody conjugates with intermediate/high antibody density in the liver. Dose titration studies may

elucidate whether application of higher doses of PB-aDEC205(2) yields higher frequency of addressed CD8a⁺DEC205⁺ DC without increasing unspecific binding to non-DC. However, in early studies that assessed the potency of DC to evoke primary T cell responses, intrasplenic injection of 1,000 antigen presenting DC was sufficient to induce a maximal primary antiviral T cell response.⁶¹ Based on our results we estimate that PB-aDEC205(2) at the dose applied addressed sufficient splenic DC as would be required to evoke a sustained immune response.

We also observed that numbers of PB-antibody conjugates that were trapped in the liver decreased over time when assessed on isolated liver NPC (Fig. 6), but not by *in vivo* fluorescence imaging (Fig. 4c), which may indicate that other liver cell populations may engage PB-antibody conjugates transiently. A time-dependent decrease in PB-antibody conjugates deposition on organ level was also observed for total spleen cells (Fig. 6), but not for isolated splenic DC (data not shown). It appears possible that time-dependent intracellular degradation of the PB may alter the detection threshold for NP uptake. Further analyses are necessary to elucidate transient engagement by other cell types or metabolization of PB-antibody conjugates in spleen and liver. Of note, the overall decrease of PB binding by total liver and spleen cells between 3 and 24 hpi was paralleled by an increase in frequencies of PB-binding LN cells in case of PB with low/intermediate antibody density. Time-dependent redistribution of PB-antibody conjugates between the organs may also be a consequence of gradual loss of antibody binding to cellular FcR. However, systemic administration of Fc-blocking antibodies did not increase the overall accumulation of PB-antibody conjugates in spleen and LN (Figure 4), or the effectivity of DC targeting (Figure 7). Another cause for delayed appearance of PB with low/intermediate antibody density in LN could be that LN DC may not be able to sample blood-derived NP with the same efficacy as splenic DC or LSEC.^{62,63} Moreover, a fraction of PB conjugates may also be distributed by the lymphatic system known to transport of macromolecules at much lower speed than in blood.^{64,65} Of note, the time-dependent decrease

of PB-aDEC205(12) in liver and spleen was not accompanied by an increase in LN as observed for PB-aDEC205(2), suggesting that high avidity PB-aDEC205(12) antibody conjugates may subsequently bind FcR-expressing immune cells localized throughout the body, thus preventing their time-dependent redistribution towards their target cells.

We demonstrated that FcR blockade reduced liver accumulation of subsequently applied PB formulations with intermediate/high antibody density, and concomitantly increased their concentration in blood. However, this approach did not result in elevated binding of these PB-antibody formulations to DC as the intended target cell type in either organ monitored. A possible explanation is that FcR are rapidly recycled after antibody engagement,⁶⁶ and that PB released from the liver upon FcR blockade are rapidly engaged by FcR-expressing cells in other organs. Thus, FcR blockade may reduce unwanted binding of nano-vaccines to liver cells and thereby minimize potential antigen-specific tolerance induction by LSEC and Mph. However, it is not suitable to enhance addressing of intended target cells.

As mentioned above we are not aware of other comparative studies that addressed antibody density of NP a determinant of unspecific liver accumulation versus targeting cell type-specific binding. However, in several studies the role of antibody number and density for tissue accumulation has been addressed. For example, Zern and co-workers reported that a moderate number of ICAM-1 specific antibodies per NP achieved a better targeting specificity of inflamed vasculature expressing ICAM-1 than NP decorated with high antibody numbers.^{11, 14}

In order to avoid FcR binding, natural or engineered antibody fragments devoid of the Fc region, such as Fab fragments and single chain Fv fragments⁶⁷ as well as other epitope-binding moieties like affibodies⁶⁸ or aptamers⁹, may be used for NP decoration. In comparison to full antibodies these alternative targeting agents can offer higher affinity and improved pharmacokinetic properties.⁶⁷ It remains possible that PB formulations that utilize these antibody derivatives may yield even better DC targeting as observed for the full antibody

conjugates used in this study. However, full antibodies do not need expensive engineering and several of them are commercially available in GMP grade, thus facilitating clinical translation. Furthermore, the Fc part may play an additional functional role as exemplified for agonistic CD40 antibodies which require the Fc part to trigger target cell stimulation.⁶⁹

Moreover, as mentioned above, most types of functionalized NP tested so far show liver deposition at considerable extent after systemic application, largely irrespective of the kind of surface functionalization.^{32,35} Liver accumulation is the result of recognition of NP surface structures by pattern recognition receptors expressed by LSEC and Mph such as mannose⁷⁰ and scavenger receptors.⁷¹ Nano-vaccines often are intended to address antigen presenting cells to induce adaptive immune responses as required for tumor therapy and the treatment of chronic infections. Although *in vivo* stimulation of LSEC with TLR1/2⁷² and NOD2 ligands⁷³, or of Kupffer cells with TLR3 ligands⁷⁴ may convert their default tolerance-promoting state towards T effector cell induction, unwanted antigen delivery to tolerance-promoting LSEC⁴¹ and Mph⁵⁴ may diminish the success of vaccination. Therefore, taking into account that a fraction of any kind of nano-vaccines will likely be engaged by LSEC and Mph in the liver, adjuvants or optimized combinations thereof should be delivered which not only stimulate the intended target immune cell⁷⁵, but also LSEC and Mph to override their default state of tolerance induction.⁷⁶ Nevertheless, this work demonstrates that LSEC and liver Mph can be bypassed for the most part by using a highly inert NP and reducing the amount of targeting antibody on the NPs surface.

CONCLUSIONS

Our results indicate that decoration of NP with targeting antibodies that have an exposed Fc-residue results in pronounced liver accumulation upon intravenous application of the NP.

To demonstrate this, we generated sarcosine-based polymer brushes with defined average antibody numbers reaching from a “low” amount (2 molecules), over “intermediate” amount (6 molecules) to a high amount (12 molecules). These conjugates were similar in size and free of unbound antibodies. We were able to show that two antibodies are sufficient to reach an acceptable percentage of target cells in lymphoid organs while bypassing the liver. Peptobrushes decorated with more than two antibodies accumulate rapidly in the liver. We demonstrate that liver accumulation of antibody-coated NP is due to binding of NP surface antibodies to FcR expressed by LSEC. Most importantly, capture of antibody-coated NP by LSEC can be greatly reduced if antibody numbers per NP are kept low, thus preventing liver accumulation while retaining effective target-specific binding in secondary lymphatic organs. Since LSEC are potent inducers of antigen-specific tolerance, nano-vaccines intended to induce immunity should minimize uptake by LSEC and other FcR-expressing cells in order to prevent tolerance induction.

MATERIALS AND METHODS

Peptobrush (PB) synthesis

Synthesis of Sarcosine N-Carboxyanhydride

Synthesis of sarcosine NCA was performed as described with some modifications.^{24, 77} First, 20.52 g (230.2 mmol) sarcosine (dried under vacuum for 1 h) was weighed into a three-neck, round-bottom flask. Then, 300 mL of abs. THF (tetrahydrofuran) was added under a nitrogen flow, and 184 mmol of diphosgene were added using a syringe. This solution was mildly refluxed for 3 h. The outlet was connected to two gas washing bottles containing aqueous NaOH solution to neutralize phosgene, and Dry nitrogen was led through the solution for 3 h. The obtained brownish oil was dried under reduced pressure ($1 \cdot 10^{-3}$ mbar for 2 h). The obtained amorphous solid crude product was redissolved in 40 mL of THF and was precipitated using 300 mL of dry hexane. The solution was stored overnight in a -20 °C freezer. On the next day, the precipitated product was filtered under dry nitrogen atmosphere and dried sequentially for 60–90 min using dry nitrogen, and for 2 h under high vacuum in a sublimation apparatus. Then, the product was sublimated (85 °C, $1 \cdot 10^{-3}$ mbar), and was collected from the sublimation apparatus in a glovebox on the same day. The purified product (156 mmol, 68% yield,) (constitutes colorless crystallites with a melting point of 102–104 °C (lit:⁷⁸ 102-105 °C) was stored in a Schlenk tube at -80 °C, and was handled in a glovebox all times.

¹H NMR (300 MHz, CDCl₃): δ [ppm] = 4.22 (2 H, s, -CH₂-CO-), 2.86 (3 H, s, -CH₃).

Synthesis of Azido-butyric acid Pentafluorophenylester

γ -azido butyric acid (7.74 mmol) was dissolved in pre-dried THF, and triethylamine (15.0 mmol, 2 eq.) was added. The solution was stirred at room temperature for 30 min. Then,

two volumes of pentafluorophenol trifluoro acetat (15.0 mmol) were added dropwise. The reaction mixture was stirred over night at room temperature. Completion of the reaction was evaluated with TLC (thin layer chromatography). THF was distilled, and the remaining solid was dissolved first in dichloromethane, and then was extracted three times with water. The organic phase was dried with MgSO₄ and DCM (dichloromethane) was distilled off the product. The product was purified by column chromatography.

¹H NMR (400 MHz, CDCl₃): δ [ppm] = 3.46 (2 H, t, -CH₂-CH₂-CH₂-N₃), 2.80 (2 H, t, -CH₂-CH₂-CH₂-N₃), 2.05 (2 H, m, -CH₂-CH₂-CH₂-N₃).

¹⁹F NMR (400 MHz, CDCl₃): δ [ppm] = -153.95 (2F, d, *o*-CF), -158.90 (1F, t, *p*-CF), -163.32 (2F, t, *m*-CF).

PB synthesis

The synthesis was performed as described with some modifications.⁷⁸ The following stock solutions were prepared directly prior to use under dry nitrogen atmosphere: 228 mg ml⁻¹ DIPEA (diisopropylethylamin) in 3.7 mL DMF (dimethylformamid), 7.83 g Sarcosine NCA in 40 mL DMF and 218 mg azido-butyricacid pentafluorophenylester in 2 mL DMF. The following operations were performed under a steady flow of dry nitrogen. 0.80 mL (351 μmol) of DIPEA-DMF was added *via* syringe to a Schlenk tube containing 71 mg (292 μmol) of poly(L-lysine trifluoroacetate) (DP = 258) dissolved in 2 mL DMF solution. After 1 hour stirring, 16.8 mL (29 mmol) Sarcosine NCA in DMF was added. The solution was stirred at room temperature and kept at a constant pressure of 1.25 bar of dry nitrogen via the Schlenk line to prevent impurities from entering the reaction vessel while allowing CO₂ to escape. When the reaction was finished (completion of the reaction was confirmed by IR [infrared] spectroscopy by the disappearance of the NCA peaks), 0.95 mL azido-butyricacid pentafluorophenylester in DMF

(1.2 fold excess based on the amine groups) was added and the reaction mixture was stirred for 2 days at 40°C. The final azide functionalized polymer brush was precipitated in ether and centrifuged (4,500 rpm at 4°C for 15 min). After discarding the liquid fraction, fresh ether was added and the polymer was resuspended using a sonic bath. The suspension was centrifuged again and the procedure was repeated. The polymer was dissolved in MilliQ water, and purified using Amicon Ultra Centrifugal Filters (50 kDa, 4000xg, 4x20 min). After lyophilization, a colorless product was obtained. Yield: 63%.

Dye labeling of PB

The dyes AlexaFluor647-DBCO and 800CW-DBCO were conjugated to the PB *via* SPAAC. In a typical experiment, PB was dissolved in DPBS (Dulbecco's Phosphate Buffered Saline) ($c_{PB} = 50 \text{ g}\cdot\text{L}^{-1}$) and the dye was dissolved in DMSO ($c_{Dye} = 5 \text{ mM}$). As the reaction is quantitative, 1 eq. of the desired amount of dyes per brush was added. After incubation over night at RT under light exclusion, the reaction mixture was purified by Amicon Ultra Centrifugal Filter Devices to remove unbound dye (15 mL, 50 kDa, 4000xg, 10 times). The resulting solution was concentrated with Amicon Ultra Centrifugal Filter Devices (50 kDa, 4000xg) and filtered through sterile 0.22 μm Millex-GS filters. R_h was measured by DLS (dynamic light scattering) and FCS (fluorescence correlation spectroscopy). FCS was also used to prove the absence of unconjugated dye and to determine the number of dyes per brush. To evaluate quenching effects, emission spectra of the free dye and the dye-labeled PB were recorded, using solutions of the same optical density. If quenching effects were detected, the number of dyes determined by FCS were corrected by the extent of quenching.

Synthesis of DBCO-functionalized aDEC205

In a typical experiment, 2 eq. of DBCO-PEG₄-NHS-Ester (dissolved in DMSO (dimethylsulfoxide), $c = 10 \text{ g}\cdot\text{L}^{-1}$) were added to the antibodies. aDEC205 and ratIgG2a were used as received (dissolved in DPBS, $C_{\text{aDEC205}} = 4 - 7 \text{ g/L}$). After incubation over night at RT, the reaction mixture was purified by Amicon Ultra Centrifugal Filter Devices (15 mL, 10 kDa, 4000xg, 10 times) to remove unbound DBCO-PEG₄-NHS-Ester and NHS. Afterwards, preparative size-exclusion chromatography was performed using a Sepharose 4 FF XK 16/70 column (flow $0.5 \text{ ml}\cdot\text{min}^{-1}$) to remove aggregates (aDEC205-DBCO fraction 80 – 110 mL). The resulting solution was concentrated with Amicon Ultra Centrifugal Filter Devices (10 kDa, 4000xg) and filtered through sterile $0.22 \mu\text{m}$ Millex-GS filters. $R_{\text{h,antibody-DBCO}} = 5 - 6 \text{ nm}$. The antibody concentrations as well as the number of DBCO per bioactive component were determined by UV-VIS spectroscopy as described in literature.

Synthesis of dye labeled PLys250

PLys258 (20 mg, 320 nmol) were dissolved in 2 mL DPBS, and AlexaFluor647-NHS Ester (2.5 eq., 1 mg, 800 nmol) dissolved in DMSO ($160 \mu\text{L}$) was added. The reaction mixture was incubated overnight under light exclusion at RT. The reaction product was purified using Amicon Ultra Centrifugal Filter Devices (15 mL, 10 kDa, 4000xg, 20 times). $R_{\text{h}}(\text{FCS}) = 7.6 \text{ nm}$. Each molecule contained two dye residues as determined by FCS is 2. FCS analysis demonstrated that the solution contained 15 % of free dye, taken into account for calculations of the dye concentrations. The pLys concentration was determined by dividing the dye concentration of the conjugated dye by two.

Synthesis of dye labeled aDEC205

In a typical experiment, 2 eq. of AlexaFluor647-NHS Ester (dissolved in DMSO, $c = 5 \text{ mM}$) were added to the antibodies, respectively. aDEC205 antibody (clone NLDC145) was used as

received (dissolved in DPBS, $c_{aDEC205} = 4 - 7 \text{ g/L}$). After incubation over night at RT, the reaction mixture was purified using Amicon Ultra Centrifugal Filter Devices (15 mL, 10 kDa, 4000xg, 10 times) to remove unbound AlexaFluor647-NHS Ester and NHS. The resulting solution was filtered sequentially through Anotop 20 nm filters and sterile 0.22 μm Millex-GS filters. $R_{h,antibody-FD} = 5 - 6 \text{ nm}$. FCS shows that there is still 15-20 % free dye in the solution. The antibody concentration is calculated from the UV-Vis spectrum using the specific antibody absorption at 280 nm.

Synthesis of PB conjugates with aDEC205 and ratIgG2a

Antibody conjugates aimed to attach 2, 6 and 12 antibodies per PB were synthesized. The amount of the DBCO-modified antibody that was added to the brush depends on the number of DBCO (N_{DBCO}) per component. $1/(0.34 \cdot N_{DBCO})$ eq. of the DBCO-modified component (dissolved in DPBS, $c_{antibody-DBCO} = 5 - 15 \text{ g} \cdot \text{L}^{-1}$) were added to the dye-labeled brush dissolved in DPBS ($c_{PB} = 1 \cdot 10^{-5} - 1 \cdot 10^{-6} \text{ M}$). The reaction mixture was incubated over night at RT. To remove bridged brushes and unconjugated antibodies, PB-conjugates were purified *via* preparative SEC using a Sepharose 4 FF XK 16/70 column (flow $0.5 \text{ ml} \cdot \text{min}^{-1}$). The fraction from 55 mL to 75 mL was collected, concentrated using Amicon Ultra Centrifugal Filter Devices (50 kDa, 4000xg) and filtered through sterile 0.22 μm Millex-GS filters. Each conjugate was analyzed by DLS, FCS, UV-VIS spectroscopy and SDS-PAGE (sodium dodecyl sulfate polyacrylamide gel electrophoresis).

Biological Materials and Assays

Animals

Female C57/B16 (*in vitro* studies) and BALB/c (*in vivo* studies) mice were purchased from Envigo.

Antibodies

CD45-FITC (invitrogen), CD31-PE (eBioscience), CD11c-APC (eBioscience), F4/80-eFluor450 (invitrogen), CD19-AF488 (eBioscience), CD8a-PE (BD Pharmingen), aCD16/CD32 (clone 2.4G2), In Vivo Ready™ anti-mouse CD16/CD32 and isotype control (TONBO Bioscience).

Isolation of liver NPC

Non-parenchymal liver cells of female C57/B16 and BALB/c mice were isolated by an organ perfusion method including collagenase digestion as previously described.⁷⁹ In short, mice were anesthetized with a ketamine/rompun mixture and the abdominal cavity was opened. By cannulating the *vena portae*, 20 ml of HBSS (Hank's Balanced Salt Solution) (ThermoFisher Scientific) solution containing collagenase A (Sigma-Aldrich) and DNase I (Sigma-Aldrich) flushed the liver after the aorta had been cut. The liver, largely devoid of erythrocytes or other loosely bound cells, was then dissected into pieces and incubated for 15 min at 37 °C in a 50 ml tube containing the perfusion enzyme solution. After incubation the liver was put through a 70 µm nylon cell strainer and the enzymatic reaction was stopped with medium (DMEM (Dulbecco's Modified Eagle Medium) /F-12 GlutaMAX™, ThermoFisher Scientific). To remove hepatocytes the cell suspension was centrifuged at 300 g for 15 min. The remaining cells in the suspension were further purified by 30% Histodenz-HBSS gradient centrifugation

as specified before.⁸⁰ The obtained liver NPCs (non-parenchymal cells) were then either cultured in medium (DMEM/F-12, GlutaMAX™, ThermoFisher Scientific) (described in the following section) or subjected to antibody staining for subsequent flow cytometry analysis. For *ex vivo* studies the Liver Dissociation Kit from Milteny was used following the instructions.

In vitro NP incubation

After isolation, NPC were seeded into a non-treated 12-well plate in a volume of 1 ml and 1 million cells per well. NPC were treated with different brush-antibody conjugates at 37 °C for 1 h. For this 10¹² particles were used. Following incubation, NPC were rinsed on ice and transferred to flow cytometry tubes for staining.

Flow cytometry

Single cells suspensions of respective organs were obtained after mechanical digestion and filtering using 70 µm nylon cell strainer. Livers were digested previously using the Liver Dissociation Kit (Milteny). After lysis of erythrocytes (liver, spleen), cells were incubated with receptor-specific antibodies for FACS analysis. For this cell were washed (2 % FCS in PBS), and Fc receptors were blocked with aCD16/CD32 (2.4G2 clone) for 10 min. Afterwards, liver NPC were incubated with receptor-specific antibodies (CD45-FITC, CD31-PE, CD11c-APC and F4/80-eFluor450) for 20 min at 4 °C. Within the CD45⁺ liver NPC fraction, DC (CD11c⁺), EC (CD31⁺), and Mph (F4/80⁺) were identified according to expression of their corresponding lineage marker. Spleen and LN cells were incubated with CD11c-APC to detect DC, and in case of spleen cells in addition with CD8a-PE to differentiate CD8a⁺ and CD8a⁻ DC subpopulations. All antibodies were obtained from Thermo Scientific. Cells were fixed with 0.7 % PFA, and subjected to flow cytometry (Attune NxT Flow Cytometer, Thermo Scientific). Results were evaluated with Attune NxT Flow Cytometer Software.

cLSM (confocal laser scanning microscopy)

Liver NPC were incubated with 10^{12} particles for 1 h at 37 °C as described above. After washing the cells with PBS, Hoechst dye (2 μ M) was added and samples were incubated at RT for 30 min to stain the nucleus. To flag LSEC samples were incubated with a CD146-specific antibody (APC-labeled) for 20 min at 4 °C. Cells were washed twice with PBS and images were taken using a TCS SP5 Confocal Microscope at the Institute of Molecular Biology (IMB), Mainz.

Biodistribution and blood circulation

The PB-antibody conjugates (0.5-1.8 mg, equimolar amounts of PB) and Fc receptor blocking antibody (each 50 μ g) were injected i.v. into BALB/c mice. Particle injection followed 3 h after injection of the blocking antibody. The animals were imaged at the indicated time points using IVIS Spectrum Imaging System (Perkin Elmer) with excitation/emission filter set of 745/800nm. Blood was retrieved retroorbitally and also imaged to measure fluorescence intensities. Mice were sacrificed at the indicated time points, organs (liver, heart, lungs, spleen and inguinal as well as popliteal LN) were dissected and imaged as above. Fluorescence intensities are presented as total radiant efficiency ($[\text{p/s}]/[\mu\text{W}/\text{cm}^2] \times 10^8$).

ACKNOWLEDGEMENTS

The authors acknowledge funding by the DFG (SFB1066) and would like to thank XXXXXXXXXX and coworkers for their support, as well as the Institute of Molecular Biology (IMB).

ASSOCIATED CONTENT

The Supporting Information is available free of charge via the Internet at <http://pubs.acs.org>.

Binding of peptobrush derivatives to liver cell populations, effects of Fc receptor blockade on binding to liver cell populations, lymph node and spleen DC populations.

AUTHOR INFORMATION

Author Contributions

██████████ and ██████████ contributed equally to this work.

Notes

The authors declare no competing financial interest.

REFERENCES

1. Maeda, H.; Nakamura, H.; Fang, J., The EPR effect for macromolecular drug delivery to solid tumors: Improvement of tumor uptake, lowering of systemic toxicity, and distinct tumor imaging in vivo. *Advanced drug delivery reviews* **2013**, *65* (1), 71-9.
2. Germic, N.; Frangez, Z.; Yousefi, S.; Simon, H. U., Regulation of the innate immune system by autophagy: monocytes, macrophages, dendritic cells and antigen presentation. *Cell death and differentiation* **2019**, *26* (4), 715-727.
3. Shen, L.; Tenzer, S.; Storck, W.; Hobernik, D.; Raker, V. K.; Fischer, K.; Decker, S.; Dzionek, A.; Krauthausen, S.; Diken, M.; Nikolaev, A.; Maxeiner, J.; Schuster, P.; Kappel, C.; Verschoor, A.; Schild, H.; Grabbe, S.; Bros, M., Protein corona-mediated targeting of nanocarriers to B cells allows redirection of allergic immune responses. *The Journal of allergy and clinical immunology* **2018**, *142* (5), 1558-1570.
4. Bros, M.; Nuhn, L.; Simon, J.; Moll, L.; Mailander, V.; Landfester, K.; Grabbe, S., The Protein Corona as a Confounding Variable of Nanoparticle-Mediated Targeted Vaccine Delivery. *Frontiers in immunology* **2018**, *9*, 1760.
5. Hey, Y. Y.; O'Neill, H. C., Murine spleen contains a diversity of myeloid and dendritic cells distinct in antigen presenting function. *Journal of cellular and molecular medicine* **2012**, *16* (11), 2611-9.
6. Tran, T. H.; Tran, T. T. P.; Nguyen, H. T.; Phung, C. D.; Jeong, J. H.; Stenzel, M. H.; Jin, S. G.; Yong, C. S.; Truong, D. H.; Kim, J. O., Nanoparticles for dendritic cell-based immunotherapy. *International journal of pharmaceutics* **2018**, *542* (1-2), 253-265.
7. Frenz, T.; Grabski, E.; Duran, V.; Hozsa, C.; Stepczynska, A.; Furch, M.; Gieseler, R. K.; Kalinke, U., Antigen presenting cell-selective drug delivery by glycan-decorated nanocarriers. *European journal of pharmaceutics and biopharmaceutics : official journal of Arbeitsgemeinschaft fur Pharmazeutische Verfahrenstechnik e.V* **2015**, *95* (Pt A), 13-7.
8. Mohr, N.; Kappel, C.; Kramer, S.; Bros, M.; Grabbe, S.; Zentel, R., Targeting cells of the immune system: mannosylated HPMa-LMA block-copolymer micelles for targeting of dendritic cells. *Nanomedicine (London, England)* **2016**, *11* (20), 2679-2697.
9. Hu, P. P., Recent Advances in Aptamers Targeting Immune System. *Inflammation* **2017**, *40* (1), 295-302.
10. Sivaram, A. J.; Wardiana, A.; Howard, C. B.; Mahler, S. M.; Thurecht, K. J., Recent Advances in the Generation of Antibody-Nanomaterial Conjugates. *Advanced healthcare materials* **2018**, *7* (1).
11. Zern, B. J.; Chacko, A. M.; Liu, J.; Greineder, C. F.; Blankemeyer, E. R.; Radhakrishnan, R.; Muzykantov, V., Reduction of nanoparticle avidity enhances the selectivity of vascular targeting and PET detection of pulmonary inflammation. *ACS nano* **2013**, *7* (3), 2461-9.
12. Sondermann, P.; Szymkowski, D. E., Harnessing Fc receptor biology in the design of therapeutic antibodies. *Current opinion in immunology* **2016**, *40*, 78-87.
13. Alkilany, A. M.; Zhu, L.; Weller, H.; Mews, A.; Parak, W. J.; Barz, M.; Feliu, N., Ligand density on nanoparticles: A parameter with critical impact on nanomedicine. *Advanced drug delivery reviews* **2019**.
14. Faria, M.; Bjornmalm, M.; Thurecht, K. J.; Kent, S. J.; Parton, R. G.; Kavallaris, M.; Johnston, A. P. R.; Gooding, J. J.; Corrie, S. R.; Boyd, B. J.; Thordarson, P.; Whittaker, A. K.; Stevens, M. M.; Prestidge, C. A.; Porter, C. J. H.; Parak, W. J.; Davis, T. P.; Crampin, E. J.; Caruso, F., Minimum information reporting in bio-nano experimental literature. *Nature nanotechnology* **2018**, *13* (9), 777-785.
15. Buhler, J.; Gietzen, S.; Reuter, A.; Kappel, C.; Fischer, K.; Decker, S.; Schaffel, D.; Koynov, K.; Bros, M.; Tubbe, I.; Grabbe, S.; Schmidt, M., Selective uptake of cylindrical

poly(2-oxazoline) brush-antiDEC205 antibody-OVA antigen conjugates into DEC-positive dendritic cells and subsequent T-cell activation. *Chemistry* **2014**, *20* (39), 12405-10.

16. Bargheer, D.; Giemsa, A.; Freund, B.; Heine, M.; Waurisch, C.; Stachowski, G. M.; Hickey, S. G.; Eychmuller, A.; Heeren, J.; Nielsen, P., The distribution and degradation of radiolabeled superparamagnetic iron oxide nanoparticles and quantum dots in mice. *Beilstein journal of nanotechnology* **2015**, *6*, 111-123.

17. Shen, L.; Krauthauser, S.; Fischer, K.; Hobernik, D.; Abassi, Y.; Dzionek, A.; Nikolaev, A.; Voltz, N.; Diken, M.; Krummen, M.; Montermann, E.; Tubbe, I.; Lorenz, S.; Strand, D.; Schild, H.; Grabbe, S.; Bros, M., Vaccination with trifunctional nanoparticles that address CD8(+) dendritic cells inhibits growth of established melanoma. *Nanomedicine (London, England)* **2016**, *11* (20), 2647-2662.

18. Birke, A.; Ling, J.; Barz, M., Polysarcosine-containing copolymers: Synthesis, characterization, self-assembly, and applications. *Progress in Polymer Science* **2018**, *81*, 163-208.

19. Klein, P. M.; Klinker, K.; Zhang, W.; Kern, S.; Kessel, E.; Wagner, E.; Barz, M., Efficient Shielding of Polyplexes Using Heterotelechelic Polysarcosines. *Polymers* **2018**, *10* (6).

20. Negwer, I.; Best, A.; Schinnerer, M.; Schafer, O.; Capeloa, L.; Wagner, M.; Schmidt, M.; Mailander, V.; Helm, M.; Barz, M.; Butt, H. J.; Koynov, K., Monitoring drug nanocarriers in human blood by near-infrared fluorescence correlation spectroscopy. *Nature communications* **2018**, *9* (1), 5306.

21. Zimpel, A.; Al Danaf, N.; Steinborn, B.; Kuhn, J.; Hohn, M.; Bauer, T.; Hirschle, P.; Schrimpf, W.; Engelke, H.; Wagner, E.; Barz, M.; Lamb, D. C.; Lachelt, U.; Wuttke, S., Coordinative Binding of Polymers to Metal-Organic Framework Nanoparticles for Control of Interactions at the Biointerface. *ACS nano* **2019**, *13* (4), 3884-3895.

22. Fenaroli, F.; Repnik, U.; Xu, Y.; Johann, K.; Van Herck, S.; Dey, P.; Skjeldal, F. M.; Frei, D. M.; Bagherifam, S.; Kocere, A.; Haag, R.; De Geest, B. G.; Barz, M.; Russell, D. G.; Griffiths, G., Enhanced Permeability and Retention-like Extravasation of Nanoparticles from the Vasculature into Tuberculosis Granulomas in Zebrafish and Mouse Models. *ACS nano* **2018**, *12* (8), 8646-8661.

23. Bonifaz, L. C.; Bonnyay, D. P.; Charalambous, A.; Darguste, D. I.; Fujii, S.; Soares, H.; Brimnes, M. K.; Moltedo, B.; Moran, T. M.; Steinman, R. M., In vivo targeting of antigens to maturing dendritic cells via the DEC-205 receptor improves T cell vaccination. *The Journal of experimental medicine* **2004**, *199* (6), 815-24.

24. Ulbricht, J.; Jordan, R.; Luxenhofer, R., On the biodegradability of polyethylene glycol, polypeptoids and poly(2-oxazoline)s. *Biomaterials* **2014**, *35* (17), 4848-61.

25. <Shortman_et_al-2010-Immunological_Reviews.pdf>

26. Yi, G.; Son, J.; Yoo, J.; Park, C.; Koo, H., Application of click chemistry in nanoparticle modification and its targeted delivery. *Biomaterials research* **2018**, *22*, 13.

27. Sadauskas, E.; Wallin, H.; Stoltenberg, M.; Vogel, U.; Doering, P.; Larsen, A.; Danscher, G., Kupffer cells are central in the removal of nanoparticles from the organism. *Particle and fibre toxicology* **2007**, *4*, 10.

28. Zhang, Y. N.; Poon, W.; Tavares, A. J.; McGilvray, I. D.; Chan, W. C. W., Nanoparticle-liver interactions: Cellular uptake and hepatobiliary elimination. *Journal of controlled release : official journal of the Controlled Release Society* **2016**, *240*, 332-348.

29. Ganesan, L. P.; Kim, J.; Wu, Y.; Mohanty, S.; Phillips, G. S.; Birmingham, D. J.; Robinson, J. M.; Anderson, C. L., FcγRIIb on liver sinusoidal endothelium clears small immune complexes. *Journal of immunology* **2012**, *189* (10), 4981-8.

30. Anania, J. C.; Chenoweth, A. M.; Wines, B. D.; Hogarth, P. M., The Human Fcγ₂RII (CD32) Family of Leukocyte FcR in Health and Disease. *Frontiers in immunology* **2019**, *10*, 464.
31. <Kronin et al. - 2000 - DEC-205 as a marker of dendritic cells with regulatory effects on CD8 T cell responses.pdf>.
32. Tate, J. A.; Petryk, A. A.; Giustini, A. J.; Hoopes, P. J., In vivo biodistribution of iron oxide nanoparticles: an overview. *Proceedings of SPIE--the International Society for Optical Engineering* **2011**, *7901*, 790117.
33. De Jong, W. H.; Hagens, W. I.; Krystek, P.; Burger, M. C.; Sips, A. J.; Geertsma, R. E., Particle size-dependent organ distribution of gold nanoparticles after intravenous administration. *Biomaterials* **2008**, *29* (12), 1912-9.
34. Cheng, W. W.; Allen, T. M., Targeted delivery of anti-CD19 liposomal doxorubicin in B-cell lymphoma: a comparison of whole monoclonal antibody, Fab' fragments and single chain Fv. *Journal of controlled release : official journal of the Controlled Release Society* **2008**, *126* (1), 50-8.
35. Chattopadhyay, N.; Fonge, H.; Cai, Z.; Scollard, D.; Lechtman, E.; Done, S. J.; Pignol, J. P.; Reilly, R. M., Role of antibody-mediated tumor targeting and route of administration in nanoparticle tumor accumulation in vivo. *Molecular pharmaceuticals* **2012**, *9* (8), 2168-79.
36. Jain, N.; Smith, S. W.; Ghone, S.; Tomczuk, B., Current ADC Linker Chemistry. *Pharmaceutical research* **2015**, *32* (11), 3526-40.
37. Kedmi, R.; Veiga, N.; Ramishetti, S.; Goldsmith, M.; Rosenblum, D.; Dammes, N.; Hazan-Halevy, I.; Nahary, L.; Leviatan-Ben-Arye, S.; Harlev, M.; Behlke, M.; Benhar, I.; Lieberman, J.; Peer, D., A modular platform for targeted RNAi therapeutics. *Nature nanotechnology* **2018**, *13* (3), 214-219.
38. Tonigold, M.; Simon, J.; Estupinan, D.; Kokkinopoulou, M.; Reinholz, J.; Kintzel, U.; Kaltbeitzel, A.; Renz, P.; Domogalla, M. P.; Steinbrink, K.; Lieberwirth, I.; Crespy, D.; Landfester, K.; Mailander, V., Pre-adsorption of antibodies enables targeting of nanocarriers despite a biomolecular corona. *Nature nanotechnology* **2018**, *13* (9), 862-869.
39. Samuelsson, E.; Shen, H.; Blanco, E.; Ferrari, M.; Wolfram, J., Contribution of Kupffer cells to liposome accumulation in the liver. *Colloids and surfaces. B, Biointerfaces* **2017**, *158*, 356-362.
40. Park, J. K.; Utsumi, T.; Seo, Y. E.; Deng, Y.; Satoh, A.; Saltzman, W. M.; Iwakiri, Y., Cellular distribution of injected PLGA-nanoparticles in the liver. *Nanomedicine : nanotechnology, biology, and medicine* **2016**, *12* (5), 1365-74.
41. Knolle, P. A.; Wohlleber, D., Immunological functions of liver sinusoidal endothelial cells. *Cellular & molecular immunology* **2016**, *13* (3), 347-53.
42. Malovic, I.; Sorensen, K. K.; Elvevold, K. H.; Nedredal, G. I.; Paulsen, S.; Erofeev, A. V.; Smedsrod, B. H.; McCourt, P. A., The mannose receptor on murine liver sinusoidal endothelial cells is the main denatured collagen clearance receptor. *Hepatology* **2007**, *45* (6), 1454-61.
43. Seckert, C. K.; Renzaho, A.; Tervo, H. M.; Krause, C.; Deegen, P.; Kuhnappel, B.; Reddehase, M. J.; Grzimek, N. K., Liver sinusoidal endothelial cells are a site of murine cytomegalovirus latency and reactivation. *Journal of virology* **2009**, *83* (17), 8869-84.
44. Oie, C. I.; Appa, R. S.; Hilden, I.; Petersen, H. H.; Gruhler, A.; Smedsrod, B.; Hansen, J. B., Rat liver sinusoidal endothelial cells (LSECs) express functional low density lipoprotein receptor-related protein-1 (LRP-1). *Journal of hepatology* **2011**, *55* (6), 1346-52.
45. Ganesan, L. P.; Mates, J. M.; Cheplowitz, A. M.; Avila, C. L.; Zimmerer, J. M.; Yao, Z.; Maiseyeu, A.; Rajaram, M. V.; Robinson, J. M.; Anderson, C. L., Scavenger receptor B1, the HDL receptor, is expressed abundantly in liver sinusoidal endothelial cells. *Scientific reports* **2016**, *6*, 20646.

46. Chaubey, P.; Mishra, B., Mannose-conjugated chitosan nanoparticles loaded with rifampicin for the treatment of visceral leishmaniasis. *Carbohydrate polymers* **2014**, *101*, 1101-8.
47. Mates, J. M.; Yao, Z.; Cheplowitz, A. M.; Suer, O.; Phillips, G. S.; Kwiek, J. J.; Rajaram, M. V.; Kim, J.; Robinson, J. M.; Ganesan, L. P.; Anderson, C. L., Mouse Liver Sinusoidal Endothelium Eliminates HIV-Like Particles from Blood at a Rate of 100 Million per Minute by a Second-Order Kinetic Process. *Frontiers in immunology* **2017**, *8*, 35.
48. Burlak, C.; Paris, L. L.; Chihara, R. K.; Sidner, R. A.; Reyes, L. M.; Downey, S. M.; Tector, A. J., The fate of human platelets perfused through the pig liver: implications for xenotransplantation. *Xenotransplantation* **2010**, *17* (5), 350-61.
49. Carambia, A.; Freund, B.; Schwinge, D.; Heine, M.; Laschtowitz, A.; Huber, S.; Wraith, D. C.; Korn, T.; Schramm, C.; Lohse, A. W.; Heeren, J.; Herkel, J., TGF-beta-dependent induction of CD4(+)CD25(+)Foxp3(+) Tregs by liver sinusoidal endothelial cells. *Journal of hepatology* **2014**, *61* (3), 594-9.
50. Xu, X.; Jin, R.; Li, M.; Wang, K.; Zhang, S.; Hao, J.; Sun, X.; Zhang, Y.; Wu, H.; Zhang, J.; Ge, Q., Liver sinusoidal endothelial cells induce tolerance of autoreactive CD4+ recent thymic emigrants. *Scientific reports* **2016**, *6*, 19861.
51. Schildberg, F. A.; Hegenbarth, S. I.; Schumak, B.; Scholz, K.; Limmer, A.; Knolle, P. A., Liver sinusoidal endothelial cells veto CD8 T cell activation by antigen-presenting dendritic cells. *European journal of immunology* **2008**, *38* (4), 957-67.
52. Liu, Q.; Wang, X.; Liu, X.; Kumar, S.; Gochman, G.; Ji, Y.; Liao, Y. P.; Chang, C. H.; Situ, W.; Lu, J.; Jiang, J.; Mei, K. C.; Meng, H.; Xia, T.; Nel, A. E., Use of Polymeric Nanoparticle Platform Targeting the Liver To Induce Treg-Mediated Antigen-Specific Immune Tolerance in a Pulmonary Allergen Sensitization Model. *ACS nano* **2019**, *13* (4), 4778-4794.
53. Nakamoto, N.; Kanai, T., Role of toll-like receptors in immune activation and tolerance in the liver. *Frontiers in immunology* **2014**, *5*, 221.
54. Crispe, I. N., Immune tolerance in liver disease. *Hepatology* **2014**, *60* (6), 2109-17.
55. Li, M.; Sun, R.; Xu, L.; Yin, W.; Chen, Y.; Zheng, X.; Lian, Z.; Wei, H.; Tian, Z., Kupffer Cells Support Hepatitis B Virus-Mediated CD8+ T Cell Exhaustion via Hepatitis B Core Antigen-TLR2 Interactions in Mice. *Journal of immunology* **2015**, *195* (7), 3100-9.
56. Yuan, F.; Zhang, W.; Mu, D.; Gong, J., Kupffer cells in immune activation and tolerance toward HBV/HCV infection. *Advances in clinical and experimental medicine : official organ Wroclaw Medical University* **2017**, *26* (4), 739-745.
57. Amoozgar, Z.; Goldberg, M. S., Targeting myeloid cells using nanoparticles to improve cancer immunotherapy. *Advanced drug delivery reviews* **2015**, *91*, 38-51.
58. Lu, L.; Bonham, C. A.; Liang, X.; Chen, Z.; Li, W.; Wang, L.; Watkins, S. C.; Nalesnik, M. A.; Schlissel, M. S.; Demestris, A. J.; Fung, J. J.; Qian, S., Liver-derived DEC205+B220+CD19- dendritic cells regulate T cell responses. *Journal of immunology* **2001**, *166* (12), 7042-52.
59. Percin, G. I.; Eitler, J.; Kranz, A.; Fu, J.; Pollard, J. W.; Naumann, R.; Waskow, C., CSF1R regulates the dendritic cell pool size in adult mice via embryo-derived tissue-resident macrophages. *Nature communications* **2018**, *9* (1), 5279.
60. Wilson, N. S.; Young, L. J.; Kupresanin, F.; Naik, S. H.; Vremec, D.; Heath, W. R.; Akira, S.; Shortman, K.; Boyle, J.; Maraskovsky, E.; Belz, G. T.; Villadangos, J. A., Normal proportion and expression of maturation markers in migratory dendritic cells in the absence of germs or Toll-like receptor signaling. *Immunology and cell biology* **2008**, *86* (2), 200-5.
61. Ludewig, B.; Ehl, S.; Karrer, U.; Odermatt, B.; Hengartner, H.; Zinkernagel, R. M., Dendritic cells efficiently induce protective antiviral immunity. *Journal of virology* **1998**, *72* (5), 3812-8.

62. Ager, A., High Endothelial Venules and Other Blood Vessels: Critical Regulators of Lymphoid Organ Development and Function. *Frontiers in immunology* **2017**, *8*, 45.
63. Jindal, A. B., Nanocarriers for spleen targeting: anatomico-physiological considerations, formulation strategies and therapeutic potential. *Drug delivery and translational research* **2016**, *6* (5), 473-85.
64. Trevasakis, N. L.; Kaminskas, L. M.; Porter, C. J., From sewer to saviour - targeting the lymphatic system to promote drug exposure and activity. *Nature reviews. Drug discovery* **2015**, *14* (11), 781-803.
65. Tanaka, M.; Iwakiri, Y., The Hepatic Lymphatic Vascular System: Structure, Function, Markers, and Lymphangiogenesis. *Cellular and molecular gastroenterology and hepatology* **2016**, *2* (6), 733-749.
66. Mellman, I.; Plutner, H.; Ukkonen, P., Internalization and rapid recycling of macrophage Fc receptors tagged with monovalent antireceptor antibody: possible role of a prelysosomal compartment. *The Journal of cell biology* **1984**, *98* (4), 1163-9.
67. Richards, D. A.; Maruani, A.; Chudasama, V., Antibody fragments as nanoparticle targeting ligands: a step in the right direction. *Chemical science* **2017**, *8* (1), 63-77.
68. Leenheer, D.; Ten Dijke, P.; Hipolito, C. J., A current perspective on applications of macrocyclic-peptide-based high-affinity ligands. *Biopolymers* **2016**, *106* (6), 889-900.
69. White, A. L.; Chan, H. T.; Roghanian, A.; French, R. R.; Mockridge, C. I.; Tutt, A. L.; Dixon, S. V.; Ajona, D.; Verbeek, J. S.; Al-Shamkhani, A.; Cragg, M. S.; Beers, S. A.; Glennie, M. J., Interaction with FcγRIIB is critical for the agonistic activity of anti-CD40 monoclonal antibody. *Journal of immunology* **2011**, *187* (4), 1754-63.
70. Higuchi, Y.; Nishikawa, M.; Kawakami, S.; Yamashita, F.; Hashida, M., Uptake characteristics of mannosylated and fucosylated bovine serum albumin in primary cultured rat sinusoidal endothelial cells and Kupffer cells. *International journal of pharmaceutics* **2004**, *287* (1-2), 147-54.
71. Armengol, C.; Bartoli, R.; Sanjurjo, L.; Serra, I.; Amezaga, N.; Sala, M.; Sarrias, M. R., Role of scavenger receptors in the pathophysiology of chronic liver diseases. *Critical reviews in immunology* **2013**, *33* (1), 57-96.
72. Liu, J.; Jiang, M.; Ma, Z.; Dietze, K. K.; Zelinsky, G.; Yang, D.; Dittmer, U.; Schlaak, J. F.; Roggendorf, M.; Lu, M., TLR1/2 ligand-stimulated mouse liver endothelial cells secrete IL-12 and trigger CD8⁺ T cell immunity in vitro. *Journal of immunology* **2013**, *191* (12), 6178-90.
73. Huang, S.; Wu, J.; Gao, X.; Zou, S.; Chen, L.; Yang, X.; Sun, C.; Du, Y.; Zhu, B.; Li, J.; Yang, X.; Feng, X.; Wu, C.; Shi, C.; Wang, B.; Lu, Y.; Liu, J.; Zheng, X.; Gong, F.; Lu, M.; Yang, D., LSECs express functional NOD1 receptors: A role for NOD1 in LSEC maturation-induced T cell immunity in vitro. *Molecular immunology* **2018**, *101*, 167-175.
74. Sokolova, V.; Shi, Z.; Huang, S.; Du, Y.; Kopp, M.; Frede, A.; Knuschke, T.; Buer, J.; Yang, D.; Wu, J.; Westendorf, A. M.; Epple, M., Delivery of the TLR ligand poly(I:C) to liver cells in vitro and in vivo by calcium phosphate nanoparticles leads to a pronounced immunostimulation. *Acta biomaterialia* **2017**, *64*, 401-410.
75. Passlick, D.; Piradashvili, K.; Bamberger, D.; Li, M.; Jiang, S.; Strand, D.; P, R. W.; Landfester, K.; Bros, M.; Grabbe, S.; Mailander, V., Delivering all in one: Antigen-nanocapsule loaded with dual adjuvant yields superadditive effects by DC-directed T cell stimulation. *Journal of controlled release : official journal of the Controlled Release Society* **2018**, *289*, 23-34.
76. Wu, J.; Meng, Z.; Jiang, M.; Zhang, E.; Trippler, M.; Broering, R.; Bucchi, A.; Krux, F.; Dittmer, U.; Yang, D.; Roggendorf, M.; Gerken, G.; Lu, M.; Schlaak, J. F., Toll-like receptor-induced innate immune responses in non-parenchymal liver cells are cell type-specific. *Immunology* **2010**, *129* (3), 363-74.

77. (a) Fetsch, C.; Grossmann, A.; Holz, L.; Nawroth, J. F.; Luxenhofer, R., Polypeptoids from N-Substituted Glycine N-Carboxyanhydrides: Hydrophilic, Hydrophobic, and Amphiphilic Polymers with Poisson Distribution. *Macromolecules* **2011**, *44* (17), 6746-6758; (b) Birke, A.; Huesmann, D.; Kelsch, A.; Weilbacher, M.; Xie, J.; Bros, M.; Bopp, T.; Becker, C.; Landfester, K.; Barz, M., Polypeptoid-block-polypeptide copolymers: synthesis, characterization, and application of amphiphilic block Copolypept(o)ides in drug formulations and miniemulsion techniques. *Biomacromolecules* **2014**, *15* (2), 548-57.
78. Hörtz, C.; Birke, A.; Kaps, L.; Decker, S.; Wächtersbach, E.; Fischer, K.; Schuppan, D.; Barz, M.; Schmidt, M.
79. Gehring, S.; Dickson, E. M.; San Martin, M. E.; van Rooijen, N.; Papa, E. F.; Harty, M. W.; Tracy, T. F., Jr.; Gregory, S. H., Kupffer cells abrogate cholestatic liver injury in mice. *Gastroenterology* **2006**, *130* (3), 810-22.
80. Fichter, M.; Baier, G.; Dedters, M.; Pretsch, L.; Pietrzak-Nguyen, A.; Landfester, K.; Gehring, S., Nanocapsules generated out of a polymeric dexamethasone shell suppress the inflammatory response of liver macrophages. *Nanomedicine : nanotechnology, biology, and medicine* **2013**, *9* (8), 1223-34.

5.7 Publication 7

Cylindrical Bottle Brush Polymer Vaccines: Influence of Size, Shape and Surface Functionality on Vaccination Efficiency

Manuscript in preparation

†Biopharmaceutical New Technologies (BioNTech) Corporation, An der

Goldgrube 12, Mainz 55131, Germany.

KEYWORDS. Polypeptoids, Polypeptides, brush polymers, immune therapy, dendritic cells,

ABSTRACT

Nanoparticle based vaccines combining antigen, immune activator and targeting to antigen - presenting cells have shown to enable antigen specific systemic immunity and are therefore a potent molecularly defined class of vaccines. This work reports on the synthesis of such vaccines based on cylindrical brush polymers, in which properties like size, shape and surface functionality can be completely controlled chemically. The synthesized cylindrical brush polymers consist of a polylysine backbone and polysarcosine side chains (Peptobrushes) and are thus completely based on endogenous amino acids. The investigated Peptobrushes exhibit molecular weights of $2.2 \cdot 10^5$ to $10.4 \cdot 10^5$ g·mol⁻¹ and dispersity indices of around 1.2 as confirmed by static light scattering and size exclusion chromatography. Dynamic light scattering reveals hydrodynamic radii of 11 to 21 nm. Peptobrushes were very well tolerated by cells, did not cause aggregation in concentrated blood serum and showed extended circulation in the blood stream of mice (70% remaining brushes after 24h) after intravenous injection independent on size and shape. Additionally, a detailed protocol for the step-wise conjugation of the peptobrushes with the antigen ovalbumin (OVA), the immune activator (CpG) and the antibody (aDEC205) is reported, that allows the precise control of the average number of each of these components per peptobrush, that enables us to establish a vaccine platform of adjustable size, shape and functionality. Interestingly the vaccine with the rod-like shape led to the most potent T cell proliferation response *in vitro* (OTI model) and was able to provide a protection from tumor growth in mice after subcutaneous vaccination. The reported findings underline the importance of nanoparticle design to maximize immunity.

INTRODUCTION

Vaccination is the administration of antigenic material (a vaccine) to stimulate an individual's immune system to develop adaptive immunity to a given pathogen. While traditional vaccines are derived from live attenuated, killed, or inactivated pathogens, synthetic subunit antigen vaccines can be derived by synthetic methods, ensuring rapid and cost effective production.¹ However, researcher learned over the last decades that synthetic peptides often lack the immunogenicity to induce adaptive immunity.^{2,3} Therefore, efficient vaccination requires the use of adjuvants, molecules that stimulate immune cells.³ In the field of tumor immunotherapy, adjuvants are particularly important to overcome tumor immune suppression mediated, e.g., by regulatory T cells or myeloid-derived suppressor cells.^{4,5} Adjuvants, among other things, promote the maturation of antigen-presenting cells, such as dendritic cells. Only mature dendritic cells are able to generate co-stimulatory signals, which together with the presented antigen lead to potent T cell responses. Therefore, an effective vaccination requires co-delivery of antigen and adjuvant to antigen presenting cells or more precisely to dendritic cells (DC). Besides uptake in DCs the uptake into cells with immune suppressive potential, e.g. myeloid suppressor cells, M2 macrophages, needs to be reduced to a minimum, which generates vice versa the need for active targeting of DC associated cell surface receptors. In this respect, it is reasonable to use the most common marker for DCs, the aDEC205 antibody to facilitating uptake into dendritic cells, while reducing uptake in in other immune cell populations. The desired combination of antigen and adjuvant with antibody mediated active targeting creates the rational for the use of nanoparticles to combine all desirable functions on a single object, which is additionally of a size of common pathogens and thus very well suited to be recognized and processed by the immune system.

The combination of these three components on a synthetic nanoparticle, however, is complex in terms of synthesis and characterization. Therefore, synthetic vaccines combining an antigen, adjuvant and antibody are mostly limited to encapsulation by nanoparticles^{6,7,8,9,10} or antibody-antigen conjugates coinjected with bare adjuvant.¹¹ Conjugation of an antigen and adjuvant directly to an antibody, however, can easily result in a loss of in vivo targeting capability. We

recently reported a study on cylindrical brushes with poly-2-ethyl-oxazolin side chains, that have been decorated with several DEC205 antibodies and SIINFEKL. In vitro experiments revealed selective uptake into CD8⁺ dendritic cells and efficient T-cell proliferation after external stimulation with lipopolysaccharides.¹² In addition, Grabbe and coworkers demonstrate the reduction of tumor growth using dextran particles that were decorated with a DEC205-specific antibody, antigen and adjuvant.¹³ However, these dextran particles not only engaged CD8⁺ dendritic cells, but also B cells as a consequence of dextran-triggered complement activation.¹⁴ This observation underscores the necessity to develop nanomaterials that interact with serum factors at low extent only to diminish unspecific binding.

While first studies have investigated the influence of particle size of vaccines in the nanometer to micrometer range or organic^{15,16,17,18,19,20} and inorganic particles^{21,22} or beyond^{23,24}, investigations on the influence of size and shape of nanoparticle based vaccines, combining a specific average number of antigen, adjuvant, and targeting moiety on a single particles have so far not been reported.

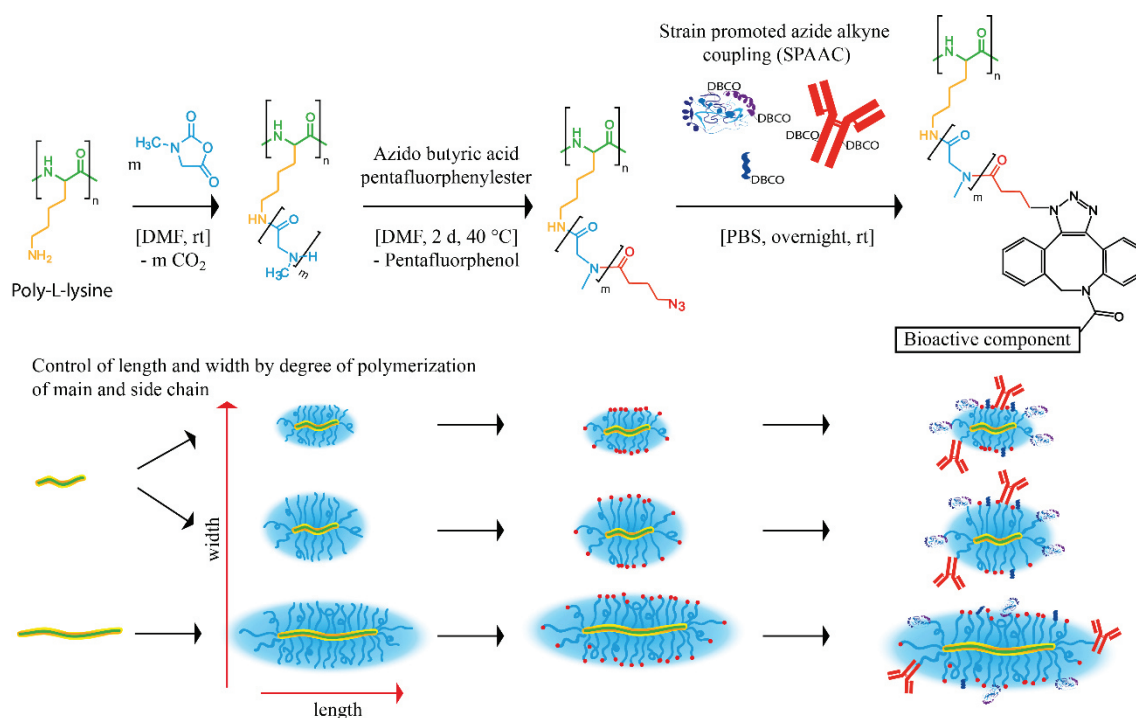
One class of materials, which allows for the adjustment of size and shape by chemical synthesis are cylindrical brush polymers.²⁵ After its discovery in 1994²⁶ cylindrical brush polymers (sometimes called “bottlebrushes”) have received considerable attention, because any flexible main chain can be forced to adopt an expanded cylindrical conformation due to the repulsive interaction of the densely grafted side chains. Most importantly, due the high grafting density the chain length ratio of main and side chains directly determines the length (backbone) and width (side chain) of the final polymeric nanoparticle.

Thus, a variety of cylindrical brush polymers (CPBs) have been synthesized by “grafting through”^{27,28,29}, “grafting from”^{30,31,32} and “grafting onto”^{33,34} techniques with various combinations of main and side chain monomers. Also branched or dendritic side chains were introduced as “dendronized polymers”, leading to cylindrical objects of similar conformations.^{35,36,37} Recently, we have reported the synthesis of CPBs with polysarcosine (pSar)

side chains using poly(N-(6-aminohexyl)methacrylamide) (PAHMA) and poly(L-lysine) (pLys) macroinitiators.³⁸ Both macroinitiators displayed elevated weight average molecular weights (M_w) of 3.7 (PAHMA) and 5.8×10^5 g mol⁻¹ (pLys) and rather high dispersity indices of around 1.7 due to the broad molar mass distribution of the macroinitiators utilized. Since main chain and side chain length of cylindrical brushes can be controlled independently, their size and their shape (aspect ratio) may be continuously varied from spherical (main chain < side chain length) to ellipsoidal (main chain > side chain length) to rod- or wormlike brushes (main chain >> side chain length).

Besides nanoparticle morphology, flexibility and functionality the particle material itself determines its biological properties. Besides established materials for nanomedicines³⁹, polymers combining polypeptides and polypeptoids have gained increasing attention over the last years^{40,41,42,43,44,45,46,47} Accordingly, the pLys-gr-pSar cylindrical brushes constitute interesting candidates to study the effect of size and shape in biomedical applications in terms of cell uptake and blood circulation.

In light of this information, we aim for the development of “all polypept(o)ide” CPBs (cylindrical Peptobrushes) exclusively consisting of polypept(o)ides^{40,48} with more defined morphology in terms of a narrow main chain length distribution in combination with a high end group integrity for controlled conjugation of the antigen ovalbumin (OVA), adjuvant CpG oligodeoxynucleotide (CpG) and antibody aDEC205 by strain promoted azide alkyne coupling enabling to adjust the average number of each component on cylindrical polymer brushes.



Scheme 1. Sequential synthesis of Peptobrush based triple conjugates for vaccination: Synthesis of CPBs by sequential ring opening polymerization of α -amino acid N-carboxyanhydrides, end group modification for strain promoted azide-alkyne coupling (SPAAC) and adjustment of CPBs properties by degree of polymerization of main and side chain and adjustment of antigen, adjuvant and antibody loading.

RESULTS AND DISCUSSION

Synthesis and Characterization of Peptobrushes

Cylindrical brushes with polylysine backbone and polysarcosine side chains (Peptobrushes) were synthesized by nucleophilic ring opening polymerization using narrowly distributed polylysines as multivalent macroinitiators (see scheme 1). The pLys had a degree of polymerization of $P_{n,1} = 102$, $\mathcal{D} = 1.07$ and $P_{n,2} = 258$, $\mathcal{D} = 1.09$. Dynamic light scattering experiments at a concentration of $1 \text{ g}\cdot\text{L}^{-1}$ in 0.1 M NaBr revealed hydrodynamic radii $R_{h,1} = 3.9 \text{ nm}$ and $R_{h,2} = 7 \text{ nm}$. For preparation of the peptobrushes the pLys was dissolved in purified DMF and predetermined amounts of Sar NCA in DMF were added via a syringe. At full conversion the PSar side chain lengths were calculated to $P_{n,\text{theo}} = 50$ and 100 for PLys_1 and $P_{n,\text{theo}} = 100$ for PLys_2 . After full Sar-NCA conversion has been ensured by FTIR (disappearance of the NCA carbonyl vibration band at 1850 cm^{-1} and 1778 cm^{-1}) the secondary amine end groups were quenched with azido butyric acid pentafluorophenyl ester introducing terminal azide functionalities for subsequent selective conjugation of biologically active substrates.

Size exclusion chromatography revealed that all CPBs display a narrow monomodal molecular weight distribution. With dispersity indices (\mathcal{D}) of around 1.2 (see Fig. 1a). The GPC plots, however, display a slight high molecular weight tailing, that is currently not understood. Nevertheless, dispersity index values of all brushes can be considered low for such large molecules and underline the well-controlled synthesis. Interestingly, low molecular weight tailing is not visible. The molar masses determined (see Fig. 1a) in hexafluoroisopropanol ($c = 2 \text{ g}\cdot\text{L}^{-1}$) relative to linear PMMA standards, however, were much smaller than the absolute SLS molar masses as expected (see table 1). At the same hydrodynamic volume the CPBs are known to possess a much higher molar mass than linear flexible coils. Therefore, static light scattering was performed to determine the molar mass of the brushes and to derive the average PSar side chain length. A typical Zimm-plot for **PB3** is shown in Fig. 1c and the results are summarized in Tab.

1 displaying the average molecular weights of 2.2×10^5 g/mol for **PB1** (Fig. S1), 4.2×10^5 g/mol for **PB2** (Fig. S2) and 10.4×10^5 g/mol for **PB3** (Fig. 1c).

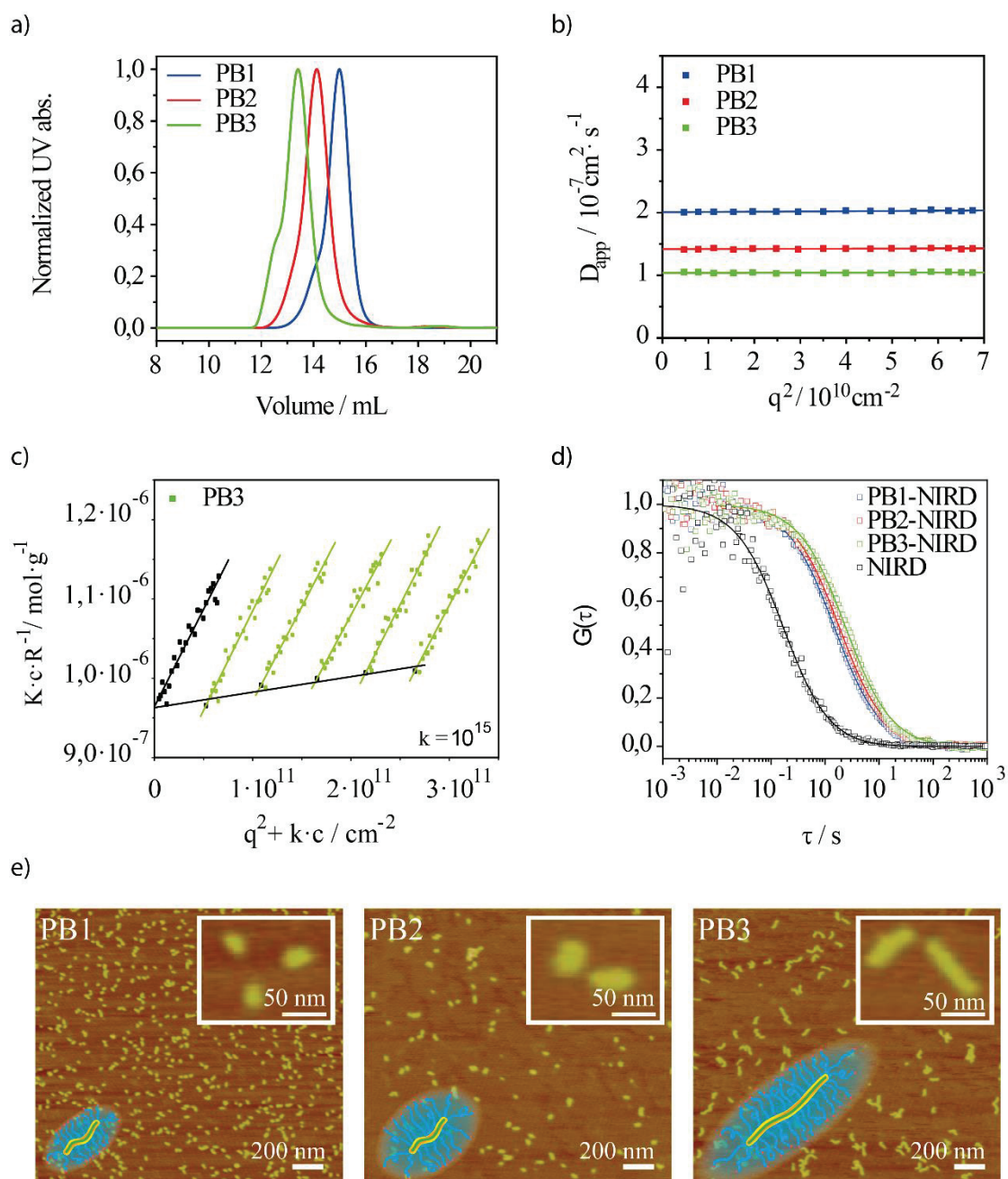


Figure 1. Characterization of PeptoBrushes **PB1**, **PB2** and **PB3**: a) GPC in HFIP ($c = 2 \text{ g}\cdot\text{L}^{-1}$), b) multi angle dynamic lightscattering (DLS) in PBS ($c = 1 \text{ g}\cdot\text{L}^{-1}$), c) Zimm-Plot for **PB3** in PBS d) Near Infrared Fluorescence correlation spectroscopy (NIR-FCS) of near infrared dye (NIRD) and NIRD-labeled PeptoBrushes in PBS ($c = 2 \cdot 10^{-8} \text{ M}$), e) Atomic force microscopy (AFM) of PeptoBrushes on mica in dry state.

Besides the analysis of molecular weight distribution SEC was also used to determine the enzymatic degradability of peptobrushes. Therefore, we used the enzyme *Streptomyces griseus* and incubated the CPBs in its presence at 37°C for up to 2 weeks (see Fig S3). The SEC plots reveal that brushes are degraded over the time frame of weeks. Since the degradation by the applied peptidase is restricted to the pLys backbone, degradation yields the pSar side chains. The side chains can be analyzed applying a pSar calibration.⁴⁹ The obtained side chain lengths are 25 for PB1, 108 for PB2 and 96 for PB3. Comparing the obtained side chain lengths after enzymatic degradation with the average side chain lengths calculated from SLS leads to grafting densities of 94 % for PB1, 43 % for PB2 and 44 % for PB3. The reason for the variation in the grafting density is currently not understood. According to literature⁴⁹ the corresponding R_h to a polymerization degree of 108 is 2.3 nm. The remaining pSar segments are well below the renal excretion limit and thus can ensure rapid elimination upon enzymatic degradation (Refs).

Table 1. Characterization of Peptobrushes PB1, PB2, PB3.

PB	$\langle \frac{1}{R_h} \rangle_z^{-1} / \text{nm}^{\text{a)}$	$M_w / \text{g} \cdot \text{mol}^{-1}$ ^{b)}	$R_g / \text{nm}^{\text{c)}$	$D_{\text{HFIP}}^{\text{d)}$	Average side chain length ^{e),f)}	$\zeta. / \text{mV}^{\text{g)}$	Aspect ratio ^{h)}
PB1	11	2.2E5	10	1.2	24 / 25	-6 ± 4	1.6
PB2	15	4.2E5	15	1.2	47 / 108	-4 ± 3	1.5
PB3	21	10.4E5	23	1.3	42 / 96	-3 ± 5	3.9

a) determined by dynamic light scattering in PBS

b,c) determined by static light scattering in PBS

d) determined by size exclusion chromatography in hexafluoroisopropanol

- e) determined by static light scattering in PBS (estimating 100% grafting density)
- f) determined by size exclusion chromatography in hexafluoroisopropanol after enzymatic degradation
- g) determined by zeta potential measurements in 10 mM NaCl
- h) determined by atomic force microscopy on mica substrates (measured particles to determine the aspect ratio: PB1 = 177, PB2 = 97, PB3 = 109)

Dynamic light scattering (DLS) experiments were performed at a concentration of $1 \text{ g}\cdot\text{L}^{-1}$ in PBS buffer and yielded hydrodynamic radii $R_h = 11 \text{ nm}$ for **PB1**, $R_h = 15 \text{ nm}$ for **PB2** and $R_h = 21 \text{ nm}$ for **PB3**. We could not detect any angle dependency of the scattering vector q^2 (see Figure 1b) as expected for narrowly distributed polymer brushes in this size regime. The hydrodynamic radii were confirmed by fluorescence correlation spectroscopy (FCS) after subsequent labeling of polymers with Carboxyrhodamin110 employing strain promoted azide alkyne coupling. (Fig. S4). The autocorrelation functions of NIR-dye labeled brushes show no free dye, that is an important criterion for reliable biodistribution experiments (Figure 3d). Finally, the morphology of Peptobrushes was visualized by atomic force microscopy (AFM) on mica substrates. The brushes were spin cast from aqueous solution and analyzed in dry state. As displayed in Figure 2 for **PB1** ellipsoidal structures with an average length of 29 nm and a width of 18 nm are observed leading to an average aspect ratio of 1.6. For **PB2** we found an average length of 46 nm and a width of 30 nm leading to a comparable average aspect ratio of 1.5. AFM experiments of **PB3** visualize nanoparticles with an average length of 79 nm, a width of 20 nm and thus an aspect ratio of 3.9. It should be noted that the AFM dimensions discussed above should be treated with caution, because the brushes are strongly adsorbed on Mica resulting in deformed, i.e. strongly flattened, structures. Moreover, a sample-tip deconvolution was not performed, i.e. the resulting AFM sizes are most likely too large.

In conclusion, our findings demonstrate that the side chain length in peptobrushes can be controlled yielding bottlebrush polymers with low dispersity (\mathcal{D}), which is a first requirement in order to control both, length and width, of brushes simply by the degree of polymerization of macroinitiator and side chains. Moreover, enzymatic degradability was ensured by *Streptomyces griseus* assay. Before any *in vivo* application, cytotoxicity and aggregation in serum was analyzed *ex vivo*. Cytotoxic effects of the polymer brushes were assessed in DC-like DC2.4 cells, and in fibroblast-like HEK293T cells (Fig. S5). In both cell types the metabolic activity was not affected at major extent by the different types of polymer brushes applied over a large range of concentrations (0.05 to 5 mg/mL). Only at the highest concentration tested (5 mg/ml) **PB1** and **PB2** attenuated metabolic activity of DC2.4. Similarly, **PB2** at the highest concentrations tested (5 mg/ml) attenuated metabolic cellular activity of HEK293T cells significantly. Besides material related cytotoxicity *in vivo* toxicity can occur due to aggregation of polymeric nanoparticles or high ionic strength.^{50,51} To ensure that the peptobrushes do not cause aggregate formation in human serum, they were analyzed by DLS in serum, a method introduced and described in detail by Rausch *et al.*⁵² Firstly, the intensity-time correlation function of polymer and serum are measured separately. Secondly, a mixture of polymer and serum is measured. If there are no aggregates formed, the autocorrelation function of the mixture can be well described by a force fit which is the sum of the correlation functions of each of the components. The formation of larger aggregates would require an additional exponential term to describe the autocorrelation function of the mixture. Upon mixing the NIR dye labeled peptobrushes **PB1**, **PB2** and **PB3** with human serum, the mixture autocorrelation function can be well described by the force fit (Figure 2). This indicates that all three peptobrushes do not induce the formation of larger aggregates in the presence of 90 % human serum. The concentration of the brushes is comparable to the concentration applied for biodistribution experiments in mice assuming 2 mL mice blood volume.

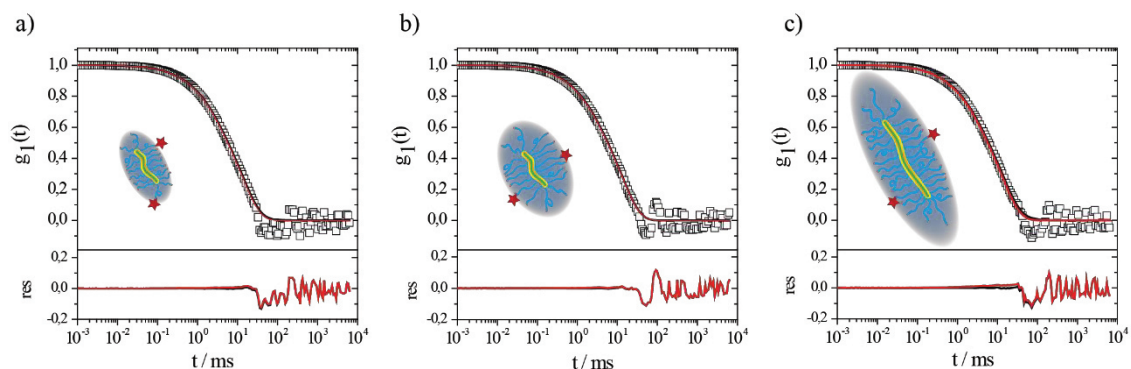


Figure 2. Characterization of NIR-Dye labeled PeptoBrushes **PB1**, **PB2** and **PB3** in 90 % human serum by DLS at 30°. Autocorrelation functions $g_1(t)$ recorded from PB1-NIRD, PB2-NIRD and PB3-NIRD in 90 % human serum (\square squares). Red line: Force fit. Black line: Fit with a variable component. a) PB1-NIRD, $c_{PB1} = 0.2 \text{ g}\cdot\text{L}^{-1}$. b) PB2-NIRD, $c_{PB2} = 0.4 \text{ g}\cdot\text{L}^{-1}$. c) PB3-NIRD $c_{PB3} = 0.8 \text{ g}\cdot\text{L}^{-1}$.

In vivo evaluation of peptobrushes

Having ensured that peptobrushes PB1-PB3 do not induce cytotoxicity at relevant doses nor aggregate or cause aggregation of serum proteins, we decided to test the CPBs *in vivo* studies. For this, zebrafish embryos and BALB/c mice were selected as models, first to study CPB circulation in healthy animals. The mouse is the classical pre-clinical model although it has its limitations for detailed imaging. In contrast the zebrafish embryo is naturally transparent and ideal for high resolution, live imaging, including of nanoparticles.⁵³ The latter publication pointed out that the zebrafish is an ideal model to screen NP rapidly prior to the more costly mouse model.

For the subsequent systemic applications aimed at tumor or granuloma targeting by passive accumulation^{54,55} peptobrushes needed to exhibit prolonged *in vivo* circulation. Towards this goal, all PeptoBrushes were labeled with 800CW, an NIR dye enabling us to study the size and shape dependency of circulation in two different animals.

First, peptobrushes PB1-PB3 labeled with AlexaFluor647 were injected into the caudal vein of 2 day old zebrafish embryos exhibiting fluorescent vasculature, *tg(fli1a:EGFP)* (see figure 3a). This animal model is rapidly emerging as a tool to study NP flow⁵⁶, biodistribution in healthy zebrafish^{57,58} as well as in animals bearing tumors⁵⁹ or tuberculosis granulomas^{53,60}. The circulation time was determined by fluorescence microscopy at different time points over the course of 7 days (Figure 3b). Control NP made of polylysine exhibited very poor circulation and already at 5 minutes after intravenous injection they showed high level of aggregation with virtually no nanoparticle being seen flowing (Figure 3a). Peptobrushes PB1-PB3 behaved very differently and despite a slight but detectable decrease in intravascular fluorescence during the first hours post fertilization (Figure 3b), a substantial amount (31, 28 and 26 % for **PB1**, **PB2** and **PB3**) was still circulating even 7 days post injection (Figure 3b). This is currently the longest circulating nanoparticle we have seen in this model; previously, the longest circulating NP described in the literature for zebrafish larvae were PEGylated liposomes which circulate until about 3 days post injection.⁵⁹ Morphology associated differences are, however, not significant and therefore we need to conclude that circulation times in zebra fish embryos do not depend on size or shape of nanoparticles in the investigated range of hydrodynamic diameters or aspect ratio. Second, peptobrushes have been applied to BALB/c mice as a standard rodent model. After systemic administration in mice the brushes circulate without specific accumulation in liver, lung or kidney (Fig. 3c, d). After 24 h still more around 70 % of the injected particle concentration was retained in the blood stream (Fig. 3e). **PB1**, **PB2** and **PB3** exhibit half times well above 2 days (see Fig. 3e).

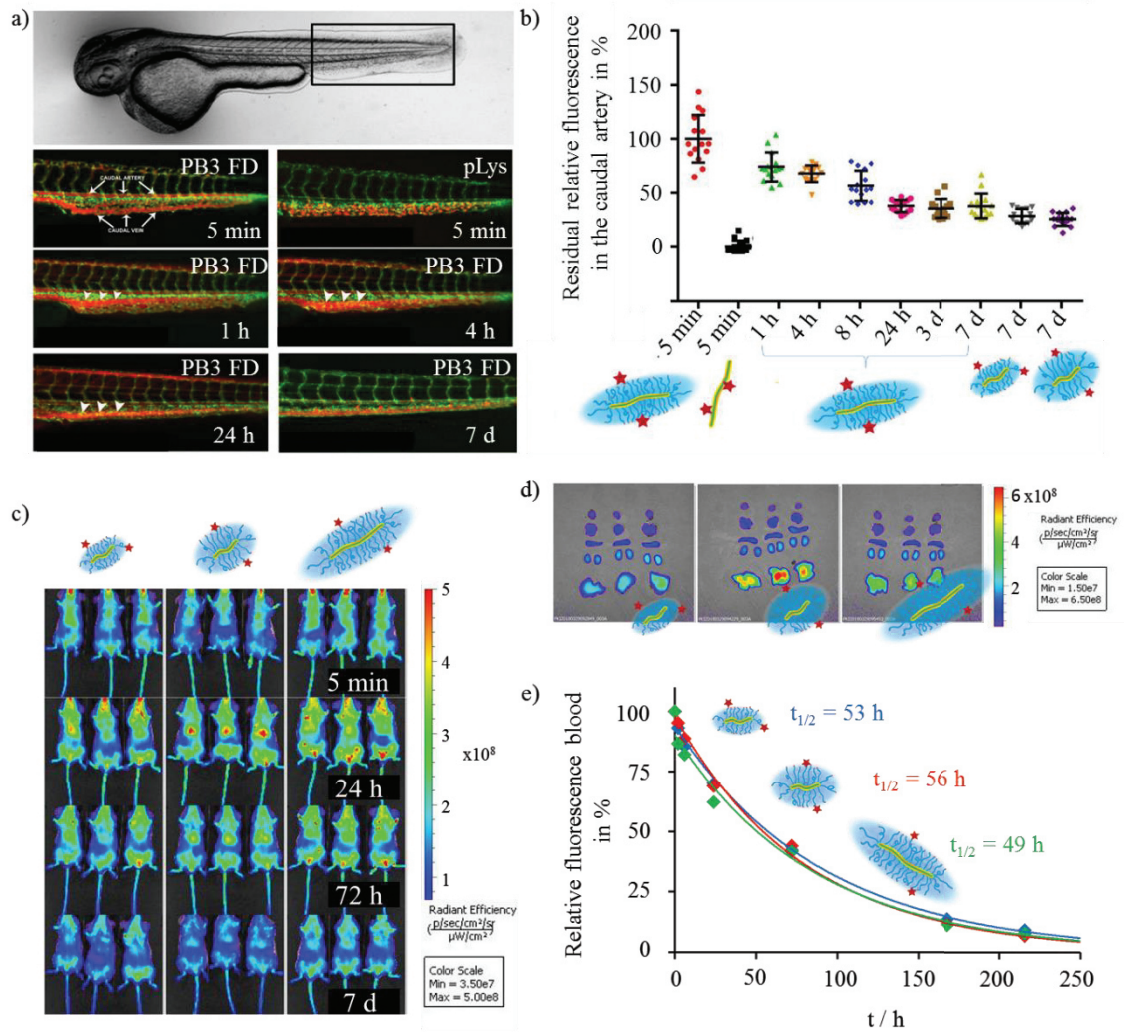


Figure 3. Biological evaluation of PeptoBrushes in zebrafish embryos and mice. a) *In vivo* imaging of zebrafish embryos. b) Fluorescence intensity in zebrafish embryos at indicated time points. Intensity at 5 min set as 100%. c) *In vivo* Imaging of mice. Intensity at 5 min set as 100%. d) Imaging of organs taken from mice after 9 days. e) Fluorescence intensity in blood taken from mice at indicated time points. Intensity at 5 min set as 100%. Solid curve is a single exponential fit.

In conclusion, peptobrushes **PB1**, **PB2** and **PB3** circulate stably in zebra fish embryo and mice. In both models, an initial drop as often observed for synthetic nanoparticles is absent. Blood half-lives are in the range of 3-4 days in zebra fish and well above 2 days in mice applying an exponential fit (one component model). In mice even after 9 days particle associated fluorescence was detectable by fluorescence imaging, which underlines the stealth like behavior of a dense pSar corona of peptobrushes. These findings may relate to the fact that peptobrushes of

comparable size like PB3 do not increase their hydrodynamic radius in full blood.⁶¹ These circulation times indicate that the synthesized particles are themselves invisible to the immune system and may thus be a suitable basis for the development of vaccines, in which ideally only antigen specific immune responses should be generated.

Synthesis and characterization of peptobrush conjugates

Besides the stealth like nature, the high surface to volume ratio of worm-like peptobrushes seems most interesting for the synthesis of vaccines, because elevated aspect ratios are expected to present ligands, e.g. antibodies, or immune activators, more efficiently to receptors outside or inside of cells^{62,63,64} we utilized PeptoBrushes **PB1** and **PB3** to prepare triple conjugates comprising an average number of 3 aDEC205 antibodies, 7 immune activators (CpG1826) and 7 antigens (OVA). Since the end groups on polymer brushes bear azide end groups, strain promoted azide alkyne coupling (SPAAC) was chosen to conjugate the different biomolecules to the brush.^{65,66} Therefore, aDEC205 and OVA have been modified with DBCO-PEG₄-NHS ester following the protocol established by S. Gietzen and Bühler *et al.*^{12,67} The purification procedure to achieve aggregate free DBCO-modified components however was changed from spin filtration to SEC resulting in significantly improved yields (70 - 90 % compared to 20 - 30 %).⁶⁷ The first purification step is the centrifugation with 10 kDa Amicon centrifugal filters to remove unbound DBCO-PEG₄-NHS ester and NHS. Afterwards, SEC is used to purify the DBCO-modified components from larger aggregates. The average number of DBCO per aDEC205 or OVA (N_{DBCO}) was determined as demonstrated in the SI. aDEC205 antibody containing 1.5 DBCO does not affect binding efficiency to dendritic cells (Figure S8). In line with these results, the DBCO modification does also not change the properties of the antigen ovalbumin in comparison to the unmodified counterpart (Figure S8). Commercially available CpG1826 oligodeoxynucleotide with a DBCO modification at the 3' end (CpG-DBCO) is used as an activator. This CpG1826 ODN is optimized for activation of B cells and dendritic cells and

Th1-like cytokine expression.⁶⁸ CpG-DBCO shows a to the unmodified CpG comparable activation of BMDCs (Figure S8). Having obtained DBCO-modified antibody, antigen and adjuvant, the peptobrush conjugates were prepared employing the standard SPAAC protocol (Fig. 4a). In the following section, the synthesis is described exemplary for the triple conjugate **PB3 FD-OVA(7)-aDEC205(3)-CpG(7)**. The average number of bound components is indicated in brackets. A detailed description of the calculations of the average number of bioactive components per brush can be found in the SI. All conjugation reactions were performed at room temperature overnight. Firstly, **PB3** is labeled with fluorescent dye AlexaFluor647-DBCO and purified by spin filtration. The hydrodynamic radius of **PB3 FD** determined by DLS and FCS is 23 nm. Moreover, FCS experiments ensure the absence of free dye (Fig. 4b). Furthermore, the average number of dyes per brush (N_{AF647}), which is important for further calculations, can be determined directly by FCS (see SI). To synthesize OVA- or aDEC205-brush-conjugates an excess of OVA-DBCO or aDEC205-DBCO needs to be used. The yield of bound OVA or aDEC205 per brush depends on the number of DBCO per component. In the range of 1 - 2 DBCO per component an excess of $1/(0.34*N_{DBCO})$ needs to be employed (Figure S10). For the described example, a 20-fold excess of OVA-DBCO (1.2 DBCO per OVA) was added to **PB3 FD**. The conjugates were purified by SEC and analyzed by DLS, FCS, UV-VIS and PAGE. The hydrodynamic radius of **PB3 FD-OVA(7)** determined by DLS and confirmed by FCS is 22 nm. As the number of DBCO per OVA or aDEC205 is a statistical value, it is also possible that two brushes bind to one bioactive component resulting in bridged brushes. Due to the separation via SEC those bridged brushes are removed (Figure S9). During this process a part of the high molecular weight fraction is removed leading to a slight decrease of R_h of **PB3 FD-OVA(7)** ($R_h = 22$ nm) compared to **PB3 FD** ($R_h = 23$ nm). Besides, the fractionation results in a slightly lower average number of dyes per brush. As the number of dyes per brush is an important value for calculating concentrations, FCS is measured after every conjugation step. For **PB3 FD-OVA(7)** the average number of dyes per brush is 6. The OVA concentration is calculated from the absorption at 280 nm (Fig. 4e). A detailed description of the calculations of the average number of bioactive components per brush can be found in the SI yielding to 7 OVA per brush

for **PB3 FD-OVA(7)**. It should be noted that the calculations are only valid if there is no unbound OVA in the purified conjugates. The absence of free OVA was ensured by SDS-PAGE (Fig. 4 c). The synthesis, purification and characterization of aDEC205-conjugates is similar to the described procedure of the OVA-conjugate. Using a 5-fold excess of aDEC205-DBCO with 1.6 DBCO per aDEC205 yields to an average number of 3 aDEC205 per brush, determined by UV-VIS Spectroscopy (Fig. 4e). The absence of unbound aDEC205 is proven by SDS-PAGE (Fig. 4c). The hydrodynamic radius of **PB3 FD-OVA(7)-aDEC205(3)** measured by DLS and FCS is 22 nm. The last step in the exemplified triple conjugate synthesis is the addition of CpG-DBCO. In contrast to OVA-DBCO and aDEC205-DBCO, exactly 1 DBCO is attached to the CpG and the yield of the CpG coupling is found to be almost quantitative. To synthesize **PB3 FD-OVA(7)-aDEC205(3)-CpG(6)**, a 7 fold excess of CpG-DBCO was added to **PB3 FD-OVA(7)-aDEC205(3)**. As there is only 1 DBCO per CpG, no bridged brushes are formed, and the conjugates can be purified by spin filtration with Amicon 50 kDa centrifugal filters. The successful removal of CpG-DBCO can be shown by TBE-Urea PAGE (Fig. 4d) and the average number of CpG per brush can be calculated from the UV-VIS Spectra (Fig. 4e). The hydrodynamic radius determined by DLS and FCS is 22 nm (Fig. 4f). The synthesis of all combinations of bioactive components conjugated to **PB3 FD** is described in the experimental section and proves the reproducibility (table S1). To synthesize conjugates with the small brush **PB1**, the protocol can be adopted from the big brush. Due to the smaller size of **PB1**, the separation between the brush and the antibody requires the use of 2 columns in the SEC setup (Figure S13) to achieve an adequate separation (Figure S14). Although the order of the conjugation steps does not influence the number of bioactive components per brush in the case of **PB3**, the order of the conjugation reactions needs to be changed for **PB1** to achieve the same number of bioactive components compared to **PB3**. The addition of CpG in a 7-fold excess to the conjugate **PB1 FD-OVA(7)-aDEC205(2)** only yields in an average number of 2 CpG per brush. Because of these results, the CpG-DBCO was added first, followed by the addition of OVA-DBCO and aDEC205-DBCO. This reaction order leads to a triple conjugate with comparable amounts of bioactive components to the big brush **PB1 FD-OVA(7)-aDEC205(3)-CpG(7)**

(Fig. 4g). The UV-VIS spectra and PAGE analysis of the precursors of **PB1 FD-OVA(7)-aDEC205(3) -CpG(7)** are shown in the SI (Figure S13), ensuring separation from unbound bioactive components. The hydrodynamic radius determined by DLS (Fig. 4f) as well as FCS is 17 nm.

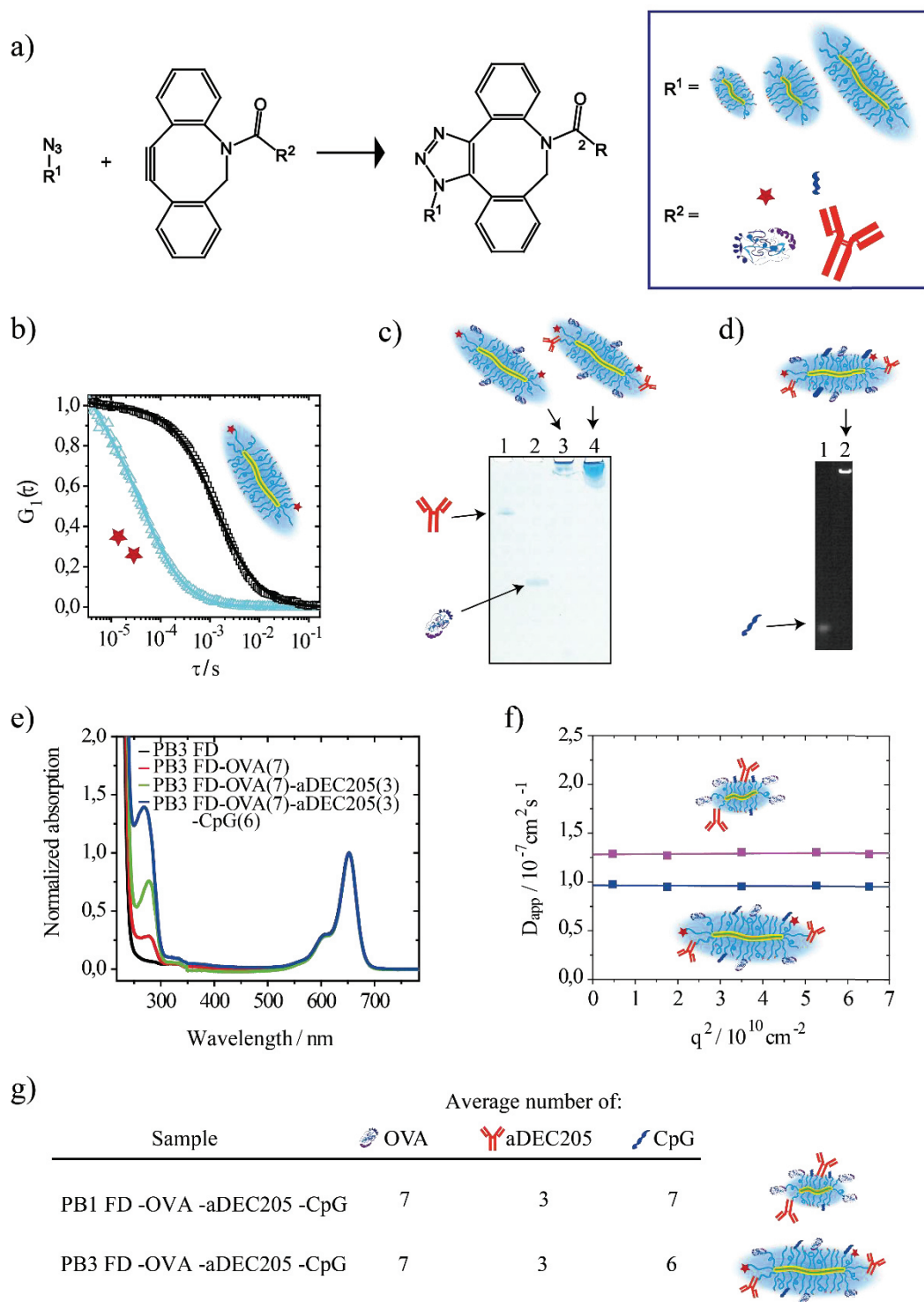


Figure 4. Characterization of PeptoBrush based triple conjugates. a) Synthesis of peptobrush conjugates by SPAAC. b) Fluorescence correlation spectroscopy (FCS) in PBS buffer ($c = 1 \cdot 10^{-8}$ M) of AF647-DBCO and **PB3 FD** confirms the labeling of **PB3**. c) SDS PAGE of the precursors of **PB3 FD-OVA(7)-aDEC205(3)-CpG(7)** shows no unbound OVA-DBCO or aDEC205-DBCO. 1 = 0.3 μ g aDEC205-DBCO, 2 = 0.5 μ g OVA-DBCO, 3 = **PB3 FD-OVA(7)** equal to 5 μ g OVA, 4 = **PB3 FD-OVA(7)-aDEC205(3)** equal to 5 μ g OVA and 8 μ g aDEC205. d) TBE Urea gel electrophoresis of **PB3 FD-OVA(7)-aDEC205(3)-CpG(7)** shows no unbound CpG-DBCO. 1 = 50 ng CpG-DBCO, 2 = **PB3 FD-OVA(7)-aDEC205(3)-CpG(7)** equal to 1000 ng CpG. e) UV-vis spectra of the triple conjugate and the triple conjugate precursors normalized to the absorption of the fluorescent dye. f) Multi angle dynamic lightscattering (DLS) in PBS buffer of the triple conjugates of the small brush **PB1 FD-OVA(7)-aDEC205(3)-CpG(6)** and big brush **PB3 FD-OVA(7)-aDEC205(3)-CpG(7)**. g) Average number of bioactive components per brush determined as described in the text.

In summary, the developed synthetic pathway allows the synthesis of peptobrushes containing antibody (aDEC205), immune activator (CpG), antigen (ovalbumin) and fluorescent dye (dye AlexaFluor647). In addition the average number of individual components can be precisely controlled and thus adjusted to the desired amount by stoichiometry yielding the final conjugates in high yields. While the peptobrushes **PB1-PB3** are well tolerated by cells and display stable circulation *in vivo* the modification with antibody, antigen and immune activator may alter these properties. Therefore, peptobrush conjugates have been also employed to studies on toxicity induced by the material or its aggregation behavior. These conjugates have been well tolerated by BMDCs and did not display detectable cytotoxic effects at the doses applied as reflected by largely unaltered cell metabolic activity doses for *in vitro* vaccination. Furthermore, DLS and FCS in serum been employed before applying the vaccines *in vivo*. While DLS is a very sensitive technique to detect larger aggregates induced by the coexistence of nanoparticles and concentrated blood serum, FCS monitors changes in the hydrodynamic radius of individual nanoparticles.^{52,61} A solution of the triple conjugate, for example **PB3 FD-OVA(13)-aDEC205(2)-CpG(6)** in PBS, was added to human serum pooled from 6 patients, thus yielding a final solution containing 90% human serum and only 10% **PB3 FD-OVA(13)-aDEC205(2)-**

CpG(6) solution in PBS. The DLS measurements indicate the absence of aggregate formation (see Fig. 5a).

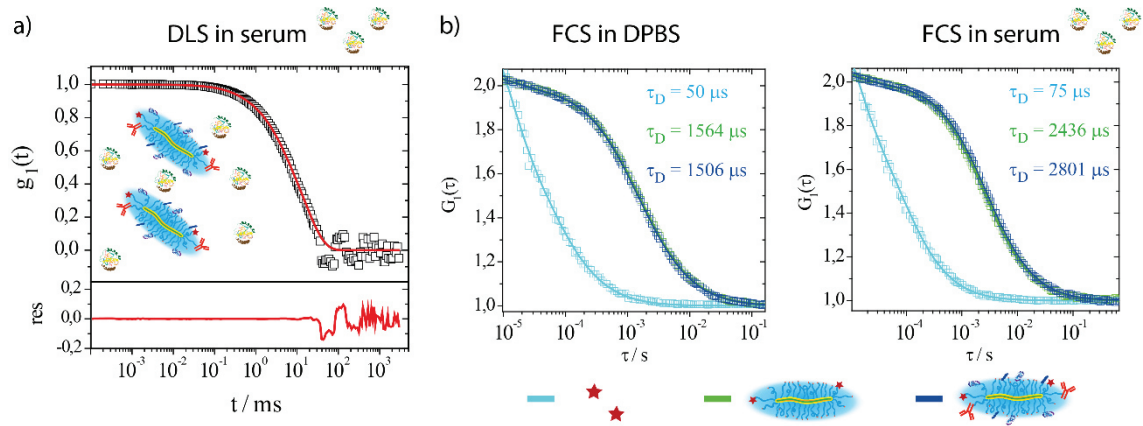


Figure 5. Evaluation of the interaction of triple conjugates with serum. a) Autocorrelation function $g_1(t)$ recorded from **PB3 FD –OVA(13)–aDEC205(2)–CpG(6)** in 90% human serum ($c_{\text{brush}} = 2 \cdot 10^{-7}$ M). Scattering angle 30° . b) Autocorrelation functions of AlexaFluor647 (light blue) **PB3 FD** (green) and **PB3 FD –OVA(8)–aDEC205(2)–CpG(6)** (dark blue) in DPBS and 90 % human serum ($c_{\text{FD}} = 5 \cdot 10^{-8}$ M).

As reported in literature⁶¹, the diffusion time τ_D of particles in serum increases due to the increased viscosity of serum compared to buffer. However, the fluorescent brightness should remain almost the same in the absence of particle aggregation. As shown in Fig. 5 b, τ_D of the dye AlexaFluor647 is 1.5 times higher in serum which is well in line with the factor 1.43 reported in literature. τ_D of PB3 FD increases by a factor of 1.56 and the fluorescence brightness stays constant in the experimental error (27 kHz in DPBS and 31 kHz in serum). Those observations indicate no significant change in the R_h of PB3 FD in serum as well as no aggregation in the presence of 90 % serum. τ_D of the triple conjugate PB3 FD –OVA(8)-aDEC205(2)-CpG(6) increases from 1506 μs to 2801 μs which belongs to an increase from 21.8 nm to 26.5 nm. As the fluorescence brightness stays almost constant (26 kHz in DPBS and 31 kHz in serum), we conclude that the increased R_h in serum is caused by the adsorption of serum proteins which may be caused by protein interactions with OVA and aDEC205 or electrostatic interactions with the

negatively charged CpG. Whether the adsorption of serum proteins influences the interaction of the conjugates with cells is not yet clear but part of current research projects.

Therefore, we can state that the peptobrush triple conjugates do not cause aggregation of serum proteins and only slightly increase in size in contact with serum proteins making peptobrushes promising candidates for local or even systemic vaccination.

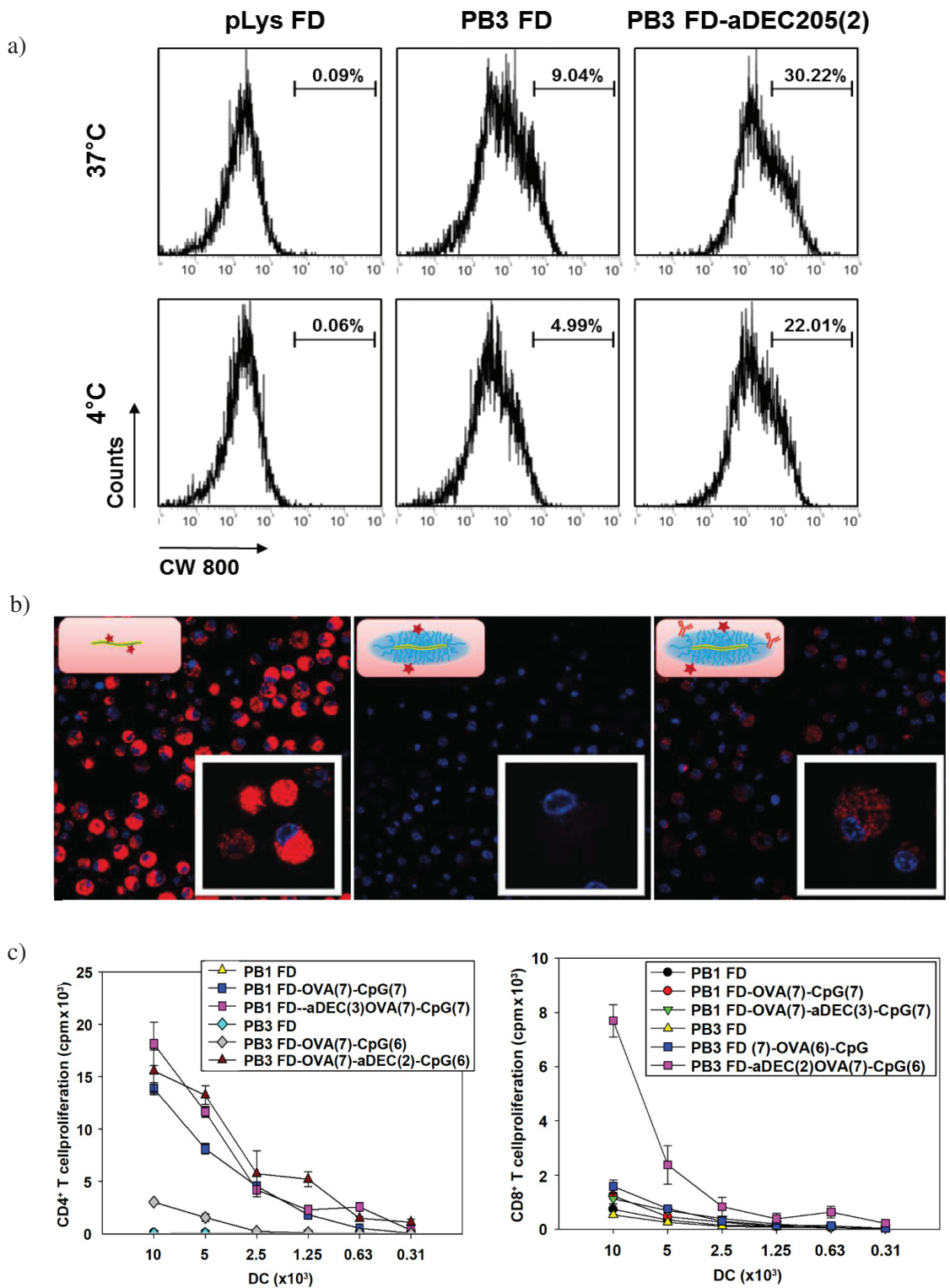


Figure 6: Functional properties of differentially functionalized peptobrushes. a) Flow cytometric analysis of BMDC incubated for 1h with pLys FD and the indicated peptobrushes (representative of 2 experiments). b) Confocal microscopy of BMDC incubated for 4h with the same compounds and incubated with Hoechst dye (blue) for nuclear staining. c) Proliferation of OVA peptide-specific T cell populations induced by BMDC preincubated overnight with the indicated peptobrushes (mean \pm SEM; representative of 3 experiments each).

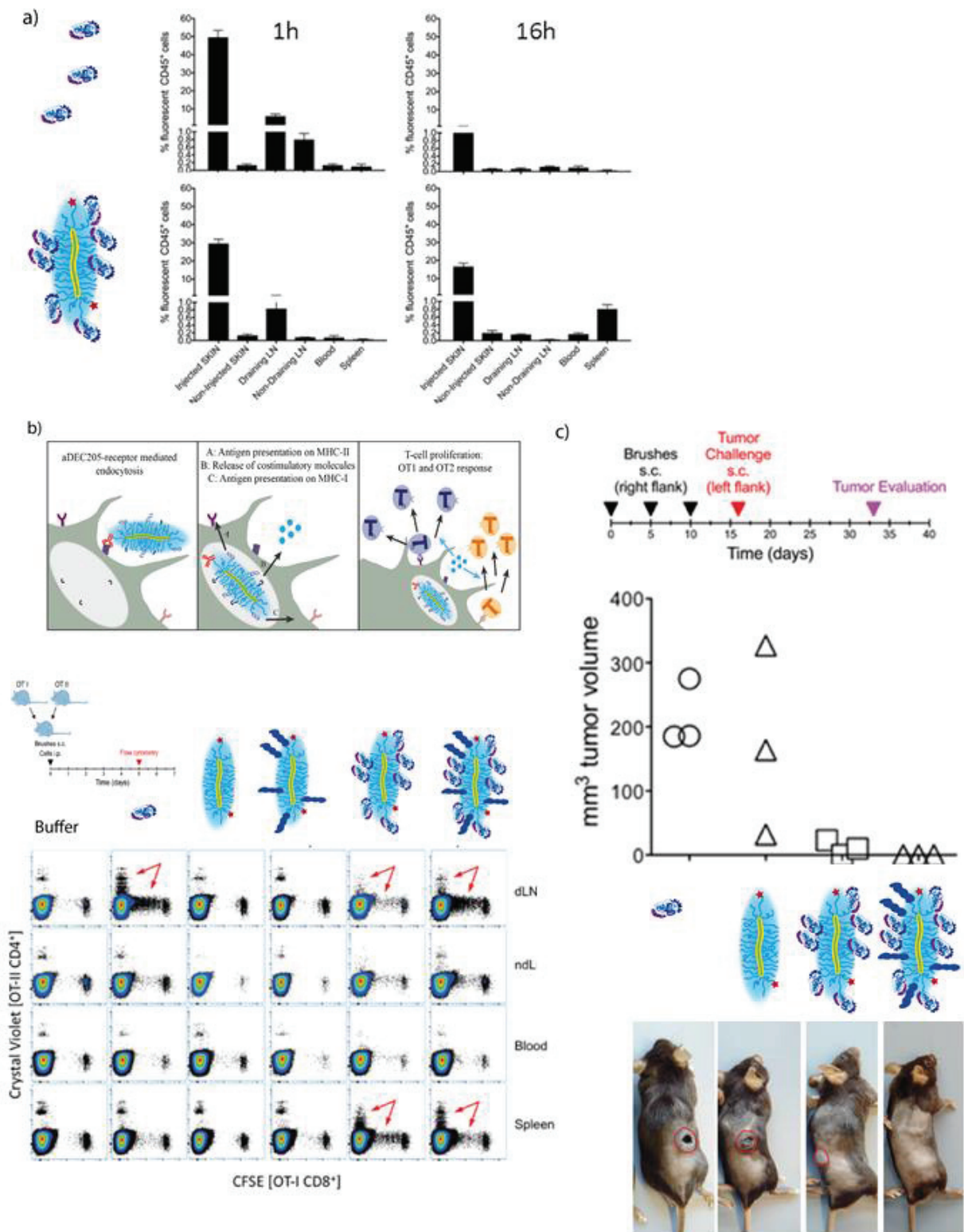


Figure 7: a) Flow cytometric analysis of skin, lymph nodes, blood and spleen after s.c. injection. Bars indicated the peptobrush positive CD45⁺ cells in % 1 hour and 16 hours after injection. b) Scheme of T cell response after engulfment of the peptobrush by dendritic and *in vivo* proliferation assay with OVA-peptide specific OTI and OTII mouse model, evaluation of T cell proliferation by flow cytometric analysis of blood, lymph nodes and spleen c) Protective vaccination B16/OVA tumor experiment; s.c. injection of PB, PB-OVA, PB-OVA-CpG and sOVA.

CONCLUSIONS

In this work we have demonstrated the synthesis of peptobrush based vaccines, which combine antibodies for dendritic cell targeting, antigens and immune activators among bottle brush polymers. The synthesis of bottle brush polymers with a lysine backbone and polysarcosine side chains allows to adjust the morphology of polypept(o)ide-based nanoparticles by the degree of polymerization of backbone and side chains. It is demonstrated that the formed peptobrushes have molecular weights of $2.2 \cdot 10^5$ to $10.4 \cdot 10^5$ g·mol⁻¹ and dispersity indices of 1.2-1.3, which underline the well-controlled synthesis. In addition, peptobrushes have been very well tolerated by cells, display low unspecific cellular uptake and do not cause any detectable aggregation of proteins in full serum. In line with these results, only a minor decrease in peptobrush concentration in blood of 40 % during 24 h could be observed in mice, clearly indicating a long circulation in mice (half times of 2 days). Thus, we have chosen these novel peptobrushes for further modification with antibodies for dendritic cell targeting (aDEC205), antigens (ovalbumin) and immune activators (CpG). Copper free strain promoted azide alkyne coupling enables the sequential chemoselective of all components onto the bottle brush polymers and allows the precise adjustment of the average number of each component. Remarkably even the final conjugate does not induce any protein aggregation in human serum, which motivates further research and development of peptobrushes for systemic vaccination in cancer therapy.

EXPERIMENTAL SECTION

Materials

DMF was purchased from Acros (99.8%, Extra Dry over Molecular Sieve) dried over BaO and distilled *in vacuo* followed by excessive stirring *in vacuo* to remove traces of dimethylamine. THF and hexane were purchased from Sigma Aldrich and distilled from sodium. DIPEA was purchased from Sigma Aldrich, dried over NaOH and freshly distilled prior to use. Triethylamine was purchased from Carl Roth and distilled from potassium hydroxide.

Used as received: aDEC205 antibody (DEC205/HB290, rat α mouse IgG2a), BioXCell; AlexaFluor647-DBCO, Invitrogen; AlexaFluor647-N₃, Invitrogen; AlexaFluor647-NHS Ester, Invitrogen; 4-azidobutyric acid, Chiralix; CpG-1826-DBCO, IBA; CW800-DBCO, LICOR; DBCO-PEG_{4-5/6}-Carboxyrhodamine 110, Jena Bioscience; DBCO-PEG₄-NHS Ester, Jena Bioscience; DMSO, Sigma Aldrich; DPBS (no calcium, no magnesium), Sigma Aldrich; poly(L-lysine trifluoroacetate) 100, Alamanda; poly(L-lysine trifluoroacetate) 250, Alamanda; EndoFit Ovalbumin, InvivoGen; Sarcosine, Sigma Aldrich; *Streptomyces griseus* Typ XIV, Sigma Aldrich.

Characterization

Static and Dynamic Light Scattering

The light scattering measurements were performed at 20 °C. All solutions were prepared in a dust free flow box and the cylindrical quartz cuvettes (Hellma, Mühlheim, Germany) were cleaned by dust free distilled acetone. Static light scattering (SLS) experiments were conducted by the following instrument: Apparatus 1 consists of an ALV SP86 goniometer, an ALV 3000 correlator, a Uniphase HeNe Laser (25 mW output power at $\lambda = 632.8$ nm wavelength) and an ALV/High QE APD avalanche diode fiber optic detection system. The scattered intensity was divided by a beam splitter (approximately 50:50), each portion of which was detected by a photomultiplier.

The two signals were cross correlated in order to minimize non-random electronic noise. Dynamic light scattering measurements were performed with a HeNe Laser (25 mW output power at $\lambda = 632.8$ nm, 25 mW) and an ALV-CGS 8F SLS/DLS 5022F goniometer with eight simultaneously working ALV 7004 correlators and eight QEAPD avalanche photodiode detectors. PB1, PB2 and PB3 were filtered through 0.2 μm pore size Millex GHP filters (Millipore). PLys1 and Plys2 were filtered through 0.02 μm pore size Whatman Anotop filters and 0.2 μm pore size Pall GHP filters.

The static scattering intensities were analyzed according to Zimm in order to yield the weight average molar mass, M_w , the square root of z-average mean square radius of gyration, $R_g = \langle R_g^2 \rangle_z^{0.5}$, and the second virial coefficient A_2 . The experimental uncertainties are estimated to be $\pm 5\%$ for M_w and R_g . The correlation functions of the particles showed a monomodal decay and were fitted using a sum of two exponentials. The z-average diffusion coefficient D_z was calculated by extrapolating D_{app} for $q = 0$. By formal application of Stokes law, the inverse z-average hydrodynamic radius is $R_h = \langle R_h^{-1} \rangle_z^{-1}$. The experimental uncertainties are estimated to $\pm 2\%$ for R_h . The experimental uncertainties are estimated to $\pm 2\%$ for R_h . For static light scattering, stock solutions of each sample were prepared. PB1, PB2 and PB3 were filtered through 0.2 μm pore size Pall GHP filters. The measurements were done in 20 mm diameter quartz cuvettes (Hellma). Further dilutions were made by subsequent addition of 0.2 μm pore size Pall GHP filtered solvent into the LS cuvette and the respective concentrations were obtained by weighing.

To investigate the aggregation behavior of PB4 in human plasma, plasma pooled from 6 patients was used. The plasma was obtained from the University Medical Center of the Johannes Gutenberg University Mainz (Germany). The plasma was filtered through a Millex GS 0.22 μm filter (Millipore). PB4 and DPBS were filtered through 0.2 μm pore size Millex GHP filters (Millipore). The following mixtures have been prepared: plasma:DPBS 9:1 and plasma:PB4 9:1 ($c_{PB4} = 3.4 \cdot 10^{-8}$ M). The cuvettes were incubated for 20 min at room temperature before measurement.

UV-VIS Spectroscopy

Measurements were done on a Carry 100 Bio UV-VIS Spectrometer (Varian, Inc). The spectra were analyzed with Cary Win UV Scan Application (V 02.00(25)).

Fluorescence Correlation Spectroscopy

The fluorescence correlation spectroscopy (FCS) experiments with AlexaFluor647 dye were performed using a commercial setup (Zeiss, Germany) consisting of the module ConfoCor 2 and an inverted microscope model Axiovert 200 with a Zeiss C-Apochromat $40 \times /1.2$ W water immersion objective. Dyes were excited by a HeNe laser (633 nm). Fluorescence light was filtered (LP650 long pass emission filter) and collected by an avalanche photodiode that enables single-photon counting. Eight-well polystyrene-chambered coverglass (Laboratory-Tek, Nalge Nunc International) was used as a sample cell. For each sample, a series of 10 measurements (10 s each) were performed. The experimental autocorrelation curves were fitted with a single component, free 3D diffusion analytical model function to obtain the diffusion coefficient and consequently through the Stokes-Einstein equation the hydrodynamic radius of the fluorescent species. The confocal observation volume was calibrated using Alexa Fluor 647 as a reference dye with a known diffusion coefficient. The fluorescence correlation spectroscopy (FCS) experiments with 800CW dye were performed on a LSM880 confocal microscope (Zeiss, Germany) coupled to a FCS detection module (PicoQuant, Germany). In all experiments a Zeiss C-Apochromat $40 \times /1.2$ W water immersion objective was used. The studied fluorophores were excited either at 633 nm or 780 nm and the fluorescence light detected after filtering with respectively LP650 or LP800 long pass emission filters. Eight-well polystyrene-chambered coverglass (Laboratory-Tek, Nalge Nunc International) was used as a sample cell. For each sample, a series of 10 measurements (30 s each) were performed. The experimental autocorrelation curves were fitted with a single component, free 3D diffusion analytical model function to obtain the diffusion coefficient and consequently through the Stokes-Einstein equation the hydrodynamic radius of the fluorescent species.

Fluorescence Spectroscopy

Fluorescence spectra were recorded using Jasco FP-6500 (ETC-273) Spectrometer equipped with the software FP-6500 JASCO-SpectraManager, Spectrum Measurement. For NIR dye labeled samples two fluorometers were used. Fluorometer 1 is a LS55 fluorometer from Perkin Elmer. The spectra were analyzed with the BL Studio (Basic FI). Fluorometer 2 is a Plate Reader Infinite™ 200 PRO (Tecan Life Sciences). The spectra were analyzed with Tecan i-control (V 1.10.4.0).

Gel permeation Chromatography (HFIP-GPC)

Hexafluoroisopropanol (HFIP) gel permeation chromatography (GPC) was performed with HFIP containing 3 g/l potassium trifluoroacetate as eluent at 40°C and a flow rate of 0.8 mL min⁻¹. The columns were packed with modified silica (PFG columns; particle size: 7 µm, porosity: 100 & 1000 Å). Polymers were detected with a refractive index detector (G 1362A RID, JASCO) and a UV/Vis Detector (UV-2075 Plus, JASCO). Molecular weights were calculated using a calibration performed with PMMA standards (Polymer Standards Services GmbH) and toluene as internal standard. Elution diagrams were analyzed using WinGPC UniChrome 8.00 (Build 994) software from Polymer Standards Services. All solutions were filtered through a 200 nm Filter.

Preparative Gel Permeation Chromatography

For purification of aDEC205-DBCO, OVA-DBCO or brush-conjugates preparative SEC was performed using a Sepharose 4 FF XK 16/70 column (GE Healthcare Life Sciences), a L-2310 LaChrom Elite (Hitachi) and a 2487 UV-detector (Waters). The UV-VIS absorption was measured at 220 nm. The spectra were analyzed with the software Chromatographica V1.0.26. DPBS buffer was used as an eluent and the flow rate was set to 0.5 mL·min⁻¹. The column was cleaned every 7 days with 1 M NaOH over night at 0.5 mL·min⁻¹, followed by 72 h with 0.1 M NaOH at 0.1 mL·min⁻¹.

Infrared Spectroscopy

Attenuated total reflectance Fourier transformed infrared (ATR-FTIR) spectroscopy was performed on a FT/IR-4100 (JASCO) with an ATR sampling accessory (MIRacle™, Pike Technologies). IR Spectra were analyzed using Spectra Manager 2.0 (JASCO).

Melting Point

The melting point of Sarcosine-NCA was determined using a METTLER FP62 (METTLER WAAGEN GMBH).

PAGE

The SDS PAGE was performed in a XCell Surelock Mini-Cell using precast NuPAGE Novex™ 4-12% Bis-Tris gels. The gels were run in a 1x NUPAGE™ SDS MES running buffer, usually at a constant voltage of 200 V for 35 min. The samples were diluted with 2.5 µl NuPAGE™ LDS sample buffer and Milli-Q water to a final volume of 10 µl. Novex™ Sharp Pre-stained Protein Standard was chosen for molecular weight estimation. The gels were stained with SimplyBlue™ SafeStain following the standard protocol. To proof the absence of unbound CpG, TBE Urea PAGE was performed in a XCell Surelock Mini-Cell using precast denaturing Novex™ 15 % TBE-Urea gels. The gels were run in a 1x TBE running buffer, usually at a constant voltage of 180 V for 75 min. The samples were diluted with 5 µl TBE-Urea sample buffer and Milli-Q water to a final volume of 10 µl. The gels were stained with SYBR Green™ II following the standard protocol. Upon excitation at 365 nm, fluorescence was imaged with a conventional digital camera. All components were purchased from Invitrogen and used as received.

Zetasizer

Measurements of the zeta potential were performed in 10 mM NaCl at 1 g·L⁻¹ with a Zetasizer Nano ZS (Malvern).

Atomic Force Microscopy

Measurements were performed with a Veeco MultiMode Scanning Probe Microscope and a Nanoscope IIIa Controller. All micrographs were taken in the Tapping mode. The samples were spin coated on mica. For measurements on the dried samples, Olympus OMCL-AC160-W2 cantilevers with a resonance frequency of 300 kHz (spring constant 42 N/m) were utilized. The length and width were analyzed with the software Pen.

¹H-NMR/¹⁹F-NMR

300 MHz ¹H-NMR spectra were recorded on a Bruker AC 300. 400 MHz ¹H-NMR and ¹⁹F-NMR measurements were performed on a Bruker Avance III HD 400. All spectra were recorded at room temperature and analyzed with MestReNova software.

Enzymatic degradation

The enzymatic degradation of the PBs was evaluated after the addition of the protease *Streptomyces griseus*. 2 mg protease (*Streptomyces griseus* Typ XIV, Sigma Aldrich) was dissolved in 1 mL protease buffer (10 mM Natriumacetate, 5 mM Calciumacetate, pH 7) and added to 20 mg PB dissolved in 1 mL protease buffer. The mixture was incubated at 37 °C. An aliquot was taken at the indicated timepoints (Fig. S3), lyophilized and analyzed by HFIP-GPC.

Endotoxin Assay

Pierce™ LAL Chromogenic Endotoxin Quantitation Kit (Thermo Fisher) was used following the standard protocol to determine the endotoxin values of the samples.

MTT Assay

Cytotoxic effects of polymer brushes were evaluated by MTT assay. For this, cells (each 5x10⁴/ml) of the mouse DC-like cell line DC2.4 and the human embryonic kidney cell line

(HEK293) were seeded in wells (each 100 μ l) of 96-well cell culture-treated plates. On the next day, polymer brushes were applied to triplicates at different concentrations (50-5,000 μ g/ml) as indicated. Samples treated with DMSO at cytotoxic concentration (10%) served as a negative control, and samples treated with DPBS (10%) as a solvent control. On the next day, the metabolic activity of the cells was assayed by sequential addition of MTT substrate and of stop solution as recommended by the manufacturer (Promega, Heidelberg, Germany). Formazan product quantification was performed using an ELISA plate reader.

Generation of bone marrow-derived DC (BMDC)

Mouse (C57BL/6) bone marrow cells were seeded in 12 well plates (2×10^5 in 1 ml) or bacterial dishes (\varnothing 10 cm; 2×10^6 /10 ml) in culture medium consisting of IMDM media containing 2 mM L-glutamine, 100 U/ml penicillin, 100 μ g/ml streptomycin (all from Sigma-Aldrich, Deisenhofen, Germany), and 50 μ M β -mercaptoethanol (Roth, Karlsruhe, Germany) supplemented with 5% FCS (Sigma-Aldrich) and 10 ng/ml recombinant murine GM-CSF (R&D Systems, Wiesbaden, Germany). Media were replenished on days 3 and 6 of culture, and BMDC were subjected to experiments on days 7-8 of culture. For treatment, on days 7-8 the sample volume was adjusted to 1 ml, and agents were applied as indicated.

Flow cytometric analysis

BMDC were harvested from bacterial dishes, reseeded in sterile FACS tubes (2×10^6 /500 μ l), and incubated with CW800-labeled brushes (each 10^{12}) for 3h in parallel at 4 $^{\circ}$ C and 37 $^{\circ}$ C. Then, samples were washed, and Fc gamma receptors were blocked by incubation with an appropriate rat anti-mouse antibody (clone 2.4G2; room temperature, 10 min). Samples were incubated with BV421-anti-CD11c (clone N418; BioLegend; San Diego, CA) for 20 min at 4 $^{\circ}$ C. Samples left untreated served as controls. After antibody incubation, samples were washed, resuspended in PBS/0.7% paraformaldehyde, and fluorescence intensities were assessed employing an Attune Nxt flow cytometer (ThermoFisher). Data were analyzed using FlowJo software (FLOWJO, Ashland, OR).

Confocal laser scanning microscopy (CLSM)

The volume of BMDC differentiated in 12 well plates was adjusted to 1ml, and cells were incubated with pLys FD and peptobrushes (each 10^{12} /sample) as indicated for 4h. Then, cells were washed, and nuclei were stained with Hoechst dye (2 μ M) for 30. Afterwards, samples were washed. The imaging of the cells was performed in ivbiTreat μ -slides (IBIDI, Germany) using a TCS SP5 confocal microscope (Leica), and Leica LAS AF software.

T cell proliferation assays

The volume of BMDC cultures set up in 12 well plates was adjusted to 1 ml, and differentially functionalized peptobrushes (10^{12} /sample), OVA protein (Merck, Darmstadt, Germany), or DBCO-modified OVA, and CpG ODN 1826 (Invivogen, San Diego, CA) were applied. On the next day, samples were harvested and thoroughly washed. Syngeneic OVA peptide-reactive CD4⁺ (OT-II) and CD8⁺ (OT-I) splenic T cells were isolated by negative immuno-magnetic separation as recommended by the manufacturer (Miltenyi Biotec, Bergisch-Gladbach, Germany). T cell purity usually exceeded 90% as assessed by flow cytometry. Titrated numbers of BMDC (starting concentration 5×10^4 /well) were cocultured with T cells (each 10^4) in triplicates (200 μ l volume) in 96-well cell culture plates for 96 h. T cell proliferation was detected by incorporation of ³H thymidine applied for the last 16h of coculture in a β counter (1205 Betaplate; LKB Wallac, Turku, Finland).

In vivo fluorescence imaging in zebrafish embryos

We used zebrafish embryos with fluorescent vasculature, tg(fli1a:EGFP) which were kept in embryo water (Cosma et al 2006, Current protocols in microbiology) containing phenylthiourea (0.003% Aldrich) at a temperature of 28,5 °C. All experiments conducted were approved by the Norwegian food safety authority. Microinjections were performed in the posterior caudal vein of 2-day old zebrafish embryos. For this, solutions of peptobrushes were loaded in a borosilicate needle (GC100T-10, Harvard Instruments) previously made using a pipette puller (P-97 Sutter

Instruments). The needles were in turn connected to a Eppendorf Femtojet express pump and micromanipulated using a Narishige MN-153 instrument. The injections were performed on previously sedated (Tricaine 0.02 % in embryo water) zebrafish larvae and placed on a dish containing hardened agarose (2% in milliQ water). In order to analyze the circulation of peptobrushes, zebrafish embryos were imaged after the injection at different times using a Leica DFC365FX stereomicroscope with a 1.0X planapo lens. For each embryo an image of the caudal region was taken at 120X while one of the whole fish was taken at 30X. For obtaining absolute values, the average fluorescence measured in three selected sites of the caudal artery (120X image) was normalized relative to the overall fluorescence of the zebrafish (30X image). These measurements were obtained using the program Fiji. The conversion of these absolute values into percentages was made by considering 0% the value associated to polylysine NP at 5 minutes while 100% was considered the value of peptobrushes 5 minutes post injection. Videos of Peptobrushes and Polylysine NP were made with a high speed Andor Dragonfly Spinning disc using a Nikon 60X 1.4 NA Lens.

In vivo fluorescence imaging in mice

In vivo fluorescence imaging of NIR dye 800CW-DBCO-labeled brushes (PB NIRD) was performed with the IVIS Spectrum Imaging system (Perkin Elmer). Briefly, mice were anesthetized with isoflurane prior to injection of the brush intravenously and were transferred to the light-tight chamber of the imaging system. 150 μ L of PB NIRD in DPBS ($C_{\text{NIR-Dye}} = 1.5 \cdot 10^{-5}$ M) were injected per mouse. Whole body imaging was performed at indicated time points using the filter set at 745 nm for excitation and at 800 nm for emission with an integration time of 3 sec. *Ex vivo* imaging of the organs was performed using the same instrumental setting. Blood kinetics were determined by retrieval of blood at indicated time points upon brush injection followed by *ex vivo* imaging as described above.

Synthesis

Synthesis of Sarcosine N-Carboxyanhydride

The synthesis of sarcosine NCA was adapted from literature and modified.⁶⁹ A total of 20.52 g (230.2 mmol) sarcosine, dried under vacuum for 1 h, was weighed into a pre-dried, three-neck, round-bottom flask. A total of 300 mL of abs. THF was added under a steady flow of nitrogen and 22.3 mL (184 mmol) of diphosgene were added slowly via syringe, and the nitrogen stream was reduced. The colorless suspension was mildly refluxed for 3 h, yielding a clear solution. Afterward, a steady flow of dry nitrogen was led through the solution for another 3 h while the outlet was connected to two gas washing bottles filled with aqueous NaOH solution to neutralize phosgene. The solvent was evaporated under reduced pressure, yielding a brownish oil as a crude reaction product. The oil was dried under reduced pressure ($1 \cdot 10^{-3}$ mbar for 2 h) to obtain an amorphous solid, free of phosgene and HCl, confirmed by testing against silver nitrate solution. The crude product was redissolved in 40 mL of THF and precipitated with 300 mL of dry hexane. The solution was cooled to -18 °C overnight to complete precipitation. The solid was filtered under dry nitrogen atmosphere and dried in a stream of dry nitrogen for 60–90 min and afterwards under high vacuum for 2 h in the sublimation apparatus. The crude product was sublimated at 85 °C and $1 \cdot 10^{-3}$ mbar. The product was collected from the sublimation apparatus in a glovebox on the same day. The purified product (156 mmol, 68% yield, colorless crystallites; melting point: 102–104 °C (lit.⁶⁹ 102-105 °C) was stored in a Schlenk tube at -80 °C and only handled in a glovebox.

¹H NMR (300 MHz, CDCl₃): δ [ppm] = 4.22 (2 H, s, -CH₂-CO-), 2.86 (3 H, s, -CH₃).

Synthesis of Azido-butyricacid Pentafluorophenylester

1 g of γ -azido butyric acid (7.74 mmol) was dissolved in pre dried THF. After adding 2.15 mL triethylamine (15.0 mmol, 2 eq.) the solution was stirred for 30 min at room temperature. Two equivalents of pentafluorophenol trifluoro acetat (2.66 mL, 15.0 mmol) were added dropwise with a syringe and the reaction mixture was stirred over night at room temperature. Completion of the reaction was verified with thin layer chromatography (TLC). After THF was distilled, the remaining solid was taken up in dichloromethane and three times extracted with water. The organic phase was dried with $MgSO_4$ and DCM was distilled off the product. The product was purified by column chromatography.

1H NMR (400 MHz, $CDCl_3$): δ [ppm] = 3.46 (2 H, t, $-CH_2-CH_2-CH_2-N_3$), 2.80 (2 H, t, $-CH_2-CH_2-CH_2-N_3$), 2.05 (2 H, m, $-CH_2-CH_2-CH_2-N_3$).

^{19}F NMR (400 MHz, $CDCl_3$): δ [ppm] = -153.95 (2F, d, *o*-CF), -158.90 (1F, t, *p*-CF), -163.32 (2F, t, *m*-CF).

Synthesis of Peptobrushes (PBI)

The following stock solutions were prepared directly before use and under dry nitrogen atmosphere: 228 mg DIPEA in 3.7 mL DMF, 7.83 g Sarcosine NCA in 40 mL DMF and 218 mg azido-butyricacid pentafluorophenylester in 2 mL DMF. The following operations are done under a steady flow of dry nitrogen. 0.44 mL (193 μ mol) of DIPEA-DMF was added *via* syringe to a schlenk tube containing 39 mg (160 μ mol) poly(L-lysine trifluoroacetate) (DP = 102) dissolved in 2 mL DMF solution. After 1 hour stirring, 4.6 mL (8 mmol) Sarcosine NCA in DMF was added. The solution was stirred at room temperature and kept at a constant pressure of 1.25 bar of dry nitrogen via the Schlenk line to prevent impurities from entering the reaction vessel while allowing CO_2 to escape. When the reaction was finished (completion of the reaction was confirmed by IR spectroscopy by the disappearance of the NCA peaks), 0.52 mL azido-butyricacid pentafluorophenylester in DMF (1.2 fold excess based on the amine groups) was added

and the reaction mixture was stirred for 2 days at 40°C. The final azide functionalized polymer brush was precipitated in ether and centrifuged (4500 rpm at 4°C for 15 min). After discarding the liquid fraction, fresh ether was added, and the polymer was resuspended using a sonic bath. The suspension was centrifuged again, and the procedure was repeated. The polymer was dissolved in MilliQ water, centrifuged with Amicon Ultra Centrifugal Filters (50 kDa, 4000xg, 4x20 min). After lyophilization, a colorless product was obtained. Yield: 73%. The characterization of PB1 is described in the text and summarized in table 1.

Synthesis of Peptobrushes (PB2)

The synthesis of PB2 was carried out similar to PB1 using 0.45 mL DIPEA (198 μmol) dissolved in DMF, 40 mg (165 μmol) poly(L-lysine trifluoroacetate) (DP = 102), 9.5 mL (16 mmol) Sarcosine NCA in DMF and 0.53 mL azido-butyracacid pentafluorophenylester in DMF. Yield: 59%. The characterization of PB2 is described in the text and summarized in table 1.

Synthesis of Peptobrushes (PB3)

The synthesis of PB3 was carried out similar to PB1 using 0.80 mL DIPEA (351 μmol) dissolved in DMF, 71 mg (292 μmol) poly(L-lysine trifluoroacetate) (DP = 258), 16.8 mL (29 mmol) Sarcosine NCA in DMF and 0.95 mL azido-butyracacid pentafluorophenylester in DMF. Yield: 63%. The characterization of PB3 is described in the text and summarized in table 1.

Dye labeling of Peptobrushes

The dyes DBCO-PEG4-5/6-Carboxyrhodamine 110, AlexaFluor647-DBCO and 800CW-DBCO were conjugated to the peptobrushes *via* SPAAC. In a typical experiment, PB was dissolved in DPBS ($c_{\text{PB}} = 50 \text{ g}\cdot\text{L}^{-1}$) and the dye was dissolved in DMSO ($c_{\text{Dye}} = 5 \text{ mM}$). As the reaction is quantitative, 1 equivalent of the desired amount of dyes per brush was added. After incubation over night at rt under light exclusion, the reaction mixture was purified by Amicon Ultra Centrifugal Filter Devices to remove unbound dye (15 mL, 50 kDa, 4000xg, 10 times). The

resulting solution was concentrated with Amicon Ultra Centrifugal Filter Devices (50 kDa, 4000xg) and filtered through sterile 0.22 μm Millex-GS filters. R_h was measured by DLS and FCS. FCS was also used to proof the absence of unconjugated dye and to determine the number of dyes per brush. To evaluate quenching effects, emission spectra of the free dye and the dye labeled PB were recorded, using solutions of the same optical density. If quenching effects were detected, the number of dyes determined by FCS were corrected by the amount of quenching.

Synthesis of DBCO-functionalized OVA and aDEC205

In a typical experiment, 2 eq. DBCO-PEG₄-NHS-Ester (dissolved in DMSO, $c = 10 \text{ g}\cdot\text{L}^{-1}$) were added to aDEC205 or OVA. aDEC205 was used as received (dissolved in buffer, $c_{\text{aDEC205}} = 4 - 7 \text{ g}\cdot\text{L}^{-1}$) and OVA was dissolved in DPBS ($c_{\text{OVA}} = 14 \text{ g}\cdot\text{L}^{-1}$). After incubation over night at rt, the reaction mixture was purified by Amicon Ultra Centrifugal Filter Devices (15 mL, 10 kDa, 4000xg, 10 times) to remove unbound DBCO-PEG₄-NHS-Ester and NHS. Afterwards preparative SEC was performed using a Sepharose 4 FF XK 16/70 column (flow 0.5 ml·min⁻¹) to remove aggregates. OVA-DBCO (fraction 90 – 110 mL) and aDEC205-DBCO (fraction 80 – 110 mL) The resulting solution was concentrated with Amicon Ultra Centrifugal Filter Devices (10 kDa, 4000xg) and filtered through sterile 0.22 μm Millex-GS filters. Yield: 80 – 90 %. $R_{h,\text{OVA-DBCO}} = 3.3 \text{ nm}$. $R_{h,\text{aDEC205}} = 5.8 \text{ nm}$. The OVA and aDEC205 concentrations as well as the number of DBCO per bioactive component were determined by UV-VIS spectroscopy as described in the SI.

Synthesis of dye labeled PLys250

20 mg PLys258 (320 nmol) were dissolved in 2 mL DPBS. 1 mg AlexaFluor647-NHS Ester (2.5 eq., 800 nmol) dissolved in 160 μL DMSO was added and the reaction mixture was incubated over night at rt under light exclusion. Purification was done with Amicon Ultra Centrifugal Filter Devices (15 mL, 10 kDa, 4000xg, 20 times). $R_h(\text{FCS}) = 7.6 \text{ nm}$. The number of dyes per molecule is 2.

Synthesis of PB conjugates with OVA and aDEC205

The synthesis of OVA and aDEC205 Peptobrush conjugates is similar for both bioactive components. The amount of the DBCO-modified component that needs to be added depends on the number of DBCO per component (N_{DBCO} between 1 – 2, see Fig. S9). $1/(0.34 \cdot N_{DBCO})$ equivalents of the DBCO modified component (dissolved in DPBS, $c_{OVA-DBCO/aDEC205-DBCO} = 5 - 15 \text{ g} \cdot \text{L}^{-1}$) were added to the dye labeled brush dissolved in DPBS ($c_{PB} = 1 \cdot 10^{-5} - 1 \cdot 10^{-6} \text{ M}$). The reaction mixture was incubated over night at rt. To remove bridged brushes and unconjugated bioactive components, PB3-conjugates were purified *via* preparative SEC using a Sepharose 4 FF XK 16/70 column (flow $0.5 \text{ ml} \cdot \text{min}^{-1}$). The fraction from 55 mL to 75 mL was collected. For PB1-conjugates, two columns were coupled. For PB1-OVA-conjugates 110 mL to 145 mL and for PB1-aDEC205-conjugates 100 mL to 130 mL were collected. The fractions were concentrated using Amicon Ultra Centrifugal Filter Devices (50 kDa, 4000xg) and filtered through sterile $0.22 \text{ } \mu\text{m}$ Millex-GS filters. Each conjugate was analyzed by DLS, FCS, UV-VIS spectroscopy and SDS-PAGE as described in the discussion. The calculation of the average number of bioactive components per brush is described in the SI.

Synthesis of PB conjugates with CpG

The synthesis of OVA and aDEC205 Peptobrush conjugates is similar for both bioactive components. The amount of the DBCO-modified component that needs to be added depends on the number of DBCO per component (N_{DBCO} between 1 – 2, see Fig. S9). $1/(0.34 \cdot N_{DBCO})$ 1.1 equivalents of CpG-DBCO ($c_{CpG-DBCO} = 100 \text{ } \mu\text{mol} \cdot \text{L}^{-1}$) were added to the dye labeled brush dissolved in DPBS ($c_{PB} = 1 \cdot 10^{-5} - 1 \cdot 10^{-6} \text{ M}$). The reaction mixture was incubated over night at rt followed by purification with Amicon Ultra Centrifugal Filter Devices (15 mL, 50 kDa, 4000xg, 10 times) to remove unbound CpG-DBCO. After filtration through sterile $0.22 \text{ } \mu\text{m}$ Millex-GS filters the conjugate was analyzed by DLS, FCS, UV-VIS spectroscopy and TBE Urea PAGE as described in the discussion. The calculation of the average number of CpG per brush is described in the SI.

The authors would like to thank [REDACTED] for support with fluorescence measurements and [REDACTED] for analyzing NMR.

REFERENCES

- (1) Fujita, Y.; Taguchi, H. Current Status of Multiple Antigen-Presenting Peptide Vaccine Systems: Application of Organic and Inorganic Nanoparticles. *Chem. Cent. J.* **2011**, *5* (1), 48. <https://doi.org/10.1186/1752-153X-5-48>.
- (2) Hawiger, D.; Inaba, K.; Dorsett, Y.; Guo, M.; Mahnke, K.; Rivera, M.; Ravetch, J. V.; Steinman, R. M.; Nussenzweig, M. C. Dendritic Cells Induce Peripheral T Cell Unresponsiveness under Steady State Conditions in Vivo. *J. Exp. Med.* **2001**, *194* (6), 769–780. <https://doi.org/10.1084/jem.194.6.769>.
- (3) Petrovsky, N.; Aguilar, J. C. Vaccine Adjuvants: Current State and Future Trends. *Immunol. Cell Biol.* **2004**, *82* (5), 488–496. <https://doi.org/10.1111/j.0818-9641.2004.01272.x>.
- (4) Sakaguchi, S.; Yamaguchi, T.; Nomura, T.; Ono, M. Regulatory T Cells and Immune Tolerance. *Cell* **2008**, *133* (5), 775–787. <https://doi.org/10.1016/j.cell.2008.05.009>.
- (5) Gabrilovich, D. I.; Nagaraj, S. Myeloid-Derived Suppressor Cells as Regulators of the Immune System. *Nat. Rev. Immunol.* **2009**, *9* (3), 162–174. <https://doi.org/10.1038/nri2506>.
- (6) Cruz, L. J.; Rosalia, R. A.; Kleinovink, J. W.; Rueda, F.; Löwik, C. W. G. M.; Ossendorp, F. Targeting Nanoparticles to CD40, DEC-205 or CD11c Molecules on Dendritic Cells for Efficient CD8+T Cell Response: A Comparative Study. *J. Control. Release* **2014**, *192*, 209–218. <https://doi.org/10.1016/j.jconrel.2014.07.040>.

- (7) Rosalia, R. A.; Cruz, L. J.; van Duikeren, S.; Tromp, A. T.; Silva, A. L.; Jiskoot, W.; de Gruijl, T.; Löwik, C.; Oostendorp, J.; van der Burg, S. H.; et al. CD40-Targeted Dendritic Cell Delivery of PLGA-Nanoparticle Vaccines Induce Potent Anti-Tumor Responses. *Biomaterials* **2015**, *40*, 88–97. <https://doi.org/10.1016/j.biomaterials.2014.10.053>.
- (8) Tacke, P. J.; Zeelenberg, I. S.; Cruz, L. J.; van Hout-Kuijer, M. A.; van de Glind, G.; Fokkink, R. G.; Lambeck, A. J. A.; Figdor, C. G. Targeted Delivery of TLR Ligands to Human and Mouse Dendritic Cells Strongly Enhances Adjuvanticity. *Blood* **2011**, *118* (26).
- (9) van Broekhoven, C. L.; Parish, C. R.; Demangel, C.; Britton, W. J.; Altin, J. G. Targeting Dendritic Cells with Antigen-Containing Liposomes: A Highly Effective Procedure for Induction of Antitumor Immunity and for Tumor Immunotherapy. *Cancer Res.* **2004**, *64* (12), 4357–4365. <https://doi.org/10.1158/0008-5472.CAN-04-0138>.
- (10) Kwon, Y. J.; James, E.; Shastri, N.; Fréchet, J. M. J. In Vivo Targeting of Dendritic Cells for Activation of Cellular Immunity Using Vaccine Carriers Based on PH-Responsive Microparticles. *Proc. Natl. Acad. Sci. U. S. A.* **2005**, *102* (51), 18264–18268. <https://doi.org/10.1073/pnas.0509541102>.
- (11) Johnson, T. S.; Mahnke, K.; Storn, V.; Schönfeld, K.; Ring, S.; Nettelbeck, D. M.; Haisma, H. J.; Le Gall, F.; Kontermann, R. E.; Enk, A. H. Inhibition of Melanoma Growth by Targeting of Antigen to Dendritic Cells via an Anti-DEC-205 Single-Chain Fragment Variable Molecule. *Clin. Cancer Res.* **2008**, *14* (24).
- (12) Bühler, J.; Gietzen, S.; Reuter, A.; Kappel, C.; Fischer, K.; Decker, S.; Schäffel, D.; Koynov, K.; Bros, M.; Tubbe, I.; et al. Selective Uptake of Cylindrical Poly(2-Oxazoline) Brush-AntiDEC205 Antibody-OVA Antigen Conjugates into DEC-Positive Dendritic Cells and Subsequent T-Cell Activation. *Chem. - A Eur. J.* **2014**, *20* (39), 12405–12410. <https://doi.org/10.1002/chem.201403942>.

- (13) Grabbe, S.; Landfester, K.; Schuppan, D.; Barz, M.; Zentel, R. Nanoparticles and the Immune System: Challenges and Opportunities. *Nanomedicine* **2016**, *11* (20), 2621–2624. <https://doi.org/10.2217/nmm-2016-0281>.
- (14) Shen, L.; Tenzer, S.; Storck, W.; Hobernik, D.; Raker, V. K.; Fischer, K.; Decker, S.; Dzionek, A.; Krauthäuser, S.; Diken, M.; et al. Protein Corona-mediated Targeting of Nanocarriers to B Cells Allows Redirection of Allergic Immune Responses. *J. Allergy Clin. Immunol.* **2018**, 1–13. <https://doi.org/10.1016/j.jaci.2017.08.049>.
- (15) Frey, M.; Bobbala, S.; Karabin, N.; Scott, E. Influences of Nanocarrier Morphology on Therapeutic Immunomodulation. *Nanomedicine* **2018**, nmm-2018-0052. <https://doi.org/10.2217/nmm-2018-0052>.
- (16) Mottram, P. L.; Leong, D.; Crimeen-Irwin, B.; Gloster, S.; Xiang, S. D.; Meanger, J.; Ghildyal, R.; Vardaxis, N.; Plebanski, M. Type 1 and 2 Immunity Following Vaccination Is Influenced by Nanoparticle Size: Formulation of a Model Vaccine for Respiratory Syncytial Virus. *Mol. Pharm.* **2007**, *4* (1), 73–84. <https://doi.org/10.1021/mp060096p>.
- (17) Kumar, S.; Anselmo, A. C.; Banerjee, A.; Zakrewsky, M.; Mitragotri, S. Shape and Size-Dependent Immune Response to Antigen-Carrying Nanoparticles. *J. Control. Release* **2015**, *220*, 141–148. <https://doi.org/10.1016/j.jconrel.2015.09.069>.
- (18) Swartz, M. A.; Hirose, S.; Hubbell, J. A. Engineering Approaches to Immunotherapy. *Sci. Transl. Med.* **2012**, *4* (148), 1–12. <https://doi.org/10.1126/scitranslmed.3003763>.
- (19) Irvine, D. J.; Hanson, M. C.; Rakhra, K.; Tokatlian, T. Synthetic Nanoparticles for Vaccines and Immunotherapy. *Chem. Rev.* **2015**, *115* (19), 11109–11146. <https://doi.org/10.1021/acs.chemrev.5b00109>.
- (20) Yi, S.; Allen, S. D.; Liu, Y. G.; Ouyang, B. Z.; Li, X.; Augsornworawat, P.; Thorp, E. B.;

- Scott, E. A. Tailoring Nanostructure Morphology for Enhanced Targeting of Dendritic Cells in Atherosclerosis. *ACS Nano* **2016**, *10* (12), 11290–11303. <https://doi.org/10.1021/acsnano.6b06451>.
- (21) Dykman, L. A.; Staroverov, S. A.; Fomin, A. S.; Khanadeev, V. A.; Khlebtsov, B. N.; Bogatyrev, V. A. Gold Nanoparticles as an Adjuvant: Influence of Size, Shape, and Technique of Combination with CpG on Antibody Production. *Int. Immunopharmacol.* **2018**, *54* (June 2017), 163–168. <https://doi.org/10.1016/j.intimp.2017.11.008>.
- (22) Niikura, K.; Matsunaga, T.; Suzuki, T.; Kobayashi, S.; Yamaguchi, H.; Orba, Y.; Kawaguchi, A.; Hasegawa, H.; Kajino, K.; Ninomiya, T.; et al. Gold Nanoparticles as a Vaccine Platform: Influence of Size and Shape on Immunological Responses in Vitro and in Vivo. *ACS Nano* **2013**, *7* (5), 3926–3938. <https://doi.org/10.1021/nn3057005>.
- (23) Silva, A. L.; Rosalia, R. A.; Varypataki, E.; Sibuea, S.; Ossendorp, F.; Jiskoot, W. Poly-(Lactic-Co-Glycolic-Acid)-Based Particulate Vaccines: Particle Uptake by Dendritic Cells Is a Key Parameter for Immune Activation. *Vaccine* **2015**, *33* (7), 847–854. <https://doi.org/10.1016/j.vaccine.2014.12.059>.
- (24) Wendorf, J.; Chesko, J.; Kazzaz, J.; Ugozzoli, M.; Vajdy, M.; O'Hagan, D.; Singh, M. A Comparison of Anionic Nanoparticles and Microparticles as Vaccine Delivery Systems. *Hum. Vaccin.* **2008**, *4* (1), 44–49. <https://doi.org/10.4161/hv.4.1.4886>.
- (25) Zhang, M.; Müller, A. H. E. Cylindrical Polymer Brushes. *J. Polym. Sci. Part A Polym. Chem.* **2005**, *43* (16), 3461–3481. <https://doi.org/10.1002/pola.20900>.
- (26) Wintermantel, M.; Schmidt, M.; Tsukahara, Y.; Kajiwara, K.; Kohjiya, S. Rodlike Combs. *Macromol. Rapid Commun.* **1994**, *15* (3), 279–284. <https://doi.org/10.1002/marc.1994.030150315>.

- (27) Wintermantel, M.; Gerle, M.; Fischer, K.; Schmidt, M.; Wataoka, I.; Urakawa, H.; Kajiwara, K.; Tsukahara, Y. Molecular Bottlebrushes †. *Macromolecules* **1996**, *29* (3), 978–983. <https://doi.org/10.1021/ma950227s>.
- (28) Dziezok, P.; Fischer, K.; Schmidt, M.; Sheiko, S. S.; Möller, M. Cylindrical Molecular Brushes. *Angew. Chemie Int. Ed. English* **1997**, *36* (24), 2812–2815. <https://doi.org/10.1002/anie.199728121>.
- (29) Gerle, M.; Fischer, K.; Roos, S.; Müller, A. H. E.; Schmidt, M.; Sheiko, S. S.; Prokhorova, S.; Möller, M. Main Chain Conformation and Anomalous Elution Behavior of Cylindrical Brushes As Revealed by GPC/MALLS, Light Scattering, and SFM. *Macromolecules* **1999**, *32* (8), 2629–2637. <https://doi.org/10.1021/ma9816463>.
- (30) Beers, K. L.; Gaynor, S. G.; Matyjaszewski, K.; Sheiko, S. S.; Moeller, M. Synthesis of Densely Grafted Copolymers by Atom Transfer Radical Polymerization. *Macromolecules* **1998**, *31* (26), 9413–9415. <https://doi.org/10.1021/ma981402i>.
- (31) Börner, H. G.; Beers, K.; Matyjaszewski, K.; Sheiko, S. S.; Möller, M. Synthesis of Molecular Brushes with Block Copolymer Side Chains Using Atom Transfer Radical Polymerization. *Macromolecules* **2001**, *34* (13), 4375–4383. <https://doi.org/10.1021/ma010001r>.
- (32) Cheng, G.; Böker, A.; Zhang, M.; Krausch, G.; Müller, A. H. E. Amphiphilic Cylindrical Core-Shell Brushes via a “Grafting from” Process Using ATRP. *Macromolecules* **2001**, *34* (20), 6883–6888. <https://doi.org/10.1021/ma0013962>.
- (33) Deffieux, A.; Schappacher, M. Synthesis and Characterization of Star and Comb Polystyrenes Using Isometric Poly(Chloroethyl Vinyl Ether) Oligomers as Reactive Backbone. *Macromolecules* **1999**, *32* (6), 1797–1802. <https://doi.org/10.1021/ma981612v>.

- (34) Schappacher, M.; Deffieux, A. New Polymer Chain Architecture: Synthesis and Characterization of Star Polymers with Comb Polystyrene Branches. *Macromolecules* **2000**, *33* (20), 7371–7377. <https://doi.org/10.1021/ma0001436>.
- (35) Schlüter, A. D.; Rabe, J. P. Dendronized Polymers: Synthesis, Characterization, Assembly at Interfaces, and Manipulation. *Angew. Chemie Int. Ed.* **2000**, *39* (5), 864–883. [https://doi.org/10.1002/\(SICI\)1521-3773\(20000303\)39:5<864::AID-ANIE864>3.0.CO;2-E](https://doi.org/10.1002/(SICI)1521-3773(20000303)39:5<864::AID-ANIE864>3.0.CO;2-E).
- (36) Barner, J.; Mallwitz, F.; Shu, L.; Schlüter, A. D.; Rabe, J. P. Covalent Connection of Two Individual Polymer Chains on a Surface: An Elementary Step towards Molecular Nanoconstructions. *Angew. Chemie Int. Ed.* **2003**, *42* (17), 1932–1935. <https://doi.org/10.1002/anie.200250059>.
- (37) Zhang, A.; Zhang, B.; Wächtersbach, E.; Schmidt, M.; Schlüter, A. D. Efficient Synthesis of High Molar Mass, First- to Fourth-Generation Distributed Dendronized Polymers by the Macromonomer Approach. *Chem. - A Eur. J.* **2003**, *9* (24), 6083–6092. <https://doi.org/10.1002/chem.200305142>.
- (38) Hörtz, C.; Birke, A.; Kaps, L.; Decker, S.; Wächtersbach, E.; Fischer, K.; Schuppan, D.; Barz, M.; Schmidt, M. Cylindrical Brush Polymers with Polysarcosine Side Chains: A Novel Biocompatible Carrier for Biomedical Applications. *Macromolecules* **2015**, *48* (7), 2074–2086. <https://doi.org/10.1021/ma502497x>.
- (39) Barz, M.; Luxenhofer, R.; Zentel, R.; Vicent, M. J. Overcoming the PEG-Addiction: Well-Defined Alternatives to PEG, from Structure–property Relationships to Better Defined Therapeutics. *Polym. Chem.* **2011**, *2* (9), 1900–1918. <https://doi.org/10.1039/C0PY00406E>.
- (40) Klinker, K.; Barz, M. Polypept(o)ides: Hybrid Systems Based on Polypeptides and

- Polypeptoids. *Macromol. Rapid Commun.* **2015**, *36* (22), 1943–1957.
<https://doi.org/10.1002/marc.201500403>.
- (41) Huesmann, D.; Sevenich, A.; Weber, B.; Barz, M. A Head-to-Head Comparison of Poly(Sarcosine) and Poly(Ethylene Glycol) in Peptidic, Amphiphilic Block Copolymers. *Polym. (United Kingdom)* **2015**, *67*, 240–248.
<https://doi.org/10.1016/j.polymer.2015.04.070>.
- (42) Holm, R.; Klinker, K.; Weber, B.; Barz, M. Synthesis of Amphiphilic Block Copolypept (o) Ides by Bifunctional Initiators : Making PeptoMicelles Redox Sensitive. 2083–2091.
- (43) Fokina, A.; Klinker, K.; Braun, L.; Jeong, B. G.; Bae, W. K.; Barz, M.; Zentel, R. Multidentate Polysarcosine-Based Ligands for Water-Soluble Quantum Dots. *Macromolecules* **2016**, *49* (10), 3663–3671.
<https://doi.org/10.1021/acs.macromol.6b00582>.
- (44) Heller, P.; Mohr, N.; Birke, A.; Weber, B.; Reske-Kunz, A.; Bros, M.; Barz, M. Directed Interactions of Block Copolypept(o) Ides with Mannose-Binding Receptors: Peptomicelles Targeted to Cells of the Innate Immune System. *Macromol. Biosci.* **2015**, *15* (1), 63–73. <https://doi.org/10.1002/mabi.201400417>.
- (45) Heller, P.; Birke, A.; Huesmann, D.; Weber, B.; Fischer, K.; Reske-Kunz, A.; Bros, M.; Barz, M. Introducing PeptoPlexes: Polylysine-Block-Polysarcosine Based Polyplexes for Transfection of HEK 293T Cells. *Macromol. Biosci.* **2014**, *14* (10), 1380–1395.
<https://doi.org/10.1002/mabi.201400167>.
- (46) Makino, A.; Hara, E.; Hara, I.; Ozeki, E.; Kimura, S. Size Control of Core-Shell-Type Polymeric Micelle with a Nanometer Precision. *Langmuir* **2014**, *30* (2), 669–674.
<https://doi.org/10.1021/la404488n>.

- (47) Yamamoto, F.; Yamahara, R.; Makino, A.; Kurihara, K.; Tsukada, H.; Hara, E.; Hara, I.; Kizaka-Kondoh, S.; Ohkubo, Y.; Ozeki, E.; et al. Radiosynthesis and Initial Evaluation of ¹⁸F Labeled Nanocarrier Composed of Poly(L-Lactic Acid)-Block-Poly(Sarcosine) Amphiphilic Polydepsipeptide. *Nucl. Med. Biol.* **2013**, *40* (3), 387–394. <https://doi.org/10.1016/j.nucmedbio.2012.12.008>.
- (48) Birke, A.; Huesmann, D.; Kelsch, A.; Weilbacher, M.; Xie, J.; Bros, M.; Bopp, T.; Becker, C.; Landfester, K.; Barz, M. Polypeptoid-Block-Polypeptide Copolymers: Synthesis, Characterization, and Application of Amphiphilic Block Copolypeptides in Drug Formulations and Miniemulsion Techniques. *Biomacromolecules* **2014**, *15* (2), 548–557. <https://doi.org/10.1021/bm401542z>.
- (49) Weber, B.; Birke, A.; Fischer, K.; Schmidt, M.; Barz, M. Solution Properties of Polysarcosine: Absolute and Relative Molar Mass Determinations. *Macromolecules* **2018**, *51* (7), 2653–2661. <https://doi.org/10.1021/acs.macromol.8b00258>.
- (50) Wick, P.; Manser, P.; Limbach, L. K.; Dettlaff-Weglikowska, U.; Krumeich, F.; Roth, S.; Stark, W. J.; Bruinink, A. The Degree and Kind of Agglomeration Affect Carbon Nanotube Cytotoxicity. *Toxicol. Lett.* **2007**, *168* (2), 121–131. <https://doi.org/10.1016/J.TOXLET.2006.08.019>.
- (51) Chambers, B. A.; Afroz, A. R. M. N.; Bae, S.; Aich, N.; Katz, L.; Saleh, N. B.; Kirisits, M. J. Effects of Chloride and Ionic Strength on Physical Morphology, Dissolution, and Bacterial Toxicity of Silver Nanoparticles. *Environ. Sci. Technol.* **2014**, *48* (1), 761–769. <https://doi.org/10.1021/es403969x>.
- (52) Rausch, K.; Reuter, A.; Fischer, K.; Schmidt, M. Evaluation of Nanoparticle Aggregation in Human Blood Serum. *Biomacromolecules* **2010**, *11* (11), 2836–2839. <https://doi.org/10.1021/bm100971q>.

- (53) Fenaroli, F.; Repnik, U.; Xu, Y.; Johann, K.; Van Herck, S.; Dey, P.; Skjeldal, F. M.; Frei, D. M.; Bagherifam, S.; Kocere, A.; et al. Enhanced Permeability and Retention-like Extravasation of Nanoparticles from the Vasculature into Tuberculosis Granulomas in Zebrafish and Mouse Models. *ACS Nano* **2018**, acsnano.8b04433. <https://doi.org/10.1021/acsnano.8b04433>.
- (54) Matsumura, Y.; Maeda, H. A New Concept for Macromolecular Therapeutics in Cancer Chemotherapy: Mechanism of Tumoritropic Accumulation of Proteins and the Antitumor Agent Smancs. *Cancer Res.* **1986**, *46* (12 Pt 1), 6387–6392.
- (55) Maeda, H.; Wu, J.; Sawa, T.; Matsumura, Y.; Hori, K. Tumor Vascular Permeability and the EPR Effect in Macromolecular Therapeutics: A Review. *J. Control. Release* **2000**, *65* (1–2), 271–284.
- (56) Gomez-Garcia, M. J.; Doiron, A. L.; Steele, R. R. M.; Labouta, H. I.; Vafadar, B.; Shepherd, R. D.; Gates, I. D.; Cramb, D. T.; Childs, S. J.; Rinker, K. D. Nanoparticle Localization in Blood Vessels: Dependence on Fluid Shear Stress, Flow Disturbances, and Flow-Induced Changes in Endothelial Physiology. *Nanoscale* **2018**, *10* (32), 15249–15261. <https://doi.org/10.1039/C8NR03440K>.
- (57) Sieber, S.; Grossen, P.; Detampel, P.; Siegfried, S.; Witzigmann, D.; Huwyler, J. Zebrafish as an Early Stage Screening Tool to Study the Systemic Circulation of Nanoparticulate Drug Delivery Systems in Vivo. *J. Control. Release* **2017**, *264* (August), 180–191. <https://doi.org/10.1016/j.jconrel.2017.08.023>.
- (58) Campbell, F.; Bos, F. L.; Sieber, S.; Arias-Alpizar, G.; Koch, B. E.; Huwyler, J.; Kros, A.; Bussmann, J. Directing Nanoparticle Biodistribution through Evasion and Exploitation of Stab2-Dependent Nanoparticle Uptake. *ACS Nano* **2018**, *12* (3), 2138–2150. <https://doi.org/10.1021/acsnano.7b06995>.

- (59) Evensen, L.; Johansen, P. L.; Koster, G.; Zhu, K.; Herfindal, L.; Speth, M.; Fenaroli, F.; Hildahl, J.; Bagherifam, S.; Tulotta, C.; et al. Zebrafish as a Model System for Characterization of Nanoparticles against Cancer. *Nanoscale* **2016**, *8* (2), 862–877. <https://doi.org/10.1039/C5NR07289A>.
- (60) Fenaroli, F.; Westmoreland, D.; Benjaminsen, J.; Kolstad, T.; Skjeldal, F. M.; Meijer, A. H.; Van Der Vaart, M.; Ulanova, L.; Roos, N.; Nyström, B.; et al. Nanoparticles as Drug Delivery System against Tuberculosis in Zebrafish Embryos: Direct Visualization and Treatment. *ACS Nano* **2014**, *8* (7), 7014–7026. <https://doi.org/10.1021/nn5019126>.
- (61) Negwer, I.; Best, A.; Schinnerer, M.; Schäfer, O.; Capeloa, L.; Wagner, M.; Schmidt, M.; Mailänder, V.; Helm, M.; Barz, M.; et al. Monitoring Drug Nanocarriers in Human Blood by Near-Infrared Fluorescence Correlation Spectroscopy. *Nat. Commun.* **2018**, *9* (1), 5306. <https://doi.org/10.1038/s41467-018-07755-0>.
- (62) Fasting, C.; Schalley, C. A.; Weber, M.; Seitz, O.; Hecht, S.; Koksche, B.; Dervedde, J.; Graf, C.; Knapp, E. W.; Haag, R. Multivalency as a Chemical Organization and Action Principle. *Angew. Chemie - Int. Ed.* **2012**, *51* (42), 10472–10498. <https://doi.org/10.1002/anie.201201114>.
- (63) Bertozzi, C. R.; Kiessling, L. L. Chemical Glycobiology. *Science (80-.)*. **2001**, *291* (5512), 2357–2364.
- (64) Kiessling, L. L.; Gestwicki, J. E.; Strong, L. E. Synthetic Multivalent Ligands as Probes of Signal Transduction. *Angew. Chemie - Int. Ed.* **2006**, *45* (15), 2348–2368. <https://doi.org/10.1002/anie.200502794>.
- (65) Hang, H. C.; Yu, C.; Kato, D. L.; Bertozzi, C. R. A Metabolic Labeling Approach toward Proteomic Analysis of Mucin-Type O-Linked Glycosylation. *Proc. Natl. Acad. Sci.* **2003**, *100* (25), 14846–14851. <https://doi.org/10.1073/pnas.2335201100>.

- (66) Agard, N. J.; Baskin, J. M.; Prescher, J. A.; Lo, A.; Bertozzi, C. R. A Comparative Study of Bioorthogonal Reactions with Azides. *ACS Chem. Biol.* **2006**, *1* (10), 644–648.
- (67) Gietzen, S. *Synthese Und Charakterisierung von Polymer-Wirkstoff-Antikörper Konjugaten Zur Anwendung in Der Krebsimmuntherapie*, 2015.
- (68) Weiner Rasmussen, G. J.; Davis, H. L.; Waldschmidt, M.; Ballas, Z. K.; Krieg, A. M.; Warren, T.; Rasmussen, W.; Weiner, G. J. CpG Motifs Distinct Effects of Oligodeoxynucleotides with Divergent Therapeutic and Immunologic Divergent Therapeutic and Immunologic Effects of Oligodeoxynucleotides with Distinct CpG Motifs. *J Immunol Ref. J. Immunol.* **2016**, *167*, 4878–4886. <https://doi.org/10.4049/jimmunol.167.9.4878>.
- (69) Fetsch, C.; Grossmann, A.; Holz, L.; Nawroth, J. F.; Luxenhofer, R. Polypeptoids from N-Substituted Glycine n-Carboxyanhydrides: Hydrophilic, Hydrophobic, and Amphiphilic Polymers with Poisson Distribution. *Macromolecules* **2011**, *44* (17), 6746–6758. <https://doi.org/10.1021/ma201015y>.
- (70) Available online: <http://www.kerafast.com/PDF/A134.pdf> (accessed on 01 August 2018).